Real Time Observables for the Quark-Gluon Plasma from the Lattice

Dissertation
zur Erlangung des Doktorgrades
der Naturwissenschaften

vorgelegt beim Fachbereich 13
der Johann Wolfgang Goethe-Universität
in Frankfurt am Main

von
Christian Schäfer
aus Warendorf

Frankfurt am Main 2014
D30

vom Fachbereich Physik der
Johann Wolfgang Goethe-Universität als Dissertation angenommen.

Dekan: Prof. Dr. J. Stroth

Gutachter: Prof. Dr. O. Philipsen
Prof. Dr. D. Rischke

Datum der Disputation:

Zusammenfassung

Das Standardmodell der Teilchenphysik beschreibt die kleinsten Bausteine der Materie. Im Rahmen einer Quantenfeldtheorie erklärt es die elektromagnetische, schwache und starke Wechselwirkung der Elementarteilchen. Der Erfolg des Standardmodells geht auf die überragende Übereinstimmung seiner Voraussagen mit dem Experiment zurück. Als ein aktuelles Beispiel führen wir den 2013 erbrachten experimentellen Nachweis des Higgs Bosons an, welches bereits 1964 von Brout, Englert und Higgs innerhalb des Standardmodells vorhergesagt wurde.

Die starke Wechselwirkung ist für den Zusammenhalt unserer Materie auf kleinsten Skalen verantwortlich. Ihre fundamentale Beschreibung erfolgt über die Quantenchromodynamik (QCD), welche mathematisch eine nicht-abelsche Eichtheorie mit Symmetriegruppe SU(3) darstellt. Sie erklärt das Zusammenspiel der Konstituenten hadronischer Materie, den Quarks und Gluonen. Dabei wird die Erfahrungstatsache, dass freie Quarks nicht beobachtet werden können, als *confinement* bezeichnet. Ein weiterer wesentlicher Bestandteil der QCD ist der Aspekt der asymptotischen Freiheit, welche besagt, dass mit steigender Energieskala die Stärke der Wechselwirkung zwischen den Quarks abnimmt. Bereits in den 1970er Jahren realisierte man, dass bei hohen Energien die asymptotische Freiheit zumindest eine partielle Auflösung des *confinements* zur Folge haben muss. Dieser neue Zustand der QCD-Materie wird als Quark-Gluon-Plasma bezeichnet und ist zentraler Forschungsgegenstand dieser Dissertation.

Die zur Produktion eines Quark-Gluon-Plasmas benötigte hohe Energiedichte kann in Schwerionenkollisionen an Teilchenbeschleunigern erreicht werden. Dabei werden schwere Atomkerne wie die von Blei oder Gold auf nahezu Lichtgeschwindigkeit beschleunigt und dann zum Zusammenstoß gebracht. Am Relativistic Heavy Ion Collider (RHIC) des Brookhaven National Laboratory wurden dabei erstmals 2005 experimentelle Hinweise auf ein Quark-Gluon-Plasma gefunden. Diese wurden in weiteren Experimenten am RHIC und am Large Hadron Collider (LHC) des Conseil Européen pour la Recherche Nucléaire (CERN) bestätigt. Die Beschleunigeranlage Facility for Antiproton and Ion Research (FAIR), welche sich gerade im Bau befindet, wird die Erforschung dieses neuen Materiezustands noch weiter vorantreiben. Neben dem Auftreten eines Quark-Gluon-Plasmas in Schwerionenkollisionen, favorisieren aktuelle kosmologische Modelle, dass dieser Zustand auch im frühen Universum existierte.

Eine besondere Eigenschaft, die dem Quark-Gluon-Plasmas zugeordnet wird, ist, dass es sich wie eine fast perfekte Flüssigkeit verhält. Diese Aussage folgt aus der Übereinstimmung einer Beschreibung des elliptischen Flusses in relativistischer Hydrodynamik mit experimentellen Daten. Die Berücksichtigung dissipativer Effekte in einer Flüssigkeit erfolgt über das Hinzufügen weiterer Terme zu den hydrodynamischen Bewegungsgleichungen. Diese Terme sind proportional zu Transportkoeffizienten, welche Parameter der Hydrodynamik darstellen und nicht aus dieser selbst hervorgehen. Die Transportkoeffizienten sind durch die zugrunde liegende mikroskopische Theorie festgelegt, welche im Fall des Quark-Gluon-Plasmas die QCD ist. Ein Ergebnis dieser Arbeit ist die Be-

rechnung des Transportkoeffizienten zweiter Ordnung κ im Rahmen der QCD.

Der zweite Forschungsschwerpunkt dieser Arbeit beschäftigt sich mit der Thermalisierung des Quark-Gluon-Plasmas. Die Beschreibung von aus Schwerionenkollisionen gewonnenen experimentellen Daten mit thermischen Modellen, insbesondere mit relativistischer Hydrodynamik, setzt ein zumindest lokales thermisches Gleichgewicht voraus. Durch die Lorentzkontraktion der beiden Schwerionen erwartet man, dass der Zustand direkt nach der Kollision durch eine Impulsanisotropie in der transversal-longitudinalen Ebene bestimmt wird. Somit setzt das Erreichen eines thermischen Gleichgewichts zunächst eine Isotropisierung voraus. Bisherige Studien haben gezeigt, dass gluonische Moden bei dieser Isotropisierung durch Verursachung einer Instabilität eine entscheidende Rolle spielen. Diese Instabilität soll analog zur Weibel Instabilität im elektromagnetischen Plasma verlaufen und wird deshalb unter Einbeziehung der Farbladung des gluonischen Feldes chromo-Weibel-Instabilität genannt. Alles bisherigen auf der QCD basierenden Betrachtungen der Isotropisierung durch eine chromo-Weibel-Instabilität beruhen nur auf der Dynamik gluonischer Felder und haben zumeist die Farbsymmetrie SU(2) benutzt. Ausgehend von der QCD untersuchen wir in dieser Arbeit die gluonische Dynamik mit der korrekten QCD-Farbsymmetrie SU(3) und schließen zum ersten Mal dynamische Fermionen in die Betrachtung mit ein.

Fundamentale theoretische Aussagen über Eigenschaften des Quark-Gluon-Plasmas setzen das Lösen des QCD-Pfadintegrals in einem thermischen System voraus. Als Folge der asymptotischen Freiheit wird die QCD bei Energien oder Temperaturen deutlich größer als die der intrinsischen Energieskala $\Lambda_{\mathrm{QCD}} \approx 200\,\mathrm{MeV}$ zu einer schwach gekoppelten Theorie und kann im Rahmen einer Störungsrechnung zu bestimmter Ordnung in der Kopplung gelöst werden. Allerdings werden in thermischen Systemen analytische Vorhersagen durch infrarote Divergenzen erschwert und durch das Linde Problem, welches ab einer gewissen Ordnung einen Zusammenbruch der Störungsentwicklung verursacht, unmöglich. Die Einschränkung perturbativer Methoden auf schwache Kopplungen erlaubt deren Anwendung nur in einem kleinen Bereich des in einer Schwerionenkollision durchlaufenen Energiespektrums.

Die 1974 von Wilson eingeführte Gitterregularisierung ermöglicht einen nicht-perturbativen Zugang zur QCD. Diese beruht auf einem Übergang zu euklidischer Raumzeit durch eine Wickrotation, der Transformation reeller zu imaginärer Zeit, und einer anschließenden Diskretisierung der Raumzeit durch ein vierdimensionales hyperkubisches Gitter mit Gitterabstand a. Der endliche Gitterabstand dient als Regulator, indem er Impulse größer als $\frac{\pi}{a}$ abschneidet und so das Auftreten ultravioletter Divergenzen verhindert. Die Diskretisierung erlaubt es Pfadintegrale numerisch zu berechnen und somit QCD-Vakuumerwartungswerte auszuwerten. Analog zum Imaginärzeitformalismus der Quantenfeldtheorie in kontinuierlicher Raumzeit, kann auf dem Gitter die euklidische Zeitrichtung mit der Temperatur identifiziert werden, was die Berechnung von Erwartungswerten im thermischen Gleichgewicht ermöglicht. Mit der Gittereichtheorie existiert eine nichtperturbative Methode zur Berechnung von Observablen. Allerdings hilft sie uns durch ihre Beschränkung auf imaginäre Zeit beziehungsweise Systeme im thermischen Gleichgewicht in der Bestimmung von Transportkoeffizienten oder der Untersuchung von Isotropisierungsprozessen zunächst nicht weiter.

Transportkoeffizienten entsprechen den Proportionalitätskoeffizienten in hydrodynamischen Gleichungen, die die Relaxation einer Flüssigkeit oder eben eines Quark-Gluon-Plasmas von einer kleinen Störung beschreiben. Damit sind sie unmittelbar mit reeller

Zeit verknüpft und zunächst nicht durch die Gitter-QCD zugänglich. Als Folge des Fluktuations-Dissipations-Theorems lassen sie sich jedoch in Quantenfeldtheorien über Kubo-Formeln mit Gleichgewichtserwartungswerten retardierter Korrelatoren verknüpfen. Damit werden sie zwar für die QCD im thermischen Gleichgewicht zugänglich, jedoch nicht für die Gitter-QCD. Diese ist durch die Wickrotation zu euklidischer Raumzeit auf die Berechnung euklidische Korrelatoren beschränkt. Der Transportkoeffizient κ ist dadurch ausgezeichnet, dass er eine triviale analytische Fortsetzung vom euklidischen zum retardierten Korrelator besitzt und somit direkt in Gittereichtheorie berechnet werden kann. Im Gegensatz zur Scherviskosität oder elektrischen Leitfähigkeit müssen für die analytische Fortsetzung keine weiteren Annahmen wie zum Beispiel die Maximum-Entropie-Methode getroffen werden.

Der Prozess der Isotropisierung findet unmittelbar nach der Kollision der Schwerionen statt und läuft somit fern vom Gleichgewicht ab. Weiterhin ist die Isotropisierung ein dynamischer Vorgang dessen Betrachtung echte Zeit benötigt. Deshalb ist die Standardformulierung der Gittereichtheorie keine geeignete Methode zur Beschreibung des Isotropisierungsprozesses. Allerdings lassen sich die für das Problem relevanten niederenergetischen gluonischen Moden klassisch nähern. Dabei nutzen wir eine Gitterregularisierung, um die Moden mit hohen Impulsen abzuschneiden. Die Diskretisierung der Raumzeit ermöglicht eine numerische Behandlung der mit einer klassischen Theorie verknüpften Bewegungsgleichungen. Diese spiegeln die Dynamik des Systems wieder. Intrinsische Eigenschaften des Systems werden durch Anfangsbedingungen festgelegt.

Die beiden in dieser Arbeit vorgestellten Zugänge werden verwendet, um auf reeller Zeit basierende Observablen, sogenannte *real time observables*, des Quark-Gluon-Plasmas zu bestimmen. Wir präsentieren die Bestimmung des Transportkoeffizienten κ in Gittereichtheorie für das Yang-Mills-Plasma. Weiterhin untersuchen wir den durch eine chromo-Weibel-Instabilität angetriebenen Prozess der Isotropisierung des Quark-Gluon-Plasmas unter Verwendung der korrekten QCD-Farbsymmetrie SU(3) und dem Einschluss dynamischer Fermionen.

Nach der Einleitung werden im zweiten und dritten Kapitel die theoretischen Grundlagen vorgestellt. In Kapitel 2 beschäftigen wir uns mit der QCD im Kontinuum und der Einführung der Temperatur. Insbesondere leiten wir die analytische Fortsetzung vom euklidischen zum retardierten Korrelator her, welche in der Bestimmung des Transportkoeffizienten κ eine entscheidende Rolle spielt. Kapitel 3 behandelt die Formulierung der Yang-Mills-Theorie im thermischen Gleichgewicht auf dem Gitter. Wir diskutieren die Übertragung der vierdimensionalen euklidischen Raumzeit auf einen anisotropen Hyperkubus mit periodischen Randbedingungen sowie die Diskretisierung der Wirkung. Weiterhin stellen wir die Gitterstörungstheorie vor, welche perturbative Rechnungen in diskreter Raumzeit ermöglicht. Das Kapitel schließt mit der Vorstellung des benutzten numerischen Algorithmus' und einer Überprüfung der korrekten Implementierung.

Kapitel 4 behandelt die Bestimmung des Transportkoeffizienten κ. Wir beginnen mit seiner Definition in relativistischer Hydrodynamik. Transportkoeffizienten können systematisch mittels einer Gradientenentwicklung hergeleitet werden. Wir betrachten diese Entwicklung zu zweiter Ordnung in gekrümmter Raumzeit und finden neben fünfzehn weiteren Transportkoeffizienten zweiter Ordnung den Transportkoeffizienten κ. In Bezug auf das Quark-Gluon-Plasma sind alle gefundenen Transportkoeffizienten durch die zugrunde liegende mikroskopische Theorie – die QCD – festgelegt und über Kubo-Formeln mit retardierten Korrelatoren des Energie-Impuls-Tensors im thermischen Gleichgewicht

verknüpft. Der Transportkoeffizient κ geht aus einer Impulsentwicklung eines der retardierten Korrelatoren als führender Koeffizient hervor. Wie bereits angesprochen, besitzt der für den Transportkoeffizienten κ relevante retardierte Korrelator eine triviale analytische Fortsetzung zum euklidischen Korrelator, was eine Bestimmung des Transportkoeffizienten κ direkt in Gittereichtheorie ermöglicht.

Da eine Berechnung des Transportkoeffizienten κ unter Einbeziehung dynamischer Fermionen den Bereich numerischer Durchführbarkeit verlässt, bestimmen wir κ in reiner Gittereichtheorie. Dies erfordert zunächst eine Diskretisierung des Energie-Impuls-Tensors, welcher der Noetherstrom bezüglich Translationen ist. Da die Symmetrie unter Translationen auf dem Gitter reduziert ist, ist eine multiplikative Renormierung des Energie-Impuls-Tensors erforderlich. Auf einem anisotropen Gitter erfordert das die Bestimmung von zwei Renormierungskonstanten. Unser Renormierungsschema teilt sich in die nichtperturbative Bestimmung des Verhältnisses der beiden Renormierungskonstanten sowie eines absoluten Faktors auf. Das Verhältnis kann über zusätzliche Gittersimulationen aus Renormierungsgruppen-invarianten Observablen bestimmt werden. Den absoluten Faktor erhalten wir aus einer Identifikation der räumlichen Diagonalelemente des Energie-Impuls-Tensors mit dem Druck eines Yang-Mills-Plasmas, welcher aus Gittersimulationen bekannt ist.

Der benötigte Korrelator im Impulsraum geht aus einer Fouriertransformation des Energie-Impuls Korrelators hervor. Allerdings ist der Korrelator ultraviolett divergent, was eine additive Renormierung notwendig macht. Da die Divergenz temperaturunabhängig ist, entfernen wir sie durch eine Subtraktion des Vakuumerwartungswertes des Korrelators. Dadurch erfordert jede Berechnung des Transportkoeffizienten κ bei einer unterschiedlichen Temperatur eine zusätzliche Simulation mit erhöhter zeitlichen Gitterausdehnung.

Weiterhin ist zu beachten, dass der Transportkoeffizient κ aus einer Impulsentwicklung des Korrelators extrahiert wird, die nur für gegenüber der Temperatur kleine Impulse Gültigkeit besitzt. Diese Beschränkung führt dazu, dass für die numerische Bestimmung Gitter mit sehr vielen räumlichen Gitterpunkten benötigt werden. Wie nutzen ein anisotropes Gitter, um diese Anforderung abzuschwächen.

Wir berechnen den Transportkoeffizienten durch Monte-Carlo Simulationen für verschiedene Temperaturen sowie in Gitterstörungstheorie. Aufgrund der asymptotischen Freiheit ermöglicht die Simulation bei einer Temperatur von $T \approx 2,7\,\mathrm{GeV}$ den Vergleich mit der Berechnung in Gitterstörungstheorie. Wir finden eine Übereinstimmung beider Vorhersagen innerhalb der statistischen Fehler. Aus den weiteren Gittersimulationen extrahieren wir eine Temperaturabhängigkeit des Transportkoeffizienten $\kappa \sim T^2$. Dieses Resultat stimmt mit analytischen Berechnungen aus AdS/CFT (Anti-de Sitter/Conformal Field Theory) Korrespondenz und einer Yang-Mills-Schwachkopplungsentwicklung in idealer Gas Näherung überein. Mit einem über die bestimmten Temperaturen gemittelten Wert von $\kappa^{\mathrm{avr}} = 0.36(15)\,T^2$ liegt unser Ergebnis zwischen diesen beiden Vorhersagen, welche den Grenzfall starker und schwacher Kopplung darstellen. Am Ende des Kapitels stellen wir Forschungsperspektiven mit Hinblick auf eine Verringerung des statistischen Fehlers vor.

In Kapitel 5 führen wir das semi-klassische Modell der QCD auf dem Gitter ein. Im Bereich schwacher Kopplung und hoher gluonischen Besetzungen können die bosonischen Freiheitsgrade klassisch angenähert werden. Die unterdrückten hochenergetischen Moden werden durch eine Gitterregularisierung vollends abgeschnitten. Da für Fermionen

eine klassische Beschreibung nicht möglich ist, behandeln wir diese quantenmechanisch. Dazu führen wir im Rahmen der kanonischen Quantisierung eine Entwicklung der fermionischen Felder in Modenfunktionen durch. Die Zeitentwicklung der Fermionen ist dann über diese Modenfunktionen gegeben. Eine numerische Ausführung eines Zeitschrittes erfordert das Lösen der Dirac-Gleichung für jede Mode an jedem Gitterpunkt, also das Lösen eines Systems, das eine Anzahl proportional zum Quadrat des Gittervolumens an gekoppelten Differentialgleichungen enthält. Dieser hohe numerische Aufwand kann durch eine Approximation der Fermionen durch stochastische Fermionen reduziert werden. Dabei werden fermionische Korrelatoren durch einen entsprechenden Ensemble-Mittelwert stochastischer Fermionen ersetzt.

Auf dieser Basis leiten wir ausgehend von der QCD-Wirkung in diskreter Minkowski-Raumzeit über den Hamiltonformalismus die Bewegungsgleichungen des Systems her. Diese enthalten die gesamte Dynamik des Systems und sind durch die diskrete Raumzeit numerisch zugänglich. Über die Anfangsbedingungen werden intrinsische Eigenschaften des Systems festgelegt. Wir stellen eine Initialisierung der bosonischen und fermionischen Felder für ein thermisches Gleichgewicht vor und betrachten die QCD-Evolution, also die Dynamik bosonischer und fermionischer Felder mit Farbsymmetrie SU(3) in reeller Zeit, in drei räumlichen Dimensionen. Dabei finden wir während der Evolution einen Übertrag bosonischer Energie auf die Fermionen bis eine Saturierung einsetzt. In Abhängigkeit der gewählten Fermionenmasse erfolgt dieser Übertrag unterschiedlich schnell. Es ist das erste Mal, dass diese semi-klassische Näherung mit stochastischen Fermionen auf die QCD angewendet wird. Wir schließen mit einer Vorstellung von Einsatzmöglichkeiten des entworfenen Modells im thermischen Gleichgewicht.

Weiterhin benutzen wir das semi-klassische Gittermodell der QCD in Kapitel 6 um den Isotropisierungsprozess des in einer Schwerionenkollision erzeugten Quark-Gluon-Plasmas durch eine chromo-Weibel-Instabilität zu untersuchen. Die kollidierenden Ionen können als Farbglaskondensat beschrieben werden. Die Idee des Farbglaskondensats beruht auf der durch tiefinelastische Streuexperimente bei HERA gefundenen Erkenntnis, dass bei hohen Beschleunigerenergien die Gluonen die Partonverteilungsfunktion eines Nukleus dominieren. Eine Annahme im Modell ist, dass der Anteil der Gluonen soweit ansteigt, bis es auf Grund ihrer nichtlinearen Wechselwirkung zu einer Saturierung kommt. Diese Saturierung ist mit einem Impuls verknüpft, der deutlich größer als die QCD-Skala Λ_{QCD} ist. Somit sind diese Gluonen schwach gekoppelt und können in einer effektiven QCD-Theorie, der *colour glass condensate effective theory*, beschrieben werden. Sie erlaubt einen theoretischen Zugang zu den ersten Augenblicken einer Schwerionenkollision und wir nutzen eine entsprechende Übertragung auf den diskreten Raum zur Festlegung unserer Anfangsbedingungen im semi-klassischen Modell. Die schwache Kopplung und die hohe gluonische Besetzung erlaubt die Anwendung des Modells zur Beschreibung der Dynamik der ersten Phasen einer Schwerionenkollision.

Ausgehend von auf der Theorie des Farbglaskondensats basierenden Anfangsbedingungen untersuchen wir den Isotropisierungsprozess des Quark-Gluon-Plasmas. Der Grad der Isotropie kann durch das Verhältnis von longitudinalem zu transversalem Druck erfasst werden. Anzeichen für das Auftreten einer chromo-Weibel-Instabilität ist das Auffüllen des gluonischen Spektrums ausgehend von weichen Moden. Bezüglich der spektralen Zerlegung der gluonischen Felder führen wir eine neue Observable ein, die eichinvariant ist. Dadurch wird ein numerisch teures Fixieren der Eichung unnötig.

Zuerst studieren wir den Fall reiner Eichtheorie mit Farbsymmetrie SU(3). Dabei

finden wir Anzeichen für das Auftreten einer chromo-Weibel-Instabilität. Weiterhin findet eine Isotropisierung statt. Die dabei durchlaufene Dynamik des longitudinalen und transversalen Drucks gleicht der einer äquivalenten Studie mit Farbsymmetrie SU(2). Bezüglich der Isotropisierungszeit, also der Zeit wann ein bestimmtes Verhältnis von longitudinalem zu transversalem Druck erreicht ist, finden wir allerdings signifikante Unterschiede. Schließen wir Vakuumfermionen in die Betrachtung mit ein, finden wir wie schon im thermischen Gleichgewicht einen Energieübertrag von bosonischen zu fermionischen Freiheitsgraden. Weiterhin haben die Fermionen Einfluss auf die Dynamik der Isotropisierung und beeinflussen vor allem die Isotropisierungszeit.

In dieser ersten Studie haben wir gezeigt, dass die Einbeziehung fermionischer Freiheitsgrade eine Auswirkung auf den Isotropisierungsprozess hat. Die Betrachtung der korrekten QCD-Farbsymmetrie SU(3) hat auf die allgemeine Dynamik des Isotropisierungsprozesses keinen Einfluss, wohl aber auf die Extraktion konkreter Zahlen. Wir schließen das Kapitel mit Forschungsperspektiven für weitere Anwendungen des semiklassischen QCD-Modells fern vom Gleichgewicht.

Die Arbeit endet mit einer Zusammenfassung der Ergebnisse in Kapitel 7. Im Anhang folgen Anmerkungen zur Notation und mathematischen Konventionen (A), analytische Rechnungen bezüglich des Transportkoeffizienten κ (B) und Datensätze der zugehörigen numerischen Simulation, die eine Reproduktion erlauben (C). Weiterhin präsentieren wir die Herleitung der Bewegungsgleichungen des semi-klassischen Modells der QCD und die Einführung stochastischer Fermionen (D). In Anhang E gehen wir auf Diskretisierungsartefakte des semi-klassischen Modells ein.

Zusammenfassend beschäftigt sich diese Arbeit mit der Berechnung von dynamischen Größen und Prozessen des Quark-Gluon-Plasmas in der fundamentalen Theorie der starken Wechselwirkung – der QCD. Die Anwendung einer Gitterregularisierung erlaubt es, Aussagen über nichtperturbative Bereiche zu treffen. Durch Verwendung von Kubo-Formeln und einer klassisch-statistischen Näherung, ist es möglich, auf reeller Zeit basierende Größen, sogenannte *real time observables*, zu berechnen. Ausgehend von diesen Methoden haben wir unter Verwendung der Gittereichtheorie den Transportkoeffizienten κ für das Yang-Mills-Plasma bestimmt. Weiterhin haben wir mittels eines semi-klassischen Modells der QCD Isotropisierungsprozesse im Quark-Gluon-Plasma untersucht. Dabei haben wir zum ersten Mal Fermionen in die Dynamik mit eingeschlossen.

Contents

1 Introduction

Daß ich erkenne, was die Welt
Im Innersten zusammenhält [...].
— J. W. Goethe (1749–1832), Faust

Giving a scientifically established answer to the question raised in Goethe's quote took until the second half of the 20th century, i.e. when the standard model of particle physics was developed. This model constitutes a quantum field theory unifying the electromagnetic, weak and strong interactions between fundamental particles. Its great success derives from a wide variety of predictions coinciding excellently with experimental results, see for instance [1, 2] for an overview. One remarkable recent result is the discovery of the Higgs boson at the Large Hadron Collider (LHC) [3, 4], which had already been predicted by the standard model in 1964 by Brout and Englert [5] as well as Higgs [6]. The prediction was awarded with the Nobel prize 2013.

The existence of bound states of matter is explained by the theory of quantum chromodynamics (QCD) dealing with the strong interaction. QCD is a non-abelian gauge theory with symmetry group $\mathrm{SU}(N_c = 3)$ describing the interactions between quarks and gluons, both fundamental particles. QCD matter is characterised by two peculiar properties: On the one hand, there is colour confinement. It is the phenomenon that colour charged particles as quarks and gluons can not be isolated and thus escape direct observation. On the other hand, there is asymptotic freedom. It states that the interaction strength between those particles decreases as the energy is increased.

It was realised in the 1970s [7–9], that asymptotic freedom implies the existence of a state of matter with at least partially deconfined quarks and gluons at high energies – the quark-gluon plasma. Nowadays, findings of the experimental heavy ion programme at the collider facilities RHIC (Relativistic Heavy Ion Collider) and LHC (Large Hadron Collider) give evidence for the emergence of a quark-gluon plasma from heavy ion collisions [10–13]. In future the research programme at FAIR (Facility of Antiproton and Ion Research) is going to promote this exploration. Among others, enhanced strangeness production [14], jet quenching [15] as well as anomalous J/Ψ suppression and regeneration [16] are experimental signatures of a quark-gluon plasma. Alongside its occurrence in heavy ion collisions, it is assumed that the quark-gluon plasma was formed in the early stages of our universe and thus plays an important role in cosmology.

As indicated in the phase diagram of QCD (see figure 1.1 and [17, 18] for reviews), as the temperature T increases hadronic matter passes into a quark-gluon plasma. Simulations in lattice gauge theory allow a determination of the transition's nature as well as the critical temperature at vanishing chemical potential $\mu = 0$. Concerning pure gluodynamics, the Polyakov loop serves as an order parameter signalling spontaneous breaking of the centre symmetry and thus a transition to the deconfined phase at a critical temperature of $T_\mathrm{c} \approx 270\,\mathrm{MeV}$ [19]. Including dynamic fermions breaks the centre symmetry explicitly and instead of the Polyakov loop, one uses the chiral quark condensate as an

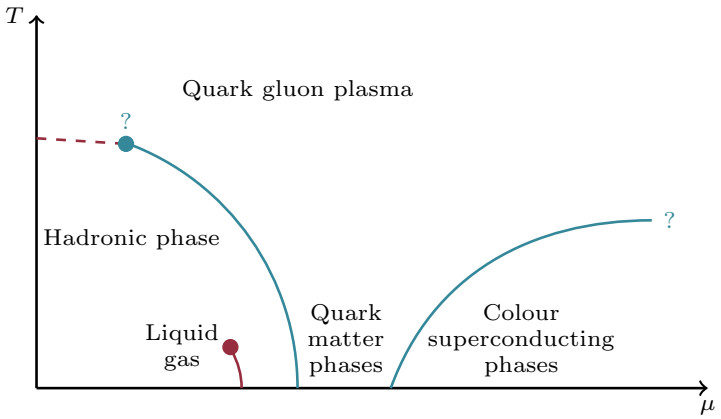

Figure 1.1: Phase diagram of QCD matter with temperature T and chemical potential μ. Increasing the chemical potential at low temperatures results in nuclear matter undergoing a first order liquid gas phase transition. Then one enters the hypothetical regime of quark matter phases and colour superconducting phases. Increasing the temperature at vanishing chemical potential, lattice simulations show that QCD matter undergoes a crossover to the quark-gluon plasma. The first order lines of the quark-gluon plasma transition are predictions of non-fundamental models. In particular the existence of a critical endpoint is an open question.

indicator for the transition to the deconfined phase[1]. One finds the transition to be a crossover with a pseudo-critical temperature in the range of $T_{\mathrm{pc}} \approx 150 - 170\,\mathrm{MeV}$ [20]. Since an inclusion of a finite chemical potential in lattice gauge theory is afflicted by the sign problem, see e.g. [19, 21], the other transition lines in figure 1.1 indicating a deconfinement transition or chiral restoration are based on QCD-inspired effective models like the Nambu-Jona-Lasinio model [22], but they are not first principle calculations. However, recent developments promise a workaround of the sign problem [23–26] and first perturbative QCD calculations including a finite chemical potential have been performed [27–29].

One of the most astonishing observations regarding the quark-gluon plasma is its behaviour as an almost ideal fluid. This conclusion is based on the fact that relativistic hydrodynamics excellently describes experimental data obtained in heavy ion collisions [30–36]. Figure 1.2 illustrates the success of hydrodynamic fits to Au+Au data from the PHOBOS and STAR experiments at RHIC. Whereas in the case of ideal hydrodynamics, the only input required is the equation of state, the case of viscous hydrodynamics including dissipative effects needs further parameters – the transport coefficients. Their theoretical prediction should be based on the underlying theory of the quark-gluon plasma, QCD. In this work we compute the second order transport coefficient κ from first principles employing the framework of lattice gauge theory at finite temperature.

Up to a few times the transition temperature of the quark-gluon plasma, the QCD coupling is not weak enough for perturbative methods to apply. Lattice gauge theory offers a non-perturbative evaluation of the QCD path integral by transferring Euclidean

[1] Strictly speaking the chiral quark condensate is an order parameter indicating restoration of chiral symmetry. The common believe is that deconfinement and chiral restoration occur at the same temperature.

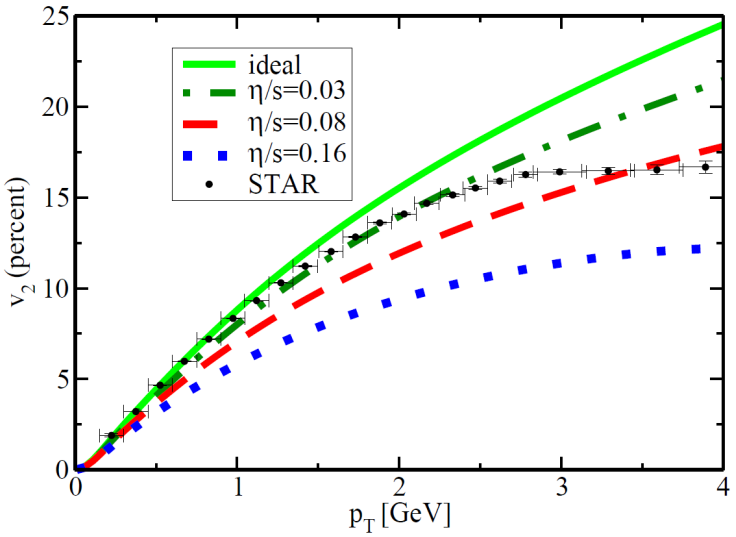

Figure 1.2: Elliptical flow v_2 versus transverse momentum p_T. The experimental data was taken from Au+Au collisions with a centre of mass energy of $\sqrt{S} = 200\,\mathrm{GeV}$ at RHIC and is fitted to relativistic hydrodynamics of various viscosity ratios η/s, where η is the shear viscosity and s the entropy density. Taken from [30].

space time to a hypercubic lattice. This renders the path integral finite dimensional and thus makes it amenable to numeric methods. Remarkable achievements of lattice gauge theory are the identification of the transition type of the quark-gluon plasma [20] as well as the computation of its equation of state [37] or the calculation of a variety of hadron masses in perfect accordance with their experimental values [38].

Unfortunately, lattice QCD is afflicted by a loss of real time due to the transition to Euclidean space time incorporating only imaginary time. Furthermore an investigation of thermal systems necessitates an identification of imaginary time with temperature restricting the application of lattice gauge theory to systems in thermal equilibrium. This is unfortunate because transport coefficients and many other phenomena of the quark-gluon plasma are of true dynamic nature, demanding a real time formulation. As a consequence, a calculation of transport coefficients like the shear viscosity [39] or electric conductivity [40, 41] is not directly possible in lattice gauge theory, but requires additional input, e.g. an ansatz for the spectral function or the use of the maximum entropy method. Among others the second order transport coefficient κ is special in the sense that its real time definition, based on a retarded correlator of the energy-momentum tensor, explicitly coincides with the corresponding Euclidean correlator, which is suitable for an evaluation using lattice gauge theory. Thus the transport coefficient κ is directly accessible from lattice gauge theory without having to resort to maximum entropy methods or functional input.

In this thesis we present the first computation of the second order transport coefficient κ from first principles using the framework of pure lattice gauge theory. We extract the transport coefficient from the low momentum expansion of a suitable two-point function of the energy-momentum tensor. In order to approach the zero momentum limit, very large lattices are required, demanding an enormous numeric effort already in pure gauge theory. Additionally, the need for additive and multiplicative renormalisation

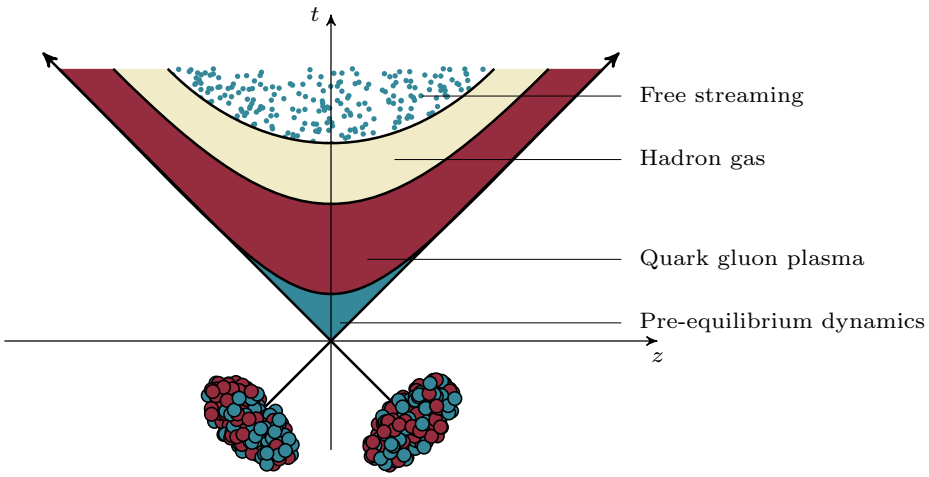

Figure 1.3: Space time evolution of a heavy ion collision. The two nuclei collide at time $t \approx 0\,\mathrm{fm/c}$. After a time $t \approx 1\,\mathrm{fm/c}$ the produced medium is equilibrated and a quark-gluon plasma is formed. Due to the longitudinal expansion (z-direction in the sketch) the medium cools down until the temperature drops below the confinement temperature T_c. Consequently, matter reenters the hadronic phase. Finally, at $t \approx 10\,\mathrm{fm/c}$, a dilute gas of free streaming particles evolves, which can be observed by detectors.

of the discretised energy-momentum tensor complicates the computation. The work is published in [42].

The second part of this thesis deals with formation of a quark-gluon plasma in heavy ion collisions whose space time evolution is sketched in figure 1.3. Due to Lorentz contraction of the colliding nuclei, a momentum anisotropy in the longitudinal-transverse plane is expected. The success of relativistic hydrodynamics in describing data from heavy ion collisions at LHC and RHIC suggests a local equilibrium implying isotropy shortly after the collision. The rapid isotropisation can easily be achieved if the plasma is strongly coupled [43]. However, asymptotic freedom in conjecture with the high energies of relativistic heavy ion collisions suggests a weakly coupled medium and the question arises, which QCD processes drive the fast isotropisation. At the moment of writing unstable plasma modes leading to a chromo-Weibel instability are the most promising candidates [44–46].

The early stages of the quark-gluon plasma are a system far from equilibrium. A powerful tool for studying non-equilibrium physics, is the classical model of weakly coupled Yang-Mills theory, which naturally involves real time in its equations of motion. It has been applied in several studies on isotropisation via the chromo-Weibel instability [47–60]. A drawback is that only bosonic degrees of freedom can be approximated classically. In this work we present the first attempt to include fermionic degrees of freedom to the isotropisation process of the quark-gluon plasma. To this end we complement the classical approximation of Yang-Mills theory with quantum mechanical fermions establishing a semi-classical model of QCD.

In this approach, equations of motion determine the QCD dynamics, while intrinsic features of the system under investigation are incorporated by specifying appropriate ini-

tial conditions. We review initial conditions for QCD in thermal equilibrium and study their evolution. However, the focus of our research lies on the isotropisation of the quark-gluon plasma. We employ initial conditions inspired by the colour glass condensate effective theory [61–63]. It describes the highly anisotropic momentum distribution in terms of classical fields in the early stages of heavy ion collisions. Then we define observables indicating isotropisation and appearance of a chromo-Weibel instability. We solve the equations of motion numerically in the case of pure SU(3) gluodynamics. Thereby we reproduce results from a similar investigation with gauge group SU(2) [60]. Furthermore we solve the full system of semi-classical QCD investigating the effect of fermionic degrees of freedom on the isotropisation process for the first time.

The thesis is organised as follows: QCD is introduced in chapter 2. We discuss the inclusion of finite temperature by the imaginary time formalism, which is the standard approach regarding systems in thermal equilibrium and also plays a major role in the introduction of temperature in lattice QCD. Furthermore we discuss the real time formalism, which additionally allows us to treat systems far from equilibrium. The chapter concludes with a discussion of the scale hierarchy arising in weakly coupled thermal systems and its consequences.

In chapter 3, we deal with finite temperature Yang-Mills theory on an anisotropic lattice. The second part of the chapter is devoted to perturbation theory within the lattice framework, the numeric algorithms as well as some consistency checks of the implementation.

We apply the established framework of lattice Yang-Mills theory in chapter 4 in order to compute the second order transport coefficient κ. We start with reviewing its definition from relativistic hydrodynamics and its connection to thermal field theory. Afterwards we review predictions for κ from AdS/CFT duality as well as from a continuum weak coupling expansion in pure gluodynamics in the ideal gas limit. Next we discuss how to extract κ from lattice Yang-Mills theory as well as discretisation and renormalisation of the energy-momentum tensor. Finally, we compute the transport coefficient in lattice perturbation theory and from Monte Carlo simulations. We identify its temperature dependence and compare our lattice result against both weak and strong coupling predictions. We give a first conclusion on the lattice computation of the transport coefficient κ as well as perspectives on computation improvements.

In the next chapter 5 we discuss our semi-classical approach to QCD. It is based on a classical description of the bosonic degrees of freedom, whose validity is explained in the first section, and a quantum mechanical treatment of fermionic degrees of freedom by their mode function expansion. We derive the corresponding equations of motion from the lattice QCD Hamiltonian and discuss their numeric evaluation. The introduction of low-cost fermions [64] reduces the numeric effort, enabling us to perform simulations in three spatial dimensions. We present results of simulations of pure bosonic and pure fermionic systems as well as QCD including one quark flavour in thermal equilibrium. The chapter concludes with research perspectives on further applications of the semi-classical model of QCD in thermal equilibrium.

In chapter 6 we deal with the isotropisation of the quark-gluon plasma produced in a heavy ion collision via a chromo-Weibel instability. We give an overview of the formation of the quark-gluon plasma and discuss isotropisation by means of a chromo-Weibel instability. Furthermore we review a description of the early stages of a heavy ion collision within the colour glass condensate effective theory defining initial conditions

regarding an investigation of the isotropisation process in a classical approach. Next we discuss the transfer of the colour glass condensate inspired initial conditions to the lattice and introduce observables indicating isotropisation and the emergence of a chromo-Weibel instability. Finally, we simulate the early stages of a heavy ion collision within the semi-classical approach. We first stick to a pure bosonic treatment, but encompass the correct colour group of QCD, SU(3), and afterwards we investigate the dynamics in a full semi-classical approach. We finish the chapter with conclusions as well as perspectives on future research projects concerning dynamics of the quark-gluon plasma within the semi-classical approach.

Last but not least we summarise conclusions of the whole work in chapter 7. Attached are five appendices: In appendix A, we discuss the used system of units and mathematical conventions. Appendix B gives detailed calculations regarding the transport coefficient κ, while appendix C gives selected numeric results to facilitate a reproduction of the computation. Since we have derived the semi-classical approach to QCD for the first time, we give the corresponding calculations in more detail in appendix D. Additionally, we give a short review on Lagrangian and Hamiltonian mechanics. The last appendix E contains numeric checks regarding simulations of chapter 6.

2 Aspects of quantum chromodynamics at finite temperature

At high temperature hadronic matter passes over to a new state – the quark-gluon plasma. The fundamental theory describing hadronic matter is quantum chromodynamics (QCD), a non-abelian gauge theory with symmetry group SU(3) describing the strong interactions between quarks and gluons. Over the years much experimental evidence for the correctness of QCD has been gathered, see for instance [1, 2, 38]. We review aspects of QCD at finite temperature, which are relevant for a description of the quark-gluon plasma.

2.1 Quantum chromodynamics

The quantum field theory representing strong interactions, namely quantum chromodynamics (QCD), is a fundamental building block in the standard model of elementary particle physics. Its origin lies in the years 1961, when Gell-Mann and Ne'eman ordered the hadrons into SU(3)-multiplets, the so called eightfold way [65, 66], and 1964, when Gell-Mann and Zweig proposed the quarks as constituents of hadrons [67, 68]. These propositions required the introduction of an additional quantum number, colour, which fitted nicely into the non-abelian gauge theory formulated by Yang and Mills in 1954 [69]. Nineteen years later, Politzer, Gross and Wilczek discovered [70, 71] that the non-abelian field theory is asymptotically free, that their interaction strength decreases at small length scales. By contrast, the interaction strength increases for larger distances, featuring colour confinement, the phenomenon that colour charged particles, such as quarks or gluons, never appear as free particles in nature. It was not until 1971, when 't Hooft proved renormalisability of gauge theories with and without spontaneous symmetry breaking [72, 73], that QCD was acknowledged by the scientific community.

In the following sections we discuss aspects of continuum QCD, which we will use later, based on [74–76]. This includes a discussion of the QCD action in section 2.1.1 and the running coupling in 2.1.2.

2.1.1 Continuum action

The non-observability of the new quantum number colour is reflected in QCD being a local gauge theory invariant under SU(3) colour transformations. The standard choice of an action fulfilling the requirements of renormalisability, gauge invariance and Lorentz invariance reads[1] in Minkowski space(see appendix A.2)

$$S[\psi_f, \overline{\psi}_f, A_\mu] = \int \mathrm{d}^4x \left(\mathcal{L}_\mathrm{F} + \mathcal{L}_\mathrm{G}\right), \tag{2.1}$$

[1] Natural units are used throughout this thesis. For conventions consult appendix A.1.

with the fermionic and pure gluonic Lagrangians

$$\mathcal{L}_{\mathrm{F}}[\psi_f, \overline{\psi}_f, A_\mu] = \sum_f \overline{\psi}_f(x) \left(\mathrm{i}\gamma^\mu \mathcal{D}_\mu - m_f\right) \psi_f(x), \tag{2.2a}$$

$$\mathcal{L}_{\mathrm{G}}[A_\mu] = -\frac{1}{4} F^a_{\mu\nu}(x) F^{\mu\nu,a}(x). \tag{2.2b}$$

The Dirac spinor $\psi_f \equiv \psi_{f,\alpha,c}$ carrying a colour index c as well as a spinor index α corresponds to a quark field with flavour f and mass m_f. It forms a Lorentz scalar[2] with the field $\overline{\psi}_f \equiv \psi_f^\dagger \gamma^0$. Their spinor representation is connected to the vector representation of the Lorentz group by the gamma matrices γ^μ (see appendix A.4).

The quarks are coupled to the gluonic gauge fields $A_\mu \equiv A^a_\mu T^a$ via the covariant derivative

$$\mathcal{D}_\mu = \partial_\mu + \mathrm{i}g A_\mu, \tag{2.3}$$

which is constructed in a way leaving the Lagrangian invariant under local SU(3) transformations. The gauge fields transform in the adjoint representation of SU(3), whereas the quark fields transform in the fundamental representation. The corresponding local gauge transformations with $G(x) \in \mathrm{SU}(3)$ read

$$\psi \to \psi'(x) = G(x)\psi(x), \tag{2.4}$$

$$A_\mu \to A'_\mu(x) = G(x) A_\mu(x) G^\dagger(x) + \frac{\mathrm{i}}{g} \left(\partial_\mu G(x)\right) G^\dagger(x). \tag{2.5}$$

The covariant derivative also defines the field strength tensor $F_{\mu\nu} \equiv F^a_{\mu\nu} T^a$ by

$$[\mathcal{D}_\mu, \mathcal{D}_\nu] = \mathrm{i}g F_{\mu\nu}. \tag{2.6}$$

The eight generators T^a of the SU(3) gauge group form a Lie algebra according to

$$\left[T^a, T^b\right] = \mathrm{i} f^{abc} T^c, \tag{2.7}$$

where f^{abc} are the totally antisymmetric structure constants. The generators are normalised by $\mathrm{Tr}\left(T^a T^b\right) = \frac{1}{2}\delta^{ab}$. Equations (2.3) and (2.6) give the field strength tensor:

$$F^a_{\mu\nu}(x) = \partial_\mu A^a_\nu(x) - \partial_\nu A^a_\mu(x) + g f^{abc} A^b_\mu(x) A^c_\nu(x), \tag{2.8}$$

which builds the kinetic term for the gauge fields in the QCD Lagrangian. The non-abelian structure of the gauge group distinguishes it from quantum electrodynamics (QED) and gives rise to the cubic and quartic self-interactions for the gluons.

2.1.2 Running coupling

The asymptotic freedom of QCD is directly connected to the running of the coupling strength $\alpha(\mu_{\mathrm{R}}) = \frac{g^2(\mu_{\mathrm{R}})}{4\pi}$ governed by the renormalisation group equation with the QCD beta function β^{QCD} and renormalisation scale μ_{R}

$$\frac{\mathrm{d}\alpha(\mu_{\mathrm{R}})}{\mathrm{d}\ln\mu_{\mathrm{R}}} = \beta^{\mathrm{QCD}}(\alpha(\mu_{\mathrm{R}})). \tag{2.9}$$

[2] If not stated otherwise, Einstein's sum convention is implied.

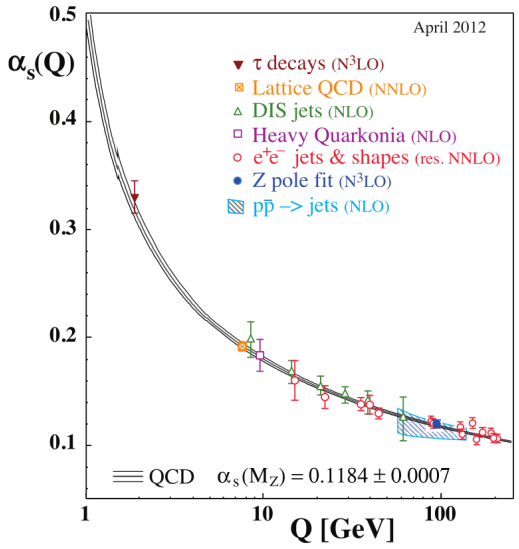

Figure 2.1: Comparison of the QCD running coupling α_s versus the respective energy scale Q between measurements by different experiments and perturbative QCD. High energies facilitate a perturbative treatment of QCD. Taken from [2].

An expansion of the beta function $\beta^{\mathrm{QCD}}(\alpha)$ in the region of vanishing coupling can be calculated perturbatively and is universal up to next-to-leading order, i.e. independent of the renormalisation scheme. In QCD with N_f flavours the expansion leads to [2]

$$\beta^{\mathrm{QCD}}(\alpha) = -\left(b_0\alpha^2 + b_1\alpha^3 + \mathcal{O}(\alpha^4)\right), \tag{2.10a}$$

$$b_0 = \frac{1}{12\pi}(33 - 2N_f), \tag{2.10b}$$

$$b_1 = \frac{1}{24\pi^2}(153 - 19N_f). \tag{2.10c}$$

The minus sign ensures asymptotic freedom for $N_f < 17$. By means of the QCD beta function (2.10) equation (2.9) can be solved analytically. One finds for the running coupling to first order

$$\alpha(\mu_{\mathrm{R}}) = \left(b_0 \ln\left(\frac{\mu_{\mathrm{R}}}{\Lambda_{\mathrm{QCD}}}\right)\right)^{-1}, \tag{2.11}$$

where $\Lambda_{\mathrm{QCD}} \approx 200\,\mathrm{MeV}$ is a constant of integration indicating the non-perturbative scale of QCD. Its inverse corresponds to $\Lambda_{\mathrm{QCD}}^{-1} \approx 1\,\mathrm{fm}$, what is approximately the radius of a nucleus.

The momentum scale Q of a given physical process enters through the renormalisation scale μ_{R} and determines the effective interaction strength $\alpha(\mu_{\mathrm{R}} \approx Q)$. As illustrated in figure 2.1 QCD enters a weakly coupled regime at high momentum transfers Q, which allows for a perturbative treatment, e.g. by a weak coupling expansion [74, 76]. For a discussion of the running coupling at finite temperature and its consequences refer to section 2.2.3.

2.2 Thermal field theory

After thermalisation, see section 6 for a detailed discussion of the thermalisation process, the quark-gluon plasma has a large temperature and the emerging fundamental physics should be described in the framework of thermal field theory. The common approach to incorporate temperature is the imaginary time formalism [77,78]. As explained in section 2.2.1 it is based on trading the temporal coordinate for the system's temperature. As discussed in section 3.1.3 the strong resemblance between the imaginary time formalism and lattice QCD allows for a straightforward introduction of temperature to this non-perturbative approach to QCD.

A way to introduce temperature to the system, without sacrificing the time direction, is the real time formalism discussed in section 2.2.2. It allows a description of systems far from equilibrium, such as the thermalisation process of the QGP discussed in chapter 6. Additionally, it can be applied to systems in equilibrium to calculate dynamic observables like transport coefficients. To achieve this, we make use of linear response theory [77, 79], which states that an equilibrium ensemble encodes the response of the system to a disturbance, which dissipates in real time. We will then see in section 2.2.3 that a perturbative approach suffers from infrared divergences. but has been done for a number of transport coefficients using resummation [80,81]. A computation in lattice QCD requires an analytic continuation from the Euclidean to the retarded correlator, which usually is an ill-posed problem [82]. We discuss in chapter 4 why this problem does not arise in a lattice computation of the second order transport coefficient κ.

2.2.1 Imaginary time formalism

Generally, the expectation value of an observable $\mathcal{O}$ in a statistical quantum system, characterised by the density matrix ϱ, is given by

$$\langle \mathcal{O} \rangle = \frac{1}{Z} \operatorname{Tr} (\mathcal{O} \varrho) \,, \tag{2.12}$$

where the normalisation Z is defined by $Z = \operatorname{Tr} \varrho$. For a system in thermal equilibrium the density matrix takes the form

$$\varrho = \frac{1}{Z} \mathrm{e}^{-\beta(H - \mu_i N_i)}, \tag{2.13}$$

where the normalisation Z corresponds to the grand-canonical partition function. The term H is the system's Hamiltonian, $\beta = \frac{1}{T}$ is the inverse temperature and μ_i are the chemical potentials for conserved particle numbers $\langle N_i \rangle$. As discussed in the introduction we only treat the case of vanishing chemical potential $\mu_i = 0$.

Evaluating the trace (2.13) by an integral over all degrees of freedom gives the partition function

$$Z = \sum_a \int \mathrm{d}\phi_a \, \left\langle \phi_a | \mathrm{e}^{-\beta H} | \phi_a \right\rangle . \tag{2.14}$$

The formal similarity to the transition amplitude $\left\langle \phi_a | \mathrm{e}^{-\mathrm{i}Ht} | \phi_a \right\rangle$ can be made genuine by a Wick rotation from real to imaginary time $t \to \mathrm{i}\tau$ illustrated in figure 2.2 and the

exchange of the time direction with a dimension of finite extent $\beta = \frac{1}{T}$, defining the temperature.

The partition function can be written as a path integral and reads for QCD

$$Z = \int \mathcal{D}\left[\psi, \overline{\psi}, A_\mu\right] \; \exp\left\{-\int_0^\beta \mathrm{d}\tau \int \mathrm{d}^3x \; \mathcal{L}_\mathrm{E}[\psi, \overline{\psi}, A_\mu]\right\}, \tag{2.15}$$

with the Euclidean QCD Lagrangian

$$\mathcal{L}^\mathrm{E}[\psi_f, \overline{\psi}_f, A_\mu] = \sum_f \overline{\psi}_f(x)\left(\gamma_\mu \mathcal{D}_\mu + m_f\right)\psi_f(x) + \frac{1}{4}F^a_{\mu\nu}(x)F^a_{\mu\nu}(x). \tag{2.16}$$

Periodic and antiperiodic temporal boundary conditions

$$A_\mu(0, \mathbf{x}) = A_\mu(\beta, \mathbf{x}), \tag{2.17a}$$
$$\psi(0, \mathbf{x}) = -\psi(\beta, \mathbf{x}) \tag{2.17b}$$

account for the difference between bosons and fermions. In particular being distributed according to the Bose-Einstein and Fermi-Dirac distribution in the non-interacting case:

$$n_\mathrm{B} = \frac{1}{\mathrm{e}^{E/T} - 1}, \tag{2.18a}$$
$$n_\mathrm{F} = \frac{1}{\mathrm{e}^{E/T} + 1}, \tag{2.18b}$$

where E denotes the relativistic energy. As a consequence of these boundary conditions the back transformation of the temporal Fourier integral is replaced by a Fourier sum, c.f. (A.17) and the corresponding momenta become discrete, defining the Matsubara frequencies

$$\omega_n = \begin{cases} 2n\pi T & \text{for bosons} \\ (2n+1)\pi T & \text{for fermions} \end{cases}, \qquad n \in \mathbb{Z}\ . \tag{2.19}$$

The bosonic zeroth component of momentum k_0 in Euclidean space time is illustrated in figure 2.2. Due to the Wick rotation and the periodic boundary conditions, it only takes discrete and imaginary values.

Finally, the expectation value of an observable $\mathcal{O}$ in the imaginary time formalism is calculated from the functional integral

$$\langle \mathcal{O} \rangle = \frac{1}{Z} \int \mathcal{D}\left[\psi, \overline{\psi}, A_\mu\right] \; \mathcal{O}\; \mathrm{e}^{-S_\mathrm{E}[\psi, \overline{\psi}, A_\mu]}, \tag{2.20}$$

with the Euclidean action $S_\mathrm{E} = \int_0^\beta \mathrm{d}\tau \int \mathrm{d}^3x \; \mathcal{L}_\mathrm{E}$. Thermodynamic quantities, such as pressure p or energy density ϵ can directly be derived from the partition function by the standard statistical relations, see e.g. [77],

$$\epsilon = -\frac{1}{V}\frac{\partial}{\partial \beta} \ln Z, \tag{2.21}$$
$$p = \frac{1}{\beta}\frac{\partial}{\partial V} \ln Z. \tag{2.22}$$

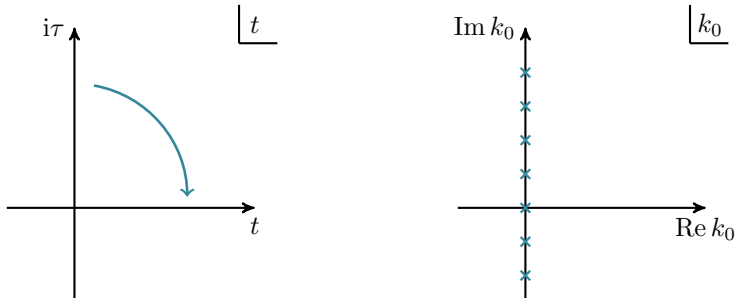

Figure 2.2: The left hand side illustrates schematically the Wick rotation $t \to \mathrm{i}\tau$ going from Minkowski to Euclidean space time. As a consequence of the Wick rotation and of periodic boundary conditions in bosonic fields the zeroth momentum component k_0 only assumes imaginary and discrete values as shown on the right hand side.

2.2.2 Real time formalism

For quantum field theories out of equilibrium [83, 84] all information can be deduced from the generating functional for correlation functions

$$Z_{\mathrm{G}}[J,R;\varrho_0] = \mathrm{Tr}\left\{\varrho_0 T_{\mathcal{C}} \exp\left(\mathrm{i}\int_x J(x)\Phi(x) + \frac{\mathrm{i}}{2}\int_{xy}\Phi(x)R(x,y)\Phi(y)\right)\right\}, \tag{2.23}$$

where J and R denote the source terms. We consider for simplicity scalar fields. The time coordinate x_0 is evaluated along a closed real time contour $\mathcal{C}$, $\int_x = \int_{\mathcal{C}} \mathrm{d}x^0 \int \mathrm{d}^3x$, which is depicted in figure 2.3. Contour time ordering is denoted by $T_{\mathcal{C}}$ with usual time ordering along the forward piece $\mathcal{C}^+$ and reverse ordering along the backward piece $\mathcal{C}^-$. The specification of an initial state enters through the initial density matrix ϱ_0. Defining the location of the field's $\Phi(x^0,\mathbf{x})$ time argument x^0 on the contour $\mathcal{C}^\pm$ by writing $\Phi^\pm(x^0,\mathbf{x})$ one evaluates the trace by introducing a set of eigenstates

$$\Phi^\pm(t_0,\mathbf{x})\left|\varphi^\pm\right\rangle = \varphi_0^\pm(\mathbf{x})\left|\varphi^\pm\right\rangle. \tag{2.24}$$

After replacing the resulting matrix element by its functional integral representation including the corresponding Lagrange density $\mathcal{L}[\varphi]$ the generating functional reads

$$\begin{aligned} Z_{\mathrm{G}}[J,R;\rho_0] = \int \mathrm{d}\varphi_0^+ \mathrm{d}\varphi_0^- \;\; & \langle\varphi^+|\varrho_0|\varphi^-\rangle \\ \times \int_{\varphi_0^+}^{\varphi_0^-} \mathcal{D}'\varphi \;\; & \exp\left(\mathrm{i}\int_x \mathcal{L}[\varphi] + \mathrm{i}\int_x J(x)\varphi(x)\right. \\ & \left. + \frac{\mathrm{i}}{2}\int_{xy}\varphi(x)R(x,y)\varphi(y)\right). \end{aligned} \tag{2.25}$$

The functional integral $\mathcal{D}'\varphi$ goes over field configurations $\varphi(x)$ satisfying the boundary conditions $\varphi^\pm(x^0 = t_0,\mathbf{x}) = \varphi_0^\pm(\mathbf{x})$ with $x^0 > t_0$, but excludes the fields with $x^0 = t_0$. The first integral describes statistical fluctuations weighted by the initial density matrix ϱ_0, whereas the second integral describes quantum fluctuations.

The real time formalism can also be applied to systems in thermal equilibrium by identifying the density matrix with (2.13) and interpreting it as an evolution operator

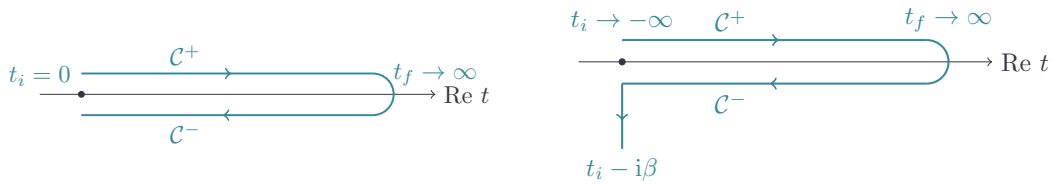

Figure 2.3: The figures show the real time contour $\mathcal{C}$ in the complex time plane $x^0 \equiv t$. The left hand side illustrates the non-equilibrium case whereas the contour on the right hand side is followed by an imaginary time branch incorporating the temperature $\beta = 1/T$ in equilibrium scenarios. The latter one is called the Schwinger-Keldysh contour.

in imaginary time. One accounts for the last point by adding an imaginary time branch to the contour $\mathcal{C}$. The resulting contour is called Schwinger-Keldysh contour and is illustrated on the right hand side of figure 2.3. In perturbative calculations both fields $\Phi^{\pm}(x)$ enter as degrees of freedom and the propagator for a neutral boson with zero spin ϕ becomes a 2×2 matrix. Defining the Wightman functions

$$D^{>}(x, x') = \left\langle \phi(x)\phi(x') \right\rangle, \tag{2.26a}$$
$$D^{<}(x, x') = \left\langle \phi(x')\phi(x) \right\rangle = D^{>}(x', x) \tag{2.26b}$$

and $x^0 \equiv t$ the propagator reads after a basis change [85]

$$D(x, x') = \begin{pmatrix} F(x, x') & G^{\mathrm{R}}(x, x') \\ G^{\mathrm{A}}(x, x') & 0 \end{pmatrix}, \tag{2.27}$$

where the symmetric, retarded and advanced correlators are given by

$$F(x, x') = \frac{1}{2}\left(D^{>}(x, x') + D^{<}(x, x')\right), \tag{2.28a}$$
$$G^{\mathrm{R}}(x, x') = \mathrm{i}\theta(t - t')\left(D^{>}(x, x') - D^{<}(x, x')\right), \tag{2.28b}$$
$$G^{\mathrm{A}}(x, x') = -\mathrm{i}\theta(t' - t)\left(D^{>}(x, x') - D^{<}(x, x')\right). \tag{2.28c}$$

The Heavyside step function $\theta(x)$ is defined in appendix A.5.1. Performing a Fourier transform to momentum space as defined in appendix A.5 the propagators can be expressed in terms of the spectral function

$$\rho(q) = D^{>}(q) - D^{<}(q), \tag{2.29}$$

by using the KMS (Kubo-Martin-Schwinger) condition $G^{>}(q) = \mathrm{e}^{\beta q^0} G^{<}(q)$:

$$F(q) = \left(n_{\mathrm{B}}(q^0) + \frac{1}{2}\right)\rho(q), \tag{2.30}$$

$$G^{\mathrm{R}}(q) = \int_{-\infty}^{\infty} \frac{\mathrm{d}q_0'}{2\pi} \, \frac{\rho(q_0', \mathbf{q})}{q_0' - q_0 - \mathrm{i}\eta}. \tag{2.31}$$

We use the expression for the symmetric correlator F in chapter 5 to justify a classical approach to QCD.

The retarded correlator is the relevant quantity in the calculation of transport coefficients [78]. Their non-perturbative determination, as pursued in this thesis, of the transport coefficient κ suffers from the restriction of the lattice formalism to Euclidean space time. On the lattice only the Euclidean correlator

$$G^{\mathrm{E}}(\tau, \mathbf{x}) = \int \frac{\mathrm{d}q_0}{2\pi} \mathrm{e}^{-q_0 \tau} D^{>}(q_0, \mathbf{x}) \tag{2.32}$$

is accessible and the connection to real time quantities, i.e. the retarded correlator requires an analytic continuation. Writing both correlators in their spectral representation, (2.31) and

$$G^{\mathrm{E}}(\mathrm{i}\omega_n, \mathbf{q}) = \int_{-\infty}^{\infty} \frac{\mathrm{d}q_0}{2\pi} \frac{\rho(q)}{q_0 - \mathrm{i}\omega_n}, \tag{2.33}$$

one finds for this analytic continuation with appropriate boundary conditions [79]

$$G^{\mathrm{R}}(q_0, \mathbf{q}) = G^{\mathrm{E}}(\mathrm{i}\omega_n \to q_0 + \mathrm{i}\eta, \mathbf{q}). \tag{2.34}$$

This relation is useful, since it connects a non-perturbatively accessible quantity, e.g. the Euclidean correlator G^{E}, to one in real time, e.g. the retarded correlator G^{R}. We will use a more specific version of this relation at vanishing frequency in chapter 4 in order to compute the second order transport coefficient κ. Further applications and limitations of this relation are illustrated in [82].

2.2.3 Weak coupling techniques at finite temperature

For thermal systems, the renormalisation scale is set by the temperature $\mu_{\mathrm{R}} \sim T$ [76,77]. As a consequence the coupling runs with the temperature (2.9). For $T \gg \Lambda_{\mathrm{QCD}}$ the coupling is sufficiently small and thermal QCD can be treated by a weak coupling expansion. In contrast to a weak coupling expansion in quantum field theory at vanishing temperature, the expansion in thermal field theory suffers from infrared divergences caused by Matsubara zero-modes [78]. Due to a missing Matsubara zero-mode (2.19) fermions are purely perturbative in this scenario.

The bosonic infrared divergences are related to particular degrees of freedom. We identify the following three momentum scales with hierarchy $g^2T < gT < 2\pi T$:

- The hard scale $\sim (2\pi T)$, where partons are only weakly affected by the heatbath due to their hard momenta.
- The soft or electric scale $\sim (gT)$, where colour-electric screening influences the longitudinal gluons and collective effects arise.
- The ultra-soft or magnetic scale $\sim (\frac{g^2T}{\pi})$, where static colour-magnetic screening of transversal gluons is absent.

This hierarchy is particularly interesting since various physical properties of QCD are sensitive to the different scales [86]. For instance, hydrodynamic transport coefficients for the quark-gluon plasma like the shear viscosity or κ are sensitive to the hard momentum scale, whereas thermalisation processes in the quark-gluon plasma are sensitive

to the soft scale. An observable sensitive to the ultra-soft scale is the Chern-Simons diffusion rate. In the following we discuss models dealing with these different scales.

Due to the separation of scales at high temperatures, QCD can be investigated by effective field theories. They are based on the idea to 'average' the behaviour of the underlying theory at large momentum scales in order to obtain a simplified model at low momentum scales. Examples for effective field theories are hard thermal loop effective field theory (HTL) [87–89] as well as dimensional reduction [90, 91]. However, perturbation theory breaks down completely at the magnetic scale, since all infrared diagrams contribute to the same order, e.g. for the partition function $Z_l \sim g^6 T^4$. This issue is known as Linde problem [92]. Recent progress on this topic has been made in reference [93].

One way to avoid the problems caused by infrared divergences is to use a classical description of Yang-Mills theory. As argued by Grigoriev and Rubakov [94] and shown formally by Bödeker [95], a classical approach offers a non-perturbative approach to the soft and ultra-soft scale. The quantum mechanical effect of suppressing thermal excitations at the hard scale can be remedied by using lattice regularisation. In chapter 5 we present a semi-classical approach to QCD on the lattice based on a classical treatment of bosons, but a quantum mechanical treatment of fermions. The fact that the semi-classical model automatically incorporates real time allows us to study non-equilibrium physics. We apply it to thermalisation processes of the quark-gluon plasma in chapter 6.

3 Lattice gauge theory

In the case of strong couplings the validity of a perturbative approach to QCD becomes questionable. Lattice gauge theory provides a mathematically well-defined regularisation of QCD and allows to solve the functional integral (2.20) non-perturbatively. It dates back to the 1970s and has primarily be developed by Wilson. It is based on a discretisation of Euclidean space time, which renders the functional integral finite. When interpreting the weight $\exp(-S)$ as a statistical Boltzmann factor it can be evaluated via Monte Carlo simulations. Temperature is introduced analogous to the imaginary time formalism, by identifying the temporal lattice direction with temperature.

3.1 Lattice Yang-Mills theory

This section summarises the main aspects concerning the formulation of Yang-Mills theory in the lattice framework. First, we discuss the discretisation of space time in section 3.1.1 leading to a loss of Poincaré invariance. Then we use the specific feature of the lattice regularisation, manifestation of gauge invariance, to build a gluonic action in section 3.1.2. Finally, we define physical variables, such as coupling and temperature on the lattice in section 3.1.3. A detailed version of the following summary can be found in one of the many textbooks on lattice gauge theory, e.g. [19, 96–98].

3.1.1 Discretisation of space time

We discretise Yang-Mills theory in $N_\mathrm{d} = 4$ dimensional Euclidean space time by the introduction of an anisotropic hypercubic lattice with periodic boundary conditions

$$\Lambda = \left\{ x \,\middle|\, \frac{x_\mu}{a_\mu} \in \mathbb{Z}, \mu = 1,2,3,4 \right\}, \tag{3.1}$$

where a_μ denotes the lattice spacings

$$a_\mu = \begin{cases} a_\sigma & \text{for } \mu = 1,2,3 \\ a_\tau & \text{for } \mu = 4 \end{cases} \tag{3.2}$$

and the anisotropy is defined by

$$\xi \equiv \frac{a_\sigma}{a_\tau}. \tag{3.3}$$

The lattice has an extent of N_σ points in the spatial and N_τ points in the temporal direction[1]. A section of discretised space time, including the main variables on the

[1] We never imply a sum over the indices of a_μ or N_μ.

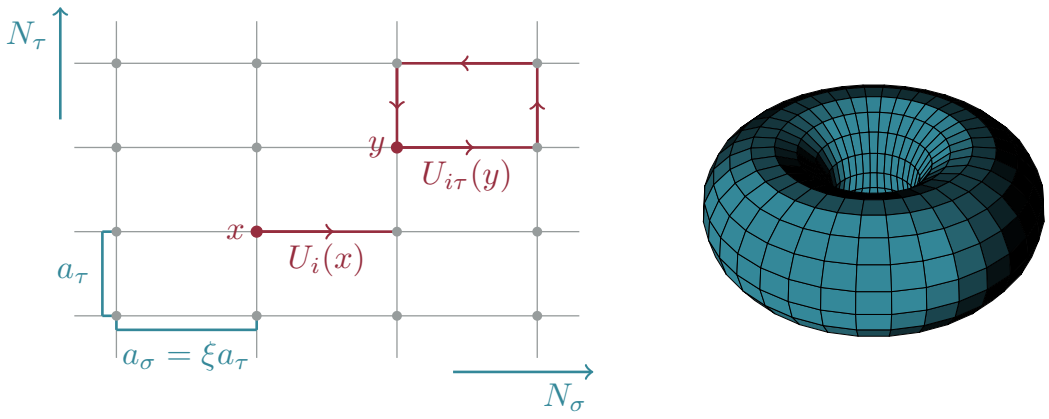

Figure 3.1: The left figure shows a two dimensional anisotropic lattice with N_τ points in the temporal, N_σ points in the spatial direction and lattice spacings a_τ and a_σ accordingly. Due to periodic boundary conditions it is compactified to a torus shown on the right hand side. On the lattice gauge fields $A_\mu(x)$ are replaced by link variables $U_\mu(x)$. The smallest gauge invariant object is the trace over the plaquette $U_{\mu\nu}(x)$.

lattice, is illustrated in figure 3.1. The differential operator is replaced by either forward, backward or central finite differences

$$\partial_\mu^{\mathrm{f}} f(x) \equiv \frac{1}{a_\mu}\left(f(x+\hat{\mu}) - f(x)\right) = \partial_\mu f(x) + \mathcal{O}(a_\mu), \tag{3.4a}$$

$$\partial_\mu^{\mathrm{b}} f(x) \equiv \frac{1}{a_\mu}\left(f(x) - f(x-\hat{\mu})\right) = \partial_\mu f(x) + \mathcal{O}(a_\mu), \tag{3.4b}$$

$$\partial_\mu^{\mathrm{c}} f(x) \equiv \frac{1}{2}\left(\partial_\mu^{\mathrm{f}} + \partial_\mu^{\mathrm{b}}\right) f(x) = \frac{1}{2a_\mu}\left(f(x+\hat{\mu}) - f(x-\hat{\mu})\right) = \partial_\mu f(x) + \mathcal{O}(a_\mu^2), \tag{3.4c}$$

where the central difference is favourable due to its improved discretisation error. The four-dimensional lattice Laplacian reads

$$\partial_\mu^{\mathrm{c}\,2} f(x) \equiv \sum_\mu \frac{1}{a_\mu^2}\left(f(x+\hat{\mu}) - 2f(x) + f(x-\hat{\mu})\right) = \partial_\mu^2 f(x) + \mathcal{O}(a_\mu^2). \tag{3.5}$$

The discrete and periodic structure of position space transfers to periodic momentum space with discrete momenta

$$q_\mu = \frac{2\pi}{a_\mu N_\mu} n_\mu, \qquad n_\mu = 0, 1, \ldots, N_\mu - 1\ , \tag{3.6}$$

residing in the first Brillouin zone. For the definition of the Fourier transform on Euclidean lattices refer to (A.18) in appendix A.5.

The discretisation of space time leads to a reduction of symmetry. QCD in continuous space time is invariant under transformations belonging to the Poincaré group. These are transformations

$$T_{\Lambda,a} : x \to T_{\Lambda,a} x^\mu = \Lambda^\mu_\nu x^\nu + a^\mu \tag{3.7}$$

with translations $a \in \mathbb{R}^{1+3}$ and Lorentz transformations Λ^{μ}_{ν}. The set of all Lorentz transformations forms the Lorentz group, corresponding to the generalised orthogonal group $O(1,3)$. Transferring QCD to the lattice reduces these symmetries to discrete groups. The Lorentz group is reduced to the hypercubic group and translations are only allowed to be a multiple of the lattice spacing corresponding to discrete translations.

3.1.2 Anisotropic Wilson gauge action

The defining quantity for the gauge action is the covariant derivative (2.3), which requires a redefinition on the lattice due to discrete space time. By analogy to the continuous gauge fields, $A_\mu(x)$, describing an infinitesimal parallel transport in colour space we introduce the link variable describing a finite parallel transporter between two space time points x and $x + a\hat{\mu}$ on the lattice

$$U(x + a_\mu \hat{\mu}, x) \equiv U_\mu(x). \tag{3.8}$$

Throughout this thesis, at every shift, a factor of the lattice spacing a_μ is implied, $x + \hat{\mu} \equiv x + a_\mu \hat{\mu}$. The link variables are elements of the adjoint representation of SU(3). Their connection to the elements of the SU(3)-Lie-algebra $A_\mu(x)$ is given by

$$U_\mu(x) = \mathrm{e}^{\mathrm{i}g a_\mu A^a_\mu(x) T^a}, \tag{3.9}$$

and they behave under local gauge transformations, $G(x) \in \mathrm{SU}(3)$ like

$$U_\mu(x) \to U'_\mu(x) = G(x) U_\mu(x) G^\dagger(x + \hat{\mu}). \tag{3.10}$$

The Wilson gauge action [99] is constructed from an elementary gauge invariant object built of link variables, the trace of the plaquette $\mathrm{Tr}\, U_{\mu\nu}(x)$ with the plaquette being defined as

$$U_{\mu\nu}(x) = U_\mu(x) U_\nu(x + \hat{\mu}) U^\dagger_\mu(x + \hat{\nu}) U^\dagger_\nu(x). \tag{3.11}$$

Link variable and plaquette are illustrated in figure 3.1. On a anisotropic lattice [100] the gauge action reads

$$S[U] = \frac{\beta}{N_c} \mathrm{Re}\, \mathrm{Tr} \left\{ \frac{1}{\xi_0} \sum_{x, i<j} (\mathbb{1} - U_{ij}(x)) + \xi_0 \sum_{x,i} (\mathbb{1} - U_{i0}(x)) \right\}, \tag{3.12}$$

where $\beta = \frac{2N_c}{g^2}$ denotes the lattice coupling[1], $N_c = 3$ the number of colours and ξ_0 the bare anisotropy, which weights the aligned plaquettes according to the lattice spacing of their direction. We discuss in the following section, how the bare anisotropy is connected to the actual anisotropy ξ. Expanding the links by (3.9) and performing the continuum limit $a_\mu \to 0$ in the Wilson gauge action we recover its Euclidean continuous equivalent

$$S^{\mathrm{E}} = \frac{1}{4} \int \mathrm{d}^4 x \; F^a_{\mu\nu}(x) F^a_{\mu\nu}(x), \tag{3.13}$$

which is a requirement of any lattice action.

[1] The lattice coupling is often mistaken for the inverse temperature. From here on we use β solely to denote the lattice coupling.

3.1.3 Lattice spacing, bare anisotropy and temperature

The discretisation of space time is connected to a momentum cutoff $\frac{\pi}{a}$, which serves as a regulator for the quantum field theory. Furthermore, it introduces a renormalisation scale connecting the lattice spacing to the running coupling. In accordance to (2.9) the renormalisation group equation reads

$$\frac{\mathrm{d}g(a_\sigma)}{\mathrm{d}\ln a_\sigma}\Big|_\xi = \beta^{\mathrm{QCD}}(g(a_\sigma)), \tag{3.14}$$

and the lattice coupling $\beta = \frac{2N_c}{g^2}$ sets the scale $a_\sigma = a_\sigma(\beta, \xi)$ at a given anisotropy ξ. With (2.10) the differential equation can in principle be solved on a perturbative level. However, in lattice gauge theory (at least when simulating at large coupling) it is preferable to set the scale non-perturbatively, which can be achieved by computing the static quark potential via Wilson loops [101, 102].

Wilson loops are also used to calculate the renormalisation factor

$$\eta(\beta, \xi) = \frac{\xi}{\xi_0(\beta, \xi)}, \tag{3.15}$$

relating the actual anisotropy (3.3) to its bare value ξ_0. They deviate from each other due to quantum fluctuations. The renormalisation factor $\eta(\beta, \xi)$ has been computed non-perturbatively for the range of anisotropies $1 \leq \xi \leq 6$ and lattice couplings $5.5 \leq \beta \leq \infty$ [103]:

$$\eta(\beta, \xi) = 1 + \left(1 - \frac{1}{\xi}\right) \frac{\hat{\eta}_1(\xi)}{6} \frac{1 + a_1 g^2}{1 + a_0 g^2} g^2, \tag{3.16}$$

$$\hat{\eta}_1(\xi) = \frac{1.002503\xi^3 + 0.39100\xi^2 + 1.47130\xi - 0.19231}{\xi^3 + 0.26287\xi^2 + 1.59008\xi - 0.18224}, \tag{3.17}$$

with $a_0 = -0.77810$ and $a_1 = -0.55055$.

Analogous to the imaginary time formalism (see section 2.2.1) the compactified temporal lattice direction can be identified as the system's temperature

$$T = \frac{1}{a_\tau N_\tau}. \tag{3.18}$$

By (3.14) and (3.3) the temporal lattice spacing a_τ and thus the temperature is connected to the lattice coupling β. Varying the temperature in lattice simulations can be performed by altering the lattice extent but keeping the lattice spacing fixed. This approach is called fixed-scale approach, since it reproduces the same scale for every temperature.

3.2 Lattice perturbation theory

As in the continuous case, c.f. section 2.1.2, the running lattice coupling depends on the temperature. At high temperatures the discretised theory enters a weakly coupled regime and a perturbative treatment becomes possible. Applications of lattice perturbation theory are the calculation of renormalisation factors required for comparison

between lattice regularisation and continuum schemes, or an investigation of the continuum approach including e.g. the restoration of symmetries broken by discretisation. In this thesis we apply lattice perturbation theory to make a prediction for the second order transport coefficient κ, including leading order discretisation errors. This can be found in section 4.4.1. The calculation is performed at vanishing coupling, which simplifies the formalism introduced in e.g. [98, 104].

In lattice perturbation theory the gauge fields $A_\mu(x)$ are once again the relevant degrees of freedom. Expanding the links in the lattice action in terms of the gauge fields creates new interaction vertices. Additionally, transforming the so-called Haar measure from the links $\mathcal{D}U_\mu$ to the gauge fields $\mathcal{D}A_\mu$ introduces a Jacobian resulting in a further contribution to the action. However, a computation in free Yang-Mills does not suffer from these difficulties since it only requires the free gauge field propagator at tree-level. Note that the reduction of N-point correlation functions into products of two-point correlation functions by Wick's theorem [105] does not change in lattice perturbation theory. Following the gauge fixing procedure of Faddeev and Popov [106] one obtains for the free gauge field propagator in Feynman-'t Hooft gauge

$$\Delta^{ab}_{\mu\nu}(q) = \frac{\delta^{ab}\delta_{\mu\nu}}{\widetilde{q}^{\,2}}, \tag{3.19}$$

where $\widetilde{q}_\mu$ denotes the lattice momenta. As a consequence of introducing a momentum cutoff, Lorentz symmetry is reduced and the lattice momenta turn into sinusoidal functions

$$\widetilde{q}_\mu \equiv \frac{2}{a_\mu}\sin\left(\frac{a_\mu q_\mu}{2}\right), \tag{3.20a}$$

$$\widetilde{\left(k_\mu + q_\mu\right)} \equiv \frac{2}{a_\mu}\sin\left(\frac{a_\mu(k_\mu + q_\mu)}{2}\right), \tag{3.20b}$$

$$\widetilde{q}^{\,2} \equiv \sum_\mu \widetilde{q}^{\,2}_\mu \equiv \sum_\mu \frac{4}{a_\mu^2}\sin^2\left(\frac{a_\mu q_\mu}{2}\right). \tag{3.20c}$$

It is favourable to perform calculations in the infinite volume limit converting momentum sums into integrals. Since temperature is incorporated in the imaginary time, we only let the spatial coordinates go to infinity. The Fourier transform of the gauge field and its inverse are then given by

$$A_\mu(q) = a_\sigma^3 a_\tau \sum_{n=1}^{N_\tau}\sum_{\mathbf{x}} \mathrm{e}^{-\mathrm{i}\left(x+\frac{a_\mu\widehat{\mu}}{2}\right)q} A_\mu(x), \tag{3.21a}$$

$$A_\mu(x) = \sum\!\!\!\!\!\!\int_q \mathrm{e}^{\mathrm{i}\left(x+\frac{a_\mu\widehat{\mu}}{2}\right)q} A_\mu(q), \qquad \sum\!\!\!\!\!\!\int_q \equiv \frac{1}{a_\tau N_\tau}\sum_{n=1}^{N_\tau}\int_{-\frac{\pi}{a_\sigma}}^{\frac{\pi}{a_\sigma}} \frac{\mathrm{d}^3 q}{(2\pi)^3}, \tag{3.21b}$$

where we add a shift $x + \frac{\mu}{2}$ in position space, which naturally arises from the gauge field being in the middle of the link. It also simplifies the calculations.

3.3 Monte Carlo simulations

The application of Monte Carlo simulations in lattice field theories is motivated by the resemblance of Euclidean functional integrals with statistical physics. The expectation

value in lattice Yang-Mills theory is given by

$$\langle \mathcal{O} \rangle = \frac{1}{Z} \int \mathcal{D}U \ \mathrm{e}^{-S[U]} \mathcal{O}[U], \qquad Z = \int \mathcal{D}U \ \mathrm{e}^{-S[U]}, \tag{3.22}$$

where the for vanishing chemical potential real and positive weighting factor $\exp(-S[U])$ can be identified as a Boltzmann factor. Due to the finite number of degrees of freedom in discretised space time the Haar measure $\mathcal{D}U$ becomes finite and the functional integral can be approximated by an average over N_{ens} gauge field configurations $U_{(n)} \equiv U$, called ensemble,

$$\langle \mathcal{O} \rangle \approx \frac{1}{N_{\mathrm{ens}}} \sum_{n=1}^{N_{\mathrm{ens}}} \mathcal{O}[U_{(n)}], \tag{3.23}$$

with the gauge field configurations generated according to the probability $\exp(-S[U])$. In the limit of an infinite amount of configurations $N_{\mathrm{ens}} \to \infty$ the approximation coincides with the actual functional integral. Considering only a finite ensemble introduces an uncertainty to our estimate which behaves like $\mathcal{O}\left(\sqrt{N_{\mathrm{ens}}}\right)$. Due to the probability entering the functional integral it is sufficient to consider only configurations with the largest weight and thus to only create a relevant subset of all possible configurations. This approach is called importance sampling. For a detailed description of Monte Carlo methods refer to [19,96,107].

The sections 3.3.1 and 3.3.2 deal with the numeric implementation of a Monte Carlo simulation in lattice Yang-Mills theory. We discuss the analysis of observables computed by Monte Carlo sampling including the errors in section 3.3.3. Numeric details and checks of the implementation are given in section 3.3.4.

3.3.1 Monte Carlo algorithm

The gauge field configurations are sampled according to the probability distribution density

$$\mathrm{d}P(U) = \frac{\mathrm{e}^{S[U]} \mathcal{D}U}{\int \mathcal{D}U \ \mathrm{e}^{S[U]}} \ , \tag{3.24}$$

called the Gibbs measure. In order to create a new configuration we start from some arbitrary one and modify it by an update $f : U \to U'$. The transition probability $W_f(U \to U')$ for one update step has the properties

$$0 \leq W_f(U \to U') \leq 1, \qquad \int \mathrm{d}U \ W_f(U \to U') = 1. \tag{3.25}$$

Sampling a functional integral by constructing a sequence of configurations, called Markov chain, the update f has to fulfil two requirements. Firstly, it preserves the equilibrium distribution $p_{\mathrm{eq}}(U) \sim \exp(-S[U])$

$$\int \mathrm{d}U \ W_f(U \to U') p_{\mathrm{eq}}(U) = p_{\mathrm{eq}}(U'), \tag{3.26}$$

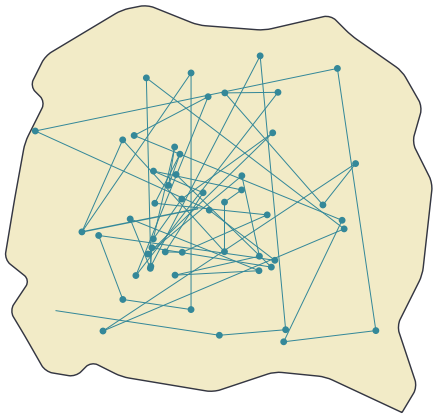

Figure 3.2: Sketch of a Markov chain traversing configuration space.

which corresponds to having a fixed point $p_{\text{eq}}(U)$. In practice this requirement is usually exchanged with the sufficient condition of detailed balance

$$\frac{W_f(U \to U')}{W_f(U' \to U)} = \frac{p_{\text{eq}}(U')}{p_{\text{eq}}(U)}, \tag{3.27}$$

which is easier to implement in algorithms. Secondly, starting from any configuration repeated updates bring one arbitrarily close to any other configuration U', called strong ergodicity:

$$\int \mathrm{d}U \; W_f(U \to U') > 0. \tag{3.28}$$

Both properties guarantee that a Markov chain built of a sufficient amount of configurations approaches the equilibrium distribution $p_{\text{eq}}(U)$ and the equilibrium distribution can be reached from any initial configuration. The process of equilibrating configurations by a sequence of updates is called thermalisation. However, the number of update steps required for thermalisation is a priori not predictable. Figure 3.2 sketches a Markov chain in the configuration space, where dots represent visited configurations. Assuming configurations in the centre of the region have a larger probability the Markov chain chooses more configurations there according to importance sampling. Due to strong ergodicity the Markov chain is able to visit any configuration inside the region.

3.3.2 Heatbath algorithm for lattice gauge theory

The heatbath algorithm fulfils the requirements of detailed balance and strong ergodicity and can be applied in lattice gauge theory at every lattice site x and in every direction μ to insert a new link $U_\mu(x)$ according to the local probability distribution

$$\mathrm{d}P(U) = \mathrm{d}U \; \mathrm{e}^{\frac{\beta}{N_c} \operatorname{Re}\operatorname{Tr}(UA)} \; , \tag{3.29}$$

derived from the Wilson gauge action (3.12). Simplifying notation we consider an isotropic lattice, $a_\tau = a_\sigma$. Since during the update all links besides U are held fixed,

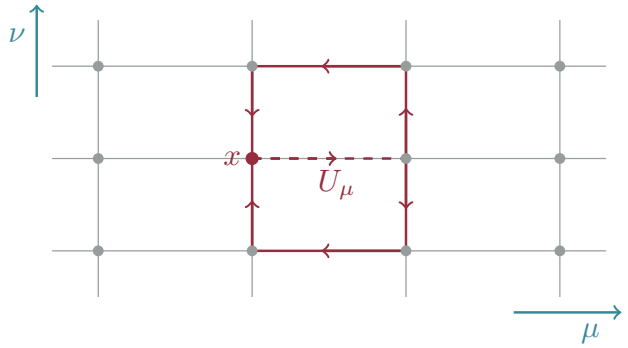

Figure 3.3: The figure illustrates two of the six staples surrounding the link $U_\mu(x)$.

only the link U and its sum of neighbours A enters the probability distribution. The term A is built from so-called staples surrounding the link $U = U_\mu$

$$A \equiv \sum_{\nu \neq \mu} \Big(U_\nu(x+\hat{\mu}) U_\mu^\dagger(x+\hat{\nu}) U_\nu^\dagger(x) + U_\nu^\dagger(x+\hat{\mu}-\hat{\nu}) U_\mu^\dagger(x-\hat{\nu}) U_\nu(x-\hat{\nu}) \Big) , \tag{3.30}$$

as depicted in figure 3.3.

In the case of SU(2), treated by Creutz [108], the sum of staples A is proportional to another SU(2) matrix given by

$$V = \frac{A}{a}, \qquad a \equiv \sqrt{\det(A)}. \tag{3.31}$$

Utilising the invariance of the Haar measure under the transformation $U \to U' = XV^\dagger$ the probability distribution (3.29) simplifies to

$$\mathrm{d}P(X) = \mathrm{d}X \; \mathrm{e}^{\frac{\beta}{N_c} a \,\mathrm{Re}\,\mathrm{Tr}\, X} \; . \tag{3.32}$$

By parametrising the matrix $X \in \mathrm{SU}(2)$ and the Haar measure according to

$$X = x_0 \cdot \mathbb{1}_{2\times 2} + \mathrm{i} x_i \sigma_i, \qquad x_0^2 + x_i^2 = 1, \tag{3.33}$$

with four real numbers $x_\mu \in \mathbb{R}$ and the Pauli matrices σ_i defined in (A.8) the distribution (3.32) takes the form

$$\mathrm{d}P(X) = \frac{1}{2\pi^2} \sqrt{1-x_0^2} \; \mathrm{e}^{\beta a x_0} \; \mathrm{d}\cos\theta \; \mathrm{d}\phi \; \mathrm{d}x_0 \; , \tag{3.34}$$

with $x_0 \in [-1,1]$, $\cos\theta \in [-1,1]$ and $\phi \in [0, 2\pi)$. Drawing these numbers randomly from their distributions (3.34) the matrix X can be constructed by (3.33) and finally related to the new link $U' = XV^\dagger$. Kennedy and Pendleton [109] improved this algorithm by increasing the acceptance rate of (3.34).

Since the projection (3.31) of the sum of two group elements back to the group does not work for SU(3), constructing links for this symmetry is more involved. Cabibbo and

Marinari developed a pseudo heatbath algorithm [110], which is based on applying the upper algorithm to the SU(2) subgroups r, s, t of SU(3). The subgroups are defined by

$$R = \begin{pmatrix} r_{11} & r_{12} & 0 \\ r_{21} & r_{22} & 0 \\ 0 & 0 & 1 \end{pmatrix}, \quad S = \begin{pmatrix} s_{11} & 0 & s_{12} \\ 0 & 1 & 0 \\ s_{21} & 0 & s_{22} \end{pmatrix}, \quad T = \begin{pmatrix} 1 & 0 & 0 \\ 0 & t_{11} & t_{12} \\ 0 & t_{21} & t_{22} \end{pmatrix}, \tag{3.35}$$

where $Y = R \cdot S \cdot T$ is one possible element of SU(3). Modifying the old link by left multiplication with e.g. R and denoting $W \equiv UA$ the probability distribution (3.29) reads

$$\mathrm{d}P(U) = \mathrm{d}U \ \mathrm{e}^{\frac{\beta}{N_c} \mathrm{Re}\,\mathrm{Tr}(RW)} \ . \tag{3.36}$$

Evaluating the trace in the exponent gives

$$\mathrm{Tr}\,(RW) = r_{11}w_{11} + r_{12}w_{21} + r_{21}w_{12} + r_{22}w_{22} + \text{terms without } r_{ij} \ , \tag{3.37}$$

which allows to compute r_{ij} by applying once again the SU(2) heatbath algorithm with w_{ij} playing the role of A. The other SU(2) subgroups s and t are determined analogously by changing $W \to W' = RW$ and $W \to W'' = RSW$, respectively. The new link is given by $U \to U' = TSRU$.

Iterated production of gauge field configurations by the heatbath algorithm creates a Markov chain, which involves a correlation between the generated configurations. The correlation can be reduced by the overrelaxation algorithm [19,97], which spreads the links in configuration space. The idea of the algorithm is to compute a gauge group element V which transforms the link by

$$U \to U' = V^\dagger U^\dagger V^\dagger \ , \tag{3.38}$$

but leaves the action invariant. For SU(2) the matrix V can be constructed similar to the heatbath algorithm, $V = \frac{A}{a}$. The extension to SU(3) follows closely the method of Cabibbo and Marinari. The transformation (3.38) moves the link in the group manifold and one alters the gauge configuration without changing the action. However, sampling the configuration space on the subspace of constant action is not ergodic and one only describes a microcanonical ensemble. For this reason the overrelaxation algorithms should be alternated with heatbath steps.

3.3.3 Data analysis

As already stated in the introduction of this chapter the generated ensemble of gauge field configurations is used to compute the expectation value of observables (3.23). One estimator for the expectation value is the average

$$\bar{x} = \frac{1}{N} \sum_{n=1}^{N} x \ , \tag{3.39}$$

over a set of N data points. The statistical process of averaging involves a variance, e.g. the standard deviation. However, one should account for the not statistically independent distribution of the data set caused by correlated configurations by e.g. jackknife-resampling [19].

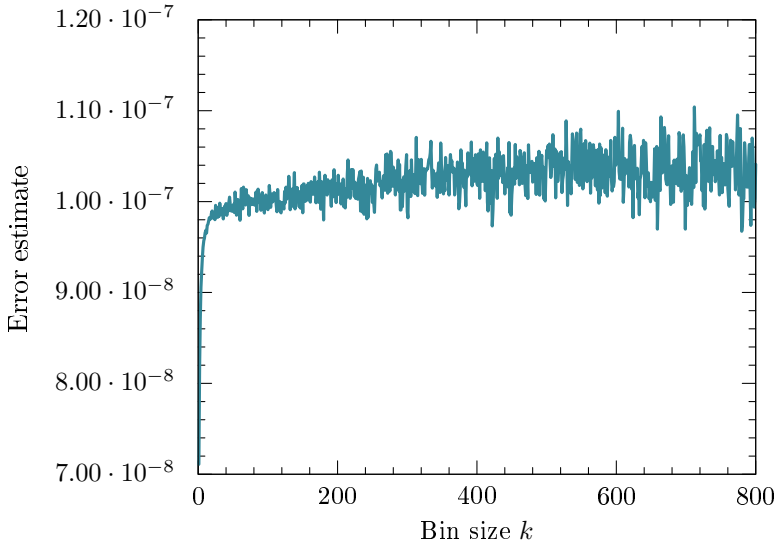

Figure 3.4: Plotting the estimated error versus the bin size k allows to identify the optimal bin size from a plateau. The jackknife resampling is performed with this value.

One divides the data set into N_k bins of size k and calculates the mean $\widetilde{x}_i$ by averaging over all data points not belonging to the block i. For a large enough number of bins N_k the central limit theorem justifies application of the usual Gaussian variance with $\bar{x}$ being the average over the original data set

$$\sigma_{\bar{x}}^2 = \frac{N_k - 1}{N_k} \sum_i^{N_k} (\widetilde{x}_i - \bar{x})^2 \,, \tag{3.40}$$

but for the removal of correlations a smaller number of bins N_k corresponding to a larger bin size k is preferable. Plotting the variance as a function of the bin size k the optimal amount of bins can be determined from a plateau as illustrated in figure 3.4.

Besides the overrelaxation algorithm one method to reduce correlation between data points is to omit configurations in the averaging process. The optimal number of skipped configurations is determined from the autocorrelation time [96]. However, in our studies of the transport coefficient κ producing the configurations is numerically costly and we do not discard any configurations, but account for the error by jackknife resampling.

In addition to the specified statistical errors one encounters systematic errors introduced by the discretisation of space time. Lattice actions and observables differ with their continuum equivalent on a power of the lattice spacing $\mathcal{O}(a^n)$, $n \in \mathbb{N}$. This lattice artefacts can be investigated in a lattice perturbation theory calculation or removed by extrapolating simulations to the continuum limit $a \to 0$. Therefore, one performs simulations with decreasing lattice spacing keeping the physical conditions, e.g. the temperature, which also depends on the lattice spacing (3.18), fixed. In lattice Yang-Mills theory the lattice artefacts are always an even power of the lattice spacing $\mathcal{O}(a^{2n})$. In order to avoid another systematic error introduced by simulating in a finite volume one chooses each spatial lattice dimension larger than the real mean free path of involved processes at finite temperature. Additionally, one should check the volume dependence of observables by altering the lattice size.

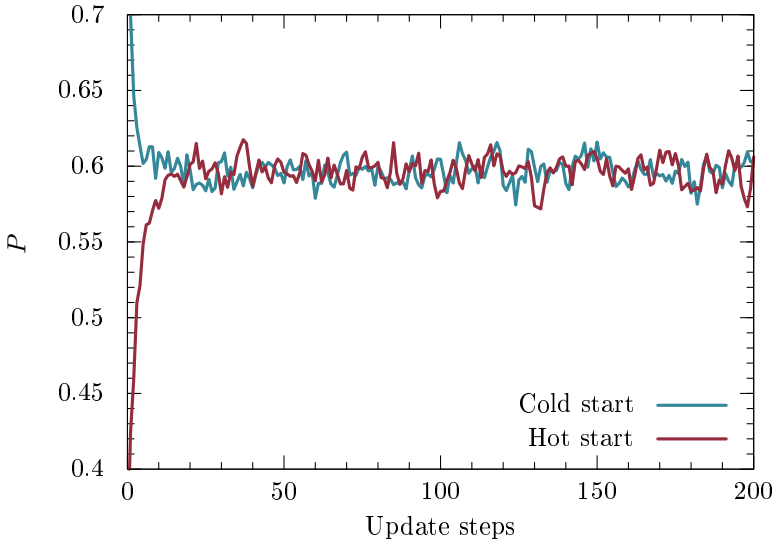

Figure 3.5: Summed plaquette P versus update steps. After a thermalisation phase the ensemble follows its equilibrium distribution $p_{\mathrm{eq}}(U)$ independent of the initial configuration.

The heatbath algorithm starts from an initial gauge field configuration. One distinguishes between a cold start setting all links to the identity $U = \mathbb{1}_{N_c \times N_c}$ and a hot start filling the links with Gaussian distributed numbers and projecting them to the group SU(3). Both approaches involve a thermalisation phase, driving the configurations to their equilibrium distribution $p_{\mathrm{eq}}(U)$. In order to reflect the correct distribution in an expectation value one has to discard all configurations from this phase. The end of the thermalisation can be noted by monitoring an observable, e.g. the summed plaquette

$$P = N_P \sum_x \sum_{\substack{\mu,\nu \\ \nu<\mu}} \mathrm{Re}\,\mathrm{Tr}\, U_{\mu\nu}, \qquad N_P \equiv 2\left((N_\tau N_\sigma^3)(N_c N_{\mathrm{d}}(N_{\mathrm{d}}-1))\right)^{-1}, \tag{3.41}$$

versus the update steps as shown in figure 3.5.

3.3.4 Application programming interface QDP++

The presented lattice QCD algorithms are implemented by use of the `C++` application programming interface `QDP++` developed by the Scientific Discovery through Advanced Computing (SciDAC) [111]. It provides an interface of data-parallel routines and data types suitable to lattice gauge theory and is the leading building block of the `Chroma` library.

The main idea of `QDP++` is to introduce lattice templates, which consist of data primitives over all sites and primarily operate on these templates. For instance the following `QDP++` types are implemented by this tensor product structure:

Template	*Lattice*		*Colour*		*Spin*		*Complexity*
`LatticeColorMatrix`	Lattice	$\otimes$	Matrix(N_c)	$\otimes$	Scalar	$\otimes$	Complex
`LatticeDiracFermion`	Lattice	$\otimes$	Vector(N_c)	$\otimes$	Vector(N_s)	$\otimes$	Complex
`Real`	Scalar	$\otimes$	Scalar	$\otimes$	Scalar	$\otimes$	Scalar

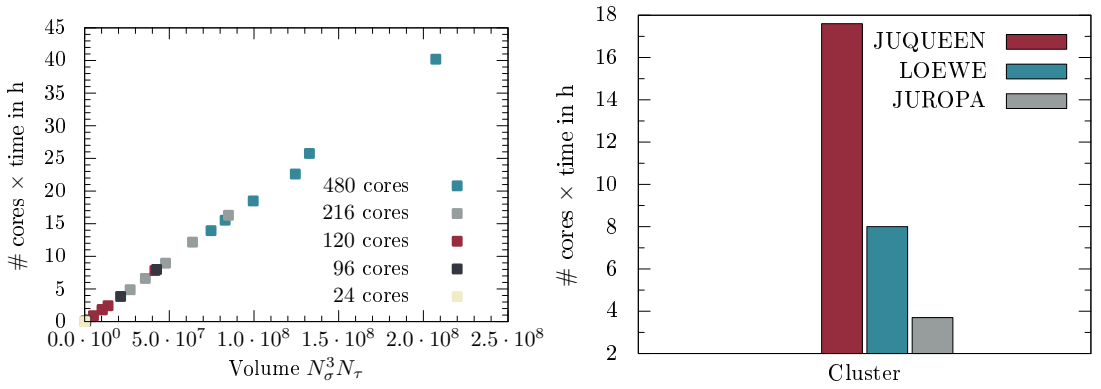

Figure 3.6: Left hand side: Average computing time versus lattice size for the anisotropic SU(3) heatbath algorithm implemented in `QDP++` and run on the LOEWE-CSC using a various amount of cores. The figure illustrates the scaling with an increasing number of cores. Right hand side: Performance of our heatbath implementation run on the clusters JUQUEEN, LOEWE-CSC and JUROPA on a lattice of size $120^3 \times 24$. The bad performance for the fastest cluster, the JUQUEEN, is explained by a missing optimisation of `QDP++` regarding Blue Gene/Q. We performed the benchmark before the LOEWE-CSC has been upgraded.

The type `LatticeColorMatrix` defines on every lattice site a $N_c \times N_c$ colour matrix built of complex numbers and corresponds to a link. The type `LatticeDiracFermion` is a tensor product of vectors in N_c dimensional colour space and N_s dimensional spin space with complex entries on every lattice site. The type `Real` is a real number $a \in \mathbb{R}$ on every site.

The interface based on lattice templates provides a high level of abstraction and hides architectural dependencies like mapping the logical problem grid onto the machine layout or the parallel communication. The parallelisation is incorporated by the library `QMP` (Lattice QCD Message Passing) based on `MPI`. The left hand side of figure 3.6 illustrates the scaling of our anisotropic SU(3) heatbath implementation in `QDP++`. We compare the run time on different clusters on the right hand side. Our code performs best on the JUROPA [112]. Although the JUQUEEN [113] is inherently faster, we perform worse due to a missing optimisation of `QDP++` regarding Blue Gene/Q. Since our computation time on the JUROPA is rather limited, we run all simulations on the LOEWE-CSC [114].

In order to examine the validity of our implementation we compute plaquette averages and compare them to results from literature [100]. On an anisotropic lattice it is common to distinguish between spatial and temporal plaquettes

$$P_{\sigma\sigma} = N_{P,\sigma} \sum_x \sum_{\substack{\mu,i \\ i<\mu}} \operatorname{Re} \operatorname{Tr} U_{\mu i}, \qquad N_{P,\sigma} \equiv 2 \left((N_\tau N_\sigma^3) N_c (N_\mathrm{d} - 1)(N_\mathrm{d} - 2) \right)^{-1}, \quad (3.42)$$

$$P_{\sigma\tau} = N_{P,\tau} \sum_x \sum_{\mu} \operatorname{Re} \operatorname{Tr} U_{\mu 0}, \qquad N_{P,\tau} \equiv \left((N_\tau N_\sigma^3) N_c (N_\mathrm{d} - 1) \right)^{-1}. \quad (3.43)$$

Figure 3.7 and table 3.1 compare the computed spatial and temporal plaquette averages with their literature values. The agreement shows that our implementation of the anisotropic SU(3) heatbath algorithm is correct.

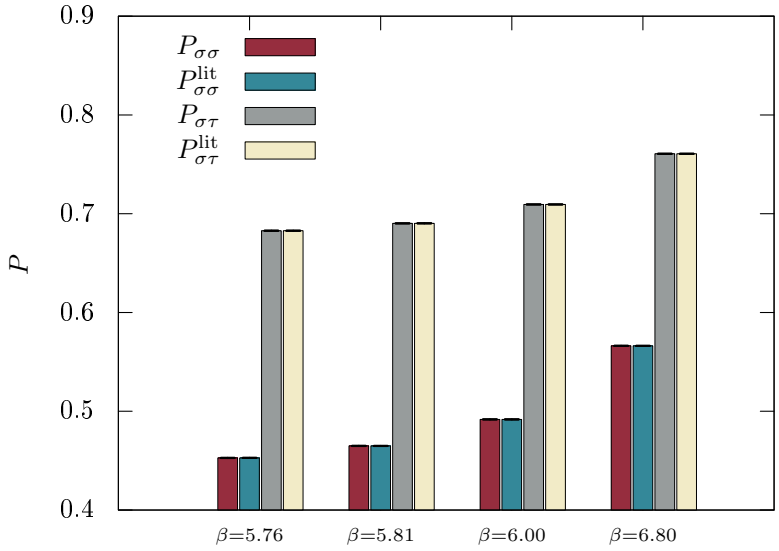

Figure 3.7: Comparison of spatial $P_{\sigma\sigma}$ and temporal $P_{\sigma\tau}$ plaquette averages to literature [100]. The runs are performed on $16^3 \times 8$ lattices with an anisotropy of $\xi = 2$. We use an ensemble size of 3000 configurations and alternate each heatbath update with four overrelaxation steps. The exact values are listed in table 3.1.

β	$P_{\sigma\sigma}$	$P^{\mathrm{lit}}_{\sigma\sigma}$	$P_{\sigma\tau}$	$P^{\mathrm{lit}}_{\sigma\tau}$
5.76	0.45274(7)	0.45278(3)	0.68275(3)	0.68278(1)
5.81	0.46490(7)	0.46491(4)	0.69026(3)	0.69028(2)
6.00	0.49176(4)	0.49177(2)	0.70940(1)	0.709406(6)
6.80	0.56623(3)	0.56622(2)	0.76068(1)	0.760672(4)

Table 3.1: Comparison of spatial $P_{\sigma\sigma}$ and temporal $P_{\sigma\tau}$ plaquette averages to literature [100]. Within the errors the values agree confirming a correct implementation of the anisotropic SU(3) heatbath algorithm.

4 Second order transport coefficient κ

One of the major findings of the experimental heavy ion programme is that QCD matter at high temperatures and low densities behaves as a nearly ideal fluid. This conclusion is based on the fact that experimental data are excellently described by relativistic hydrodynamics. The parameters of viscous hydrodynamics are the transport coefficients.

Unfortunately, lattice simulations of real time quantities like transport coefficients are in general severely limited by the need for analytic continuation. As discussed in section 3 lattice gauge theory at finite temperature is inherently connected to thermal equilibrium. Only Euclidean correlators are available on the lattice and a computation of real time quantities necessitates an analytic continuation to retarded correlators. This analytic continuation is usually based on the maximum entropy method or a model ansatz both requiring functional input and thus compromising the lattice approach being a first principle calculation.

The second order transport coefficient κ is an exception to this conceptual difficulty. Being defined from a correlator at vanishing frequency it is of thermodynamic nature and the analytic continuation becomes trivial. It is directly accessible from the lattice without having to resort to maximum entropy methods or functional input for the retarded correlator.

4.1 Definition of the second order transport coefficient κ

Transport coefficients can be derived from a gradient expansion of the dissipative energy-momentum tensor in relativistic hydrodynamics as we discuss in section 4.1.1 below. Expanding to second order in curved space time gives the second order transport coefficient κ, which couples to the Riemann and Ricci tensor. The respective values of the transport coefficients are determined by the underlying microscopic theory, which is QCD in the case of the quark gluon plasma. They can be fixed from calculations within this theory or from experiments. We pursue the former approach in this chapter.

To this end we use a connection of transport coefficients to thermal field theory established by linear response theory. Remarkably, an equilibrium ensemble encodes information on the real time quantities and thus allows their computation from correlators evaluated in thermal equilibrium.

4.1.1 Relativistic hydrodynamics

Our review of relativistic hydrodynamics follows [115]. The basic quantity in hydrodynamics is the energy-momentum tensor, which can be decomposed into an ideal part $T^{\mu\nu}_{(0)}$ and a dissipative one $\Pi^{\mu\nu}$

$$T^{\mu\nu} = T^{\mu\nu}_{(0)} + \Pi^{\mu\nu}. \tag{4.1}$$

For a relativistic system its degrees of freedom are the total energy density ϵ, the fluid's four-velocity u^μ and the pressure p. Lorentz symmetry and the identifications $T^{00}_{(0)} = \epsilon$, $T^{0i}_{(0)} = T^{i0}_{(0)} = 0$ and $T^{ij}_{(0)} = p\,\delta^{ij}$ in the local rest frame restrict the form of the ideal part to

$$T^{\mu\nu}_{(0)} = \epsilon u^\mu u^\nu + p\,(g^{\mu\nu} + u^\mu u^\nu)\,, \tag{4.2}$$

where $g^{\mu\nu}$ is the metric tensor in Minkowski space (A.5). The equations of relativistic ideal hydrodynamics are derived from conservation of the energy-momentum tensor $\partial_\mu T^{\mu\nu}_{(0)} = 0$ and are given by

$$D\epsilon + (\epsilon + p)\partial_\mu u^\mu = 0, \tag{4.3a}$$
$$(\epsilon + p)Du^\alpha - \nabla^\alpha p = 0, \tag{4.3b}$$

where we introduce the notations

$$D \equiv u^\mu \partial_\mu, \qquad \nabla^\alpha \equiv \Delta^{\alpha\mu}\partial_\mu, \qquad \Delta^{\mu\nu} = g^{\mu\nu} - u^\mu u^\nu. \tag{4.4}$$

The latter one is a projector in spatial directions. The equations (4.3) reproduce the classical Euler equation and continuity equation [116] in the non-relativistic limit.

Considering viscous effects inside the fluid the equations (4.3) must be supplemented with the dissipative contribution of the energy-momentum tensor. In a system without conserved charges we choose the Landau-Lifshitz ansatz defining the local rest frame as the frame, where the energy density is at rest, $u_\mu \Pi^{\mu\nu} = 0$. From the energy-momentum tensor's conservation follows

$$D\epsilon + (\epsilon + p)\partial_\mu u^\mu = \Pi^{\mu\nu}\nabla_{(\mu}u_{\nu)}, \tag{4.5a}$$
$$(\epsilon + p)Du^\alpha - \nabla^\alpha p = -\Delta^\alpha_\nu \partial_\mu \Pi^{\mu\nu} \tag{4.5b}$$

with the symmetrised notation $A_{(\mu}B_{\nu)} = \frac{1}{2}(A_\mu B_\nu + A_\nu B_\mu)$. In order to complete the viscous description one must specify the dissipative contribution $\Pi^{\mu\nu}$, which is usually split into a traceless part $\pi^{\mu\nu}$ and a remainder with non-vanishing trace Π

$$\Pi^{\mu\nu} = \pi^{\mu\nu} + \Delta^{\mu\nu}\Pi. \tag{4.6}$$

One way of determining the dissipative part $\Pi^{\mu\nu}$ is based on the covariant formulation of the second law of thermodynamics

$$\partial_\mu s^\mu \geq 0, \tag{4.7}$$

where s denotes the entropy density. Rewriting it in terms of the hydrodynamic degrees of freedom, it is fulfilled for the following dissipative energy-momentum tensor

$$\pi^{\mu\nu} = \eta \nabla^{<\mu}u^{\nu>}, \qquad \Pi = \zeta \nabla_\alpha u^\alpha, \tag{4.8}$$

where we use the notation $\nabla_{<\mu}u_{\nu>} \equiv 2\nabla_{(\mu}u_{\nu)} - \frac{2}{3}\Delta_{\mu\nu}\nabla_\alpha u^\alpha$. In the non-relativistic limit one obtains the Navier-Stokes equations [116] indicating that η and ζ are the shear viscosity and bulk viscosity, respectively. The relativistic Navier-Stokes equations

do not constitute a causal theory [115, 117] and suffer from numeric instabilities [118]. These problems can be overcome by including more terms into the definition of $\Pi^{\mu\nu}$.

An organised way of doing so is a gradient expansion [115] of the energy-momentum tensor (4.1). To zeroth order it reproduces the ideal hydrodynamic equations (4.3) and to first order the Navier-Stokes equations including the first order transport coefficients η and ζ. Adding second order gradients in flat space time results in the Israel-Müller-Stewart theory [119, 120] providing a causal and numerically stable description of relativistic hydrodynamics. Whereas the gradient expansion to first order resulting in the Navier-Stokes equations is complete, the classification of second order gradients in the Israel-Müller-Stewart theory is not. In particular the second order transport coefficient κ is absent.

A gradient expansion up to second order giving all second and lower order transport coefficients has to be done in curved space time and gives for the dissipative energy-momentum tensor (4.6) [121]

$$\begin{aligned}\pi^{\mu\nu} = &-\eta\sigma^{\mu\nu} + \eta\tau_\pi\left(\langle D\sigma^{\mu\nu}\rangle + \frac{\nabla u}{3}\sigma^{\mu\nu}\right) + \kappa\left(R^{<\mu\nu>} - 2u_\alpha u_\beta R^{\alpha<\mu\nu>\beta}\right)\\ &+ \lambda_1\sigma_\lambda^{<\mu}\sigma^{\nu>\lambda} + \lambda_2\sigma_\lambda^{<\mu}\Omega^{\nu>\lambda} + \lambda_3\Omega_\lambda^{<\mu}\Omega^{\nu>\lambda} + \kappa^* 2u_\alpha u_\beta R^{\alpha<\mu\nu>\beta}\\ &+ \eta\tau_\pi^*\frac{\nabla u}{3}\sigma^{\mu\nu} + \lambda_4\nabla^{<\mu}\ln s\nabla^{\nu>}\ln s,\end{aligned} \tag{4.9a}$$

$$\begin{aligned}\Pi = &-\zeta\nabla u + \zeta\tau_\Pi D\nabla u + \xi_1\sigma^{\mu\nu}\sigma_{\mu\nu} + \xi_2(\nabla u)^2 + \xi_3\Omega^{\mu\nu}\Omega_{\mu\nu} + \xi_4\nabla_\mu^\perp\ln s\nabla_\perp^\mu\ln s\\ &+ \xi_5 R + \xi_6 u^\alpha u^\beta R_{\alpha\beta},\end{aligned} \tag{4.9b}$$

where we use the notation $\nabla_\perp^\mu \equiv \Delta^{\mu\nu}\nabla_\nu$ and

$$\langle A_{\mu\nu}\rangle \equiv A^{<\mu\nu>} \equiv \frac{1}{2}\Delta^{\mu\alpha}\Delta^{\nu\beta}(A_{\alpha\beta} + A_{\beta\alpha}) - \frac{1}{3}\Delta^{\mu\nu}\Delta^{\alpha\beta}, \tag{4.10}$$

which gives symmetrised, space-projected and trace-subtracted indices. The shear and vorticity tensors are given by

$$\sigma_{\alpha\beta} \equiv \nabla_\alpha^\perp u_\beta + \nabla_\beta^\perp u_\alpha - \frac{2}{3}\Delta_{\alpha\beta}\nabla u, \tag{4.11a}$$

$$\Omega_{\mu\nu} \equiv \frac{1}{2}\left(\nabla_\mu^\perp u_\nu - \nabla_\nu^\perp u_\mu\right). \tag{4.11b}$$

The Riemann tensor $R_{\alpha\mu\nu\beta}$, the Ricci tensor $R_{\mu\nu} = R^\lambda{}_{\mu\lambda\nu}$ and the Ricci scalar $R = R^\mu_\mu$ are involved due to curved space time. The first terms on the right hand side of equations (4.9a) and (4.9b) are of first order and include the familiar shear viscosity coefficient η and bulk viscosity coefficient ζ, respectively. There are fifteen further transport coefficients τ_π, τ_π^*, κ, κ^*, λ_1, λ_2, λ_3, λ_4, τ_Π, ξ_1, ξ_2, ξ_3, ξ_4, ξ_5 and ξ_6, which are of second order. They can be classified according to their thermodynamic or dynamic nature [122]. A transport coefficient is called thermodynamic if it can contribute to the energy-momentum tensor $T^{\mu\nu}$, when the system is in equilibrium. For instance this can be the case for curved but time-independent geometries. The quantities κ, κ^*, λ_3, λ_4, ξ_3, ξ_4, ξ_5 and ξ_6 are of thermodynamic nature.

At very high temperature the quark-gluon plasma can be treated as a conformal fluid [121]. This additional symmetry restricts the number of possible gradients and

reduces the number of transport coefficients. The second order transport coefficient κ does not vanish due to this enhanced symmetry [121].

The definition of transport coefficients is based on a gradient expansion of the energy-momentum tensor in relativistic hydrodynamics, but their respective values have to be determined from experiment or an underlying microscopic theory. For the quark-gluon plasma this theory is QCD. We see in the next section that thermodynamic coefficients – such as κ – are connected to thermal field theory by retarded correlation functions evaluated at vanishing frequency and thus are accessible from the lattice.

4.1.2 Thermal field theory

For the computation of transport coefficients from QCD a relation between its definition in relativistic hydrodynamics and thermal field theory is necessary. Such a relation can be established by applying the fluctuation-dissipation theorem. It states that enforcing some small perturbation on a system generates a linear response, which is expressed in terms of fluctuations of the system in thermal equilibrium. Thus the equilibrium ensemble encodes information on the relaxation process and in particular on the involved transport coefficients. Via Kubo formulae [123] the transport coefficients can be directly connected to linear response functions, which in quantum field theory are related to retarded two-point correlation functions providing a measure of fluctuations in a system.

The transport coefficient κ can be derived by an expansion in the background geometry [122, 124]. The idea is to introduce non-vanishing shear and vorticity (4.11) to an equilibrium system in flat space time. This can be achieved by adding a perturbatively weak and slowly varying space time non-uniformity to the metric tensor

$$g'_{\mu\nu}(x) = g_{\mu\nu} + h_{\mu\nu}(x), \tag{4.12}$$

which couple to the energy-momentum tensor $T_{\mu\nu}$. A treatment of the perturbation $h_{\mu\nu}$ in linear response theory gives an expansion in correlation functions of multiple energy-momentum tensors. Their coefficients are the response of the energy-momentum tensor to a non-uniformity in the fluid and correspond to the different transport coefficients.

The detailed calculation in [122, 124] gives the following Kubo formula regarding the second order transport coefficient κ:

$$\kappa = \lim_{q_z \to 0} \frac{\partial^2}{\partial q_z^2} \, G^{\mathrm{R}}_{xy,xy}(\omega, \mathbf{q})\big|_{\omega = q_x = q_y = 0} \tag{4.13}$$

or equivalently [115, 121]

$$G^{\mathrm{R}}_{xy,xy}(\omega = 0, \mathbf{q}) = G(0) + \frac{\kappa}{2} q_z^2 + \mathcal{O}(q_z^3). \tag{4.14}$$

In contrast to [124] we changed the sign of the κ term due to using a different metric convention. The retarded correlator corresponds to a two-point function of the energy-momentum tensor evaluated in thermal equilibrium and reads

$$G^{\mathrm{R}}_{xy,xy}(x, y) = \left\langle [T_{xy}(x), T_{xy}(y)] \, \theta(x_0 - y_0) \right\rangle . \tag{4.15}$$

Its Fourier transform is given by (A.15). The transport coefficient κ can be identified as the leading coefficient in a low momentum expansion of the retarded correlator at zero

frequency $\omega = 0$. In this definition the spatial momenta are aligned orthogonally to the respective channel of the correlator, i.e. $\mathbf{q} = (0, 0, q_z)$ for $T_{xy}T_{xy}$.

Connecting the transport coefficient κ to the retarded correlator (4.15) by relation (4.14) allows to determine a real time observable from a quantity evaluated in thermal equilibrium. In particular it facilitates a computation of the transport coefficient κ from lattice gauge theory. However, on the lattice, only Euclidean correlators are accessible. Rewriting the latter and retarded correlators in their spectral representation, we find that they are connected by an analytic continuation, see section 2.2.2. Since thermodynamic transport coefficients are defined from correlators at vanishing frequency, the analytic continuation (2.34) becomes trivial. The connection between retarded and Euclidean correlator for $\omega = 0$ reads

$$G^{\mathrm{R}}(\omega = 0, \vec{q}) = G^{\mathrm{E}}(\omega = 0, \vec{q}) + B, \tag{4.16}$$

where the Euclidean correlator for the transport coefficient κ is given by

$$G^{\mathrm{E}}(x, y) = \langle T_{xy}(x) T_{xy}(y) \rangle \,, \tag{4.17}$$

and its Fourier transform by (A.17a). The contact term B arises from the missing commutator in the definition of the Euclidean correlator (4.17) compared to its retarded analogue (4.15) and corresponds to the correlator evaluated at equal space time points, e.g. $\sim T_{xy}(0)T_{xy}(0)$. An investigation of the contact term B by an operator product expansion [74] gives [125]

$$B \approx \sum_{\mu} C_{\mu} \langle T_{\mu\mu}(0) \rangle \, \delta(x), \tag{4.18}$$

with C_μ being Wilson coefficients. A perturbative evaluation to leading order [126] results in

$$B = \frac{2}{3} \langle T_{00} \rangle + \frac{1}{6} \left\langle F^a_{\mu\nu} F^a_{\mu\nu} \right\rangle , \tag{4.19}$$

and shows that the contact term is momentum independent. Hence equation (4.14) can be rewritten

$$G^{\mathrm{E}}_{xy,xy}(\omega = 0, q_z) \equiv G^{\mathrm{E}}(\omega = 0, q_z) = G'(0) + \frac{\kappa}{2} q_z^2 + \mathcal{O}(q_z^3), \tag{4.20}$$

where we absorbed the constant $G(0)$ and the contact term B, both momentum independent, into $G'(0) \equiv G(0) - B$. The transport coefficient κ can be obtained as the slope of the low momentum correlator $G^{\mathrm{E}}(q_z^2)$, which provides a possibility for a direct computation using lattice gauge theory.

Besides κ there are two other independent thermodynamic transport coefficients given by the following Kubo formula [122]

$$\lambda_3 = 2\kappa^* - 4 \lim_{p^z, q^z \to 0} \frac{\partial^2}{\partial_{p_z} \partial_{q_z}} \, G^{\mathrm{E}}_{xt,yt,xy}(p, q)\big|_{p_0, q_0 = 0} \,, \tag{4.21a}$$

$$\lambda_4 = -2\kappa^* + \kappa - \frac{c_{\mathrm{s}}^4}{2} \lim_{p^x, q^y \to 0} \frac{\partial^2}{\partial_{p_x} \partial_{q_y}} \, G^{\mathrm{E}}_{tt,tt,xy}(p, q)\big|_{p_0, q_0 = 0} \,. \tag{4.21b}$$

They are connected to Euclidean three-point functions of the energy-momentum tensor. The quantity c_s denotes the speed of sound. The further thermodynamic transport coefficients κ^*, ξ_3, ξ_4, ξ_5 and ξ_6 can be determined in terms of κ, λ_3 and λ_4 by five independent conditions found in [127,128] and listed in [122].

In general all thermodynamic transport coefficients can be connected to Euclidean correlators with vanishing frequency and are thus directly accessible from the lattice. This is in contrast to the transport coefficients η, ζ, τ_π, τ_π^*, λ_1, λ_2, τ_Π, ξ_1 and ξ_2, which are true dynamic quantities. Since their Kubo formulas involve a non-vanishing frequency [124], the analytic continuation (2.34) becomes non-trivial. It even constitutes a numerically ill-posed problem [82], since reconstructing a complex function from a finite amount of data points is required. For instance a lattice calculation of the shear viscosity η by the use of Kubo formulas requires a determination of the spectral function $\rho(\omega)$ (2.29) involving an analytic continuation of a Euclidean correlator to Minkowski space time. As illustrated in figure 2.2 in Euclidean space time the frequency is a discrete quantity, the Matsubara frequency. Furthermore the number of Matsubara frequencies (2.19) is restricted by the temporal lattice extent N_τ. Thus a computation of dynamic transport coefficients from lattice calculations as performed for the shear viscosity [39] and electrical conductivity [40,41] requires additional input, e.g. an ansatz for the spectral function or the maximum entropy method leaving the regime of a first principle calculation.

4.2 Continuum results for the transport coefficient κ

In the last section we established a connection between the transport coefficient κ and a Euclidean correlator of the energy-momentum tensor evaluated in thermal equilibrium, which allows us to compute the transport coefficient κ from QCD, which is the fundamental theory describing the quark-gluon plasma. Since an inclusion of fermions in our lattice simulations is numerically not affordable, we only deal with pure Yang-Mills theory.

We derive the energy-momentum tensor and give an analytic result for the transport coefficient κ from a weak coupling expansion in continuum in section 4.2.1. The calculation in flat space gives a non-vanishing value for the transport coefficient κ, although it is related to the Riemann and Ricci tensor by its definition in relativistic hydrodynamics (4.9a). Furthermore we review predictions of the transport coefficient κ from $\mathcal{N} = 4$ supersymmetric Yang-Mills theory applying strong-weak duality in section 4.2.2.

4.2.1 Yang-Mills theory

The basic quantity entering the computation of transport coefficients is the energy-momentum tensor. It is the Noether current regarding invariance of the Lagrangian under space time translations. In order to construct a symmetric and gauge invariant energy-momentum tensor, it is favourable to use the invariance of the Lagrangian under Poincaré transformations (3.7). Following [129] one finds for the energy-momentum tensor

$$T^\mu_\nu = 2\frac{\partial \mathcal{L}}{\partial F^a_{\mu\rho}} F^a_{\nu\rho} - \delta^\mu_\nu \mathcal{L}. \tag{4.22}$$

It is only conserved at classical level. The inclusion of quantum corrections leads to a breaking of scale invariance [74]. The same theory referred to another scale involves a different value of the renormalised coupling as discussed in section 2.1.2. As a consequence the trace of the energy-momentum tensor takes a nonzero value leading to the trace anomaly.

Finally, the energy-momentum tensor of Yang-Mills theory is

$$T_{\mu\nu} = \theta_{\mu\nu} + \frac{1}{4}\delta_{\mu\nu}\theta, \tag{4.23}$$

$$\theta_{\mu\nu} = \frac{1}{4}\delta_{\mu\nu}F^a_{\alpha\beta}F^a_{\alpha\beta} - F^a_{\mu\alpha}F^a_{\nu\alpha}, \tag{4.24}$$

where $F^a_{\mu\nu}$ denotes the field strength tensor (2.8). The term $\theta = \beta^{\mathrm{QCD}}(g)F^a_{\alpha\beta}F^a_{\alpha\beta}$ is the trace anomaly including the QCD beta function (2.10) with $N_f = 0$. Since the transport coefficient κ is extracted from a correlator including only the channel $T_{xy}T_{xy}$, the trace anomaly does not enter the computations.

The transport coefficient κ has been determined in pure gluodynamics by a weak coupling expansion [122, 130]. Considering the ideal gas limit, i.e. vanishing coupling $g = 0$, an evaluation of the correlator (4.20) at low momentum gives

$$\kappa = (N_c^2 - 1)\frac{T^2}{18}. \tag{4.25}$$

Although the transport coefficient κ solely arises from a gradient expansion in curved space time (4.9a), its value determined by a weak coupling expansion in flat space time is finite.

4.2.2 Strong-weak duality

The anti-de Sitter/conformal field theory (AdS/CFT) correspondence provides a toolkit for studying strongly coupled quantum field theories [131]. It is based on a strong-weak duality: a strongly interacting field theory corresponds to a weakly interacting gravitational field theory, which is easier to treat mathematically. The duality allows to make predictions for the physics of the quark-gluon plasma by using string theory [132, 133].

The AdS/CFT correspondence for $\mathcal{N} = 4$ supersymmetric Yang-Mills theory in the limits $N_c \to \infty$ and $g^2 N_c \to \infty$ predicts for the transport coefficient [121]

$$\kappa = \frac{\eta}{\pi T}. \tag{4.26}$$

A comparison between the results for κ from AdS/CFT and QCD requires a matching of the degrees of freedom. Since κ is an extensive quantity, it scales with the number of degrees of freedom. In order to compare with Yang-Mills theory calculations we rewrite (4.26)

$$\frac{\kappa}{T^2} = \frac{\eta}{s} \cdot \frac{s}{\pi T^3} \tag{4.27}$$

and use the AdS/CFT result for the ratio shear viscosity over entropy density $\frac{\eta}{s} = \frac{1}{4\pi}$, but take the entropy density s from a SU(3) gauge theory lattice calculation [134].

Determining the entropy density by its connection to the interaction measure I and pressure p

$$\frac{s}{T^3} = \frac{I + 4p}{T^4}, \tag{4.28}$$

we find for $\frac{\kappa}{T^2}$ the values listed in table C.1 in appendix C.1, which we use in section 4.4.4.

Note that the description of the gluon plasma by AdS/CFT correspondence is valid for $\mathcal{N} = 4$ supersymmetric Yang-Mills, which does not coincide with SU(3) Yang-Mills theory[1] and consequently does not constitute the correct fundamental theory. Although we match the field contents of both theories, further significant differences like a missing running coupling, no confinement or conformal invariance exist. In section 4.4.4 we investigate the effect of these discrepancies in terms of the transport coefficient κ.

4.3 Transport coefficient κ from lattice Yang-Mills theory

This section deals with the framework regarding a computation of the transport coefficient κ in lattice Yang-Mills theory. It relies on the content established in chapter 3. We discretise the energy-momentum tensor by plaquette variables in section 4.3.1. Its correlator entering the computation of the transport coefficient κ is transferred to the lattice in the next section 4.3.2. Thereby we derive a constraint on the temporal and spatial lattice extents restricting simulations to large lattice sizes. Due to reduced Poincaré symmetry on the lattice, a multiplicative renormalisation of the energy-momentum tensor becomes necessary. We discuss this and the need for additive renormalisation in section 4.3.3.

4.3.1 Energy-momentum tensor on the lattice

The lattice calculation of the transport coefficient κ based on the momentum expansion (4.20) of the correlator (4.17) requires a discretisation of the energy-momentum tensor of Yang-Mills theory (4.23). As explained in section 4.2.1 the energy-momentum tensor is the Noether-current regarding symmetry of the Lagrangian under translations. In the continuum it is protected from renormalisation by Ward-identities [135]. However, on the lattice translations are restricted to being a multiple of the lattice spacing a_μ and thus only form a discrete group. As a consequence the energy-momentum tensor requires multiplicative renormalisation.

For this purpose it is favourable to express the Euclidean correlator (4.17) in terms of diagonal energy-momentum tensor elements instead of non-diagonal ones. This is achieved by exploiting rotation invariance. As shown in appendix B.1 rotating the lattice by $\frac{\pi}{4}$ in the plane of the corresponding channel, i.e. the (x, y)-plane for $\mathbf{q} = (0, 0, q_z)$, gives for the correlator

$$\langle T_{xy}(x) T_{xy}(y) \rangle = \frac{1}{2} \Big(\langle \theta_{xx}(x) \theta_{xx}(y) \rangle - \langle \theta_{xx}(x) \theta_{yy}(y) \rangle \Big). \tag{4.29}$$

[1] It neither coincides with full QCD.

The trace anomaly θ does not enter the transformed correlator, although it includes diagonal elements of the energy-momentum tensor. Additionally, temporal and spatial elements of the energy-momentum tensor require separate renormalisation factors Z_τ and Z_σ on an anisotropic lattice. A renormalised diagonal element of the energy-momentum tensor reads

$$a_\sigma^3 a_\tau \theta_{ii}(x) = \frac{\beta}{N_\mathrm{c}} \operatorname{Re}\operatorname{Tr}\left(Z_\tau(\beta,\xi)\theta_{ii}^\tau(x) + Z_\sigma(\beta,\xi)\theta_{ii}^\sigma(x)\right), \tag{4.30}$$

where we refer to the lattice framework established in section 3.1. The bare elements are given by

$$\theta_{ii}^\tau(x) \equiv \xi_0 \widehat{F}_{0i}^2(x) - \xi_0 \sum_{k\neq i} \widehat{F}_{k0}^2(x), \tag{4.31a}$$

$$\theta_{ii}^\sigma(x) \equiv -\frac{1}{\xi_0} \sum_{\substack{k,j\neq i \\ k<j}} \widehat{F}_{kj}^2(x) + \frac{1}{\xi_0} \sum_k \widehat{F}_{ki}^2(x). \tag{4.31b}$$

In the naive discretisation [136] the terms $\widehat{F}_{ij}$ are implemented as ordinary plaquette variables (3.11), $\widehat{F}_{ij} = U_{ij}$. As illustrated in figure 4.1 and discussed in [137] an implementation by Clover plaquettes, $\widehat{F}_{ij} = \widetilde{F}_{ij}$, produces a better signal-to-noise ratio. The Clover plaquette [138] consists of four ordinary plaquettes surrounding the point x as depicted in figure 4.2. It is given by

$$\widetilde{F}_{\mu\nu}(x) \equiv \frac{1}{8}\left(Q_{\mu\nu}(x) - Q_{\nu\mu}(x)\right), \tag{4.32a}$$

$$Q_{\mu\nu}(x) \equiv \frac{1}{4}\left(U_{\mu\nu}(x) + U_{\nu-\mu}(x) + U_{-\mu-\nu}(x) + U_{-\nu\mu}(x)\right). \tag{4.32b}$$

4.3.2 Correlator G^E on the lattice

In order to extract κ numerically from equation (4.20), we compute the Euclidean correlator (4.17) within the lattice framework and perform a Fourier transform to momentum space with vanishing frequency $\omega = 0$ and spatial momentum $\mathbf{q} = (0, 0, q_z)$. With the discrete Fourier transform (A.18a) the correlator on the lattice reads

$$a_\sigma^3 a_\tau G^\mathrm{E}(q_z) = \frac{1}{N_\sigma^3 N_\tau} \sum_{x,y} \mathrm{e}^{-\mathrm{i}q_z(x_z - y_z)} \left\langle T_{xy}(x) T_{xy}(y)\right\rangle. \tag{4.33}$$

The two-point function $\langle T_{xy}(x)T_{xy}(y)\rangle$ is rewritten in terms of diagonal elements using the relation (4.29) and the energy-momentum tensor is discretised by means of equations (4.30), (4.31) and (4.32). The correlator is invariant under translations, it only depends on the distance $x - y$, so that we average all points with the same distance to improve statistics. Additionally, due to rotation invariance the correlator channel $T_{xy}T_{xy}$ is equivalent to $T_{xz}T_{xz}$ as well as $T_{yz}T_{yz}$. Aligning the spatial momenta accordingly, $\mathbf{q} = (0, q_y, 0)$ for $T_{xz}T_{xz}$ and $\mathbf{q} = (q_x, 0, 0)$ for $T_{yz}T_{yz}$, allows us to average all channels. Simplifying the notation we only point out the correlator $T_{xy}T_{xy}$ with momenta $\mathbf{q} = (0, 0, q_z)$ in the following and imply the mean over other channels.

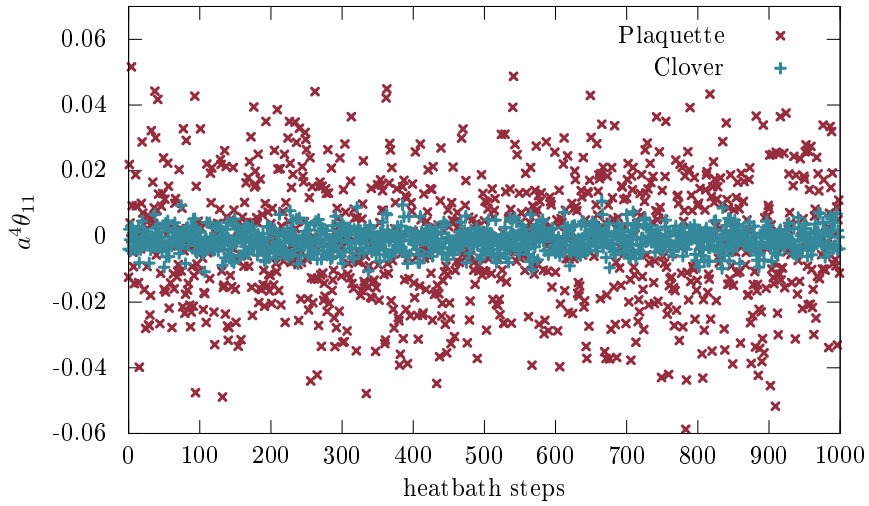

Figure 4.1: Computation of the energy-momentum tensor element θ_{11} in the plaquette and Clover discretisation on an isotropic $16^3 \times 6$ lattice for $\beta = 7.1$. The Clover discretisation has an improved signal-to-noise ratio.

Having computed the correlator (4.33) for different momenta q_z allows for extracting the transport coefficient κ from the momentum expansion (4.20) as the slope of a linear function $G^{\mathrm{E}}(q_z^2)$. One prerequisite concerning the momentum expansion is that the momenta are small compared to the temperature of the system, which sets the relevant scale, i.e. $\frac{q_z}{T} < 1$. With the discretised versions of temperature (3.18) and momenta (3.6) we find for the ratio

$$\frac{q_z}{T} = \frac{2\pi N_\tau}{\xi N_\sigma} n_z < 1, \tag{4.34}$$

where the lattice spacings a_τ and a_σ are completely absorbed by the anisotropy (3.3). In order to fit the transport coefficient κ to equation (4.17), we need at least three different momenta $n_z > 2$ satisfying this constraint (4.34). Thus the simulation requires large spatial lattice extents N_σ, which makes the calculation costly. This can be partly moderated by working with anisotropic lattices $\xi > 1$.

4.3.3 Renormalisation

The correlator defined in (4.17) suffers from ultraviolet divergences. An operator product expansion at short distances gives [125]

$$\langle T_{xy}(x) T_{xy}(0) \rangle \approx C_T \frac{1}{|x|^8} + \sum_\mu C_\mu \langle T_{\mu\mu}(0) \rangle \, \delta(x) + \dots \ , \tag{4.35}$$

where the second term on the right hand side corresponds to the contact term B, which we discussed in section 4.1.2. The first term $\sim |x|^{-8}$ diverges for small x causing an ultraviolet divergence. We remove it by additive renormalisation of the correlator. Since the divergent term is temperature independent, subtracting the vacuum part from the correlator at finite temperature eliminates the divergence. The vacuum part corresponds

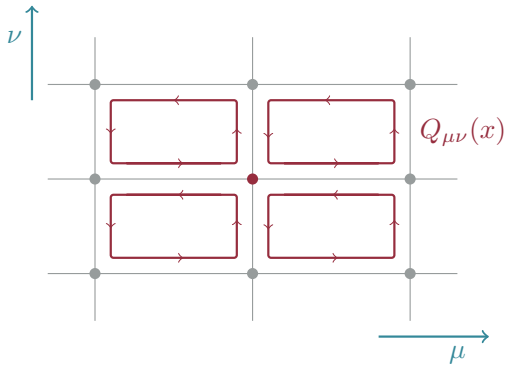

Figure 4.2: The Clover plaquette (4.32b) used in the discretisation of the energy-momentum tensor. It consists of four ordinary plaquettes surrounding the red point x.

to the correlator evaluated at vanishing temperature. We define a new vacuum corrected expectation value

$$\langle \mathcal{O} \rangle \equiv \langle \mathcal{O} \rangle_T - \langle \mathcal{O} \rangle_{T_{\text{vac}}} , \tag{4.36}$$

where $\langle \mathcal{O} \rangle_T$ is an observable evaluated at a given temperature T and $\langle \mathcal{O} \rangle_{T_{\text{vac}}}$ its vacuum contribution, i.e. evaluated at vanishing temperature $T_{\text{vac}} = 0$.

As discussed in section 4.3.1, the discretised energy-momentum tensor requires multiplicative renormalisation due to reduced translational invariance on the lattice. For an isotropic lattice the finite renormalisation factor only depends on the lattice coupling β, whereas on an anisotropic lattice it also depends on the anisotropy ξ. Additionally, temporal and spatial part of the energy-momentum tensor (4.31) require separate renormalisation factors $Z_\sigma(\beta, \xi)$ and $Z_\tau(\beta, \xi)$ [139].

Our non-perturbative renormalisation scheme only works for diagonal elements of the energy-momentum tensor. For this reason we rewrite the correlator (4.33) in terms of diagonal elements (4.30) employing the cubic symmetry (4.29)

$$\begin{aligned} a_\sigma^3 a_\tau G^{\text{E}}(q_z) = \frac{1}{2V} \sum_{x,y} \mathrm{e}^{-\mathrm{i}q_z(x_z - y_z)} \big(& Z_\tau^2 G_0^\tau(x,y) + Z_\tau Z_\sigma G_0^{\tau\sigma}(x,y) \\ & + Z_\sigma^2 G_0^\sigma(x,y) \big). \end{aligned} \tag{4.37}$$

The newly defined bare correlators read

$$G_{0,T}^\tau(x,y) \equiv \langle \theta_{11}^\tau(x)\theta_{11}^\tau(y) - \theta_{11}^\tau(x)\theta_{22}^\tau(y) \rangle_T , \tag{4.38a}$$

$$G_{0,T}^{\tau\sigma}(x,y) \equiv \langle \theta_{11}^\tau(x)\theta_{11}^\sigma(y) + \theta_{11}^\sigma(x)\theta_{11}^\tau(y) - \theta_{11}^\tau(x)\theta_{22}^\sigma(y) - \theta_{11}^\sigma(x)\theta_{22}^\tau(y) \rangle_T , \tag{4.38b}$$

$$G_{0,T}^\sigma(x,y) \equiv \langle \theta_{11}^\sigma(x)\theta_{11}^\sigma(y) - \theta_{11}^\sigma(x)\theta_{22}^\sigma(y) \rangle_T , \tag{4.38c}$$

where we introduce their vacuum subtracted versions according to (4.36)

$$G_0^i(x,y) = G_{0,T}^i(x,y) - G_{0,T_{\text{vac}}}^i(x,y), \qquad i \in \{\tau, \tau\sigma, \sigma\} . \tag{4.39}$$

In order to compute the renormalisation factors Z_τ and Z_σ, it is favourable to recast (4.30) into

$$\theta_{ii} = Z_\tau(\beta,\xi) \left(\theta_{ii}^\tau + \frac{Z_\sigma(\beta,\xi)}{Z_\tau(\beta,\xi)} \theta_{ii}^\sigma \right) , \tag{4.40}$$

so that the renormalisation procedure splits into determining the ratio $\frac{Z_\sigma(\beta,\xi)}{Z_\tau(\beta,\xi)}$ and the absolute scale $Z_\tau(\beta,\xi)$.

The former can be obtained from renormalisation group invariant quantities [139]. To this end, one introduces four expectation values on differently sized lattices

$$\begin{aligned} \langle\mathcal{O}\rangle_1 &\mathrel{\widehat{=}} 2L \times L \times L \times L, \qquad \langle\mathcal{O}\rangle_2 \mathrel{\widehat{=}} L \times 2L \times L \times L, \\ \langle\mathcal{O}\rangle_3 &\mathrel{\widehat{=}} L \times L \times 2L \times L, \qquad \langle\mathcal{O}\rangle_4 \mathrel{\widehat{=}} L \times L \times L \times 2L, \end{aligned} \tag{4.41}$$

and the renormalisation group invariant quantities

$$F_1 = L^4 \langle\theta_{00}\rangle_1 , \quad F_2 = L^4 \langle\theta_{11}\rangle_2 , \quad F_3 = L^4 \langle\theta_{22}\rangle_3 , \quad F_4 = L^4 \langle\theta_{33}\rangle_4 . \tag{4.42}$$

Since the renormalisation factors do not depend on temperature, all directions are symmetric and it follows

$$F_1 = F_2 = F_3 = F_4. \tag{4.43}$$

Applying equation (4.40) one can compute the ratio of renormalisation factors. Averaging the equivalent equations (4.42) one obtains

$$\frac{Z_\sigma(\beta,\xi)}{Z_\tau(\beta,\xi)} = \frac{1}{3}\left(\frac{\langle\theta^\tau_{00}\rangle_1 - \langle\theta^\tau_{11}\rangle_2}{\langle\theta^\sigma_{11}\rangle_2 - \langle\theta^\tau_{00}\rangle_1} + \frac{\langle\theta^\tau_{00}\rangle_1 - \langle\theta^\tau_{11}\rangle_3}{\langle\theta^\sigma_{11}\rangle_3 - \langle\theta^\tau_{00}\rangle_1} + \frac{\langle\theta^\tau_{00}\rangle_1 - \langle\theta^\tau_{11}\rangle_4}{\langle\theta^\sigma_{11}\rangle_4 - \langle\theta^\tau_{00}\rangle_1} \right). \tag{4.44}$$

It is possible to determine a non-perturbative value for the ratio of renormalisation factors by evaluating the expectation values by lattice simulations, c.f. chapter 3. This requires four simulations, one per lattice size given in equation 4.41. Since the ratio depends on the anisotropy ξ and lattice coupling β, we have to recalculate it for every modification in these parameters.

We obtain the absolute renormalisation factor by using the physical interpretation of the energy-momentum tensor, whose diagonal spatial elements are equivalent to the pressure

$$\langle\theta_{ii}\rangle = p. \tag{4.45}$$

The absolute renormalisation factor enters into the energy-momentum tensor correlator quadratically. Therefore the renormalisation procedure is very sensitive to the exact value of the pressure and encourages us to use a highly precise value for it. For this reason we use the continuum extrapolated lattice data from [134]. Figure 4.3 illustrates the difference between the continuum value of the pressure and the not multiplicatively renormalised energy-momentum tensor. The difference between the two at a given temperature corresponds to the absolute renormalisation factor.

4.4 Results for the transport coefficient κ from lattice Yang-Mills theory

Finally, we present the computation of the transport coefficient κ from the lattice. In the first section 4.4.1 we analytically calculate κ in lattice perturbation theory. In the next section 4.4.2 we discuss our choice of simulation parameters regarding a numeric

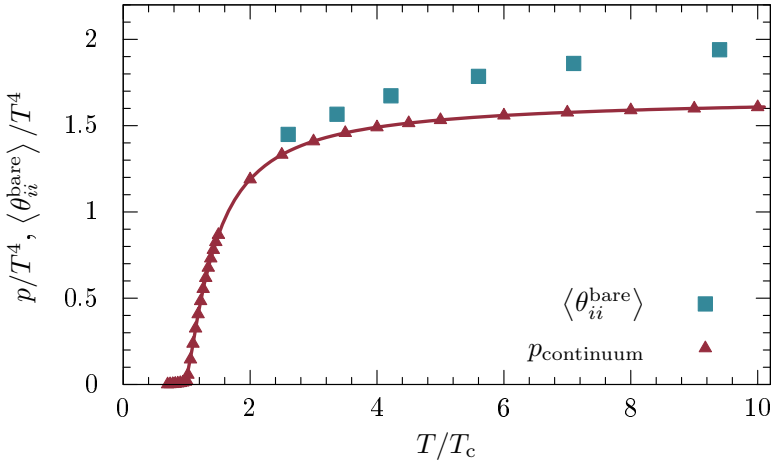

Figure 4.3: Comparison of the not multiplicatively renormalised energy-momentum tensor $\langle\theta_{ii}^{\mathrm{bare}}\rangle/T^4$ for $N_\tau = 6$ and $\xi = 2$ to the continuum extrapolated pressure p/T^4 from the lattice [134], where the line is obtained by a cubic spline interpolation. The difference between them at a given temperature corresponds to the absolute renormalisation factor.

computation. They basically follow the constraint of having low momenta for the energy-momentum tensor correlator. Then we compute κ by means of Monte-Carlo simulations in sections 4.4.3 and 4.4.4. Performing a simulation at high temperature, $T \approx 10\,T_{\mathrm{c}}$, allows to make contact with the weak coupling regime and justifies a comparison to the results from lattice perturbation theory. Furthermore we compute the temperature dependence of κ and check it against predictions from both weak and strong coupling methods.

4.4.1 Determination of κ from lattice perturbation theory

In order to estimate lattice artefacts and to provide a check of our numeric implementation, we first calculate the transport coefficient κ in lattice perturbation theory, see section 3.2. The computation is done in the ideal gas limit, $g = 0$, on an anisotropic lattice. As a consequence of the missing interaction no multiplicative renormalisation is involved.

In lattice perturbation theory the gauge fields $A_\mu(x)$ become once again the relevant degrees of freedom. Expanding the links in the lattice expression for the energy-momentum tensor by (3.9) gives for the correlator (4.17) on the lattice

$$\begin{aligned} G^{\mathrm{E}}(x,y) = \Big\langle &\Big(\partial_1^{\mathrm{c}} A_\alpha^a(x) - \partial_\alpha^{\mathrm{c}} A_1^a(x)\Big)\Big(\partial_2^{\mathrm{c}} A_\alpha^a(x) - \partial_\alpha^{\mathrm{c}} A_j^a(x)\Big) \\ &\times \Big(\partial_1^{\mathrm{c}} A_\beta^b(y) - \partial_\beta^{\mathrm{c}} A_1^b(y)\Big)\Big(\partial_2^{\mathrm{c}} A_\beta^b(y) - \partial_\beta^{\mathrm{c}} A_2^b(y)\Big)\Big\rangle, \end{aligned} \tag{4.46}$$

where $\partial_\mu^{\mathrm{c}}$ denotes the central difference (3.4c). The momentum expansion of G^{E} involves a Fourier transform of sixteen terms of the generalised form

$$C_{i_1 i_2 j_1 j_2 l_1 l_2 m_1 m_2}(x,y) = \Big\langle \partial_{i_1}^{\mathrm{c}} A_{i_2}^a(x)\partial_{j_1}^{\mathrm{c}} A_{j_2}^a(x)\partial_{l_1}^{\mathrm{c}} A_{l_2}^b(y)\partial_{m_1}^{\mathrm{c}} A_{m_2}^b(y)\Big\rangle \tag{4.47}$$

to momentum space. Because of translational invariance it is sufficient to consider $C_{i_1 i_2 j_1 j_2 l_1 l_2 m_1 m_2}(x,0)$. Transforming the individual gauge fields $A_\mu(x)$ to momentum

space by (3.21b) results in

$$C_{i_1 i_2 j_1 j_2 l_1 l_2 m_1 m_2}(x,0) = \Big\langle \mathrm{i}^4 \sum\!\!\!\!\!\!\int_{k_1,k_2,k_3,k_4} A^a_{i_2}(k_1) A^a_{j_2}(k_2) A^b_{l_2}(k_3) A^b_{m_2}(k_4) \mathrm{e}^{\mathrm{i}x(k_1+k_2)} \times \mathrm{e}^{\mathrm{i}\left(\frac{\hat{i}_2}{2}k_1 + \frac{\hat{j}_2}{2}k_2 + \frac{\hat{l}_2}{2}k_3 + \frac{\hat{m}_2}{2}k_4\right)} \widetilde{k}_1^{i_1} \widetilde{k}_2^{j_1} \widetilde{k}_3^{l_1} \widetilde{k}_4^{m_1} \Big\rangle \tag{4.48}$$

with lattice momenta $\widetilde{k}$ as defined in (3.20). We evaluate the expectation value by Wick's theorem using the free gauge field propagator (3.19). Considering only connected diagrams and performing the outer Fourier transform with momentum q we obtain

$$C_{i_1 i_2 j_1 j_2 l_1 l_2 m_1 m_2}(\omega, \vec{q}) = (N_\mathrm{c}^2 - 1) \sum\!\!\!\!\!\!\int_k \frac{\widetilde{k}_{l_1} \widetilde{(k+q)}_{m_1}}{\widetilde{k}^2 \widetilde{(k+q)}^2} \times \Big(\delta_{i_2 l_2} \delta_{j_2 m_2} \widetilde{k}_{i_1} \widetilde{(k+q)}_{j_1} + \delta_{i_2 m_2} \delta_{j_2 l_2} \widetilde{k}_{j_1} \widetilde{(k+q)}_{i_1} \Big). \tag{4.49}$$

Applying this relation to the correlator (4.46) in momentum space and aligning the outer spatial momentum to $\mathbf{q} = (0, 0, q_z)$ we find

$$G^\mathrm{E}(q) = \left(N_c^2 - 1\right) \sum\!\!\!\!\!\!\int_k \frac{1}{\widetilde{k}^2 \widetilde{(q+k)}^2} \Bigg(4 \widetilde{k}_x^2 \widetilde{k}_y^2 - 2 \widetilde{k} \widetilde{(q+k)} (\widetilde{k}_x^2 + \widetilde{k}_y^2) + \widetilde{k}^2 \widetilde{k}_x^2 + \widetilde{(q+k)}^2 \widetilde{k}_y^2 + \Big(\widetilde{k} \widetilde{(q+k)} \Big)^2 \Bigg). \tag{4.50}$$

After solving the Matsubara sums and the spatial integrals, we extract the transport coefficient κ as the low momentum coefficient in a momentum expansion (4.20) of this formula. In contrast to continuous thermal field theory the Matsubara sums are finite. The basic step in solving them is applying the residue theorem in terms of the formula [140]

$$\frac{1}{N_\tau} \sum_{n=1}^{N_\tau} g(z) = -\sum_i \frac{\mathrm{Res}_{\bar{z}_i} \left(\frac{1}{z} g(z) \right)}{\bar{z}_i^{N_\tau} - 1}. \tag{4.51}$$

In appendix B.2 we list the results for the five individual terms and present the complete evaluation of one finite Matsubara sum in detail. In order to avoid ultraviolet divergences, we perform the additive renormalisation addressed in section 4.3.3 by subtracting the vacuum part. This corresponds to excluding temperature independent pieces from the results for the finite Matsubara sums (B.23). The three-momentum integration can be performed analytically after expanding the integrals around the continuum limit. This step extends the integration measure to infinite volume $[-\pi/a, \pi/a]^3 \to \mathbb{R}^3$ and produces correction terms in lattice spacings a_σ. Applying the expansion in small momenta

q_3, the remaining integrals can be solved analytically. One finds for the different terms

$$\begin{aligned}
\sum\!\!\!\!\!\!\int_k \frac{4\widetilde{k}_x^2\widetilde{k}_y^2}{\widetilde{k}^2(\widetilde{q+k})^2} &= \frac{\pi^2}{45(a_\tau N_\tau)^4} + \frac{\pi^4 a_\sigma^2}{(a_\tau N_\tau)^6}\left(\frac{1}{135}+\frac{5}{189\xi^2}\right) \\
&\quad - \frac{q^2}{72(a_\tau N_\tau)^4} + \frac{\pi^2 a_\sigma^2 q^2}{(a_\tau N_\tau)^4}\left(-\frac{1}{1440}-\frac{13}{4320\xi^2}\right), \qquad (4.52a) \\
-\sum\!\!\!\!\!\!\int_k \frac{2\widetilde{k}(\widetilde{q+k})(\widetilde{k}_x^2+\widetilde{k}_y^2)}{\widetilde{k}^2(\widetilde{q+k})^2} &= -\frac{2\pi^2}{45(a_\tau N_\tau)^4} - \frac{\pi^4 a_\sigma^2}{(a_\tau N_\tau)^6}\left(\frac{2}{189}+\frac{2}{189\xi^2}\right) \\
&\quad + \frac{q^2}{12(a_\tau N_\tau)^2} - \frac{\pi^2 a_\sigma^2 q^2}{(a_\tau N_\tau)^4}\left(-\frac{1}{2160}-\frac{13}{720\xi^2}\right), \qquad (4.52b) \\
\sum\!\!\!\!\!\!\int_k \frac{\widetilde{k}_x^2}{(\widetilde{q+k})^2} = \sum\!\!\!\!\!\!\int_k \frac{\widetilde{k}_y^2}{\widetilde{k}^2} &= \frac{\pi^2}{90(a_\tau N_\tau)^4} + \frac{\pi^4 a_\sigma^2}{(a_\tau N_\tau)^6}\left(\frac{1}{378}+\frac{1}{378\xi^2}\right), \qquad (4.52c) \\
\sum\!\!\!\!\!\!\int_k \frac{\left(\widetilde{k}(\widetilde{q+k})\right)^2}{\widetilde{k}^2(\widetilde{q+k})^2} &= -\frac{q^2}{24(a_\tau N_\tau)^2} + \frac{\pi^2 a_\sigma^2 q^2}{(a_\tau N_\tau)^4}\left(-\frac{17}{4320}+\frac{11}{1440\xi^2}\right). \qquad (4.52d)
\end{aligned}$$

As an example we present the calculation of (4.52c) in appendix B.3. For fixed temperature $T = (a_\tau N_\tau)^{-1}$ we can rewrite the dependence on lattice spacings a_τ and a_σ as a dependence on the temporal lattice extent N_τ and the anisotropy $\xi = \frac{a_\sigma}{a_\tau}$. Combining the results (4.52) we obtain the following expression for the dimensionless energy-momentum tensor correlator expanded in momentum space at vanishing frequency

$$\begin{aligned}
\frac{G^E(q_z)}{T^4} &= (N_c^2-1)\Bigg\{\frac{\pi^4}{N_\tau^2}\left(\frac{2\xi^2}{945}+\frac{4}{189}\right) \\
&\quad + \frac{q_z^2}{T^2}\left(\frac{1}{36}+\frac{\pi^2}{N_\tau^2}\left(-\frac{\xi^2}{240}+\frac{49}{2160}\right)\right)\Bigg\} + \mathcal{O}\left(q_z^4, N_\tau^{-4}\right), \qquad (4.53)
\end{aligned}$$

from which we identify the dimensionless transport coefficient $\frac{\kappa}{T^2}$ as

$$\frac{\kappa}{T^2} = (N_c^2-1)\left(\frac{1}{18}+\frac{\pi^2}{N_\tau^2}\left(-\frac{\xi^2}{120}+\frac{49}{1080}\right)\right) + \mathcal{O}\left(q_z^4, N_\tau^{-4}\right). \qquad (4.54)$$

At fixed temperature the continuum limit $a_\mu \to 0$ is performed by taking $N_\tau \to \infty$, where we reproduce the continuous result of equation (4.25).

Although the calculation has been performed in the ideal gas limit and thus lacks corrections in the coupling g, it serves as a check of our numeric implementation in section 4.4.3. Performing simulations at high temperature enables a comparison, since we approach the ideal gas limit due to the running of the coupling.

Furthermore the result helps to estimate the size of cutoff effects. The computed correction in the inverse temporal lattice extent suggests an anisotropy of $\xi_{\text{opt}} \approx 2.33$ in order to eliminate leading order lattice artefacts as illustrated in figure 4.4. In the case of other values for the anisotropy we can estimate the required temporal lattice extent to decrease the leading discretisation error under a desired threshold. As stated

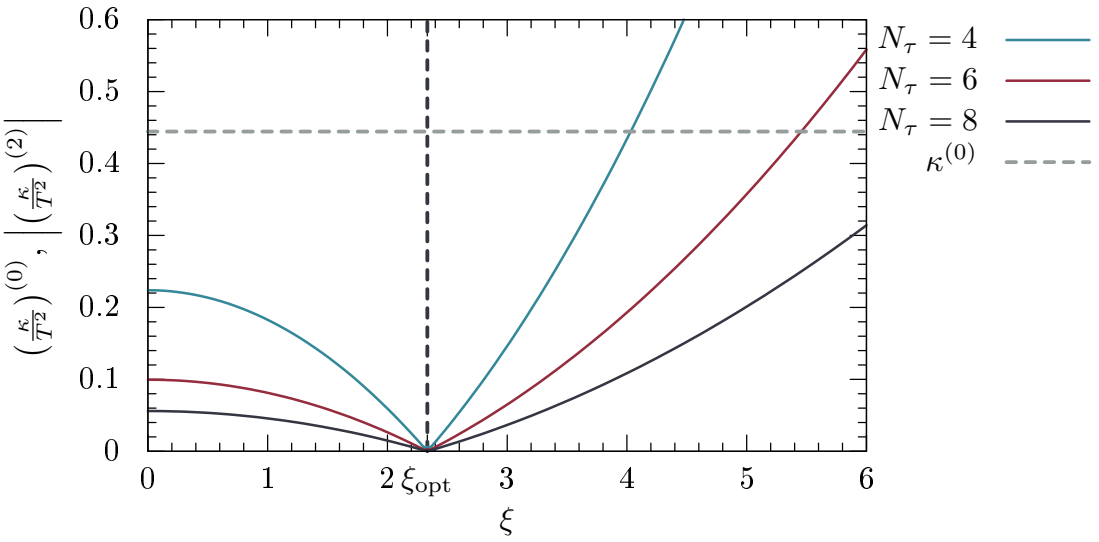

Figure 4.4: Results for the transport coefficient κ/T^2 from lattice perturbation theory in the ideal gas limit versus anisotropy ξ. The leading order result $(\kappa/T^2)^{(0)}$ is independent of the anisotropy and temporal lattice extent, whereas the absolute value of the correction $(\kappa/T^2)^{(2)}$ is plotted for different N_τ. The figure illustrates the quadratic increase of the discretisation error with higher anisotropies as well as the quadratic reduction with the temporal lattice extent. The vertical line marks the value of $\xi_{\text{opt}} = 2.33$ eliminating leading order lattice artefacts. We perform our simulations at $\xi = 2$ with $N_\tau = 6$ having a reduction of leading order corrections in the ideal gas limit below 10 %.

in section 4.4.2 we set $\xi = 2$ in order to apply previous results for setting the scale. Thus a temporal lattice extent of $N_\tau \geq 6$ is required in order to reduce the leading lattice artefacts below 10 % in the ideal gas limit.

Computing κ by means of lattice gauge theory benefits from a larger value for the anisotropy, $\xi > 1$, since it mildens the constraint (4.34). Increasing the anisotropy allows a decrease of the spatial lattice extent, which reduces the numeric effort. Notably a linear growth of the anisotropy goes along with a cubic reduction of spatial lattice points. One drawback is that an anisotropy different from $\xi_{\text{opt}} \neq 2.33$ causes a quadratic increase of the lattice artefacts seen in figure 4.4. This effect also emerges in calculations of the pressure [141, 142].

4.4.2 Numeric setup

Our lattice simulations require to set the anisotropy ξ, the lattice coupling β as well as the spatial and temporal lattices extents N_σ and N_τ, respectively. These parameters determine the lattice spacing, volume and temperature and thus the simulated physics. All simulation parameters are summarised in table 4.1.

By investigating the transport coefficient κ in lattice perturbation theory, we find an optimal value for the anisotropy, $\xi_{\text{opt}} = 2.33$, eliminating leading order discretisation artefacts in the ideal gas limit. However, we choose a value of $\xi = 2$ of the anisotropy, which is only close to the optimal value, but simplifies setting the scale. As discussed in section 3.1.3, the scale is set by the lattice spacing $a_\sigma = a_\sigma(\beta, \xi)$ in dependence on the chosen lattice coupling and anisotropy. In case of $\xi = 2$ we can use results from [100]

Run	i	ii	iii	iv
β	7.1	7.1	6.68	6.14
N_τ	6	8	6	6
N_σ	120	120	120	120
N_τ^{vac}	72	72	42	24
ξ	2	2	2	2
a_σ [fm]	0.026	0.026	0.044	0.094
T/T_c	9.4	7.1	5.6	2.6
$T_{\mathrm{vac}}/T_\mathrm{c}$	0.8	0.8	0.8	0.7
N_{ens} for T	500800	434480	403500	542000
N_{ens} for T_{vac}	455000	455000	429000	421250

Table 4.1: Simulation parameters for four evaluations of the transport coefficient κ. The temporal lattice extent N_τ^{vac} corresponding to the temperature $T_{\mathrm{vac}}/T_\mathrm{c}$ is required for additive renormalisation. The number of configurations entering one ensemble is N_{ens}, see section 3.3.

for $a_\sigma(\beta, \xi = 2)$. Considering a fixed temporal lattice extent of $N_\tau = 6$, this leads to an increase of about 6 % in the leading order lattice artefacts in comparison to the optimal value ξ_{opt} obtained in the ideal gas limit.

The choice of the temporal lattice extent $N_\tau = 6$ is based on a compromise between numeric effort and discretisation errors. The constraint of having low momenta (4.34) dictates the number of lattice points in spatial directions N_σ relative to the anisotropy ξ and temporal lattice extent N_τ. Table 4.2 illustrates the increase in the leading order lattice artefacts (4.54) with respect to the deviation from their evaluation at optimal anisotropy ξ_{opt} as well as the required spatial lattice extent for six momenta, $n_i \leq 6$. Reducing the artefacts below 10 % requires a temporal lattice extent $N_\tau > 4$. A choice of $N_\tau = 6$ already requires a spatial lattice extent of $N_\sigma = 113$, which enters the computational effort cubically. A temporal lattice extent of $N_\tau = 8$ reduces the discretisation errors below 5 %, but requires production of gauge configurations on an at least $226^3 \times N_\tau$ sized lattice, which is numerically too costly. Hence we perform our simulations with a temporal lattice extent of $N_\tau = 6$ and a spatial one of $N_\sigma = 120$. We increase the spatial lattice extent from $N_\sigma = 113$ to $N_\sigma = 120$, since parallelised codes favour an even lattice extent and regarding simulations on the LOEWE-CSC the number of lattice points should be divisible by 24, which is the number of cores per node.

The remaining parameter is the lattice coupling β, which is connected to the lattice spacing a_σ, see section 3.1.3. In terms of the experimental string tension σ_{exp} and the dimensionless lattice string tension σ_{lat} this connection reads

$$a_\sigma^{-1}(\beta, \xi) = \frac{\sqrt{\sigma_{\mathrm{exp}}}}{\sqrt{\sigma_{\mathrm{lat}}(\beta, \xi)}}. \tag{4.55}$$

For a specific value of the anisotropy, $\xi = 2$, the lattice string tension σ_{lat} has been extracted from the static quark potential in [100]. By comparing this lattice result to the experimental string tension, $\sqrt{\sigma_{\mathrm{exp}}} = 440\,\mathrm{MeV}$ [143], we obtain the lattice spacing relative to the lattice coupling, $a_\sigma(\beta, \xi = 2)$. Determining the temporal lattice spacing

ξ	N_τ	Deviation to ξ_{opt}	N_σ
2	4	13.4 %	75
2	6	5.9 %	113
2	8	3.3 %	151
1	6	18.3 %	226

Table 4.2: In dependence on the anisotropy ξ and temporal lattice extent N_τ the table shows the increase of leading order lattice artefacts (4.54) by deviating from its evaluation at optimal anisotropy $\xi_{\text{opt}} = 2.33$. Furthermore it shows the required spatial lattice extent N_τ to fulfil the constraint (4.34) with six momenta $n_i \leq 6$. Reducing the discretisation errors below 10 % and ensuring numeric feasibility we simulate with parameters $\xi = 2$ and $N_\tau = 6$. The values of the last row indicate the benefit of introducing an anisotropic lattice.

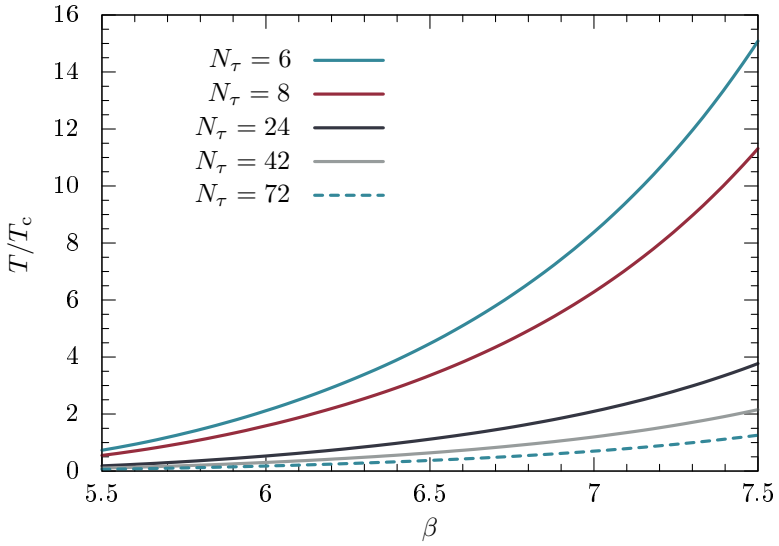

Figure 4.5: Dimensionless temperature T/T_c versus lattice coupling β for different temporal lattice extents N_τ.

a_τ from its relation to the anisotropy (3.3) we obtain the temperature from equation (3.18). It is plotted in figure 4.5 as a function of the lattice coupling β for different temporal lattice extents. As further discussed in sections 4.4.3 and 4.4.4 we choose the lattice couplings $\beta = \{6.14, 6.68, 7.1\}$. Their respective lattice spacings and temperatures are listed in table 4.1. In the deconfined phase topological fluctuations are suppressed [144] and we expect no difficulties in using very fine lattices.

In the following we specify parameters concerning the renormalisation procedure, see section 4.3.3. The additive renormalisation requires a determination of the vacuum contribution that is a computation of the correlator (4.37) at vanishing temperature. In order to keep constant physics, we reduce the temperature by increasing the temporal lattice extent N_τ^{vac} instead of the lattice spacing. For our fine and spatially large lattices this is very costly. We therefore choose $T_{\text{vac}} \approx 0.8\, T_c$. For our purposes this temperature is low enough since first the vacuum divergence is temperature independent. Second, it is well known that the pressure or the deviation of screening masses from their vacuum values are exponentially small in the confined phase, see [134, 145–147] for numeric

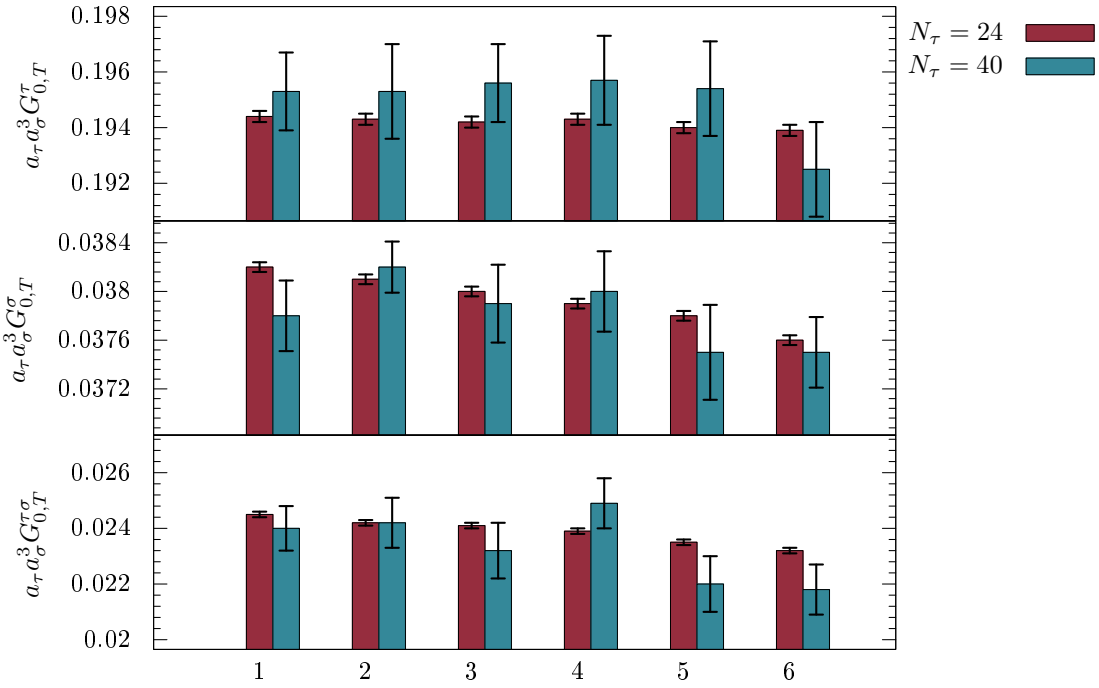

Figure 4.6: Correlators (4.38) entering the computation of the transport coefficient κ versus momenta at different vacuum temperatures. The agreement of our chosen temperature $T_{\text{vac}} \approx 0.8\,T_{\text{c}}$ corresponding to $N_\tau = 24$ with a lower value of $T_{\text{vac}} \approx 0.4\,T_{\text{c}}$ corresponding to $N_\tau = 40$ justifies use of a vacuum temperature unequal to zero. The large error bars of the simulation at $N_\tau = 40$ originate from a factor of ~ 55 lower statistics.

evidence and [148] for an analytic explanation. Furthermore figure 4.6 illustrates the difference regarding the correlator (4.38) between the used vacuum temperature $T_{\text{vac}} \approx 0.8\,T_{\text{c}}$ and a lower value of $T_{\text{vac}} \approx 0.4\,T_{\text{c}}$ corresponding to a temporal lattice extent of $N_\tau = 24$ and $N_\tau = 40$, respectively.

The multiplicative renormalisation procedure necessitates knowledge of the renormalisation factor ratio $Z_\sigma(\beta,\xi)/Z_\tau(\beta,\xi)$. As described in section 4.3.3 we determine it from a computation of renormalisation group invariant quantities (4.42) on lattices (4.41) with $L = 48$. The simulations must be performed for every lattice coupling $\beta = \{6.14, 6.68, 7.1\}$. The absolute renormalisation factor $Z_\tau(\beta,\xi)$ is obtained from an identification of the spatial diagonal energy-momentum tensor elements with the pressure (4.45). Since determining the transport coefficient κ goes together with the computation of the bare diagonal energy-momentum tensor elements (4.31), we extract the quantities from the simulations listed in table 4.1.

4.4.3 Numeric reproduction of results from lattice perturbation theory

Our first simulation aims at making contact to lattice perturbation theory, section 4.4.1. The weak coupling regime is reached for high temperatures. For fixed anisotropy and temporal lattice extent the temperature is raised by increasing the lattice coupling β. Choosing $\beta = 7.1$ for the lattice coupling corresponds to a temperature of $T = 9.4\,T_{\text{c}}$. The full set of parameters is given in column (i) of table 4.1. In the following we give a

q^2/T^2	0.02	0.10	0.22	0.39	0.62
$G(q)/T^4$	0.68(6)	0.72(6)	0.77(6)	0.75(6)	0.82(6)

Table 4.3: Numeric results of run (i) of table 4.1 regarding the dimensionless correlator $G(q)/T^4$.

detailed description of determining the transport coefficient κ, which directly transfers to the other simulations. Intermediate numeric results are shown in table C.2 to C.5 in appendix C.2.

In order to compute the transport coefficient κ we calculate the bare diagonal energy-momentum tensor elements (4.31) using the Clover discretisation (4.32) in lattice Yang-Mills theory. The additive renormalisation requires a computation of these elements on two lattices. On the one hand, with temporal lattice extent $N_\tau = 6$, giving the finite temperature contribution. On the other hand, with $N_\tau^{\text{vac}} = 72$, giving the vacuum contribution. The elements enter the bare correlators in position space (4.38) and are used along with the renormalisation group invariant quantities (4.42) to compute the multiplicative renormalisation factors $Z_\tau(\beta, \xi)$ and $Z_\sigma(\beta, \xi)$. Table C.2 shows numeric results of the bare correlators and table C.3 for the vacuum subtracted ones. The data of the renormalisation group invariant quantities are shown in table C.4 and the one relevant for determining the absolute renormalisation factor in table C.5. After Fourier transforming the bare correlators to momentum space we perform the additive and multiplicative renormalisation to build the final Euclidean correlator (4.37), listed in table 4.3.

As discussed in the previous section we choose our simulation parameters in such a way that the momenta fulfil the constraint (4.34). This allows us to extract the transport coefficient κ from a momentum expansion of the computed correlator according to (4.20). Figure 4.7 shows the dimensionless correlator $\frac{G^{\text{E}}(q)}{T^4}$ for different momenta $\frac{q^2}{T^2} < 1$. Fitting the data points to a line [149]

$$\frac{G^{\text{E}}\left(\frac{q^2}{T^2}\right)}{T^4} = \frac{G'(0)}{T^4} + \frac{\kappa}{T^2}\frac{q^2}{2T^2} \tag{4.56}$$

yields for the y-intercept $\frac{G'(0)}{T^4} = 0.69(4)$ and for the transport coefficient $\frac{\kappa}{T^2} = 0.40(26)$. These numbers are consistent with the leading order lattice perturbation theory results $\frac{G'_{\text{LPT}}(0)}{T^4} = 0.64$ and $\frac{\kappa_{\text{LPT}}}{T^2} = 0.47$, respectively. Full agreement is not yet expected since at $T = 9.4\,T_{\text{c}}$ there are still significant corrections due to interactions, i.e. we are still far from the ideal gas limit.

Sources for statistical errors are the Monte Carlo sampling, see section 3.3, the multiplicative renormalisation scheme (4.45), adding the error of the continuum extrapolated lattice pressure and the linear fit of the correlator (4.56). The large error bars of the correlator are almost entirely due to the additive renormalisation procedure. In table C.2 there are data of the bare correlators (4.38) regarding this simulation, whereas table C.3 shows the data of the additively renormalised correlators (4.39). The vacuum subtraction causes a significant loss of accuracy as schematically illustrated in figure 4.8. Computing the pressure by means of the interaction measure [145] suffers from the same phenomenon. Thus, we create a large amount of statistics, see table 4.1, to provide a significant signal for the correlators. In terms of error reduction it is highly favourable

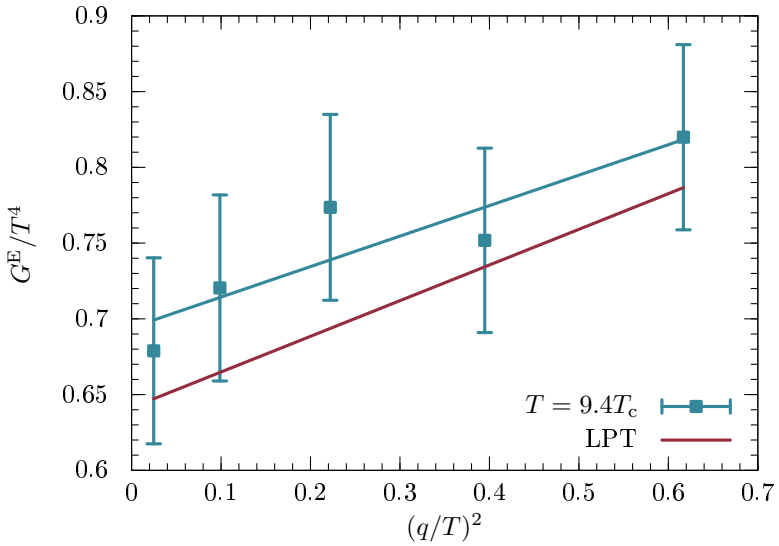

Figure 4.7: Correlator $G^{\mathrm{E}}(q)/T^4$ for momenta $q^2/T^2 < 1$ compared to results from lattice perturbation theory (LPT). The slope of the linear fit gives $\kappa/2$. The exact data points of the correlator are listed in table 4.3.

to perform the additive renormalisation before the multiplicative one. Otherwise, the propagated errors entering from the multiplicative renormalisation add to the described loss of precision.

4.4.4 Temperature dependence

This section deals with computing the temperature dependence of the transport coefficient κ. In principle, the temperature can be varied at fixed lattice coupling β and lattice spacing by changing N_τ, where lower temperature implies larger N_τ. Thus one keeps constant physics, while altering the temperature. However, due to the constraint on momenta from equation (4.34), this would require an increase of the spatial volume and thus an approximately cubic growth of the numeric effort. Hence the fixed scale approach is not practical for temperatures approaching the phase transition.

We therefore investigate the temperature dependence of κ at fixed $\frac{N_\tau}{N_\sigma}$ by simulating at various lattice couplings β listed in table 4.1. In this case the different temperatures are evaluated at different lattice spacings, and consequently also different spatial volumes in physical units. However, since our lattice spacings are all $a_\sigma < 0.1\,\mathrm{fm}$, we expect the lattice artefacts on the temperature dependence of the transport coefficient $\frac{\kappa}{T^2}$ to be negligible. As a check for this, we perform simulations at different temperatures, $T = 9.4\,T_{\mathrm{c}}$ and $T = 7.1\,T_{\mathrm{c}}$, but same lattice spacing, $a_\sigma = 0.026\,\mathrm{fm}$. All other parameters are given in lines (i) and (ii) of table 4.1.

The results of all four simulations are shown in table 4.4 and figure 4.9. The extraction of the transport coefficient κ from the correlator in momentum space follows the procedure presented in section 4.4.3. We check the effect of varying both temperature and lattice spacing by comparing the values of $\frac{\kappa}{T^2}$ for $T = 9.4\,T_{\mathrm{c}}$ and $T = 7.1\,T_{\mathrm{c}}$. The data point at $T = 7.1\,T_{\mathrm{c}}$ suffers from large error bars, since the spatial lattice extents have been kept fixed while increasing the temporal lattice extent N_τ. This results in

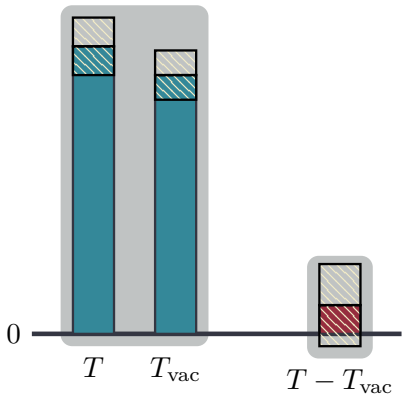

Figure 4.8: Schematic illustration of additive renormalisation, i.e. subtracting the vacuum part. Subtracting two equally sized numbers including errors shown on the left causes a significant loss of precision as shown on the right. We use high statistics to avoid a correlator consistent with zero.

T/T_{c}	9.4	7.1	5.6	2.6
a_σ [fm]	0.026	0.026	0.044	0.094
κ/T^2	0.40(26)	0.41(84)	0.39(30)	0.28(20)

Table 4.4: Lattice results for the transport coefficient κ/T^2 at different spatial lattice spacings a_σ and temperatures T/T_{c}.

less momenta fulfilling the constraint (4.34) and generates a loss of accuracy in the fit (4.56). Within the error bars, the data points are consistent suggesting that we do not alter the physics in our approach.

Taking the other simulations at $T = 5.6\,T_{\mathrm{c}}$ and $T = 2.6\,T_{\mathrm{c}}$ into account, we find that the temperature dependence of the transport coefficient κ behaves like $\kappa \sim T^2$. This result agrees with predictions of perturbative methods both in the continuum (4.25) and on the lattice (4.54) in the ideal gas limit. Additionally, it coincides with the prediction of AdS/CFT correspondence (4.26) using $\eta \sim s \sim T^3$. Since the former represents the weak coupling limit and the latter the strong coupling limit, we expect the lattice result to lie in between. Indeed, rescaling the AdS/CFT result to the field content of Yang-Mills theory by (4.27), we find this expectation confirmed as illustrated in figure 4.9.

Since we do not resolve a temperature dependence beyond $\kappa \sim T^2$, we may increase the accuracy of our lattice results by averaging the data points with $N_\tau = 6$ to give our final result,

$$\kappa^{\mathrm{avr}} = 0.36(15)T^2. \tag{4.57}$$

4.4.5 Noise reduction methods

The lattice computation of the transport coefficient κ suffers from large statistical errors. The largest contribution to the statistical errors arises from the additive renormalisation.

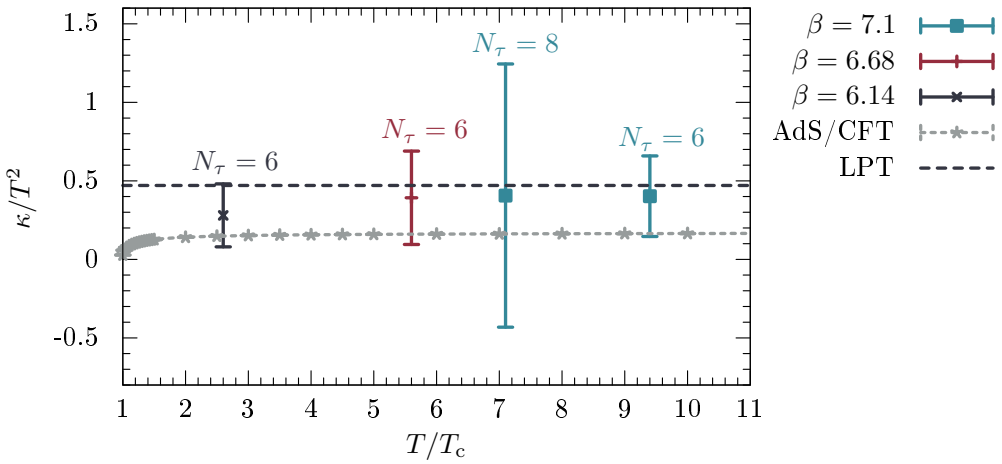

Figure 4.9: Temperature dependence of the transport coefficient κ/T^2 from lattice Yang-Mills theory. The lines mark the prediction of AdS/CFT correspondence (4.27) and lattice perturbation theory (4.54), respectively. As one would expect the lattice result lies in between the weak and strong coupling predictions.

As discussed in section 4.4.3 the vacuum correction causes a significant loss of accuracy. Usually, improving the signal of the correlator by numeric means helps in alleviating this loss.

One way to improve the correlation signal is the smearing of gauge fields removing short distance fluctuations. Smearing algorithms connect the endpoints of a given link along certain paths. APE smearing [150], HYP smearing [151] and Stout smearing [152] are variants of smearing algorithms. Figure 4.10 illustrates the increased numeric cost for applying smearing algorithms to our implementation.

Although the smearing procedure modifies the short-distance behaviour of the correlator of interest, it might not alter the result for the transport coefficient κ. The extraction of the transport coefficient rests upon a low momentum expansion of the correlator, which corresponds to large distances. Thus modifications on short scales should be negligible. As an example performing one APE smearing iteration on an isotropic lattice increases the width of a plaquette from one lattice spacing to three, $a \to 3a$. We establish a connection of this width to our momenta, $\frac{q}{T} < 1$, by means of the de Broglie wavelength, $\lambda = 3a_\mu = \frac{2\pi}{q}$,

$$3 = \frac{\lambda}{a} < 2\pi N_\tau \leq \frac{2\pi N_\tau}{q/T}. \tag{4.58}$$

This condition is easy to fulfil with an appropriate choice for the temporal lattice extent.

The effect of smearing links on the transport coefficient κ should be checked numerically. A first study of the vacuum corrected correlator $G(z) \equiv \langle T_{ii}(z) T_{ii}(0) \rangle$, which enters the calculation of the transport coefficient κ, based on smeared gauge field configurations is illustrated in figure 4.11. On the one hand, the smeared correlators show reduced statistical errors, on the other hand, the data points differ regarding the (not) applied smearing routines. A full calculation of the transport coefficient κ, fulfilling the momentum constraint, which implies large lattice sizes as well as enough statistics, is required to investigate these effects. However, as shown in figure 4.10 smearing the

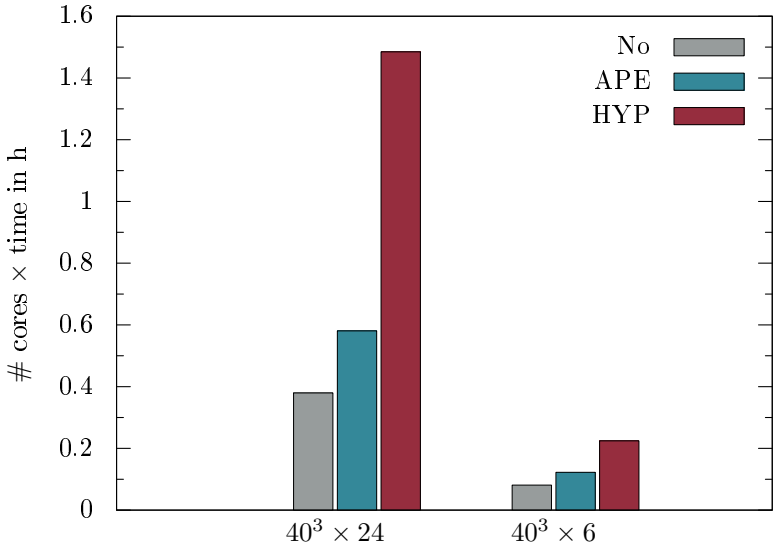

Figure 4.10: Simulation time taken for one calculation of the correlator (4.37) including a heatbath step combined with four overrelaxation steps for no, APE and HYP smearing. On the chosen lattice sizes the extra time amount for the smearing procedure is substantial compared to total computation time.

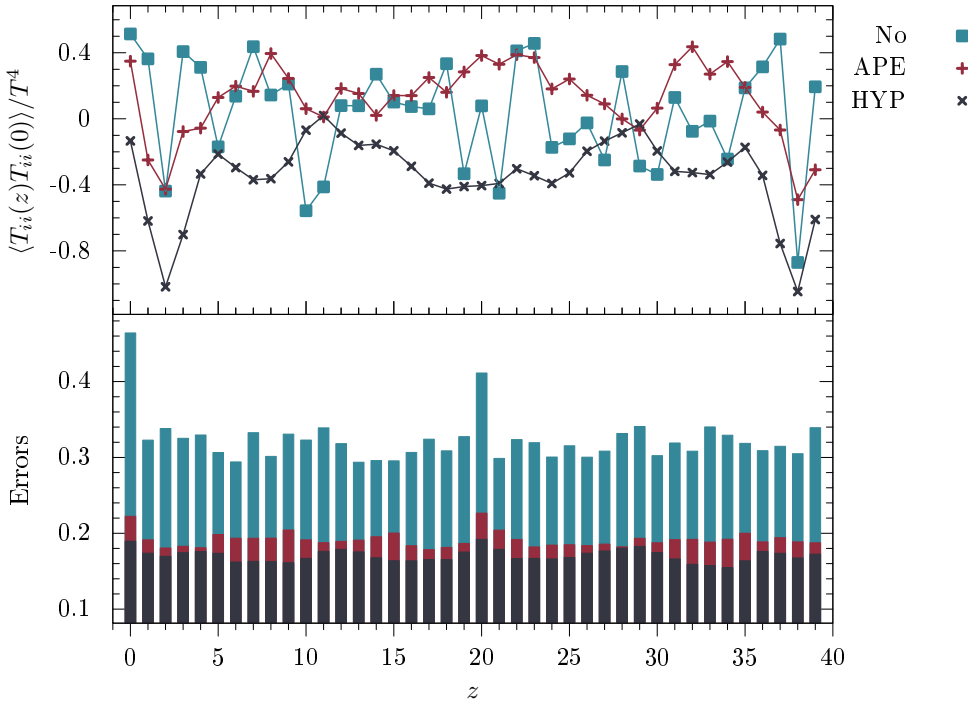

Figure 4.11: Correlator $G(z) \equiv \langle T_{ii}(z)T_{ii}(0)\rangle$ entering the calculation of the transport coefficient κ based on not, APE and HYP smeared gauge field configurations. The upper plot illustrates the dependence on the distance z of the correlator and the lower plot shows the corresponding error bars. All error bars begin from the x-axis. On the one hand, the smeared correlators show reduced statistical errors, on the other hand, the data points differ regarding the (not) applied smearing routines even including the error bars. A full computation of the transport coefficient κ is required to check the effect of smearing routines on its value.

gauge field configurations increases the already high numeric effort even more with the consequence of leaving the regime of numeric feasibility. One solution to this problem is to analyse effects of the smearing routines on the transport coefficient κ for a reduced colour symmetry, e.g. SU(2).

4.5 Future research perspectives

In the following we discuss different ideas to improve the numeric results. One contribution to the large statistical errors is our multiplicative renormalisation procedure. Matching the spatial diagonal energy-momentum tensor elements to the continuum extrapolated lattice pressure and computing the renormalisation factor ratio introduces errors, which enter quadratically into the correlator of interest. We review two other ideas of renormalisation schemes, which might reduce the errors.

Giusti and Meyer propose a renormalisation scheme based on lattice Ward identities [153]. In finite volume Poincaré symmetry implies exact relations among energy-momentum tensor correlations defined with different sets of periodic boundary conditions. This relations can be used to compute the required renormalisation factors non-perturbatively.

Moore and Sohrabi suggest a renormalisation procedure [122], which uses the connection of the energy-momentum tensor to curvature of space time. The strategy is to add an energy-momentum tensor component with small coefficient to the action and investigate its effect on the lattice spacing, e.g. by evaluating the static quark potential. Both approaches refer to isotropic lattices and should be generalised to anisotropic ones in order to milden the constraint on momenta (4.34).

This constraint basically dictates the high numeric effort. We have mildened this constraint by using an anisotropic lattice with $\xi = 2$. Introducing higher anisotropies lowers the required spatial lattice volume, e.g. setting $\xi = 4$ allows to run the simulations of section 4.4 with a lattice size of $60^3 \times N_\tau$ points. Choosing an anisotropy $\xi \neq 1$ or $\xi \neq 2$ goes along with two disadvantages. Firstly, as our investigation of the transport coefficient κ in lattice perturbation theory shows, changing the anisotropy from its optimal value $\xi_{\text{opt}} \neq 2.33$ involves a quadratic rise of lattice artefacts. This problem can be remedied by taking the continuum limit. This step might necessitate the usage of an improved lattice action and improved observables, e.g. following the Symanzik improvement programme [154, 155]. Secondly, since the lattice spacing depends on the anisotropy, $a_\mu = a_\mu(\beta, \xi)$, extra simulations are required to set the scale for anisotropic lattices, where $a_\mu(\beta, \xi)$ has not been determined, i.e. lattices with $\xi \neq 1$ or $\xi \neq 2$. The running of the lattice spacing can be obtained from the static potential [100].

All in all we suggest the following steps to facilitate an advanced calculation of the transport coefficient κ: First, study the effects of using APE and HYP smeared gauge field configurations on the transport coefficient κ. Check if the modifications of the correlator alter the value of the transport coefficient and if they improve the signal-to-noise ratio. Since this analysis will be numerically costly, we recommend a first investigation in the colour group SU(2) instead of SU(3). Secondly, try the other proposed multiplicative renormalisation schemes and check if they result in lower statistical errors. Last but not least use higher anisotropies $\xi > 2$ to reduce the required spatial lattice volume and thus the numeric cost. Improved lattice formulations might be necessary to compensate

the effect of lattice artefacts.

If one makes progress in these aspects further studies of thermodynamic transport coefficients from the lattice become numerically feasible. Further possible investigations include a determination of the temperature dependence for a continuum extrapolated transport coefficient κ or a calculation of other thermodynamic transport coefficients.

4.6 Conclusions

We have calculated the second order hydrodynamic transport coefficient κ for the Yang-Mills plasma using lattice perturbation theory as well as Monte Carlo simulations. The transport coefficient parametrises the low momentum behaviour of a retarded correlator of the energy-momentum tensor. Since the retarded correlator is evaluated at vanishing frequency, the analytic continuation of the corresponding Euclidean correlator becomes trivial and makes a pure lattice computation possible.

Due to the need for additive and multiplicative renormalisation of the energy-momentum tensor the lattice calculation is rather involved. Additionally, the realisation of the correlator as a low momentum expansion requires large spatial lattice extensions, making a numeric computation very challenging. As a consequence, our results suffer from large statistical errors. We investigated first steps towards reducing noise by applying smearing routines.

In the evaluated temperature range $2T_\mathrm{c} < T < 10T_\mathrm{c}$ our data are consistent with $\kappa \sim T^2$, as predicted both by weak and strong coupling methods. Because of large error bars, our result also quantitatively covers both the leading order perturbative result as well as the AdS/CFT prediction rescaled by the Yang-Mills entropy. This would suggest that, besides improved simulation methods, next-to-leading order analytic calculations should be able to give a result closer to the real value of κ.

5 Semi-classical formulation of quantum chromodynamics

We saw in the last chapter that a computation of the second order transport coefficient κ is possible from thermal equilibrium, even though it is a real time quantity. Unfortunately, to predict many other physical phenomena a true real time treatment is still necessary. One example is the evolution from the early stages of a heavy ion collision to a quark-gluon plasma, which we investigate in chapter 6. A mighty tool for studying these far from equilibrium physics is a classical approximation of Yang-Mills theory on the lattice. It naturally incorporates an evolution in real time by the equations of motion and is straightforward to implement on the lattice.

The first reduction to a classical theory was realised by Grigoriev and Rubakov [94]. Later followed studies of electroweak sphaleron transitions [156–159], the static potential in hot QCD [160], string-breaking [161] and in particular the early stages of the quark-gluon plasma (for citations refer to chapter 6) within the framework of classical Yang-Mills theory on the lattice.

We establish a real time lattice formulation of full QCD in this chapter. Since fermions can not be approximated classically, we treat the fermionic degrees of freedom quantum mechanically by a mode function expansion [162] resulting in a semi-classical formulation of QCD. The introduction of stochastic fermions [64] reduces the numeric effort and enables simulations in three-dimensional space. Although the semi-classical approach to QCD can in principle handle a finite chemical potential [163], we do not include it due to the exploratory nature of this study. The next section deals with the validity of a classical approximation of Yang-Mills theory defining its range of application.

5.1 Classical approximation of Yang-Mills theory

The classical approximation of quantum field theories at finite temperature is a powerful tool to study time dependent phenomena in a non-perturbative regime. In the following, we discuss the validity of this approximation.

The basic quantity for a perturbative treatment of massless bosons in the real time formalism is the propagator matrix (2.27), where temperature only enters through the symmetric propagator (2.30). An expansion of the involved Bose-Einstein distribution function (2.18a) for infrared momenta at high temperatures ($q^0 \ll T$) yields a behaviour $\sim \frac{T}{q^0} + \mathcal{O}(\frac{q^0}{T})$ for the correlator [164]. Following [85] the classical correlator analogous to (2.30) is proportional to $\sim \frac{T}{q^0}$. Hence, the infrared regime of a bosonic quantum field theory at high temperature behaves classically[1] at leading order. Expanding the symmetric correlator in the fermionic case with the Bose-Einstein distribution replaced by the Fermi-Dirac distribution (2.18b) one finds its first contribution at $\sim \mathcal{O}(\frac{q^0}{T})$.

[1] This also holds for massive bosons, if $T \gg m$.

Consequently, a classical description of fermions is not possible. Refer to section 5.2.3 for an inclusion of quantum mechanical fermions in the classical theory.

As discussed in section 2.2.3 the high temperature limit requires the classical approximation to correspond to a weakly coupled theory, which allows for an identification of the infrared momentum regime with scales gT and g^2T. Thus, the soft and ultra soft momentum scales of a weakly coupled Yang-Mills theory can be described by a classical theory. However, the classical theory does not approximate the hard scale $\sim 2\pi T$. A natural way of excluding these non-classical hard modes but preserving gauge invariance is the introduction of a momentum cutoff by a lattice regularisation, c.f. chapter 3. The ultraviolet cutoff makes the classical theory well-defined since it removes the Rayleigh-Jeans divergences [158].

Naturally, one must deal with the missing ultraviolet behaviour of the theory. Its perturbative effects on the infrared scale can be expressed in the framework of hard thermal loop effective theory, which in turn can be connected to kinetic theory [77, 79]. The corresponding transport equations are the Boltzmann-Vlasov equations [165–167]. In this thesis we pursue a pure classical treatment of Yang-Mills theory ignoring its ultraviolet sector. This approach is justified for physical phenomena and observables dominated by infrared modes as originally suggested by [94]. In general Yang-Mills theory with a high occupation of gauge fields can be treated classically, since then quantum fluctuations are suppressed compared to statistical fluctuations [168, 169].

All in all, the dynamics of gauge fields with a high occupation in weakly coupled Yang-Mills theory is classical in nature and we investigate it by real time lattice techniques. Moreover, the classical approximation does not loose its validity in systems far from equilibrium [83, 169] and facilitates the study of early stages of the QGP addressed in chapter 6.

5.2 Lattice formulation of semi-classical QCD

In the last section we have learnt that under certain conditions a weakly coupled Yang-Mills theory can be treated classically. As the classical approximation is not valid for fermionic degrees of freedom, we employ the framework of canonical quantisation and rewrite the fermions in a mode function expansion including anticommuting ladder operators. In order to reduce the numeric effort for dealing with mode functions in three-dimensional space, we apply a stochastic quantisation. For that the anticommutator relations of ladder operators are replaced by Gaussian distributed complex numbers. We discuss these steps in section 5.2.3. Treating the bosons classically and the fermions quantum mechanically we end up with a semi-classical model for QCD.

We investigate this semi-classical system by solving its equations of motion in a lattice framework. To this end, we derive the Hamiltonian of QCD in discretised space in section 5.2.1 and the corresponding equations of motion by Hamilton's principle in section 5.2.2. Applying the classical formulation for the first time to full QCD, we give the relevant calculations in some detail in appendix D.

In the last section of this chapter, we explain how to calculate observables in the derived model. The computation is based on averaging trajectories dictated by the equations of motion, which start from random initial conditions. We introduce the energy-density and discuss the requirements as well as the consequences of gauge fixing.

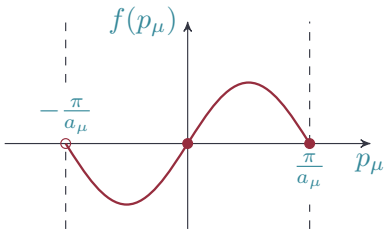

Figure 5.1: The lattice propagator has additional poles at $+\pi/a_\mu$, which give rise to the doubling of fermionic degrees of freedom. Note that momenta $-\pi/a_\mu$ do not give additional poles, since they are not within the first Brillouin zone.

5.2.1 QCD Hamiltonian in discrete space

In contrast to section 3.1 we transfer the fermionic and gluonic Lagrangians defined in (2.2) to a hypercubic lattice in Minkowski space time. We discretise the gluonic contribution analogous to (3.12) but account for the different metric by an extra minus sign in the first term

$$\mathcal{L}_{\mathrm{G}}^{\mathrm{M}}[U] = \frac{1}{a_\sigma^3 a_\tau}\frac{\beta}{N_c}\,\mathrm{Re}\,\mathrm{Tr}\left\{-\frac{1}{\xi_0}\sum_{i<j}\left(\mathbb{1}-U_{ij}(x)\right)+\xi_0\sum_i\left(\mathbb{1}-U_{i0}(x)\right)\right\}. \tag{5.1}$$

At the classical level a renormalisation of the anisotropy is not required, $\xi_0 = \xi$.

A discretisation of the fermionic part requires a more sophisticated approach due to its equations of motion being of first order. Substituting the continuum derivative with a naive finite difference (3.4) in the free Lagrangian (2.2a) one finds for the massless propagator in momentum space and its continuum limit

$$D^{-1}(p)\big|_{m=0} = -\frac{\sum_\mu a_\mu^{-1}\gamma_\mu \sin(a_\mu p_\mu)}{\sum_\mu a_\mu^{-2}\sin^2(a_\mu p_\mu)} \to -\frac{\sum_\mu \gamma_\mu p_\mu}{p^2}. \tag{5.2}$$

On the lattice, new poles arise at the edge of the Brillouin zone as illustrated in figure 5.1 and cause a doubling of fermionic degrees of freedom. One solution, which removes the unphysical poles at $p_\mu = +\frac{\pi}{a_\mu}$ but keeps the physical one with $p = 0$ is to add a so-called Wilson term to the Dirac operator. In momentum space it reads

$$D(p) \sim -\sum_\mu \frac{r}{a_\mu}\left(1-\cos(p_\mu a_\mu)\right) \tag{5.3}$$

with the Wilson parameter $r \in \{0, 1\}$ switching the Wilson term off and on. It removes the additional poles by providing an extra contribution at $p_\mu = +\frac{\pi}{a_\mu}$ acting as an additional mass term, which vanishes in the continuum limit. As a direct consequence of the Nielsen-Ninomiya theorem [170–172], the introduction of a Wilson term leads to a loss of chiral symmetry even in the massless case.

In order to ensure gauge invariance of the Lagrangian, one introduces covariant deriva-

tives according to

$$\mathcal{D}^{\mathrm{f}}_{\mu}\psi(x) \equiv \frac{1}{a_\mu}\left(U_\mu(x)\psi(x+\mu) - \psi(x)\right), \tag{5.4a}$$

$$\mathcal{D}^{\mathrm{b}}_{\mu}\psi(x) \equiv \frac{1}{a_\mu}\left(\psi(x) - U^\dagger_\mu(x-\mu)\psi(x-\mu)\right), \tag{5.4b}$$

$$\widetilde{\mathcal{D}}_{\mu}\psi(x) \equiv \frac{1}{2}\left(\mathcal{D}^{\mathrm{f}}_{\mu} + \mathcal{D}^{\mathrm{b}}_{\mu}\right)\psi(x) = \frac{1}{2a_\mu}\left(U_\mu(x)\psi(x+\mu) - U^\dagger_\mu(x-\mu)\psi(x-\mu)\right), \tag{5.4c}$$

as in the continuous case (2.3). Finally, the discretised fermionic Lagrangian in Minkowski space time with a Wilson term reads

$$\begin{aligned}\mathcal{L}^{\mathrm{M}}_{\mathrm{F}}[\psi,\overline{\psi},U] =& \mathrm{i}\overline{\psi}(x)\gamma_0\widetilde{\mathcal{D}}_0\psi(x) + \mathrm{i}\overline{\psi}(x)\gamma_i\widetilde{\mathcal{D}}_i\psi(x) - m\overline{\psi}(x)\psi(x)\\ &+ \frac{ra_\sigma}{2}\overline{\psi}(x)\mathcal{D}^{\mathrm{b}}_i\mathcal{D}^{\mathrm{f}}_i\psi(x).\end{aligned} \tag{5.5}$$

We do not introduce a temporal Wilson term for reasons discussed at the end of this section. Furthermore the sign of the Wilson term is opposite to its Euclidean formulation in order to account for the likewise opposite sign of the mass term in Minkowski space time. The total Lagrangian is given by

$$\mathcal{L}^{\mathrm{M}}_{\mathrm{tot}}[\psi,\overline{\psi},U_\mu] = \mathcal{L}^{\mathrm{M}}_{\mathrm{F}}[\psi,\overline{\psi},U_\mu] + \mathcal{L}^{\mathrm{M}}_{\mathrm{G}}[U_\mu]. \tag{5.6}$$

The classical equations of motion follow from the principle of stationary action, which is reflected in the theory of Hamiltonian mechanics discussed in appendix D.1. However, for gauge theories, the equations of motion loose their unambiguity due to the action's invariance under temporal gauge transformations or stated in other words, due to gauge freedom the stationary point is not unique. We remedy this situation by applying a temporal gauge

$$A_0(x) = 0 \qquad \Leftrightarrow \qquad U_0(x) = \mathbb{1}, \tag{5.7}$$

which only fixes the gauge partially up to time independent gauge transformations. We define the chromo-magnetic and the chromo-electric fields as

$$U_i(x) = \mathrm{e}^{\mathrm{i}ga_\sigma A_i(x)}, \tag{5.8a}$$

$$E_i(x) = \dot{A}_i(x) \tag{5.8b}$$

with $\dot{A}_i(x) = \partial_0 A_i(x)$ being the time derivative. The links U_i and gauge fields $A_i \equiv A^a_i T^a$ are in the adjoint representation of $\mathrm{SU}(N_c)$. The fields transform under local gauge transformations $G(x) \in \mathrm{SU}(N_c)$ as follows

$$E_i(x) \to E'_i(x) = G(x)E_i(x)G^\dagger(x), \tag{5.9a}$$

$$U_i(x) \to U'_i(x) = G(x)U_i(x)G^\dagger(x+\hat{i}), \tag{5.9b}$$

$$\psi(x) \to \psi'(x) = G(x)\psi(x). \tag{5.9c}$$

Following the calculation in appendix D.2 with the canonical coordinates

$$\phi^a_{\mathrm{G},i}(x) = A^a_i(x), \qquad \pi^a_{\mathrm{G},i}(x) = E^a_i(x), \tag{5.10a}$$

$$\phi_{\mathrm{F}}(x) = \psi(x), \qquad \pi_{\mathrm{F}}(x) = \mathrm{i}\overline{\psi}(x)\gamma_0, \tag{5.10b}$$

the Hamiltonian function can be derived from a Legendre transformation of the Lagrangian and reads in terms of the rescaled fields and mass (D.15)

$$\begin{aligned} H[U_i, E_i, \psi, \overline{\psi}] = \frac{1}{a_\sigma} \sum_{\mathbf{x}} \Bigg\{ & \beta \sum_{i<j} \left(1 - \frac{1}{N_c} \operatorname{Re} \operatorname{Tr} U_{ij}(x) \right) + \frac{\beta}{4N_c} E_i^a(x) E_i^a(x) \\ & - \frac{\mathrm{i}}{2} \overline{\psi}(x) \gamma_i \left(U_i(x) \psi(x+\hat{i}) - U_i^\dagger(x-\hat{i}) \psi(x-\hat{i}) \right) \\ & - \frac{r}{2} \sum_i \overline{\psi}(x) \Big(U_i(x) \psi(x+\hat{i}) - 2\psi(x) + U_i^\dagger(x-\hat{i}) \psi(x-\hat{i}) \Big) \\ & + m \overline{\psi}(x) \psi(x) \Bigg\}. \end{aligned} \tag{5.11}$$

We end up with a Hamiltonian discretised on a three-dimensional spatial lattice as first employed by Kogut and Susskind [173]. Without loss of generality we assume the time dimension to still be continuous. Consequently, no temporal fermionic doublers occur and we only add a spatial Wilson term to remove the spatial doublers. Under certain conditions, described in section 5.1, the pure bosonic part of the Hamiltonian already approximates quantum effects. By contrast, the fermionic part still requires a quantisation, which we perform in section 5.2.3. Beforehand we derive the equations of motion governing the field dynamics.

5.2.2 Equations of motion

In the case of chromo-electric fields E_i and fermionic fields ψ we derive the equations of motion from Hamilton's equations (D.5), while we employ Poisson brackets (D.6) for the links $U_i(x)$. The fermionic fields $\overline{\psi} = \psi^\dagger \gamma_0$ do not form independent degrees of freedom. The complete derivation is given in appendix D.3. The field dynamics are governed by[1]

$$\dot{U}_i(x) = \frac{\mathrm{i}}{a_\sigma} E_i(x) U_i(x), \tag{5.12}$$

$$\begin{aligned} \dot{E}_i(x) = & -\frac{2}{a_\sigma} T^a \sum_{j \neq i} \operatorname{Im} \operatorname{Tr} \left\{ T^a \Big(U_{ij}(x) - U_{ij}(x-\hat{j}) \Big) \right\} \\ & - \frac{N_c}{\beta a_\sigma} T^a \Big(\overline{\psi}(x) \gamma_i T^a U_i(x) \psi(x+\hat{i}) + \overline{\psi}(x+\hat{i}) \gamma_i U_i^\dagger(x) T^a \psi(x) \Big) \\ & + \mathrm{i} \frac{r N_c}{\beta a_\sigma} T^a \Big(\overline{\psi}(x) T^a U_i(x) \psi(x+\hat{i}) - \overline{\psi}(x+\hat{i}) U_i^\dagger(x) T^a \psi(x) \Big), \end{aligned} \tag{5.13}$$

$$\begin{aligned} \dot{\psi}(x) = & -\mathrm{i} \frac{m}{a_\sigma} \gamma_0 \psi(x) - \frac{1}{2a_\sigma} \gamma_0 \gamma_i \left(U_i(x) \psi(x+\hat{i}) - U_i^\dagger(x-\hat{i}) \psi(x-\hat{i}) \right) \\ & + \mathrm{i} \frac{r}{2a_\sigma} \gamma_0 \sum_i \Big(U_i(x) \psi(x+\hat{i}) - 2\psi(x) + U_i^\dagger(x-\hat{i}) \psi(x-\hat{i}) \Big). \end{aligned} \tag{5.14}$$

Equations (5.12) and (5.13) are the lattice versions of Faraday's law of induction and Ampere's circuital law, respectively. An additional constraint is derived considering the variation regarding the gauge field in temporal direction A_0^a before fixing the gauge.

[1] We never imply Einstein's sum convention in the evolution equations of U_i and E_i.

Since the formulation of a Hamiltonian requires a temporal gauge, we derive this constraint, the so-called Gauss law, from the Euler-Lagrange equations (D.2). The Gauss constraint reads

$$\frac{N_c}{\beta}\overline{\psi}(x)\gamma_0 T^a \psi(x) = \sum_i \operatorname{Re}\operatorname{Tr}\left\{T^a\Big(E_i(x) - U_i^\dagger(x-\hat{i})E_i(x-\hat{i})U_i(x-\hat{i})\Big)\right\} \tag{5.15}$$

We discretise the time direction in section 5.3 in order to evaluate the equations of motion numerically.

Taking the continuum limit $a_\sigma \to 0$ we reproduce the continuum equations of motion. One expands the links (3.9) in small lattice spacings and reverses the field's rescaling (D.15). A Taylor expansion of the shifted fermionic fields gives $\psi(x+\hat{i}) = \psi(x) + \mathcal{O}(a_i)$. We obtain Faraday's law of induction, Ampere's circuit law, Gauss law and the Dirac equation

$$\dot{\mathbf{B}} = -\boldsymbol{\mathcal{D}} \times \mathbf{E}, \tag{5.16}$$

$$\dot{\mathbf{E}} = \boldsymbol{\mathcal{D}} \times \mathbf{B} - \mathbf{j}, \tag{5.17}$$

$$\boldsymbol{\mathcal{D}} \cdot \mathbf{E} = -j^0, \tag{5.18}$$

$$0 = (\mathrm{i}\gamma_\mu \mathcal{D}^\mu - m)\psi(x), \tag{5.19}$$

where $\mathcal{D}_\mu$ denotes the covariant derivative (2.3), j_μ the fermionic current

$$j_\mu^a(x) = \frac{g^2}{2}\overline{\psi}(x)\gamma_\mu T^a \psi(x), \tag{5.20}$$

and $\mathbf{B}$ the magnetic field

$$B_i^a(x) = -\frac{1}{2}\epsilon_{ijk}F_{jk}^a(x). \tag{5.21}$$

The next section deals with a quantum mechanical description of fermions in our model.

5.2.3 Mode function expansion with stochastic fermions

The classical approximation discussed in section 5.1 is not valid for fermions and a quantisation of the fermionic degrees of freedom is required. Following the framework of canonical quantisation [74] an expansion of the fermionic fields with the anticommuting ladder operators

$$\Big\{a_r(\mathbf{p}), a_s^\dagger(\mathbf{q})\Big\} = \Big\{b_r(\mathbf{p}), b_s^\dagger(\mathbf{q})\Big\} = (2\pi)^3\delta(\mathbf{p}-\mathbf{q})\delta_{rs} \tag{5.22}$$

in mode functions reads

$$\psi(x) = \int \frac{\mathrm{d}^3p}{(2\pi)^3}\,\frac{1}{\sqrt{2p_0}}\sum_s \left(a_s(\mathbf{p})u_s(\mathbf{p})\mathrm{e}^{-\mathrm{i}px} + b_s^\dagger(\mathbf{p})v_s(\mathbf{p})\mathrm{e}^{\mathrm{i}px}\right), \tag{5.23a}$$

$$\overline{\psi}(x) = \int \frac{\mathrm{d}^3p}{(2\pi)^3}\,\frac{1}{\sqrt{2p_0}}\sum_s \left(a_s^\dagger(\mathbf{p})\bar{u}^s(\mathbf{p})\mathrm{e}^{\mathrm{i}px} + b_s(\mathbf{p})\bar{v}_s(\mathbf{p})\mathrm{e}^{-\mathrm{i}px}\right). \tag{5.23b}$$

The expansion in mode functions incorporates the time evolution of the initial ladder operators as a Bogolyubov transformation [174–176] and, as pursued in e.g. [162], the time evolution of the fermions can be completely transferred to the mode functions, which obey the same Dirac equation (5.14). However, a numeric evaluation of the evolution of one fermionic field requires the solution of a coupled set of $16 \times N_\sigma^6$ complex ordinary differential equations[2].

Borsányi and Hindmarsh improved numeric feasibility by the introduction of low-cost fermions [64] reducing at least on higher dimensional lattices the numeric effort by several orders of magnitude. Their idea is to substitute the ladder operators in fermionic correlators by an ensemble of complex numbers. This can be achieved by the introduction of stochastic fermions

$$\psi_{\mathrm{M/F}}(x) = \frac{1}{\sqrt{2}} \int \frac{\mathrm{d}^3 p}{(2\pi)^3} \, \frac{1}{\sqrt{2p_0}} \sum_s \left(\xi_s(\mathbf{p}) u_s(\mathbf{p}) \mathrm{e}^{-\mathrm{i}px} \pm \eta_s(\mathbf{p}) v_s(\mathbf{p}) \mathrm{e}^{\mathrm{i}px} \right), \tag{5.24a}$$

$$\overline{\psi}_{\mathrm{M/F}}(x) = \frac{1}{\sqrt{2}} \int \frac{\mathrm{d}^3 p}{(2\pi)^3} \, \frac{1}{\sqrt{2p_0}} \sum_s \left(\xi_s^*(\mathbf{p}) \bar{u}_s(\mathbf{p}) \mathrm{e}^{\mathrm{i}px} \pm \eta_s^*(\mathbf{p}) \bar{v}_s(\mathbf{p}) \mathrm{e}^{-\mathrm{i}px} \right). \tag{5.24b}$$

The only difference between male ψ_{M} and female ψ_{F} fermions is the different sign $\pm$, combining the waves propagating in forward and backward direction. If the complex numbers are sampled according to

$$\langle \xi_s(\mathbf{p}) \xi_r^*(\mathbf{q}) \rangle = (2\pi)^3 \delta(\mathbf{p} - \mathbf{q}) \delta_{rs}, \tag{5.25a}$$

$$\langle \eta_s(\mathbf{p}) \eta_r^*(\mathbf{q}) \rangle = (2\pi)^3 \delta(\mathbf{p} - \mathbf{q}) \delta_{rs}, \tag{5.25b}$$

the ensemble average can be used to reproduce physical correlators. The presented initialisation applies to vacuum fermions. It can easily be extended to thermal equilibrium by adding the Fermi-Dirac distribution (2.18b) to the sampling

$$\langle \xi_s(\mathbf{p}) \xi_r^*(\mathbf{q}) \rangle = (2\pi)^3 \delta(\mathbf{p} - \mathbf{q}) \delta_{rs} \left(1 - 2 n_{\mathrm{F}}(\mathbf{p})\right), \tag{5.26a}$$

$$\langle \eta_s(\mathbf{p}) \eta_r^*(\mathbf{q}) \rangle = (2\pi)^3 \delta(\mathbf{p} - \mathbf{q}) \delta_{rs} \left(1 - 2 n_{\mathrm{F}}(\mathbf{p})\right). \tag{5.26b}$$

Following the computation in appendix D.4 one finds the following substitution rules for correlators

$$\left\langle \overline{\psi}(x) \psi(y) \right\rangle = -\frac{1}{2} \left(\left\langle \overline{\psi}_{\mathrm{M}}(x) \psi_{\mathrm{F}}(y) \right\rangle_{\mathrm{e}} + \left\langle \overline{\psi}_{\mathrm{F}}(x) \psi_{\mathrm{M}}(y) \right\rangle_{\mathrm{e}} \right), \tag{5.27a}$$

$$\left\langle \left[\psi_\alpha(x), \overline{\psi}_\beta(y) \right] \right\rangle = \frac{1}{2} \left(\left\langle \psi_\alpha^{\mathrm{M}}(x) \overline{\psi}_\beta^{\mathrm{F}}(y) \right\rangle_{\mathrm{e}} + \left\langle \psi_\alpha^{\mathrm{F}}(x) \overline{\psi}_\beta^{\mathrm{M}}(y) \right\rangle_{\mathrm{e}} \right), \tag{5.27b}$$

where we have used the interchangeability of male and female fermions. The calculation in appendix D.4 shows that only one gender, either male or female, is insufficient to build the correlators. The substitution rules also hold for bilinear covariants.

In order to reproduce the correlators of complex numbers, (5.25) and (5.26), correctly, an ensemble of stochastic fermions is necessary. To produce the correct physics we have to average over this ensemble in the fermionic correlators (5.27) and their bilinear covariants. The quantity $\langle \dots \rangle_{\mathrm{e}}$ denotes the ensemble average over N_{e} gendered fermions.

[2] On a three-dimensional lattice a fermionic field consists of $2N_\sigma^3$ momentum modes each being a spinor (4) with two spin states (2) and must be computed on every lattice site (N_σ^3).

However, every member of the ensemble as well as any gender must be evolved separately by the fermionic equation of motion (5.14).

The numeric benefit of this approach is that instead of the full set of N_σ^3 momentum modes, only an ensemble of $2N_\mathrm{e}$ stochastic fermions must be evolved. Naturally, checking for the dependence of observables on the ensemble size N_e is required, especially since statistical errors are transferred to the bosonic degrees of freedom by the coupled equations of motion.

We initialise the stochastic fermions by solving the free Dirac equation on the lattice. Following the calculation in appendix D.5 we recover the continuum form of the Dirac equation by defining

$$s_0 \equiv \xi \sin(a_\tau p_0), \qquad s_i \equiv \sin(a_\sigma p_i), \qquad \mu \equiv m + r \sum_i \left(1 - \cos(a_\sigma p_i)\right), \tag{5.28}$$

where the lattice mass μ includes the Wilson term, and the energy-momentum relation is

$$s_0(\mathbf{p}) = \sqrt{s_i^2(\mathbf{p}) + \mu^2(\mathbf{p})}. \tag{5.29}$$

In the following lines we do not explicitly write the dependence on momenta, $s_\mu = s_\mu(\mathbf{p})$ and $\mu = \mu(\mathbf{p})$. Solutions to the free Dirac equation with γ-matrices in Dirac representation (c.f. appendix A.4) are given by the spinors in spin states $s = 0, 1$

$$u_0(\mathbf{p}) = N \begin{pmatrix} s_0 + \mu \\ 0 \\ s_3 \\ s_1 + \mathrm{i}s_2 \end{pmatrix}, \qquad u_1(\mathbf{p}) = N \begin{pmatrix} 0 \\ s_0 + \mu \\ s_1 - \mathrm{i}s_2 \\ -s_3 \end{pmatrix}, \tag{5.30a}$$

$$v_0(\mathbf{p}) = N \begin{pmatrix} s_3 \\ s_1 + \mathrm{i}s_2 \\ s_0 + \mu \\ 0 \end{pmatrix}, \qquad v_1(\mathbf{p}) = N \begin{pmatrix} s_1 - \mathrm{i}s_2 \\ -s_3 \\ 0 \\ s_0 + \mu \end{pmatrix}. \tag{5.30b}$$

They are normalised by

$$N \equiv \sqrt{\frac{2\mu}{(s_0 + \mu)^2 - s_i^2}} = \sqrt{\frac{1}{\mu + s_0}} \tag{5.31}$$

according to

$$\bar{u}_r(\mathbf{p}) u_s(\mathbf{p}) = 2\mu\delta^{rs}, \qquad \bar{v}_r(\mathbf{p}) v_s(\mathbf{p}) = -2\mu\delta^{rs}, \tag{5.32a}$$

$$u_r^\dagger(\mathbf{p}) u_s(\mathbf{p}) = 2s_0\delta^{rs}, \qquad v_r^\dagger(\mathbf{p}) v_s(\mathbf{p}) = 2s_0\delta^{rs}. \tag{5.32b}$$

The computed initial conditions (5.30) together with the sampled complex numbers (5.25) or (5.26) enable us to construct initial male and female fermions (5.24). The detailed numeric implementation is discussed in section 5.4.2.

5.2.4 Determination of physical observables

In the framework of the Hamiltonian formalism with canonical coordinates ϕ and π the basic quantity in non-equilibrium statistical mechanics is the phase space distribution $\varrho[\phi, \pi, t]$. Its time evolution is governed by Liouville's equation [177]

$$\partial_0 \varrho[\phi, \pi, t] = \{H, \varrho\}. \tag{5.33}$$

The expectation value of an observable at time t is given by a with $\varrho[\phi, \pi, t]$ weighted average over the phase space [178]

$$\langle \mathcal{O}(t) \rangle = \int \mathrm{d}\phi \, \mathrm{d}\pi \; \varrho[\phi, \pi, t] \mathcal{O}[\phi, \pi, t]. \tag{5.34}$$

However, the evaluation of Liouville's equation as a partial differential equation is in practice difficult, due to the large number of degrees of freedom. An equivalent approach is to start from an initial phase space distribution $\varrho_0 \equiv \varrho[\phi_0, \pi_0, t_0]$ and average over all phase space trajectories $(\phi_{\mathrm{cl}}, \pi_{\mathrm{cl}})$ dictated by Hamilton's equations (D.5). Then the expectation value corresponds to an integral over the observable evaluated at all trajectories starting from equivalent initial conditions and reads [179]

$$\langle \mathcal{O}(t) \rangle = \int \mathrm{d}\phi_0 \, \mathrm{d}\pi_0 \; \varrho_0 \mathcal{O}[\phi_{\mathrm{cl}}, \pi_{\mathrm{cl}}, t]. \tag{5.35}$$

It bears resemblance to (2.25), where the path integral is replaced by a classical approximation in terms of trajectories following Hamilton's equations. Since the initial field configurations ϕ_0 and π_0 are based on random numbers as discussed in section 5.4, equation (5.35) can be evaluated by means of Monte Carlo sampling. We generate an ensemble of N_{ens} initial field configurations and evolve each independently in time defining the trajectories $(\phi^n_{\mathrm{cl}}, \pi^n_{\mathrm{cl}})$. Then the expectation value can be approximated in analogy to (3.23) by

$$\langle \mathcal{O}(t) \rangle \approx \frac{1}{N_{\mathrm{ens}}} \sum_{n=1}^{N_{\mathrm{ens}}} \mathcal{O}[\phi^n_{\mathrm{cl}}, \pi^n_{\mathrm{cl}}, t] \tag{5.36}$$

and we take the average (3.39) as an estimator for the expectation value. In contrast to the Monte Carlo algorithm of section 3.3 based on a Markov chain, the classical configurations $(\phi^n_{\mathrm{cl}}, \pi^n_{\mathrm{cl}})$ are completely uncorrelated. Thus the statistical error can be estimated without any binning by the standard deviation [149]

$$\sigma_{\bar{x}} = \left(\frac{1}{N-1} \sum_{i=1}^{N} (x_i - \bar{x})^2 \right)^{1/2}. \tag{5.37}$$

One standard observable in semi-classical approaches is the system's energy density. The energy corresponds to the element T^{00} of the energy-momentum tensor, which can be connected to the Hamiltonian function [74] by

$$H = \int \mathrm{d}^3x \; T^{00}. \tag{5.38}$$

The total energy density can be separated into the contributions of the fields E_i, U_i as well as ψ and is given by

$$\epsilon_{\text{tot}} = \epsilon_E + \epsilon_B + \epsilon_\psi = \frac{H}{V}, \tag{5.39}$$

where V denotes the volume. Although the separate contributions are time dependent $\epsilon = \epsilon(t)$, the total energy density is constant due to energy conservation. We derive the explicit lattice expressions from the Hamiltonian function (5.11)

$$a_\sigma^4 \epsilon_E(t) = \frac{\beta}{2N_c N_\sigma^3} \sum_{\mathbf{x}} \operatorname{Re}\operatorname{Tr}\left(E_i(x) E_i(x)\right), \tag{5.40a}$$

$$a_\sigma^4 \epsilon_B(t) = \frac{\beta}{N_\sigma^3} \sum_{\mathbf{x}} \sum_{i<j} \left(1 - \frac{1}{N_c} \operatorname{Re}\operatorname{Tr} U_{ij}(x)\right), \tag{5.40b}$$

$$\begin{aligned} a_\sigma^4 \epsilon_\psi(t) = \frac{1}{N_\sigma^3} \sum_{\mathbf{x}} \Bigg(& \mathrm{i}\frac{1}{2} \left\langle \overline{\psi}_{\mathrm{M}}(x) \gamma_i U_i(x) \psi_{\mathrm{F}}(x+\hat{i}) - \overline{\psi}_{\mathrm{M}}(x) \gamma_i U_i^\dagger(x-\hat{i}) \psi_{\mathrm{F}}(x-\hat{i}) \right\rangle_{\mathrm{e}} \\ & + \frac{r}{2} \sum_i \Big\langle \overline{\psi}_{\mathrm{M}}(x) U_i(x) \psi_{\mathrm{F}}(x+\hat{i}) - 2\overline{\psi}_{\mathrm{M}}(x) \psi_{\mathrm{F}}(x) \\ & \qquad + \overline{\psi}_{\mathrm{M}}(x) U_i^\dagger(x-\hat{i}) \psi_{\mathrm{F}}(x-\hat{i}) \Big\rangle_{\mathrm{e}} \\ & - m \left\langle \overline{\psi}_{\mathrm{M}}(x) \psi_{\mathrm{F}}(x) \right\rangle_{\mathrm{e}} \Bigg), \end{aligned} \tag{5.40c}$$

where we substitute fermionic correlators by their ensemble average over stochastic fermions (5.27a). We omit the average over interchanged genders to simplify notation. The computation of the fermionic energy density requires an additive renormalisation in terms of subtracting the vacuum energy. We discuss this in more detail in section 5.4.2.

If an observable under investigation is not gauge invariant, one has to handle redundant degrees of freedom in the field variables. This can be prevented by fixing the gauge. Initially, we only fixed the gauge in temporal direction (5.7), leaving the freedom of spatial gauge transformations. We remedy this in case of gauge dependent observables by applying the Coulomb gauge

$$\partial_i A_i(x) = 0. \tag{5.41}$$

We deal with its numeric implementation in section 5.3.2. Gribov discovered that the gauge fixing is not necessarily unique [180]. From a geometrical point of view the gauge orbit, defined by the field A^G as a function of the gauge transformation G, can intersect the plane defined by the gauge condition $f(A^G) = 0$ more than once as depicted in figure 5.2. These Gribov copies can disturb the lattice measurement, e.g. as a source of additional statistical noise in Monte Carlo sampling [181]. Unfortunately, an exclusion of Gribov copies is in practice not possible and their occurrence should be kept in mind for the evaluation of gauge fixed observables.

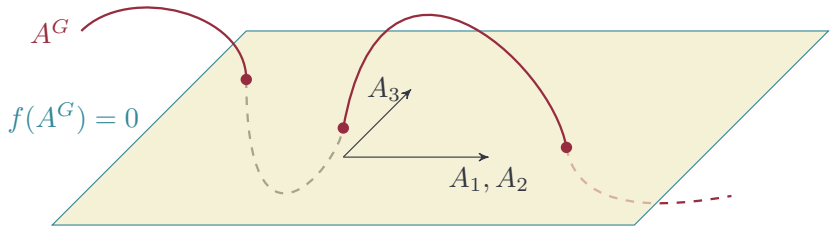

Figure 5.2: Schematic illustration of the appearance of Gribov copies. The gauge orbit A^G intersects the submanifold defined by the gauge condition $f(A^G) = 0$ several times and each intersection point represents one Gribov copy. Ideally, there is only one point of intersection, corresponding to a unique gauge fixed configuration.

5.3 Details of numeric implementation

Having established a semi-classical formulation of QCD on the lattice in the last section, we now discuss details of the numeric implementation. In order to solve the equations of motion, we discretise the time dimension in section 5.3.1. From the Courant condition [149] follows a constraint on the ratio of spatial to temporal lattice spacing, i.e. $\frac{a_\sigma}{a_\tau} > 3$. We propose algorithms to enforce Gauss law and fix the gauge in section 5.3.2 and check that our enforcement of Gauss law is implemented correctly. Additionally, we introduce a further check of our code by random gauge transformations.

5.3.1 Equations of motion in discrete time

A numeric treatment of the classical lattice system (5.12) to (5.15) requires a discretisation of time. We divide the total time into N_{time} discrete steps of size a_τ. One point of time is given by $t \equiv a_\tau \Delta t$ with $\Delta t = 0, 1, \ldots, N_{\text{time}} - 1$ counting the number of steps. Replacing the continuous time derivative with finite differences (3.4) in the equations of motion (5.12) to (5.14) and Gauss law (5.15) we find

$$U_i(x + \hat{0}) = \exp\left(\mathrm{i}\xi^{-1} E_i(x)\right) U_i(x), \tag{5.42a}$$

$$\begin{aligned} E_i(x + \hat{0}) = E_i(x) &- \frac{2}{\xi} T^a \sum_{j \neq i} \operatorname{Im} \operatorname{Tr} \left\{ T^a \Big(U_{ij}(x) - U_{ij}(x - \hat{j}) \Big) \right\} \\ &+ \frac{N_c}{\beta\xi} T^a \big\langle \overline{\psi}_{\mathrm{M}}(x) \gamma_i T^a U_i(x) \psi_{\mathrm{F}}(x + \hat{i}) + \overline{\psi}_{\mathrm{M}}(x + \hat{i}) \gamma_i U_i^\dagger(x) T^a \psi_{\mathrm{F}}(x) \big\rangle_{\mathrm{e}} \\ &- \mathrm{i} \frac{r N_c}{\xi\beta} T^a \big\langle \overline{\psi}_{\mathrm{M}}(x) T^a U_i(x) \psi_{\mathrm{F}}(x + \hat{i}) \\ &\qquad - \overline{\psi}_{\mathrm{M}}(x + \hat{i}) U_i^\dagger(x) T^a \psi_{\mathrm{F}}(x) \big\rangle_{\mathrm{e}}, \end{aligned} \tag{5.42b}$$

$$\psi_{\mathrm{G}}(x+\hat{0}) = \psi_{\mathrm{G}}(x-\hat{0}) - \mathrm{i}\frac{2m}{\xi}\gamma_0\psi_{\mathrm{G}}(x) - \frac{1}{\xi}\gamma_0\gamma_i\Big(U_i(x)\psi_{\mathrm{G}}(x+\hat{i}) - U_i^\dagger(x-\hat{i})\psi_{\mathrm{G}}(x-\hat{i})\Big) + \mathrm{i}\frac{r}{\xi}\gamma_0\sum_i\Big(U_i(x)\psi_{\mathrm{G}}(x+\hat{i}) - 2\psi_{\mathrm{G}}(x) + U_i^\dagger(x-\hat{i})\psi_{\mathrm{G}}(x-\hat{i})\Big), \tag{5.42c}$$

$$0 = \frac{N_c}{2\beta}\big\langle\overline{\psi}_{\mathrm{M}}(x)\gamma_0 T^a\psi_{\mathrm{F}}(x+\hat{0}) + \overline{\psi}_{\mathrm{M}}(x+\hat{0})\gamma_0 T^a\psi_{\mathrm{F}}(x)\big\rangle_{\mathrm{e}} - \sum_i \mathrm{Re}\,\mathrm{Tr}\left\{T^a\Big(E_i(x) - U_i^\dagger(x-\hat{i})E_i(x-\hat{i})U_i(x-\hat{i})\Big)\right\}, \tag{5.42d}$$

where we evolve each of the N_{e} gendered fermions $\psi_{\mathrm{G}} = \psi_{\mathrm{M/F}}$ and substitute fermionic correlators by their ensemble average over stochastic fermions (5.27a). We omit the average over interchanged genders to simplify notation. Rewriting the time evolution of the links (5.42a) as an exponential is favourable to incorporate the matrix structure of the chromo-electric field, $E_i = E_i^a T^a$. The exponential function is evaluated by a Taylor series expansion in the inverse anisotropy ξ^{-1}, which is small as explained later. A numeric evaluation of the equations of motion requires an explicit representation of the generators T^a. We choose the Gell-Mann matrices given in equation (A.9) in the appendix.

A numerically stable as well as physically meaningful simulation requires a fulfilment of Gauss law at all times. To this end we introduce an algorithm to reduce the Gauss violation in section 5.3.2. Furthermore the order in which we evaluate the equations of motion is crucial in order to conserve Gauss law. Since the colour-magnetic and fermionic fields enter the Gauss constraint, it is necessary to directly evolve the chromo-electric field after Gauss law has been enforced. Because of that we use the following sequence of evaluation:

1. Enforce Gauss law on the chromo-electric field by the algorithm we give in section 5.3.2 or by construction.
2. Evolve the chromo-electric field according to (5.42b).
3. Evolve the ensemble of gendered fermionic fields according to (5.42c).
4. Evolve the links according to (5.42a).

The steps 2 to 4 are repeated to compute the evolution of the fields. We discuss the initialisation of the fields in thermal equilibrium in section 5.4.

After discretising the time dimension, the system's evolution is determined by the anisotropy ξ instead of the spatial or temporal lattice spacing a_σ and a_τ. Consequently, the system's scale is completely set by the initial conditions imposed on the fields. As illustrated in figure 5.3 the Courant condition [149]

$$3\frac{|v|a_\tau}{a_\sigma} < 1 \tag{5.43}$$

with v being the speed of propagating information gives an upper bound for the anisotropy. The factor 3 originates from having three spatial dimensions. Solving partial

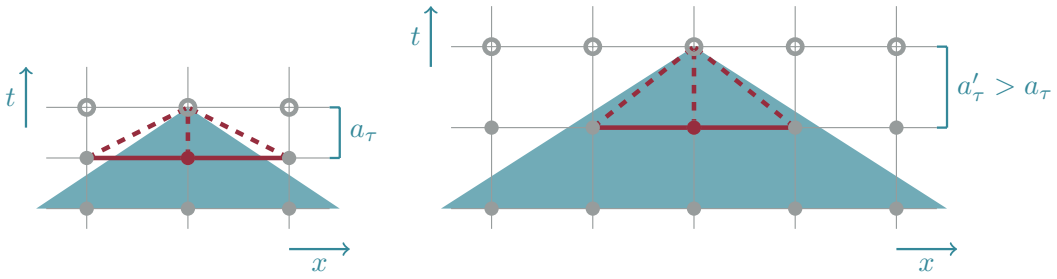

Figure 5.3: A solution to partial differential equations at one time depends on information within some domain of dependency to the past, e.g. the initial conditions. This area is illustrated blue shaded. Evolving to this time from one time slice before requires consideration of points connected by the red line. Their influence on the new time point is depicted by the dashed red lines. If the shaded area is within this dashed triangle the Courant condition (5.43) is fulfilled. Thus the left hand side is numerically stable whereas the right hand side is not due to an increased temporal lattice spacing $a'_\tau > a_\tau$.

differential equations the Courant condition is a necessary condition for numeric stability. In case of elementary particle physics v corresponds to the speed of light $c = 1$ and it follows for the anisotropy $\xi^{-1} < \frac{1}{3}$. We show the emergence of numeric instabilities originating from too small anisotropies in figure 5.11 of section 5.4.1.

5.3.2 Gauss law, gauge fixing and random gauge transformations

When solving the equations of motion we also have to satisfy Gauss law (5.42d). The Gauss constraint is preserved as can be shown by performing explicitly the time derivative and plugging in the equations of motion. Thus we enforce Gauss law only on the initial conditions and check for numeric errors, which could violate the constraint, during the time evolution.

Concerning a bosonic system in thermal equilibrium we implement an enforcement of Gauss law following [163]. The Gauss violation in matrix form reads

$$\begin{aligned} C(x) \equiv \frac{N_c}{2\beta} T^a \big\langle \overline{\psi}_{\mathrm{M}}(x)\gamma_0 T^a \psi_{\mathrm{F}}(x+\hat{0}) + \overline{\psi}_{\mathrm{M}}(x+\hat{0})\gamma_0 T^a \psi_{\mathrm{F}}(x)\big\rangle_{\mathrm{e}} \\ - T^a \sum_i \mathrm{Re}\,\mathrm{Tr}\left\{ T^a \Big(E_i(x) - U_i^\dagger(x-\hat{\imath}) E_i(x-\hat{\imath}) U_i(x-\hat{\imath}) \Big) \right\}. \end{aligned} \tag{5.44}$$

The idea is to correct the electric field repeatedly for the amount it violates Gauss law

$$E_i(x) \to E_i(x) + \gamma \left(U_i C(x+\hat{\imath}) U_i^\dagger(x) - C(x) \right), \tag{5.45}$$

where the optimal parameter γ can be obtained from a Fourier analysis of $C(x)$. According to the reference we choose $\gamma = 0.12$. A measure for the Gauss violation at time t is given by

$$C(t) \equiv \sqrt{\sum_{\mathbf{x}} \mathrm{Tr}\, C^\dagger(t,\mathbf{x}) C(t,\mathbf{x})}. \tag{5.46}$$

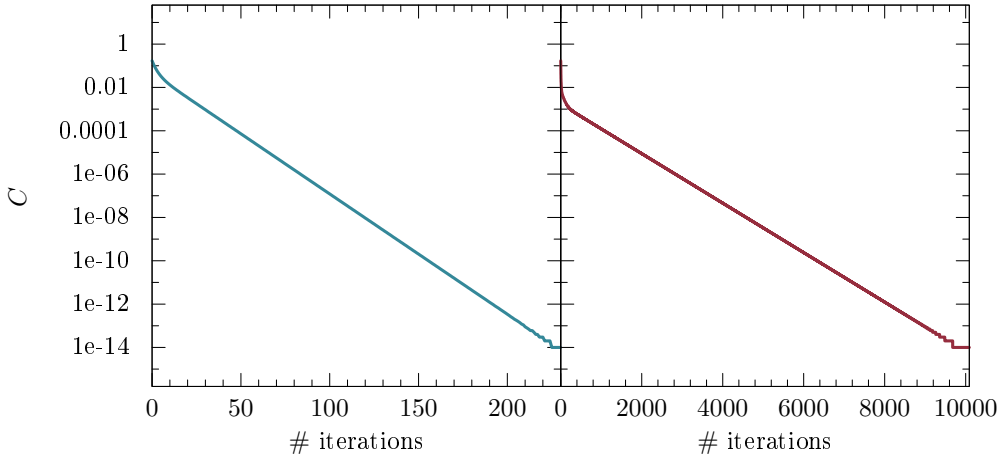

Figure 5.4: Reduction of the Gauss violation C by the relaxation algorithm on a 4^3 sized lattice for a pure bosonic system on the left hand side and a system including vacuum fermions on the right hand side. The simulation parameters are $g = 0.2$, $\xi = 20$, $a_\sigma m = 0$, $r = 0$, and $N_\mathrm{e} = 20$.

The left hand side of figure 5.4 illustrates the decrease of the measure per application of the relaxation algorithm. We only compute observables when the Gauss violation is reduced below a certain threshold. Additionally, we monitor its value for the total time evolution. The relaxation algorithm can also be applied to systems including fermions. As illustrated on the right hand side of figure 5.4 the enforcement of Gauss law needs many more iterations. While the pure bosonic system requires $\sim$ 230 iterations to decrease the Gauss violation below machine precision, the combined system requires $\sim$ 10000 steps.

As discussed in section 5.2.4 some observables require an entirely fixed gauge field. In addition to the temporal gauge (5.7) one has to fix the spatial degrees of freedom. This can be accomplished by applying the Coulomb gauge (5.41). On the lattice fixing a link configuration to Coulomb gauge translates to minimising the functional [182]

$$F[G] \equiv -\sum_{\mathbf{x},i} \mathrm{Re}\,\mathrm{Tr}\, U_i^{G(\mathbf{x})}(\mathbf{x}), \tag{5.47a}$$

$$0 = \left.\frac{\delta F}{\delta G}\right|_{G^*}, \tag{5.47b}$$

where G denotes a gauge transformation and G^* the final gauge fixing transformation. Imposing the requirement (5.47) iteratively on every lattice site at fixed time by

$$G'(\mathbf{x}) = V(\mathbf{x})G(\mathbf{x}), \tag{5.48a}$$

$$V(\mathbf{x}) = \sum_i \Big(G(\mathbf{x})U_i(\mathbf{x})G^\dagger(\mathbf{x}+\hat{i}) + G(\mathbf{x}-\hat{i})U_i^\dagger(\mathbf{x}-\hat{i})G^\dagger(\mathbf{x}-\hat{i}) \Big)_{\mathrm{SU(3)}}, \tag{5.48b}$$

$$U_i^{G(\mathbf{x})}(\mathbf{x}) = G'(\mathbf{x})U_i(\mathbf{x})G^{\dagger\prime}(\mathbf{x}+\hat{i}), \tag{5.48c}$$

we approach the final gauge fixing transformation G^* step by step. Since the sum of two SU(3) matrices leaves the group closure, the matrix V must be projected back to the group SU(3). This can be achieved by a decomposition into its SU(2) subgroups as

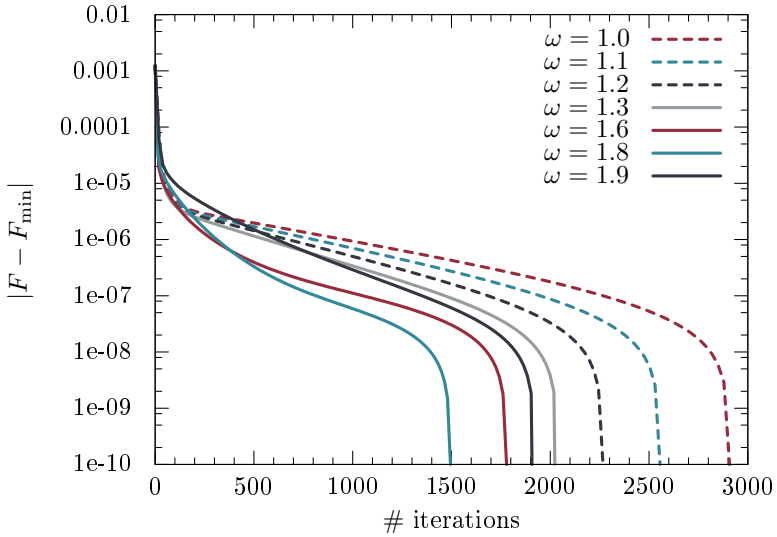

Figure 5.5: Deviation of the functional (5.47a) from its value at the final gauge fixing transformation. The required number of iterations to fix the gauge up to a precision of 10^{-10} depends strongly on the overrelaxation parameter ω.

discussed in section 3.3.2. A slight variation of the vector x in (3.33) by a parameter $\omega \in [1, 2)$ can be used to speed up the gauge fixing procedure. This algorithm is called overrelaxation and is especially useful to moderate the critical slowing-down for larger lattices [183, 184].

The procedure stops, when the next computed gauge fixing transformation does not differ from the former one up to a predefined precision or when a maximum number of gauge fixing steps N_{OR} is exceeded. Figure 5.5 shows the gauge fixing procedure up to a precision of 10^{-10} for different overrelaxation parameters ω. The optimal value of $\omega = 1.8$ only requires half as many iterations as $\omega = 1$, corresponding to no overrelaxation. Because of that we determine the optimal overrelaxation parameter for every simulation run on a different lattice size. Figure 5.6 shows the composition of the total computation time $\approx 42\,\mathrm{h}$ for a run on a $32^2 \times 96$ sized lattice from chapter 6. We fixed the gauge in each of the 8000 time steps. The fact that the gauge fixing procedure takes the majority of the computation time, is one reason to investigate gauge invariant observables.

The gauge freedom in the directions can be used to check the numeric implementation. Applying a random gauge transformation $V(x)$ to the fields E_i, U_i and ψ_{G} should not change the expectation value of gauge invariant observables. Figure 5.7 shows the difference between the energy densities 5.40a to 5.40c based on usual and random gauge transformed fields. The minor deviation attests a correct numeric implementation of the semi-classical model. We perform this test for every gauge invariant observable including those introduced in chapter 6.

5.4 Thermal equilibrium

In order to become acquainted to the formalism developed in the last sections, we apply it to a system in thermal equilibrium. We perform consistency checks, especially to test the numeric implementation of the model. We start with the study of a pure bosonic

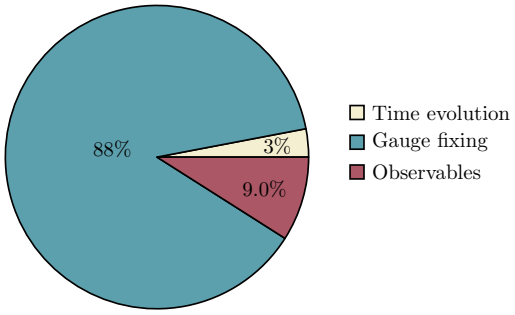

Figure 5.6: The gauge fixing procedure constitutes the major contribution to the total computation time of a run from chapter 6. We request a precision of 10^{-10} with a maximum of 8000 iterations for the gauge fixing procedure.

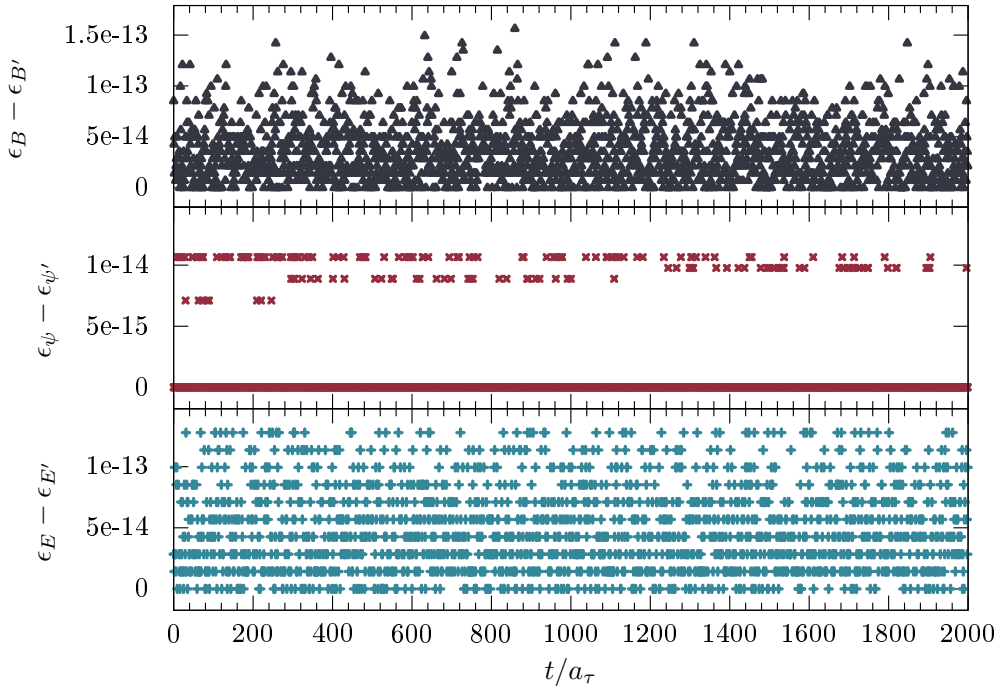

Figure 5.7: Difference in the energy densities between usual and random gauge fixed fields E_i, U_i and ψ_{G} run on a 8^3 sized lattice. The minor deviation is caused by the finite machine precision.

Run	β_{cl}	N_σ	ξ	N_{ens}	N_{reinit}	N_{therm}	N_{time}
i	66.7	8	20	30	10	200	2000
ii	24	–	20	5	10	500	4000

Table 5.1: Simulation parameters for pure bosonic runs. The second run (ii) is performed on a $32^2 \times 96$ lattice to accommodate more momentum modes.

system with colour group SU(3) in section 5.4.1. Most of the former work on classical bosonic systems as for instance [86, 156, 158, 163, 185] is limited to the colour group SU(2). Although an investigation within SU(3) would be interesting, we proceed to our primarily goal, the inclusion of fermions.

To this end we study an ideal Fermi gas in section 5.4.2 and a system consisting of bosonic and fermionic fields in section 5.4.3. The semi-classical model has already been applied to fermion production in QED [186, 187] and scalar theories [64] as well as to the weak sector of the standard model describing baryogenesis [188–190]. We present the first study of full QCD within the semi-classical description. However, we only use the thermal equilibrium case to get acquainted to the formalism and check our numeric implementation. We ultimately apply the semi-classical model to isotropisation processes of the quark-gluon plasma in chapter 6. Since all statistical errors are below 1 %, we do not show any error bars in our plots.

5.4.1 Pure bosonic system

We determine the initial bosonic fields by a Monte Carlo sampling. In the case of classical Yang-Mills theory in thermal equilibrium the fields are distributed according to

$$\delta(G)\mathrm{e}^{-\frac{1}{T}H_{\mathrm{B}}}, \tag{5.49}$$

where $\delta(G)$ enforces the Gauss constraint (5.15) and H_{B} is the pure bosonic part of the lattice Hamiltonian (5.11). Defining an effective classical coupling

$$\beta_{\mathrm{cl}} \equiv \frac{2N_c}{Tg^2 a_\sigma}, \tag{5.50}$$

the chromo-electric field amplitudes E_i^a can be drawn from a Gaussian distribution

$$g(x) = \frac{1}{\sigma\sqrt{2\pi}}\mathrm{e}^{-\frac{1}{2}\left(\frac{x-\mu_G}{\sigma}\right)^2} \tag{5.51}$$

with mean $\mu_G = 0$ and squared width $\sigma^2 = \frac{\beta_{\mathrm{cl}}}{4N_c}$ and combined with the matrix $E_i = E_i^a T^a$. Gauss law is enforced by applying (5.45) several times. Starting from cold initial links $U_i = \mathbb{1}$, they are thermalised by a pure bosonic evolution in time, (5.42b) and (5.42a), which mixes the chromo-electric and chromo-magnetic fields [163]. A repeated reinitialisation of E_i, keeping the U_i untouched, thermalises the system according to the Boltzmann weight given in (5.49). Figure 5.8 illustrates the bosonic thermalisation process for simulation parameters (i) shown in table 5.1.

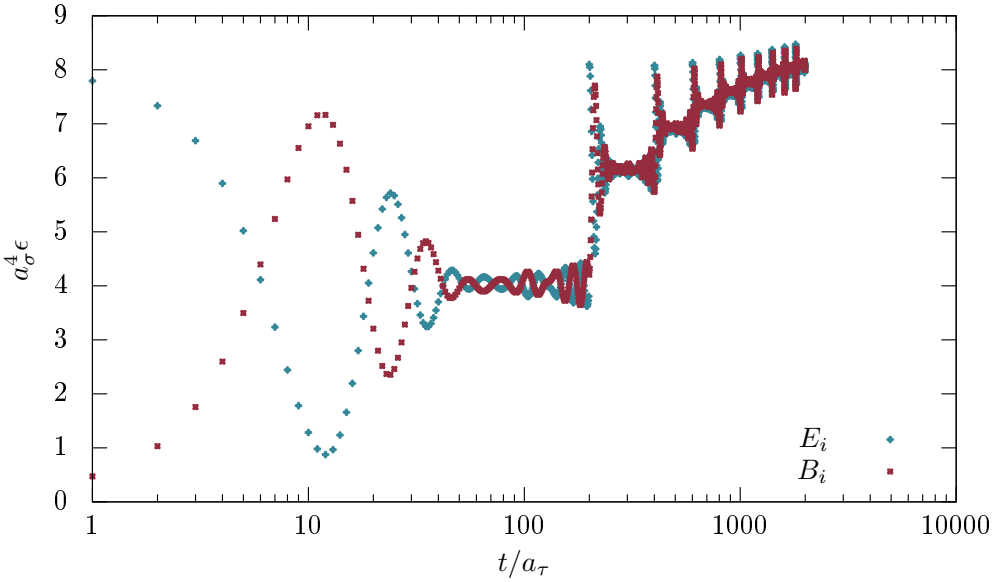

Figure 5.8: Thermalisation procedure for bosonic degrees of freedom according to run (i) of table 5.1. We reinitialise the chromo-electric fields E_i every $\Delta t = 200$ time steps according to their distribution (5.49). The links U_i are thermalised by interaction with the E_i through their equations of motion (5.12) and (5.13), excluding the fermionic contributions.

The effective classical coupling is the only parameter entering a pure bosonic simulation. It can be used to set the scale by connecting it to the Debye mass. Its continuum value for Yang-Mills theory is given by [79]

$$m_{\mathrm{D}}^2 = \frac{N_c}{3} g^2 T^2, \tag{5.52}$$

whereas its lattice value in three-dimensional Yang-Mills theory is [191]

$$m_{\mathrm{D,L}}^2 = \frac{N_c \Sigma g^2 T}{2\pi a_\sigma}, \qquad \Sigma = 3.175911536\ldots\ . \tag{5.53}$$

Equating both expressions relates the spatial lattice spacing to the Debye mass

$$a_\sigma^2 = \frac{N_c^2 \Sigma}{\pi \beta_{\mathrm{cl}} m_{\mathrm{D}}^2}, \tag{5.54}$$

or equivalently to the temperature

$$a_\sigma = \frac{3\Sigma}{2\pi T}. \tag{5.55}$$

Our lattice cutoff being proportional to the Debye mass, $\Lambda \sim \frac{1}{a_\sigma} \sim m_{\mathrm{D}}$, is exactly what we want in order to separate the ultraviolet scale from the soft scales. The further requirement of soft field modes with a high population can be checked by introducing estimates for the occupancy of transversal and longitudinal chromo-electric field

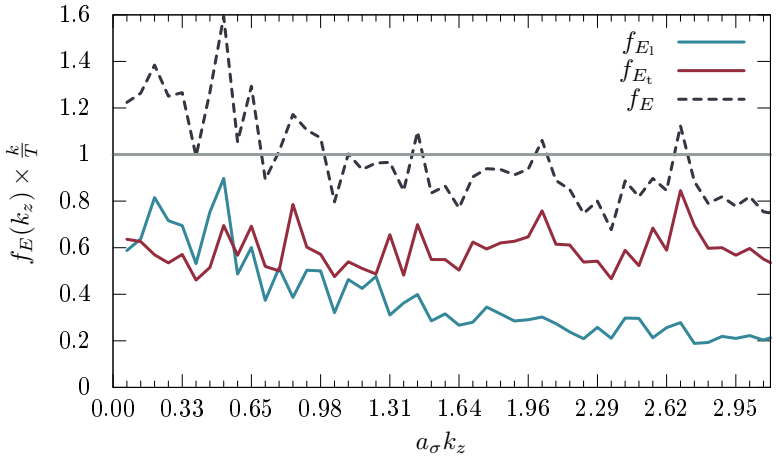

Figure 5.9: Normalised estimates for the occupation of chromo-electric field modes in thermal equilibrium with simulation parameters given of run (ii) of table 5.1. Transversal and longitudinal occupation sum to the total occupation, $f_E = f_{E_\mathrm{t}} + f_{E_\mathrm{l}}$. The classical approximation is valid, if the estimated occupation for low momentum modes is larger than one, $f_E(k_z) \times k/T > 1$.

modes [185]

$$f_{E_\mathrm{t}}(t, \mathbf{p}) = \frac{\mathcal{P}^T_{ij}\delta^{ab}}{2(N_c^2-1)|\mathbf{p}\,|} \int \mathrm{d}^3x \; \mathrm{e}^{-\mathrm{i}\mathbf{p}\mathbf{x}} \left\langle E_i^a(x) E_j^b(0) \right\rangle , \tag{5.56a}$$

$$f_{E_\mathrm{l}}(t, \mathbf{p}) = \frac{p_i p_j \delta^{ab}}{(N_c^2-1)|\mathbf{p}\,|^3} \int \mathrm{d}^3x \; \mathrm{e}^{-\mathrm{i}\mathbf{p}\mathbf{x}} \left\langle E_i^a(x) E_j^b(0) \right\rangle , \tag{5.56b}$$

where $\mathcal{P}^\mathrm{T}_{ij} = \delta_{ij} - \frac{p_i p_j}{|\mathbf{p}\,|^2}$ is the transversal projection operator. The lattice equivalents are given by

$$f_{E_\mathrm{t}}(t, p_z) = \frac{1}{(N_c^2-1)p_z} \sum_{\mathbf{x}} \mathrm{e}^{-\mathrm{i}p_z z} \,\mathrm{Tr}\, \langle E_1(x)E_1(0) + E_2(x)E_2(0) \rangle , \tag{5.57a}$$

$$f_{E_\mathrm{l}}(t, p_z) = \frac{2}{(N_c^2-1)p_z} \sum_{\mathbf{x}} \mathrm{e}^{-\mathrm{i}p_z z} \,\mathrm{Tr}\, \langle E_3(x)E_3(0) \rangle . \tag{5.57b}$$

Since these observables are not gauge invariant, we fix the gauge to Coulomb gauge by the algorithm discussed in 5.3.2. Figure 5.9 shows the simulation results normalised to the prediction from hard thermal loop effective theory [185]. Since the occupation number within a pure bosonic thermal system is a static quantity, we enlarge our Monte Carlo ensemble by including each time step as a configuration. The classical regime of validity is reached for normalised occupation numbers $f(q_z)\frac{q_z}{T} > 1$. We perform the normalisation by using that the temperature is proportional to the inverse lattice spacing (5.55). On our lattice with $32^2 \times 96$ lattice sites and a classical coupling of $\beta_\mathrm{cl} = 24$ the low momentum modes are inside the regime of validity.

We show the time evolution of a pure bosonic system in figure 5.10 using parameters (i) of table 5.1. The thermalisation process has already been depicted in figure 5.8. The energy from the chromo-electric fields is transferred to the chromo-magnetic one and vice versa leaving the total energy density constant up to numeric fluctuations. Figure 5.11 illustrates the evolution of energy density for different temporal lattice spacings

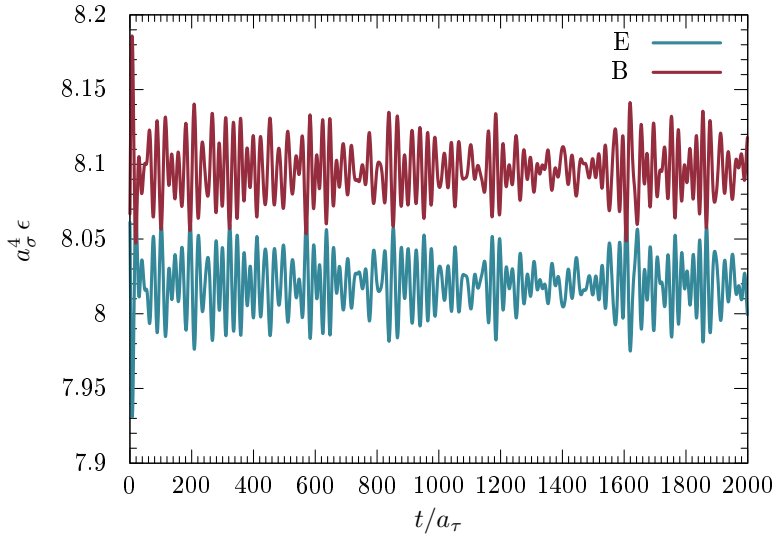

Figure 5.10: Evolution of a pure bosonic system with parameters according to run (i) of table 5.1. The chromo-electric energy density is denoted E and the chromo-magnetic one B. The total energy is conserved as should be the case in a finite box.

a_τ, but fixed spatial lattice spacing a_σ. A numeric instability arises for anisotropies not fulfilling the Courant condition (5.43).

5.4.2 Pure fermionic system

The initialisation of stochastic fermions introduced in section 5.2.3 on the lattice follows from a straightforward discretisation of the gendered fermions (5.24) at initial time $t = 0$

$$\psi_{\mathrm{M/F}}(t=0,\mathbf{x}) = \frac{1}{\sqrt{2}N_\sigma^3}\sum_{\mathbf{n}}\sum_{s}\left(\xi_s(\mathbf{n})u_s(\mathbf{n})\mathrm{e}^{\mathrm{i}\frac{2\pi}{N_\sigma}\mathbf{nx}} \pm \eta_s(\mathbf{n})v_s(\mathbf{n})\mathrm{e}^{-\mathrm{i}\frac{2\pi}{N_\sigma}\mathbf{nx}}\right), \tag{5.58a}$$

$$\overline{\psi}_{\mathrm{M/F}}(t=0,\mathbf{x}) = \frac{1}{\sqrt{2}N_\sigma^3}\sum_{\mathbf{n}}\sum_{s}\left(\xi_s^*(\mathbf{n})\bar{u}_s(\mathbf{n})\mathrm{e}^{-\mathrm{i}\frac{2\pi}{N_\sigma}\mathbf{nx}} \pm \eta_s^*(\mathbf{n})\bar{v}_s(\mathbf{n})\mathrm{e}^{\mathrm{i}\frac{2\pi}{N_\sigma}\mathbf{nx}}\right), \tag{5.58b}$$

where we include the normalisation $\frac{1}{\sqrt{2p_0}}$ in the definition of the spinors (5.30) and the three-vector $\mathbf{n}$ originates from the lattice momenta (3.6). The distributions of the complex numbers (5.26) replacing the ladder operators read in discretised form

$$\left\langle \xi_{s,a}(\mathbf{n})\xi_{r,b}^*(\mathbf{m})\right\rangle = N_\sigma^3\delta(\mathbf{n}-\mathbf{m})\delta_{rs}\delta_{ab}\left(1-2n_{\mathrm{F}}(\mathbf{n})\right), \tag{5.59a}$$

$$\left\langle \eta_{s,a}(\mathbf{n})\eta_{r,b}^*(\mathbf{m})\right\rangle = N_\sigma^3\delta(\mathbf{n}-\mathbf{m})\delta_{rs}\delta_{ab}\left(1-2n_{\mathrm{F}}(\mathbf{n})\right). \tag{5.59b}$$

They are sampled by a decomposition into

$$\xi_{r,a}(\mathbf{n}) = A_{r,a}(\mathbf{n})\mathrm{e}^{\mathrm{i}\phi_{r,a}(\mathbf{n})}, \qquad \eta_{r,a}(\mathbf{n}) = B_{r,a}(\mathbf{n})\mathrm{e}^{\mathrm{i}\theta_{r,a}(\mathbf{n})}, \tag{5.60}$$

drawing the momentum dependent amplitudes $A_{r,a}$ and $B_{r,a}$ from a Gaussian with mean $\mu_G = 0$ and squared width $\sigma^2 = N_\sigma^3\left(1-2n_{\mathrm{F}}(\mathbf{n})\right)$ and drawing the phases $\phi_{r,a}(\mathbf{n})$ and $\theta_{r,a}(\mathbf{n})$ uniformly distributed on the interval $(-\pi,\pi]$. Since male and female fermions

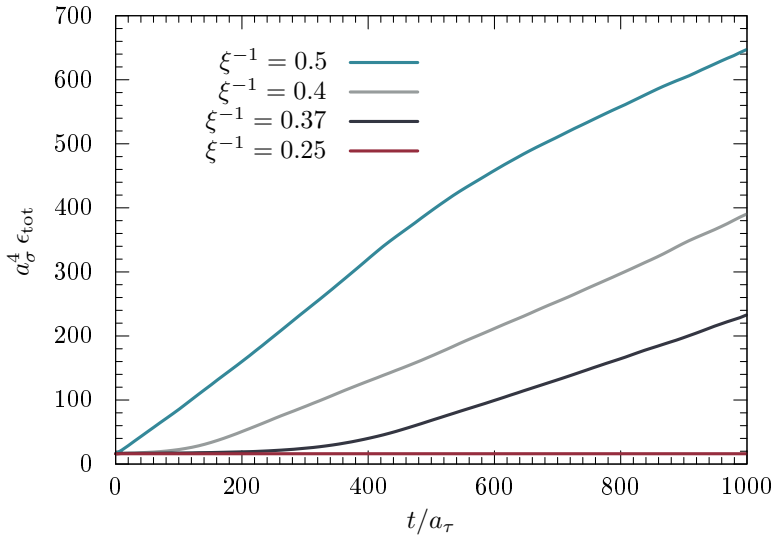

Figure 5.11: Total energy density versus time for different anisotropies ξ in a pure bosonic run. If the anisotropy does not fulfil the Courant condition (5.43), a numeric instability arises.

use the same ξ and η, we have to generate $4\times2\times N_c\times N_\sigma^3\times N_\mathrm{e}$ random numbers for each initialisation. Finally, the gendered fermions in position space (5.58) are obtained by the Fourier transform of the created complex random numbers multiplied by the spinor solutions (5.30) of the free Dirac equation including the normalisation factor. Discretising the fermionic equation of motion (5.42c) by a central difference (3.4c) requires a further initial field $\psi_\mathrm{G}(x-\hat{t})$, which we generate by one free ($U_i = \mathbb{1}_{3\times3}$) evolution step

$$\begin{aligned}\psi_\mathrm{G}(x-\hat{0}) = \psi_\mathrm{G}(x) + \mathrm{i}\frac{m}{\xi}\gamma_0\psi_\mathrm{G}(x) + \frac{1}{2\xi}\gamma_0\gamma_i\Big(\psi_\mathrm{G}(x+\hat{i}) - \psi_\mathrm{G}(x-\hat{i})\Big)\\ - \mathrm{i}\frac{r}{2\xi}\gamma_0\sum_i\Big(\psi_\mathrm{G}(x+\hat{i}) - 2\psi_\mathrm{G}(x) + \psi_\mathrm{G}(x-\hat{i})\Big).\end{aligned} \tag{5.61}$$

Employing relation (5.40c) to compute the fermionic energy density gives a negative result. This can be explained in terms of vacuum fermions. In the continuum the fermionic vacuum can be described as a Dirac sea [192] filled with an infinite amount of particles with negative energy. On the lattice the energy density becomes finite due to the ultraviolet cutoff resulting in negative values for the energy density. Since a measurement of energy and equivalently energy density is identical to measuring an energy difference, we shift our fermionic observables by subtracting the corresponding vacuum expectation value

$$\langle\epsilon_\psi(t)\rangle = \langle\epsilon_\psi(t)\rangle_T - \langle\epsilon_\psi(t=0)\rangle_{T_\mathrm{vac}}\,. \tag{5.62}$$

The correlator $\langle\epsilon_\psi\rangle_{T_\mathrm{vac}}$ can be evaluated by initialising the gendered fermions according to (5.59) with $T = 0$.

In the following we check the initialisation procedure by an investigation of the ideal Fermi gas. To this end we compare the initial energy density for different temperatures to its analytic value. In the continuum the energy density of a relativistic ideal gas of

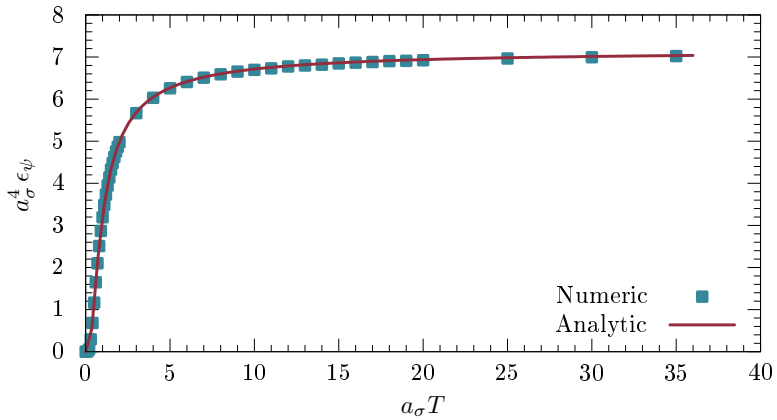

Figure 5.12: Fermionic energy density versus lattice temperature for an ideal Fermi gas on a 8^3 sized lattice. The other parameters are $N_\mathrm{e} = 50$, $a_\sigma m = 0$ and $r = 0$. We compare the numeric result initialised according to (5.59) with the analytic result (5.64). The numeric data points overlay the error bars.

N_σ	ξ	N_ens	N_time	N_e	$a_\sigma m$	$a_\sigma T$	r
8	20	30	2000	50	0.2	6	1

Table 5.2: Simulation parameters for a pure fermonic run. The coupling does not enter in the pure fermionic case. Additionally, the fermionic initialisation does not require any thermalisation.

fermions is given by [193]

$$\epsilon_\psi^\mathrm{cont} = g_\psi \int \frac{\mathrm{d}^3 p}{(2\pi)^3}\, E(\mathbf{p}) n_\mathrm{F}(\mathbf{p}), \tag{5.63}$$

where $E(\mathbf{p})$ is the energy and g_ψ the degeneracy factor. The latter one takes a value of $g_\psi = 2 \times 2 \times 3 = 12$ corresponding to fermions and antifermions, two polarisation states and three colours. Restricting the momenta to the first Brillouin zone and rewriting the momenta as sinusoidal functions (5.28) the energy density on the lattice takes the form

$$\epsilon_\psi = g_\psi \int_{-\pi}^{\pi} \frac{\mathrm{d}^3 p}{(2\pi)^3}\, s_0(\mathbf{s}) n_\mathrm{F}(\mathbf{s}). \tag{5.64}$$

Concerning the massless case, we solve the integral numerically and compare it to the result of our simulation for different temperatures in figure 5.12. We reproduce the analytic prediction for the fermionic energy density and the Fermi-Dirac distribution.

A further check of the initialisation and the fermionic equation of motion is to compute the evolution of the energy density, which should be constant in a finite box. To this end we run a simulation with parameters given in table 5.2. Figure 5.13 shows that the energy density fluctuates around a constant value, $\epsilon_\psi(t) = \epsilon_0$.

5.4.3 Semi-classical QCD

In this section we investigate a system in thermal equilibrium including both bosonic and fermionic degrees of freedom. Figure 5.14 sketches the semi-classical real time

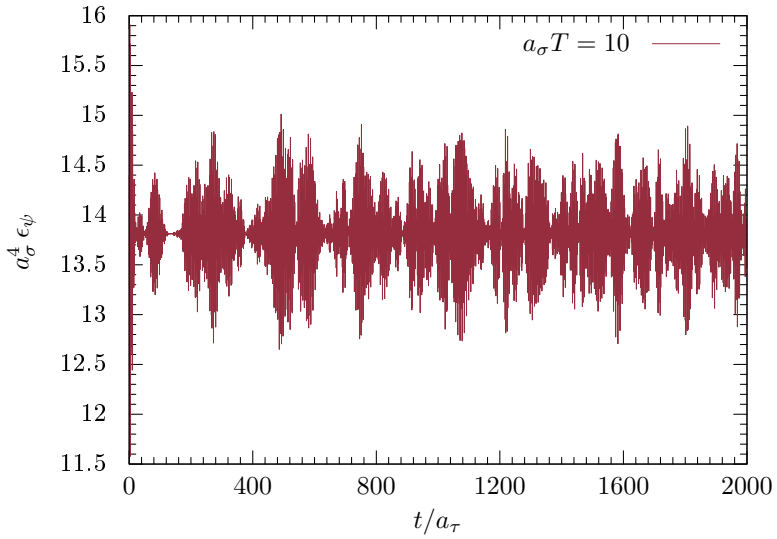

Figure 5.13: Energy density of an ideal Fermi gas over time. The simulation parameters are given in table 5.2.

Run	g	N_σ	ξ	N_{ens}	N_{reinit}	N_{therm}	N_{time}	N_{e}	$a_\sigma m$	$a_\sigma T$	r
i	2	8	20	12	5	200	8000	50	0	0	1
ii	2	8	20	–	5	200	8000	–	0.2	0	1
iii	2	8	20	–	5	200	8000	50	–	0	1
iv	2	8	20	14	5	200	8000	50	0	0	0
v	2	8	20	14	5	200	8000	50	0.2	10	1

Table 5.3: Simulation parameters for runs in thermal equilibrium. Zero temperature corresponds to vacuum initialised fermions. We vary the fermionic ensemble size in run (ii) using $N_{\text{e}} \in \{50, 75, 100\}$ on $N_{\text{ens}} \in \{14, 9, 6\}$ configurations, respectively. The mass is varied in run (iii) using $a_\sigma m =\in \{0, 0.2, 0.4, 0.6, 0.8\}$ on $N_{\text{ens}} \in \{11, 14, 11, 14, 11\}$ configurations, respectively.

algorithm. The fermionic fields are initialised according to the procedure described in section (5.23). The initialisation of the bosonic fields follows the strategy of section 5.4.1, but we include the fermions into the enforcement of Gauss law as well as the time evolution.

We show simulation parameters in table 5.3. Some of the listed parameters correspond to more than one run, since we vary different parameters. Our first simulation (i) aims at illustrating the thermalisation process as well as the time evolution. In the next simulation, run (ii), we vary the fermionic ensemble size N_{e} in order to study the effect of stochastic fermion modelling. We investigate the effects of adding a finite mass to the fermions and neglecting the Wilson term by simulations (iii) and (iv), respectively. The last run, (v), uses fermions initialised from a thermal distribution. At the end of this section we employ a different thermalisation procedure with the parameters given in table 5.4.

Figure 5.15 illustrates the time evolution of bosonic and fermionic fields on the basis of the corresponding energy densities (5.40) with simulation parameters given in (i) of table 5.3. During the first time steps, $0 < \frac{t}{a_\tau} < 1000$, energy is shifted from the chromo-

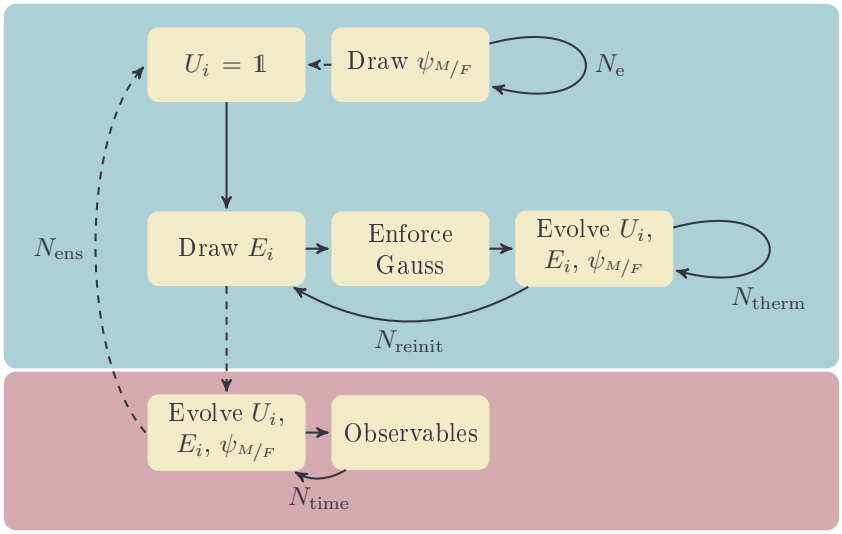

Figure 5.14: Sketch of the complete semi-classical real time algorithm for thermal equilibrium. The blue field indicates the initialisation process, the red field the time evolution. The initialisation starts from cold links and an ensemble of gendered fermions of size N_e initialised according to section 5.2.3. The next step is to draw a set of E_i from the corresponding Gaussian (5.49). After enforcing Gauss law the links U_i are thermalised by their interaction with the E_i and $\psi_{M/F}$ through the equations of motion. After N_therm steps, new E_i are drawn, but the U_i and $\psi_{M/F}$ kept fixed. Repeating this procedure N_reinit times, the fields U_i are thermalised. Evolving all fields according to their equations of motion allows for a measurement of observables at progressing times. After an evolution with N_time steps, one repeats the algorithm another N_ens times to produce a Monte Carlo sample for the measured observables.

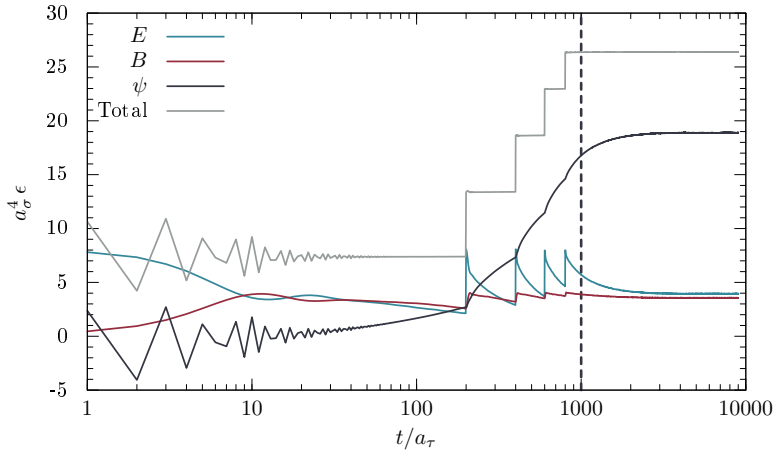

Figure 5.15: Thermalisation and evolution of a system consisting of fermionic and bosonic fields. The simulation parameters are given by run (i) of table 5.3. The thermalisation phase ends at $t/a_\tau = 1000$ and is indicated by the black dashed line.

electric field to the chromo-magnetic field, thermalising the chromo-magnetic fields. The heavy fluctuations of the fermionic energy density in the first 20 time steps are due to the Wilson term. We discuss this aspect later. The steps in the total energy density arise from the reinitialisation of the chromo-electric fields pumping new energy into the system. After the thermalisation phase ended, the total energy density is conserved as should be the case in a finite box. The fields keep on interacting and more energy is transferred to the fermionic field until at $\frac{t}{a_\tau} \approx 3000$ saturation sets in. In order to keep the following plots straightforward, we do not show all energy densities in every plot. If fields are not depicted, their dynamics are similar to the curves depicted in figure 5.15. We check that during the evolution the total energy is always conserved.

We investigate the effect of the fermionic ensemble size N_e on the dynamics in run (ii) of table 5.3 and show results in figure 5.16. At time $\frac{t}{a_\tau} \approx 7000$ the fermionic energy densities are $\epsilon_\psi = \{19.39(2), 19.71(2), 19.91(2)\}$ with ensemble sizes $N_\mathrm{e} = \{50, 75, 100\}$, respectively. As found by other authors using stochastic fermions [190] a fixed value is reached by increasing the ensemble size. Not being interested in a high precision measurement of an observable, our small ensemble sizes are sufficient for now, especially since the field dynamics do not change with the fermionic ensemble size. Note that the different ensemble sizes are also reflected in the bosonic energy density due to coupled equations of motion.

Figure 5.17 shows the evolution of the fermionic energy density using different masses, see run (iii) of table 5.3. All fermionic fields acquire energy over time and saturate around an energy density $\epsilon_\psi \approx 19$, as illustrated by the curves $a_\sigma m = 0$ and $a_\sigma m = 0.2$. The heavier fermonic fields have a higher energy density. Furthermore it takes much longer to excite the heavier fermionic fields.

The Wilson term can be interpreted as an additional mass. We study its effect by the runs (i) and (iv) and show the outcome in figure 5.18. As with the massive fermions, the excitation of the fermionic field including a Wilson term takes much longer and the saturated energy density is larger. The heavy fluctuations in the first 20 time steps do not arise when we neglect the Wilson term. In particular the fermionic energy density

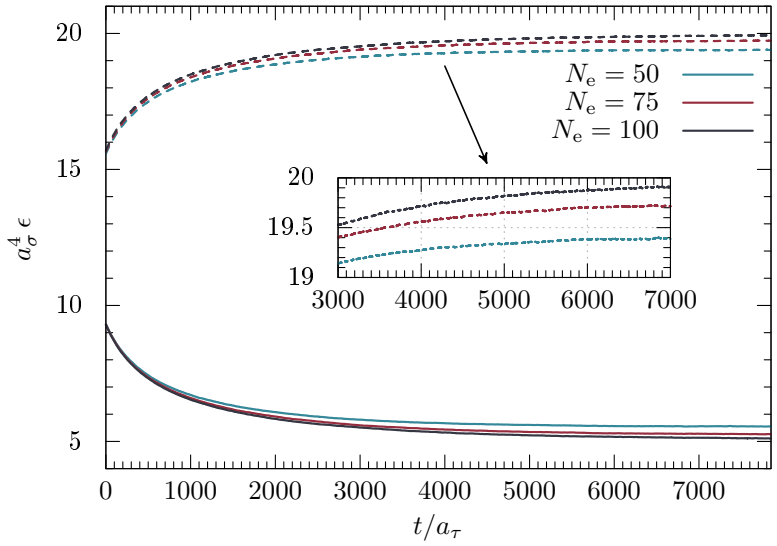

Figure 5.16: Evolution of energy densities for different fermionic ensemble sizes N_e, see run (ii) of table 5.3. We summarise chromo-magnetic and chromo-electric energy densities as a bosonic energy density. The solid lines correspond to the bosonic energy density and the dashed lines to the fermonic ones. The inlet shows an enlarged snippet of the fermionic curves.

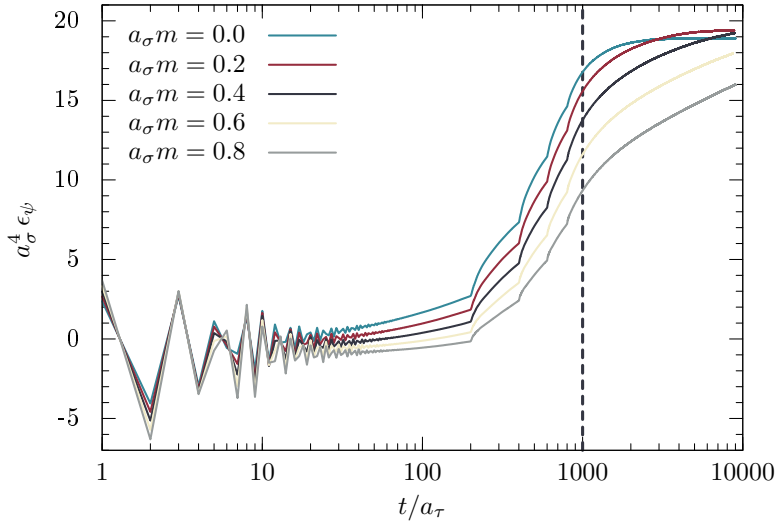

Figure 5.17: Thermalisation and evolution of the fermionic energy density using different masses, see run (iii) of table 5.3. The dashed line at $t/a_\tau = 1000$ indicates the end of the thermalisation phase.

g	N_σ	ξ	N_{ens}	N_{reinit}	N_{therm}	N_{time}	N_{e}	$a_\sigma m$	$a_\sigma T$	r
2	6	20	5	5	200	8000	20	0.4	0	1

Table 5.4: Simulation parameters for a run in thermal equilibrium using a different thermalisation procedure.

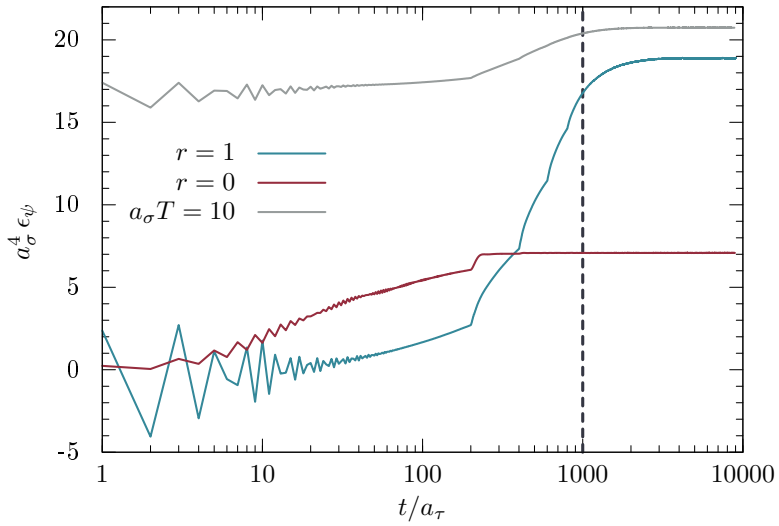

Figure 5.18: Thermalisation and evolution of the fermionic energy density with and without Wilson term, see runs (i) and (iv) of table 5.3. The dashed line at $t/a_\tau = 1000$ indicates the end of the thermalisation phase. The figure also shows the results of run (v) including a thermal initialisation of the fermionic fields with temperature $a_\sigma T = 10$.

stays positive. The figure also shows the fermionic energy density of run (v) including a thermal initialisation of the fermionic fields. The thermal fermions have a much larger initial energy density, as already found in figure 5.12. Their saturated energy density is also higher.

Finally, we present the evolution of the fields applying a different thermalisation algorithm. The bosonic and fermionic fields are independently thermalised and merged afterwards. Before merging we reinitialise the chromo-electric field once more and enforce Gauss law including the fermionic current. The evolution is shown in figure 5.19 and the simulation parameters are given in table 5.4. Although the fermionic field is not involved in the thermalisation process, it gains energy. This is due to the links entering the fermionic energy density (5.40c). In principle this additional energy shift can be removed by the additive renormalisation (5.62). Apart from that, the thermalisation procedure resembles the pure bosonic process discussed in section 5.4.1. The further evolution of the fields is similar to the other results of this section with the difference that the energy transfer between the bosonic and fermionic fields is enhanced due to the lower fermionic energy density at time $\frac{t}{a_\tau} \approx 1000$.

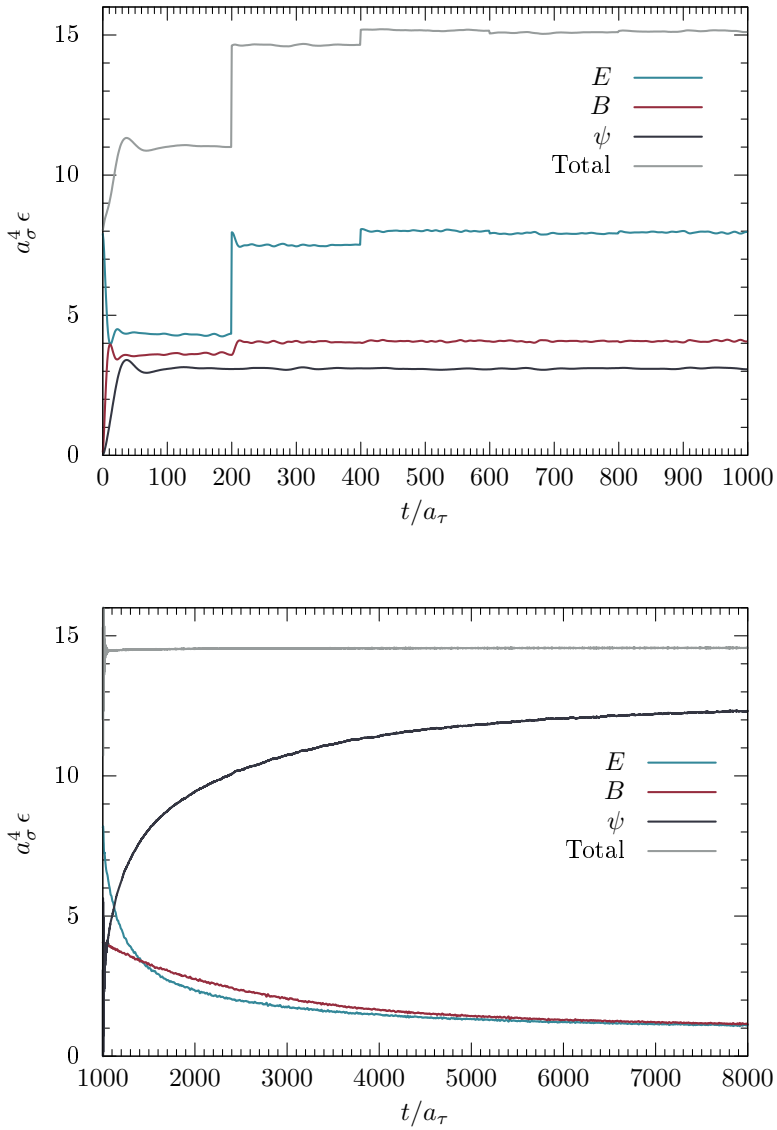

Figure 5.19: Thermalisation and evolution of a system consisting of fermionic and bosonic fields using a different thermalisation procedure. The procedure is described in the text. The simulation parameters are given by (vi) of table 5.4. The upper plot shows the thermalisation and the lower plot the subsequent evolution.

5.5 Future research perspectives

Possible applications of the semi-classical model of QCD in thermal equilibrium are an investigation of fermion production via the Schwinger mechanism in QCD, see reference [186] for a semi-classical real time treatment of this aspect in QED or the inclusion of external magnetic and electric fields allowing for an investigation of the chiral magnetic effect [194]. The magnetic field can be introduced in analogy to the implementation in lattice gauge theory [195,196]. A further topic is the computation of the imaginary part of the static potential [160] or the momentum diffusion constant of heavy quarks [197] including dynamic fermions.

An even wider range of applications is given by the field of non-equilibrium physics, which are directly accessible by the semi-classical model. In the next chapter 6 we investigate thermalisation processes of the quark-gluon plasma in the early stages of heavy ion collisions.

5.6 Conclusions

Many phenomena related to standard model physics at finite temperature involve true dynamic processes and require a treatment in real time. In this chapter we presented an approach to QCD incorporating real time. It is based on a semi-classical description of QCD on the lattice.

We implemented initial conditions describing thermal equilibrium and investigated the field dynamics of systems including bosons, fermions and both types of fields. In the pure fermionic system we reproduced the energy density of an ideal Fermi gas. With the full system we found an enhancement of the fermionic energy density by energy transfer from the bosonic fields. Introducing a fermionic mass term to the simulations reflected the physical expectation, namely a delayed excitation from the bosonic degrees of freedom and a higher saturated energy density.

The established semi-classical model of QCD is the foundation for an investigation of isotropisation processes in the quark-gluon plasma in the next chapter 6.

6 Isotropisation of the quark-gluon plasma via the chromo-Weibel instability

The success of equilibrium models in describing data from heavy ion collisions at LHC and RHIC suggests a local equilibrium shortly after the collision. Due to Lorentz contraction of the colliding nuclei, a momentum anisotropy in the longitudinal-transverse plane is expected. However, thermal equilibrium implies isotropy and we therefore investigate the process of isotropisation towards a thermalised quark-gluon plasma. The isotropisation time can be inferred from studies of elliptical flow using ideal hydrodynamics. Results from RHIC give $t_{\mathrm{iso}} \approx 1\,\mathrm{fm}$ [32,34,198,199]. Such a short isotropisation time can be explained assuming a strongly coupled quark-gluon plasma [43] and has been reproduced by computing holographic thermalisation processes in gauge-string dualities [200–204]. However, due to the high energy density in heavy ion collisions, the quark-gluon plasma is usually assumed to be weakly coupled because of asymptotic freedom. With this, the question arises: Which processes drive the isotropisation fast enough to obtain an isotropisation time competitive with predictions from strongly coupled approaches or hydrodynamics? First theoretical estimates based on perturbative scattering processes [205, 206] yield too long isotropisation times. They miss one essential aspect of plasma dynamics, which is the development of plasma instabilities. Unstable chromo-electric and chromo-magnetic modes can lead to a fast restoration of momentum space isotropy in the early stages of the quark-gluon plasma [44–46].

In this work we investigate the isotropisation of the quark-gluon plasma via the chromo-Weibel instability. In particular, we are interested in the effect of fermions on the isotropisation process. In order to capture the far from equilibrium real time dynamics of the involved processes, we employ the semi-classical lattice approach to QCD presented in chapter 5. In the weak coupling limit, the colliding nuclei may be described as colour glass condensates. One intrinsic feature of a colour glass condensate is a high population of gauge fields, which justifies a classical approximation of the bosonic degrees of freedom. Additionally, the colour glass condensate effective theory serves as an inspiration for the initial conditions which describe the early stages of a heavy ion collision within the semi-classical approach. Due to the explorative nature of this study, we only simulate in a static system instead of an expanding one. Although the expansion has a large effect on the gauge dynamics, and consequently the isotropisation, a static simulation should be sufficient for a first estimate on the impact of fermions.

6.1 Formation of the quark-gluon plasma

The formation of a quark-gluon plasma in relativistic heavy ion collisions is a dynamic process far from equilibrium. As we discuss in section 6.1.1 the colliding nuclei can be de-

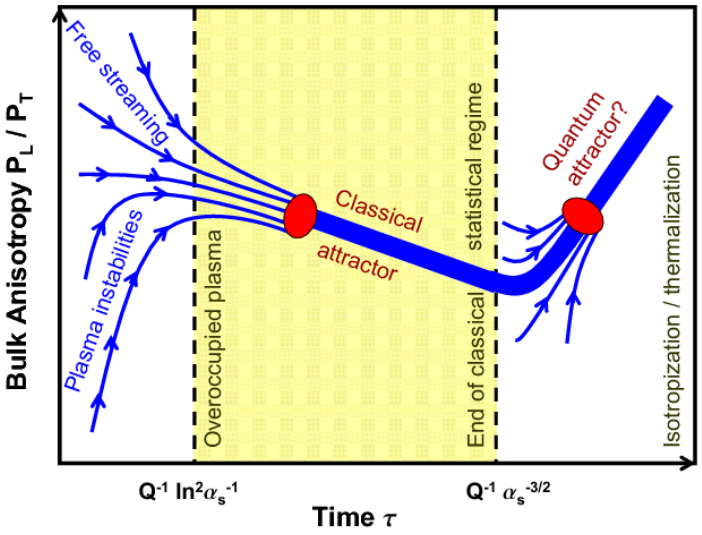

Figure 6.1: Schematic picture of the thermalisation process at weak coupling. The figure shows the ratio of longitudinal over transverse pressure versus longitudinal proper time τ. It indicates the different dynamic regimes discussed in section 6.1. Taken from [207].

scribed in the colour glass condensate framework. The evolution towards a thermalised quark-gluon plasma starts at a time immediately after the collision and is governed by different dynamic regimes. Considering a longitudinally (in z-direction) expanding medium, they are characterised by longitudinal proper time $\tau \equiv \sqrt{(x^0)^2 + z^2}$ and momentum scale Q. The pre-equilibrium stage of a heavy ion collision is believed to consist of four distinct regimes [178, 207] (the mentioned time scales are indicative approximations):

- Strong fields ($0 < Q\,\tau \lesssim 1$): This initial state is described within the colour glass condensate framework.
- Plasma instabilities ($1 \lesssim Q\,\tau \lesssim \log^2(\alpha_s^{-1})$): The anisotropic medium leads to an instability, i.e. the chromo-Weibel instability discussed in section 6.1.2, which in turn isotropises the medium partially.
- Turbulent regime ($\log^2(\alpha_s^{-1}) \lesssim Q\,\tau \lesssim \alpha_s^{-3/2}$): Turbulences drive the system towards a scaling behaviour indicated by an attractor solution.
- Quantum thermalisation ($Q\,\tau \gtrsim \alpha_s^{-3/2}$): Finally, quantum effects become relevant and the classical approximation breaks down.

This thermalisation process is depicted in figure 6.1 in terms of the ratio of longitudinal over transverse pressure. Describing the colliding nuclei as colour glass condensates, the stages towards forming a thermalised quark-gluon plasma are called glasma [63, 208], a contraction of the words “glass” and “plasma”.

In this work we study the first two regimes. We use the semi-classical model of QCD employed in chapter 5 to investigate the isotropisation of the medium formed in heavy

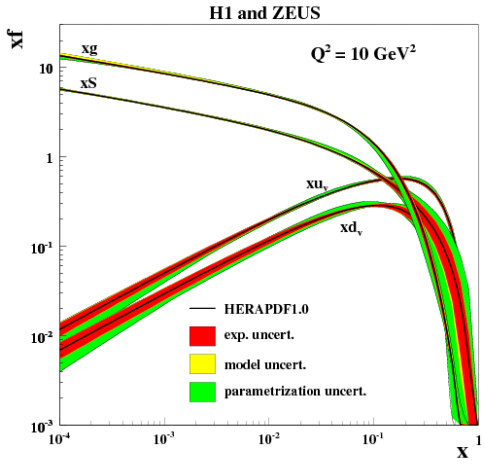

Figure 6.2: Results for the parton distribution function xf versus Bjorken-x from deep inelastic $e^- p$ scattering experiments at HERA [209] with four-momentum transfer $Q^2 = 10\,\mathrm{GeV}^2$.

ion collisions via chromo-Weibel instabilities. We obtain the required initial conditions from the colour glass condensate effective theory.

6.1.1 Colour glass condensate

The first stages of an ultra relativistic heavy ion collision involve dynamics far from equilibrium. Consequently, a first principles description requires a real time treatment of QCD according to equation (2.25), where the initial density matrix consists of two incoming nuclei. Although a full computation in QCD is beyond the scope of our theoretical models, the problem can be approximated by the colour glass condensate effective theory as can be seen in the following consideration. For a more detailed review on the colour glass condensate effective theory refer to e.g. [61–63].

We show results for the parton distribution function in a proton obtained from deep inelastic $e^- p$ scattering experiments at HERA [209] in figure 6.2. The quantity $Q^2 = 10\,\mathrm{GeV}^2$ represents the squared four-momentum transferred in the scattering process, and $x = \frac{Q^2}{2M\nu}$ is the Bjorken-x variable with energy loss ν of the incoming electron, and M the target nucleon mass. As Bjorken-x is the longitudinal momentum fraction carried by the parton, it is a measure of inelasticity of scattering processes and is inversely proportional to the rest frame energy. Thus small x values correspond to deep inelastic scattering processes. This is also the regime for heavy ion collisions. As can be seen in figure 6.2, at small x, the contribution of valence quarks to the parton distribution function xf is negligible compared to the gluonic contribution. Furthermore sea quarks produced from gluon splitting $g \to q\bar{q}$ are suppressed by the coupling α. Hence as an approximation, the colour glass condensate effective theory takes only gluonic fields into account .

Due to non-linear interactions among the gluons, the growth of the gluon distribution is limited. This limit is associated with a saturation momentum Q_s of the gluons, which is proportional to the collision energy. Refer to figure 6.3 for a descriptive explanation. In ultra-relativistic heavy ion collision experiments at RHIC and the LHC, Q_s takes

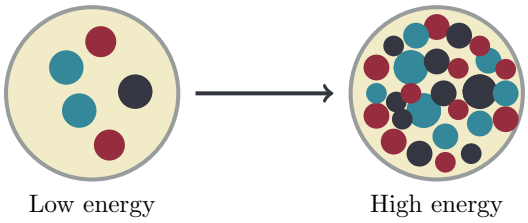

Figure 6.3: Following [61], we descriptively identify the inverse gluon momentum with the size of a gluon. At a given momentum only a finite amount of gluons can be packed into a nucleon. At higher momenta the gluon size becomes smaller and more gluons can be added. Increasing the momentum, at some point their density becomes so large that interactions between them can not be neglected anymore. As a consequence the density saturates. The corresponding gluon momentum is called saturation momentum Q_s.

values of approximately 2 GeV and $2-3$ GeV respectively [210]. Since the saturation momentum is much larger than the QCD scale, $Q_\mathrm{s} \gg \Lambda_\mathrm{QCD} \approx 0.2\,\mathrm{GeV}$, a weak coupling treatment of the saturated gluons inside the colliding nuclei is justified.

Although the interaction strength is weak, the system eludes a perturbative treatment. The high gluon density goes along with a high interaction probability, defined as the relevant parton cross-section times the parton density. Thus the effects of the interaction are amplified by the large gluon density, and a resummation of high density effects becomes necessary. A computation up to order g^2 in the coupling requires a resummation of all tree-level diagrams, which can be performed in classical Yang-Mills theory.

The effective degrees of freedom are the gluonic fields at small x. Due to time dilatation, the nuclei being colour sources can be seen as static. When looking at a heavy ion collision they are described as a colour current of the form

$$J_a^\mu(t, \mathbf{x}_\perp, z) = \delta^{\mu+}\rho_1^a(x_\perp)\delta(x^-) + \delta^{\mu-}\rho_2^a(x_\perp)\delta(x^+), \tag{6.1}$$

where we employ light-cone coordinates defined in appendix A.2.2. The Kronecker-deltas, $\delta^{\mu+}$ and $\delta^{\mu-}$, indicate that the colour charge densities $\rho_m^a(x_\perp)$ of the two nuclei $m \in \{1, 2\}$ are on the light cone. The δ-distributions reflect the Lorentz contraction of the nuclei towards sheets of vanishing width. The colour charges are distributed randomly from event to event. The classical gluonic fields are obtained by solving the Yang-Mills equations in the presence of the two sources

$$D_\mu F^{\mu\nu} = J^\nu. \tag{6.2}$$

In section 6.2.1 the solution of this equation enters our initial conditions regarding the formation of a quark-gluon plasma in heavy ion collisions.

6.1.2 Chromo-Weibel instability

The colour fields existing in the early stages of nucleus-nucleus collision may exhibit instabilities [211–213], which drive the fast isotropisation of the glasma [44–46,205]. One candidate for such an instability is the chromo-Weibel instability. Its occurrence has been investigated in different approaches such as Vlasov-Yang-Mills simulations [47–51],

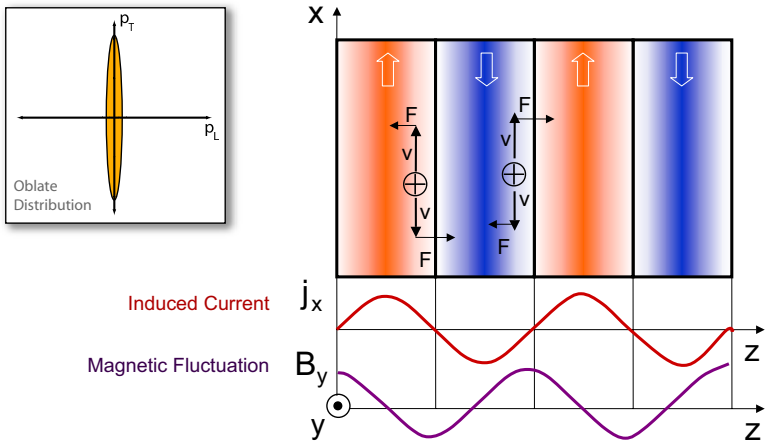

Figure 6.4: Formation of the Weibel instability in a medium with anisotropic momentum distribution. This sketch was first shown by Mrówczyński at Quark Matter 1993. This figure is a revised version made by Strickland. The fluctuating current (6.3) pointing in x-direction generates a magnetic field (6.4) in y-direction, which in turn produces filaments aligned in z-direction. The arrows in the first filament on the left indicate a particle's movement and its change due to the Lorentz force (use Fleming's right-hand rule). Particles moving up ($+\mathbf{e}_x$) are transferred to the left ($-\mathbf{e}_z$), whereas particles moving down ($-\mathbf{e}_x$) are transferred to the right ($+\mathbf{e}_z$), thus enhancing the left and right currents. In turn the increased currents enhance the magnetic fields, leading to the Weibel instability. If one adds charged particles moving in z-direction, their magnetic field would reduce the B_y magnetic field, hence reducing the instability.

classical Yang-Mills simulations [52–60] or analytic studies [214, 215], including both expanding or non-expanding backgrounds.

The mechanism of the chromo-Weibel instability is analogous to the Weibel instability [216] arising in electromagnetic plasmas with anisotropic momentum distribution. Consider the setup of an anisotropic electromagnetic system with a fluctuating current of magnitude j in direction $\mathbf{e}_x$ [217, 218]

$$\mathbf{j}(x) = j\cos(k_z z)\mathbf{e}_x. \tag{6.3}$$

From this and $\nabla \times \mathbf{B}(x) = \mathbf{j}(x)$ follows that a magnetic field in the y-direction emerges

$$\mathbf{B}(x) = \frac{j}{k_z}\sin(k_z z)\mathbf{e}_y. \tag{6.4}$$

As illustrated in figure 6.4, the fluctuating current creates filaments with particles moving in opposite x-directions. The Lorentz force moves particles to their corresponding filaments, thus enhancing the current and consequently the magnetic field. Thus the magnetic Weibel instability appears. Due to the creation of filaments it is also referred to as filamentation instability. This mechanism can be transferred to colour fields and is assumed to occur in the early phases of the quark-gluon plasma, driving isotropisation.

As a consequence, a local momentum space anisotropy in the quark-gluon plasma causes soft transverse modes to grow exponentially. Due to the non-abelian interaction these unstable modes generate longitudinal chromo-electric and chromo-magnetic colour fields, which grow even faster and thus lead to an isotropisation of the system [219]. We

formulate anisotropic initial conditions inspired by the colour glass condensate in order to investigate the isotropisation using a classical real time lattice simulation in the next section 6.2.

6.2 Real time simulations on the lattice

As discussed in the last section, the formation of the quark-gluon plasma is a dynamic process far from equilibrium. The semi-classical lattice approach to QCD established in chapter 5 offers a suitable framework to describe the physical processes in real time. Imposing a colour glass condensate as initial state, the requirements concerning a valid classical description, large gluon occupation numbers as well as weak coupling, are met. At first we establish the framework for a pure bosonic investigation and add fermions in section 6.4. Due to the explorative nature of the inclusion of fermions, we only consider a non-expanding system. However, in contrast to most other works, we account for the full non-abelian gauge group of QCD, SU(3).

During this chapter we distinguish between the longitudinal and transverse dimensions. We identify the former with the z-direction and the latter with the corresponding perpendicular xy-plane. Accordingly, we have the longitudinal lattice spacing a_z and lattice extent N_z as well as the perpendicular values, $a_\perp$ and $N_\perp$. We define transverse and longitudinal displacement vectors by $x_\perp = (x, y)$ and $x_z = z$, respectively. A function depending on only one of these displacements vector is meant to be kept constant along the absent direction, e.g. $f(x_\perp)$ is constant along the longitudinal z-direction.

We review in section 6.2.1 initial conditions inspired by the colour glass condensate which describe our initial state. Section 6.2.2 deals with the simulation parameters. In particular we explain how to obtain dimensional physical quantities. We introduce observables relevant for isotropisation and the appearance of a chromo-Weibel instability in section 6.2.3. In particular we introduce a gauge invariant spectral decomposition, which avoids numerically costly gauge fixing.

6.2.1 Colour glass condensate inspired initial conditions on the lattice

Describing the evolution of the non-equilibrium system produced in ultra-relativistic heavy ion collision in the classical-statistical model requires us to specify the initial conditions. As we have learnt in section 6.1.1, this initial state can be treated as a colour glass condensate. In this approximation, the colliding nuclei are colour sources, see equation (6.1), which are distributed randomly from event to event. According to the McLerran-Venugopalan model [220–222] they have a Gaussian distribution

$$\left\langle \rho_m^a(x_\perp)\rho_n^b(y_\perp)\right\rangle = g^4\mu^2 a_\perp^2 \delta_{mn}\delta^{ab}\delta(x_\perp - y_\perp). \tag{6.5}$$

The variance is closely related to the saturation momentum, $g^2\mu \approx Q_\mathrm{s}$. The quantity $\mu^2 \sim A^{1/3}\,\mathrm{fm}^{-2}$ is the colour charge squared per unit area in one of the colliding nuclei with atomic number A. Since it is the only dimensionful parameter in the initial conditions, we use it to set the scale in our simulations, see section 6.2.2.

Imposing the Gaussian distribution of the colour sources on the current (6.1) allows us to solve the equation of motion (6.2). The solutions are chromo-electric and chromomagnetic fields describing the colour glass condensate state to leading order. We use

these fields as initial conditions for our semi-classical model. Following [223] they can be transferred to the lattice.

On the lattice the chromo-magnetic fields U_i and chromo-electric fields E_i are constructed from intermediate quantities U_i^m with $m = \{1, 2\}$ for each nuclei. Starting from the colour sources ρ_m^a they are computed by:

$$\Delta_{\mathrm{L}} \Lambda_m^a(x_\perp) = -\rho_m^a(x_\perp), \tag{6.6a}$$

$$V^m(x_\perp) = \exp\left(\mathrm{i}\Lambda_m(x_\perp)\right), \tag{6.6b}$$

$$U_i^m(x_\perp) = V^m(x_\perp) V^m(x_\perp + \hat{i}), \qquad i = x, y, \tag{6.6c}$$

where the colour sources ρ_m^a are sampled from equation (6.5). The shorthand notation $U_i^m(x_\perp)$ means that $U_i^m(x)$ is kept constant along the z-direction. Equation (6.6a) is the Poisson equation with the lattice Laplacian in the transverse plane

$$\Delta_{\mathrm{L}} \Lambda(x_\perp) = \sum_{i=x,y} \Big(\Lambda(x_\perp + \hat{i}) - 2\Lambda(x_\perp) + \Lambda(x_\perp - \hat{i}) \Big). \tag{6.7}$$

We discuss its numeric solution in appendix E.1. Fukushima suggests [60] a momentum cutoff of 3.4 GeV to be introduced, since the initial energy density is ultraviolet divergent. Because of that, we drop modes with $k_\perp > 3.4\,\mathrm{GeV}$ when solving the Poisson equation.

In the non-expanding case the transverse links are constructed from

$$U_i(x_\perp) = \Big(U_i^{(1)}(x_\perp) + U_i^{(2)}(x_\perp) \Big) \Big(U_i^{(1)\dagger}(x_\perp) + U_i^{(2)\dagger}(x_\perp) \Big)^{-1}, \qquad i = x, y, \tag{6.8}$$

where we project the result back to the group SU(3). A summation over i is not implied. The longitudinal link is given by

$$U_z(x) = \mathbb{1}_{3\times 3} \tag{6.9}$$

and the longitudinal chromo-electric field by

$$\begin{aligned} E_z^a(x_\perp) = -\frac{\mathrm{i}}{4} \sum_{i=x,y} \mathrm{Re}\,\mathrm{Tr} \Big\{ T^a \Big(& \left(U_i(x_\perp) - \mathbb{1}_{3\times 3}\right) \Big(U_i^{(1)\dagger}(x_\perp) + U_i^{(2)\dagger}(x_\perp) \Big) \\ & + \Big(U_i^\dagger(x_\perp - \hat{i}) - \mathbb{1}_{3\times 3} \Big) \\ & \times \Big(U_i^{(2)\dagger}(x_\perp - \hat{i}) - U_i^{(1)\dagger}(x_\perp - \hat{i}) \Big) - (\mathrm{h.c.}) \Big) \Big\}. \end{aligned} \tag{6.10}$$

The transverse chromo-electric fields are

$$E_i^a(x) = 0, \qquad i = x, y. \tag{6.11}$$

More realistic initial conditions for a heavy ion collision are obtained by adding fluctuations to the recently defined background [54, 55, 60]. This corresponds to violating boost invariance of an expanding medium as well as smearing the colour sources (6.5) in $x^\pm$-direction instead of using the idealised δ-distributions. The fluctuations δE_i are added on top of the background initial conditions for the chromo-electric field

$$E_i(x) \to E_i(x) + \delta E_i(x). \tag{6.12}$$

The transverse fields, $i = x, y$, are constructed by

$$\delta E_i^a(x) = (f(z) - f(z - \hat{z}))\, \xi_i^a(x_\perp), \tag{6.13a}$$

$$\left\langle \xi_i^a(x_\perp) \xi_j^b(y_\perp) \right\rangle = \delta^{ab} \delta_{ij} \delta(x_\perp - y_\perp), \tag{6.13b}$$

$$f(z) = \Delta \cos\left(\frac{2\pi z}{N_z}\right), \tag{6.13c}$$

where the seed Δ controls the magnitude of the fluctuations. Although it is in principle determined by the colour glass condensate initial conditions, there is no theoretical prediction for its value. We will vary it in our simulations. The longitudinal component is created so that it fulfils Gauss law (5.42d) without fermions

$$\delta E_z(x) = -f(z) \sum_{i=x,y} \Big(\xi_i(x_\perp) - U_i^\dagger(x_\perp - \hat{i}) \xi_i(x_\perp - \hat{i}) U_i(x_\perp - \hat{i}) \Big). \tag{6.14}$$

In contrast to the bosonic initialisation in thermal equilibrium, see section 5.4.1, we do not need to apply an algorithm enforcing Gauss law, since it is fulfilled by construction and continues to be so due to its conservation.

The presented initial conditions are anisotropic and as we see in section 6.3 lead to formation of a chromo-Weibel instability in our classical real time approach.

6.2.2 Parameters and setting the scale

For real time simulations in non-equilibrium, the scale of the system is set by the initial conditions. Regarding our initial conditions from section 6.2.1 the only dimensional scale introduced is $g^2\mu$, where one assumes for simulations of collisions at RHIC [56,224]

$$g^2\mu = g^2 \frac{\mu^{\mathrm{L}}}{a_\perp} \approx 2\,\mathrm{GeV} \tag{6.15}$$

with $g = 2$ and the dimensionless quantity $\mu^{\mathrm{L}} \equiv a_\perp \mu$. Additionally, the lattice size should correspond to the radius $R_{\mathrm{A}} = 1.2 A^{1/3}\,\mathrm{fm} \approx 7\,\mathrm{fm}$ of an Au atom with atomic number $A = 197$, $\pi R_{\mathrm{A}}^2 = N_\perp^2 a_\perp^2$. Combining both scales gives

$$g^2 \mu^{\mathrm{L}} N_\perp = 120. \tag{6.16}$$

In our lattice simulations we set the spatial lattice extents $N_\perp$ and N_z first. Then we use equation (6.16) to determine the value of $g^2\mu^{\mathrm{L}} = \frac{120}{N_\perp}$. The transverse lattice spacing follows from equation (6.15)

$$a_\perp = \frac{g^2 \mu^{\mathrm{L}}}{2\,\mathrm{GeV}}, \tag{6.17}$$

where the conversion from energy to length can be performed according to appendix A.1. Following the literature we specify the time in units of $g^2\mu$. Since we simulate in a static box, our lattice is isotropic in spatial directions, implying $a_\perp = a_z$.

Further parameters entering our simulations are the anisotropy ξ relating temporal and spatial lattice spacings, the longitudinal lattice extent N_z and the magnitude of fluctuations Δ. Fulfilling the Courant condition (5.43) we choose the anisotropy to be $\xi = 20$. We show in appendix E.2 that our results are independent of variations of this parameter. We choose the longitudinal lattice extent larger than the spatial one in order to accommodate as many longitudinal momenta as possible.

6.2.3 Observables

In this section we introduce observables in order to investigate the isotropisation of the quark-gluon plasma as well as the appearance of a chromo-Weibel instability. Therefore it is favourable to obtain separate information on the longitudinal and transverse directions. In analogy to (5.40) we introduce the chromo-electric and chromo-magnetic energies

$$H_i^E(t,\mathbf{x}) = \frac{\beta}{2N_c}\,\mathrm{Re}\,\mathrm{Tr}\,(E_i(x)E_i(x))\,, \tag{6.18a}$$

$$H_i^B(t,\mathbf{x}) = \beta \sum_{\substack{j<k\\ j,k\neq i}} \Big\{1 - \frac{1}{N_c}\,\mathrm{Re}\,\mathrm{Tr}\,(U_{jk}(x))\Big\}, \tag{6.18b}$$

which define the transverse and longitudinal energy densities regarding the chromo-electric field

$$\epsilon_{E_\perp}(t) = \frac{1}{N_\perp^2 N_z}\sum_{\mathbf{x}}\sum_{i=x,y} H_i^E(x), \tag{6.19a}$$

$$\epsilon_{E_z}(t) = \frac{1}{N_\perp^2 N_z}\sum_{\mathbf{x}} H_z^E(x) \tag{6.19b}$$

and the chromo-magnetic field

$$\epsilon_{B_\perp}(t) = \frac{1}{N_\perp^2 N_z}\sum_{\mathbf{x}}\sum_{i=x,y} H_i^B(x), \tag{6.20a}$$

$$\epsilon_{B_z}(t) = \frac{1}{N_\perp^2 N_z}\sum_{\mathbf{x}} H_z^B(x). \tag{6.20b}$$

The composite energies are obtained from

$$\epsilon_E(t) = \epsilon_{E_\perp}(t) + \epsilon_{E_z}(t), \tag{6.21a}$$

$$\epsilon_B(t) = \epsilon_{B_\perp}(t) + \epsilon_{B_z}(t), \tag{6.21b}$$

$$\epsilon_{\mathrm{tot}}(t) = \epsilon_E(t) + \epsilon_B(t). \tag{6.21c}$$

From the spatial diagonal elements of the energy-momentum tensor T_{ii} we find the transverse and longitudinal pressure [55]

$$P_{\mathrm{T}}(x) = -\frac{1}{2}\left(T_x^x(x) + T_y^y(x)\right), \tag{6.22a}$$

$$P_{\mathrm{L}}(x) = -T_z^z(x). \tag{6.22b}$$

Their ratio $\frac{P_{\mathrm{L}}}{P_{\mathrm{T}}}$ is a measure for the system's isotropisation. Since we only consider an anisotropic distribution of the bosonic degrees of freedom, see section 6.2.1, we do not include the fermionic contribution to the pressure. Employing explicitly the energy-momentum tensor of Yang-Mills theory (4.24) we find for the transverse and longitudinal pressure in the continuum

$$P_{\mathrm{T}}(t) = \epsilon_{E_z}(t) + \epsilon_{B_z}(t), \tag{6.23a}$$

$$P_{\mathrm{L}}(t) = \epsilon_{E_\perp}(t) - \epsilon_{E_z}(t) + \epsilon_{B_\perp}(t) - \epsilon_{B_z}(t). \tag{6.23b}$$

Their discretisation follows from the lattice versions (6.19) and (6.20) of the energy densities.

An effect of the chromo-Weibel instability is a population of higher momentum modes, which can be investigated by computing the spectral decomposition of the chromo-electric field. Due to the instability being connected to a rapid growth of modes in longitudinal direction, one computes the spectrum as a function of the longitudinal momentum k_z, while the other momentum modes k_x and k_y are averaged. The usual approach to defining the spectrum is based on the Fourier transform of the chromo-electric field

$$E_i(t, \mathbf{k}) = \sum_{\mathbf{x}} \mathrm{e}^{-\mathrm{i}\mathbf{k}\mathbf{x}} E_i(x) \tag{6.24}$$

and reads

$$\Sigma(t, k_z) = \frac{\beta}{2N_c N_\perp^2} \sum_{k_x, k_y} \sum_i \mathrm{Re}\,\mathrm{Tr}\left(E_i(t, \mathbf{k}) E_i^\dagger(t, \mathbf{k})\right). \tag{6.25}$$

This definition does not constitute a gauge invariant quantity and one has to fix the gauge, e.g. by applying Coulomb gauge (5.41). The gauge fixing routine is numerically expensive, especially in the case of SU(3). Furthermore the choice of gauge is arbitrary restricting the significance of the observables. Because of that we give an alternative definition for the spectral decomposition, which is gauge invariant. It is based on the Fourier transform of the energy

$$H^E(t, \mathbf{k}) = \sum_{\mathbf{x}} \mathrm{e}^{-\mathrm{i}\mathbf{k}\mathbf{x}} \sum_i H_i^E(x) \tag{6.26}$$

and is given by

$$\Sigma^H(t, k_z) = \frac{1}{N_\perp^2} \sum_{k_x, k_y} \left|H^E(t, \mathbf{k})\right|. \tag{6.27}$$

We investigate both approaches in section 6.3.1. Since the connection between the links and the chromo-magnetic fields B is non-trivial [56], especially for SU(3), we only consider the spectral decomposition of chromo-electric fields.

6.3 Classical SU(3) Yang-Mills theory

We investigate the evolution of observables defined in the previous section in the framework of classical SU(3) Yang-Mills theory on the lattice. From a physical point of view one expects simulations of the non-equilibrium stage to be highly sensitive to the chosen initial conditions. We use initial conditions inspired by the colour glass condensate effective theory. We compute all observables by a Monte Carlo sampling according to (3.23) with an ensemble size of N_{ens} configurations. Since all statistical errors are below 1 %, we do not show any error bars in our plots.

We investigate our gauge invariant implementation of the spectral decomposition in section 6.3.1. Section 6.3.2 deals with observables indicating the process of isotropisation and section 6.3.3 with the emergence of a chromo-Weibel instability.

$g^2\mu^{\mathrm{L}}$	$N_\perp$	N_z	ξ	Δ	N_{ens}	$\mathrm{N}_{\mathrm{time}}$
3.75	32	96	20	0.4	5	8000

Table 6.1: Simulation parameters for the investigation of the gauge invariant and gauge dependent spectral decomposition.

6.3.1 Gauge invariant and gauge dependent spectral decomposition

In section 6.2.3 we proposed two approaches to compute the spectral decomposition of the chromo-electric field. Whereas the first one (6.25) is based on the product of chromo-electric fields in momentum space $E_i(t,k_z)E_i^\dagger(t,k_z)$, the second one (6.27) is based on the chromo-electric energy (6.18a) in momentum space. Thus the latter one constitutes a gauge invariant object. In the following we investigate their differences by simulations with parameters given in table 6.1. Concerning the gauge dependent observable (6.25) we fix the gauge to Coulomb gauge by the algorithm explained in section 5.3.2.

The spectral decomposition for both observables is shown in figure 6.5. We give a physical interpretation of the results in section 6.3.3. Focusing on the differences between the two observables, we note that concerning the observable $\Sigma(t,k_z)$ the hard momentum modes are populated more quickly than $\Sigma^H(t,k_z)$. This can be explained by the additional peak in the ultraviolet region of $\Sigma^(t,k_z)$ at initial time. It is an artefact of the gauge fixing procedure. Another difference is that at initial time, $\Sigma^H(t,k_z)$ has three soft occupied modes $a_\sigma k_z = 0,1,2$, whereas $\Sigma(t,k_z)$ only has two, $a_\sigma k_z = 0,1$.

All in all, the two approaches give similar results. For all further investigations in this chapter, we choose the gauge invariant observable Σ^H. It does not necessitate gauge fixing, which consumes a large amount of computation time as shown in figure 5.6 for the Coulomb gauge fixing procedure given in section 5.3.2. Furthermore gauge invariant observables give a cleaner physical interpretation, since they do not include any ambiguities such as the choice of gauge or Gribov copies, see section 5.2.4.

6.3.2 Isotropisation

In order to learn something about the isotropisation of the created medium we study the time evolution of the energy densities (6.21) as well as transverse and longitudinal pressures (6.23). We initialise the chromo-electric and chromo-magnetic fields according to the colour glass condensate inspired initial conditions presented in section 6.2.1. In the following we discuss the results of the simulation with parameters given in table 6.2.

Figure 6.6 shows the results for the energy densities. At initial time the chromo-electric energy density dominates. Over time energy is transferred from the chromo-electric field to the chromo-magnetic one until both carry the same amount of energy at approximately $a_\tau \Delta t \approx 700$. The total energy density mildly fluctuates until a balance is reached. The total energy of the system is conserved as should be the case in a finite box.

The longitudinal and transverse pressure and their ratio are plotted in figure 6.7. The upper plot shows the two pressure components separately. As discussed in section 6.1.1 the state immediately after the collision can be described as a colour glass condensate.

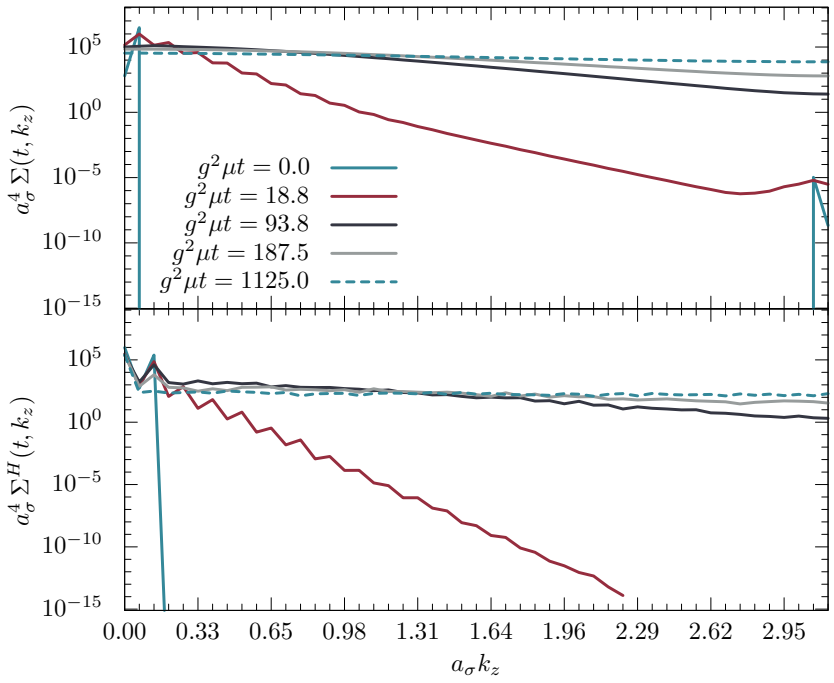

Figure 6.5: Spectral decomposition of the chromo-electric field at different times. The lower plot shows the gauge invariant definition (6.27), whereas the upper plot shows the gauge dependent one (6.25). Simulation parameters are given in table 6.1.

$g^2\mu^{\mathrm{L}}$	$N_\perp$	N_z	ξ	Δ	N_{ens}	$\mathrm{N_{time}}$
3.0	40	126	20	0.4	15	8000

Table 6.2: Simulation parameters for our run with the largest lattice extents.

The corresponding energy-momentum tensor to leading order is given by [208]

$$T^{\mu\nu}_{\mathrm{CGC,LO}} = \mathrm{diag}\,(\epsilon, \epsilon, \epsilon, -\epsilon)\,, \tag{6.28}$$

which indicates a longitudinal pressure opposite to the transverse one, $P_{\mathrm{L}} = -P_{\mathrm{T}}$. The negative pressure reflects the force between the two colliding nuclei. Our simulation exactly reproduces this initial condition. Due to exchange of energy between the longitudinal and transverse field components the corresponding pressures approach each other. When $P_{\mathrm{L}} = P_{\mathrm{T}}$, the system is completely isotropised. However, studies in viscous relativistic hydrodynamics [30, 120, 225–230] and AdS/CFT correspondence [204, 231, 232] suggest that hydrodynamic models are already applicable at a pressure ratio of $\frac{P_{\mathrm{L}}}{P_{\mathrm{T}}} \approx 0.7$. Therefore in the following we describe the system as isotropised with a pressure ratio of $\frac{P_{\mathrm{L}}}{P_{\mathrm{T}}} \approx 0.7$ and call the time it takes, isotropisation time t_{iso}. We plot the ratio $\frac{P_{\mathrm{L}}}{P_{\mathrm{T}}}$ obtained from our simulation in the lower part of figure 6.7. The peak at time $g^2\mu t \approx 2.3$ is followed by an oscillating phase until the system isotropises. The oscillating behaviour of the pressure originates from turbulent pattern formation and diffusion [60]. Note that the oscillating pressure corresponds to a fast time component in the equation of state and thus does not allow an application of hydrodynamics. An anisotropy of $\frac{P_{\mathrm{L}}}{P_{\mathrm{T}}} \approx 0.7$

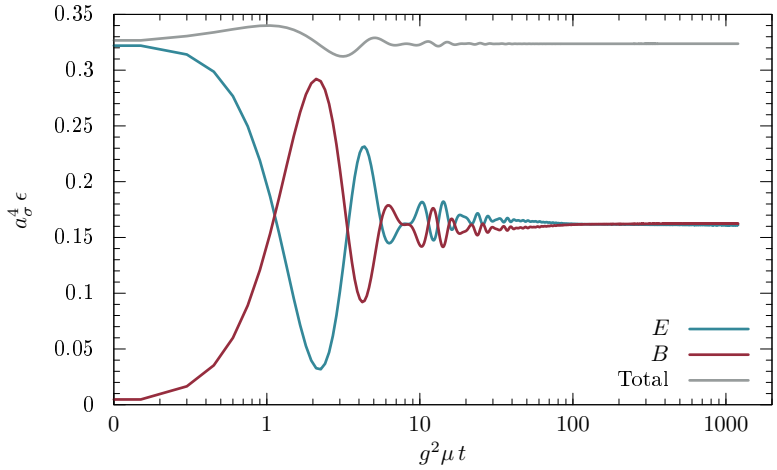

Figure 6.6: Energy densities of the bosonic fields from the run with parameters given in table 6.2. Chromo-electric and chromo-magnetic fields exchange energy until the system is in balance. The total energy density is conserved up to small fluctuations.

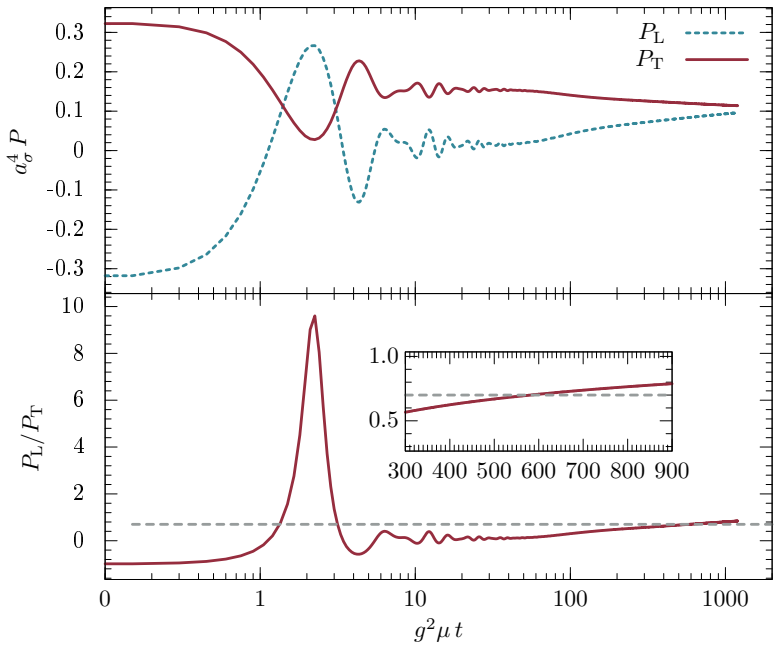

Figure 6.7: Longitudinal P_L and transverse pressure P_T versus time from the simulation with parameters given in table 6.2. The lower plot shows the ratio of both pressures. We say that isotropisation is reached, when the ratio takes a value $\frac{P_\mathrm{L}}{P_\mathrm{T}} \approx 0.7$, which is indicated by the grey line. Its intersection with the curve is enlarged in the embedded plot.

is reached at time step $g^2\mu t \approx 580.8$. Following section 6.2.2 this corresponds to an isotropisation time of $t_{\text{iso}} \approx 57\,\text{fm}$, which is larger than the prediction of hydrodynamics, $t_{\text{iso}} \approx 1\,\text{fm}$. We reach a smaller isotropisation time by increasing the seed Δ.

We investigate the dependence on the fluctuation seed Δ by means of the ratio of longitudinal over transverse pressure. We present selected results of simulations with parameters given in table 6.3 in figure 6.8. To guide the eye we draw a straight line at $\frac{P_\text{L}}{P_\text{T}} = 0.7$ indicating isotropisation. Within the investigated range, all seeds give the same overall behaviour of $\frac{P_\text{L}}{P_\text{T}}$. Due to the initial conditions the ratio starts from $\frac{P_\text{L}}{P_\text{T}} = -1$ and isotropises at some point. In between, the curve has one dominant peak at $g^2\mu t \approx 3$ and oscillatory behaviour afterwards. The amplitude of the peak takes its maximum value for $\Delta = 0.3$ and decreases for higher or lower seeds. Increasing the seed the oscillation decreases and the system isotropises faster until the seed is $\Delta > 1$, when the isotropisation time grows again. Using the seed $\Delta = 1.5$ the initial peak is almost gone, and no oscillation occurs. Since the seed determines the initial energy density of the fluctuations, the fluctuations exceed the background and the initial condition does not reflect the correct colour glass condensate initial state anymore. The isotropisation times are listed in table 6.4.

An isotropisation time of $t_{\text{iso}} \approx 9.3\,\text{fm}$ for $\Delta = 0.7$ is comparable to the prediction of Fukushima $t_{\text{iso}} \approx 8\,\text{fm}$ [60] employing same initial conditions but simulating with colour symmetry SU(2). However, his results are computed with a seed of $\Delta = 0.2$. Thus our SU(3) simulation requires a larger seed to achieve isotropy in a similar time. The overall dynamics of the pressure ratio show close resemblance to our results.

As we check in appendix E.2 discretisation artefacts caused by the finite volume or time discretisation do not have an effect on our simulations. However, when it comes to the spectral decomposition of the fields, which we discuss in the next section, it is favourable to have larger lattices accommodating more momenta.

6.3.3 Emergence of a chromo-Weibel instability

The growth of the ratio of longitudinal over transverse pressure towards isotropy is caused by a chromo-Weibel instability. In this section we show evidence that the fields exhibit such an instability.

As discussed in section 6.1.2 a requirement for the chromo-Weibel instability is a fluctuating current, which is incorporated in our anisotropic initial conditions. Figure 6.9 shows the ratio of longitudinal over transverse pressure for a small seed $\Delta = 0.05$ compared to a vanishing seed $\Delta = 0$ which excludes fluctuations altogether. Without fluctuations no instability sets in and the longitudinal pressure approaches zero after the oscillatory phase.

A further effect of the chromo-Weibel instability is that harder modes get populated during evolution in time. We show the gauge invariant spectral decomposition of the chromo-electric energy density (6.27) in figure 6.10 at different times. Starting from soft modes $a_\sigma k_z = 0, 1$ the population of higher modes during the evolution is clearly recognisable.

Plotting the chromo-electric and chromo-magnetic energies (6.18a and 6.18b) in position space, we can even see the filaments created by the chromo-Weibel instability. Figures 6.11, 6.12 and 6.13 show the evolution of the energy of the field components

Run	$g^2\mu^{\mathrm{L}}$	$N_\perp$	N_z	ξ	Δ	N_{ens}	$\mathrm{N}_{\mathrm{time}}$
i	3.75	32	96	20	0.05, 0.1	30	20000
ii	3.75	32	96	20	0.2, 0.3	30	12000
iii	3.75	32	96	20	0.4	30	8000
iv	3.75	32	96	20	0.5, 0.7, 0.8, 0.9, 1.0, 1.5	30	6000

Table 6.3: Simulation parameters used when studying dependence on the fluctuation seed Δ. Since the value of Δ influences the isotropisation time, we adapt the number of time steps.

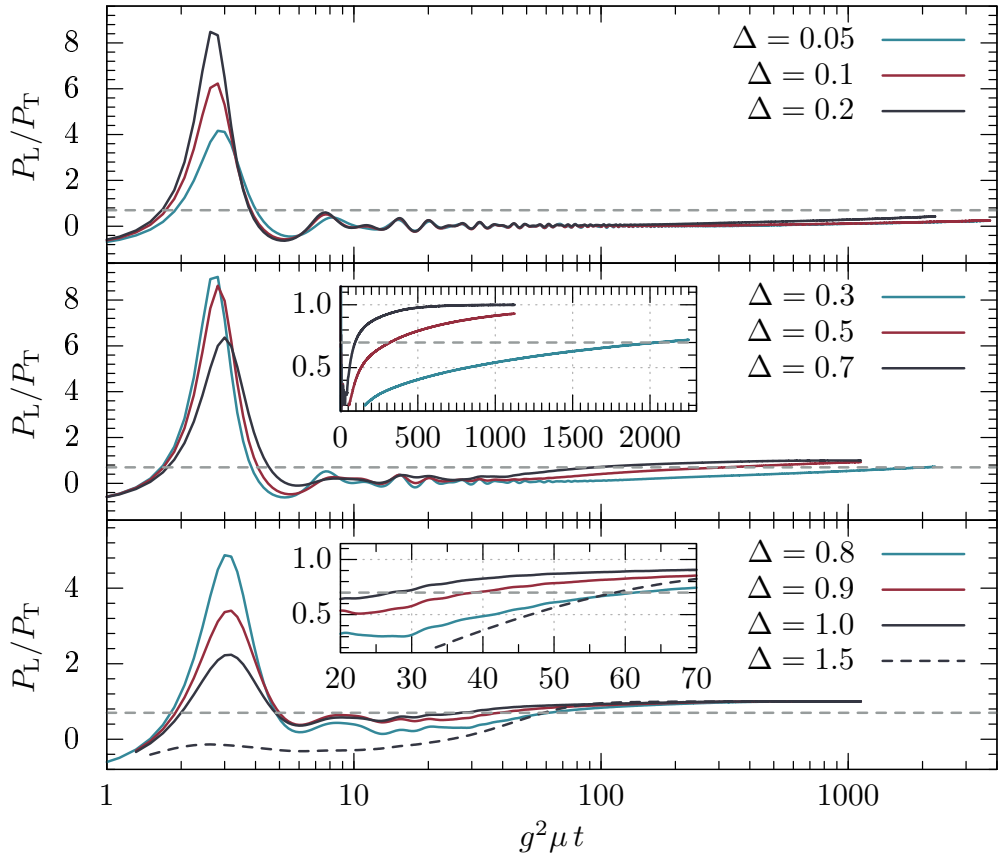

Figure 6.8: Ratio of longitudinal over transverse pressure at different fluctuation seeds Δ from selected runs of table 6.3. The grey line indicates a ratio of $\frac{P_{\mathrm{L}}}{P_{\mathrm{T}}} = 0.7$. Its intersection with the curves is enlarged in the embedded plots.

Δ	0.3	0.4	0.5	0.7	0.8	0.9	1.0	1.5
t_{iso} [fm]	202.3	72.1	31.5	9.3	6.1	3.8	2.7	5.8

Table 6.4: Isotropisation time from ratio of longitudinal over transverse pressure of $\frac{P_{\mathrm{L}}}{P_{\mathrm{T}}} \approx 0.7$ for different fluctuation seeds Δ. With values $\Delta \in \{0.05, 0.1, 0.2\}$, no isotropisation was reached within the limited simulation time.

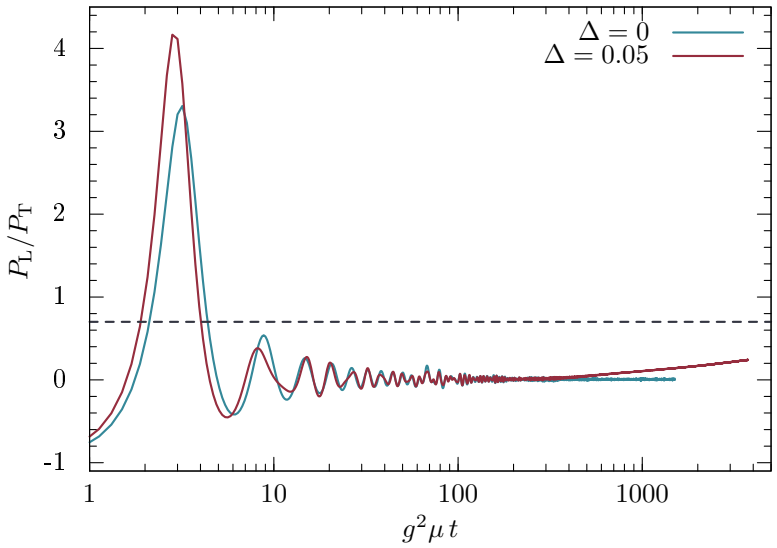

Figure 6.9: Ratio of longitudinal over transverse pressure for vanishing and small seed Δ. The other simulation parameters are given as (i) in table 6.3.

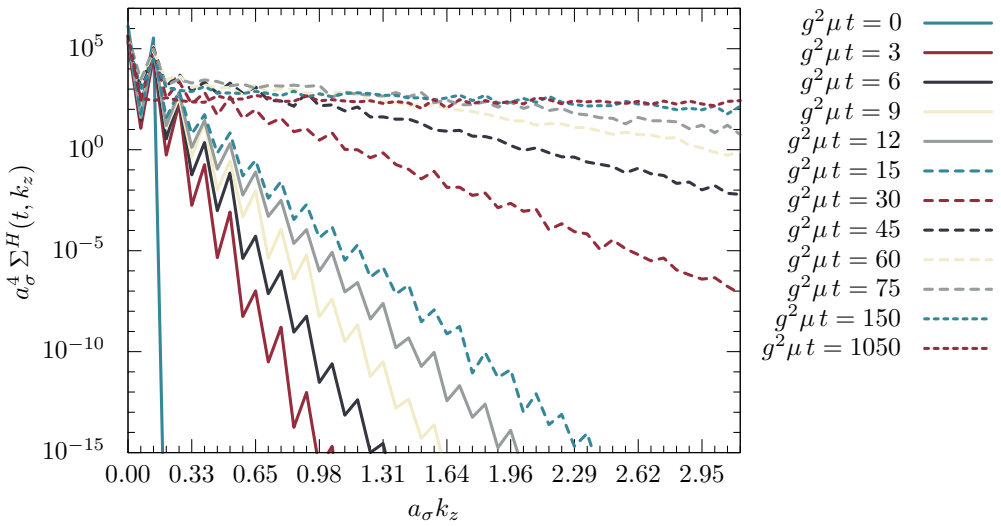

Figure 6.10: Population of momentum modes during evolution in time indicated by the gauge invariant spectral decomposition of the chromo-electric energy density. Every tick on the x-axis corresponds to one momentum mode.

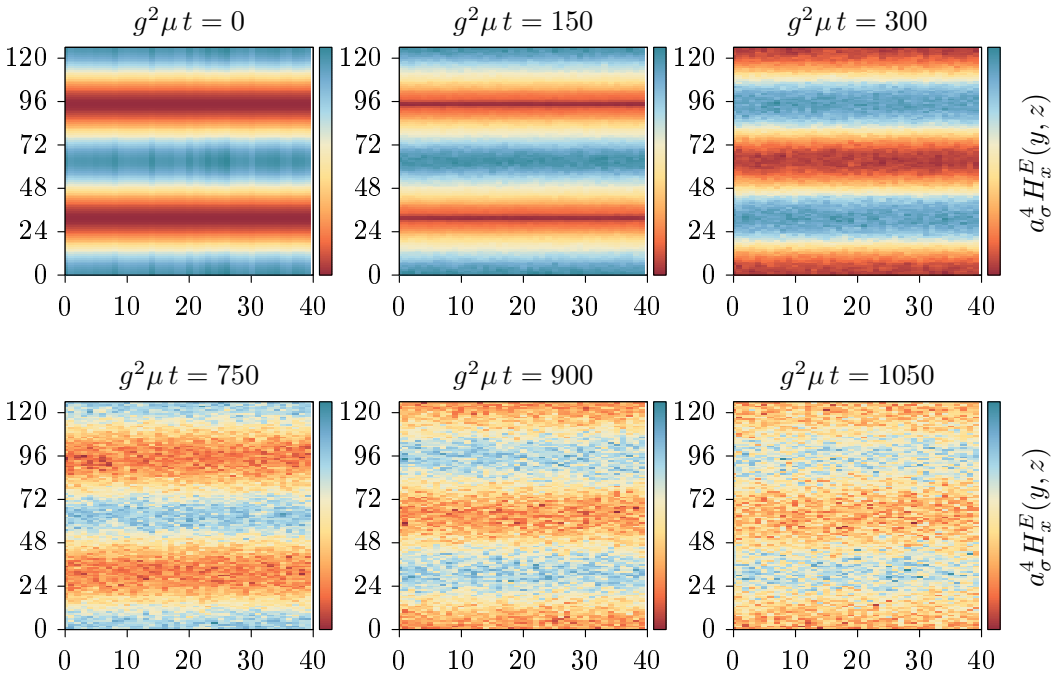

Figure 6.11: Energy of the field component E_x in the yz-plane at different times. The vertical axis denotes the z-direction.

$E_x(x)$, $B_y(x)$ and $E_z(x)$, respectively. We illustrate the amplitude of the energy in a plane transverse to the direction of the field component, e.g. in figure 6.11 we plot $E_x(x)$ in the yz-plane. We average over the remaining direction.

The fluctuating current (6.3) causing the chromo-Weibel instability is given by imposing fluctuations (6.13c) on our initial conditions. The current creates filaments in the xz and the yz-plane, which dissolve in time. No filaments arise in the xy-plane as shown in figure 6.13.

6.4 Semi-classical QCD

Finally, we investigate the effect of fermions on the isotropisation process. We initialise the bosonic fields according to the colour glass condensate inspired initial conditions given in section 6.2.1 as we have done in the last section. We then add vacuum fermions initialised by equation (5.25) to the dynamics, and solve the full set of equations of motion (5.42). Since the colour charge of vacuum fermions does not affect the colour fields at the initial time, we correct the fermionic current in Gauss law (5.42d) by a vacuum subtraction analogous to the energy density (5.62). Thus Gauss law is fulfilled at initial time. During the evolution it is only violated by numeric rounding errors, which are much smaller than the statistic errors.

The simulation parameters are given in table 6.5. For comparison we perform pure bosonic SU(3) simulations based on the same parameters. Investigating a system far from equilibrium, our simulations do not include a non-physical thermalisation phase. Because of that, the heavy fluctuations encountered by including a Wilson term, see for

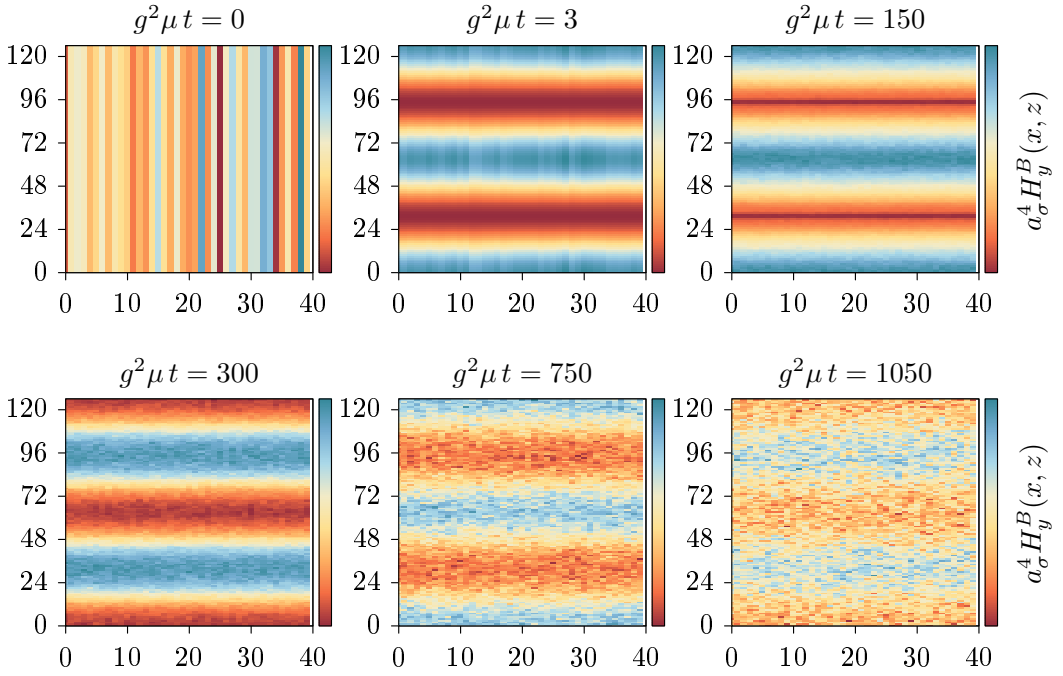

Figure 6.12: Energy of the field component B_y in the xz-plane at different times. The vertical axis denotes the z-direction. The pattern at time $a_\tau \Delta t = 0$ originates from the initial conditions.

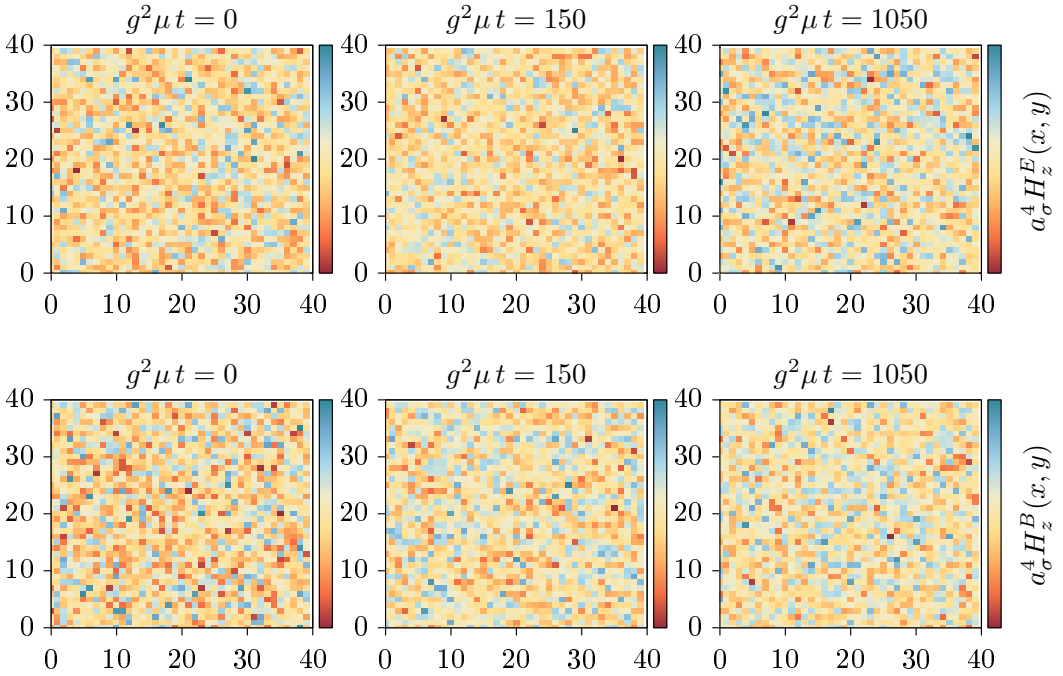

Figure 6.13: Energy of the field component E_z in the xy-plane in the upper plots and of the field component B_z in the xy-plane in the lower plots. The vertical axis denotes the y-direction. No filaments arise during the whole evolution.

$g^2\mu^{\mathrm{L}}$	$N_\perp$	N_z	ξ	Δ	N_{ens}	$\mathrm{N}_{\mathrm{time}}$	N_{e}	$a_\sigma m$	$a_\sigma T$	r
3.75	32	96	20	0.7	5	8000	50	0	0	0

Table 6.5: Simulation parameters for a run including fermions. As a comparison we use the same parameters in a pure bosonic SU(3) simulation ($N_{\mathrm{e}} = 0$).

instance figure 5.18, present a severe problem, which we avoid by temporarily neglecting the Wilson term. Analogous to the other sections we omit error bars below 1 % in the plots.

We show results for the evolution of the energy densities in figure 6.14. The upper plot illustrates the evolution in the pure bosonic case, whereas the lower plot includes fermions. The oscillating behaviour of the chromo-electric and chromo-magnetic fields is similar in both cases. However, in the full system, energy is successively transferred from the bosonic fields to the fermions. While the bosonic fields are strongly oscillating, $0.5 \lesssim g^2\mu t \lesssim 6$, only a small amount of energy is shifted. At later times the oscillation amplitude becomes smaller and the energy transfer increases. The fermionic energy density saturates at $g^2\mu t \approx 300$, when almost the entire bosonic energy has been shifted to the fermions. Using a logarithmic abscissa gives the impression that the fermionic energy density is negative during the first time steps. Indeed it is only negative at one time step ($\Delta t = 1$), which is a consequence of the numeric implementation and should be avoidable by using a smaller temporal lattice spacing.

Next we compute the isotropisation time for a system including fermions. We plot the pressure ratio $\frac{P_{\mathrm{L}}}{P_{\mathrm{T}}}$ in figure 6.15 and compare it to the corresponding pure bosonic run. We find that the initial peak has a larger amplitude and occurs earlier in time. Furthermore the subsequent oscillations have a larger frequency, which is directly connected to the additional oscillations in the energy densities, see figure 6.14. A comparison between the isotropisation times in the pure bosonic system, $t_{\mathrm{iso}} \approx 9.3\,\mathrm{fm}$, and the system including fermions, $t_{\mathrm{iso}} \approx 13.2\,\mathrm{fm}$, shows that the composite system isotropises slower.

Last but not least, we compare the spectral decomposition of the chromo-electric energy density from an evolution including fermions with a pure bosonic evolution in figure 6.16. The agreement of the initial modes shows that our inclusion of fermions does not modify the anisotropic initial conditions. However, we find a rapid occupation of the full spectrum in the case including fermions. The spectrum is already filled up after a time $g^2\mu t = 4$, whereas it takes a time $g^2\mu t = 112$ in the pure bosonic case. Due to the energy shift from bosons to fermions in the fermionic system, the final spectral amplitude is smaller.

6.5 Future research perspectives

First of all, the heavy fluctuations in the fermionic energy density caused by the Wilson term have to be removed. Reducing the temporal lattice spacing could solve the problem. However, being interested in the dynamics' late time behaviour, simulations get numerically costly with a smaller temporal lattice spacing. Use of an adaptive step size method [149] avoids this problem.

The next important step is to account for the mainly longitudinal expansion of the

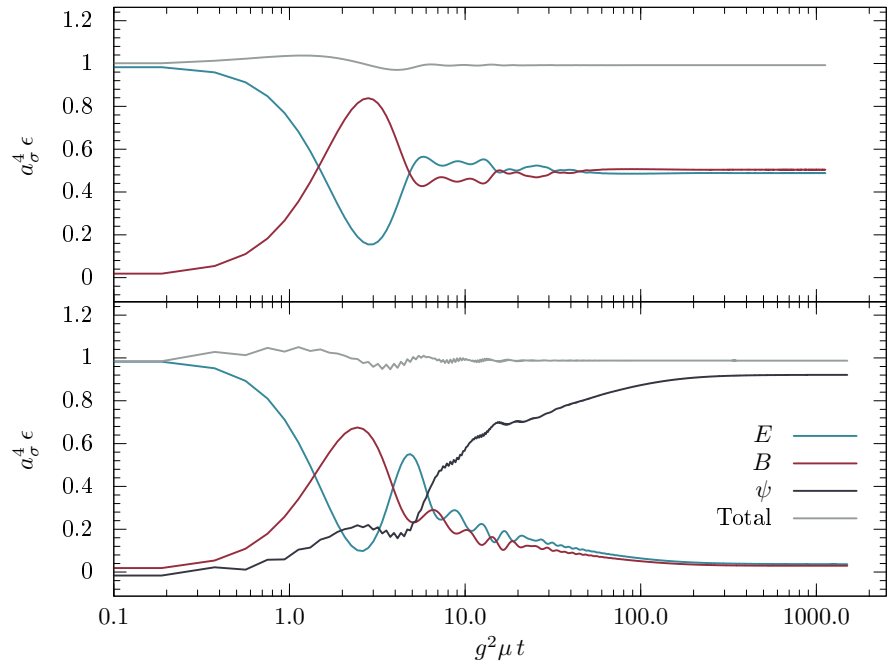

Figure 6.14: Evolution of the energy density for systems including bosons and fermions (lower plot) as well as only bosons (above) from simulations with parameters given in table 6.5.

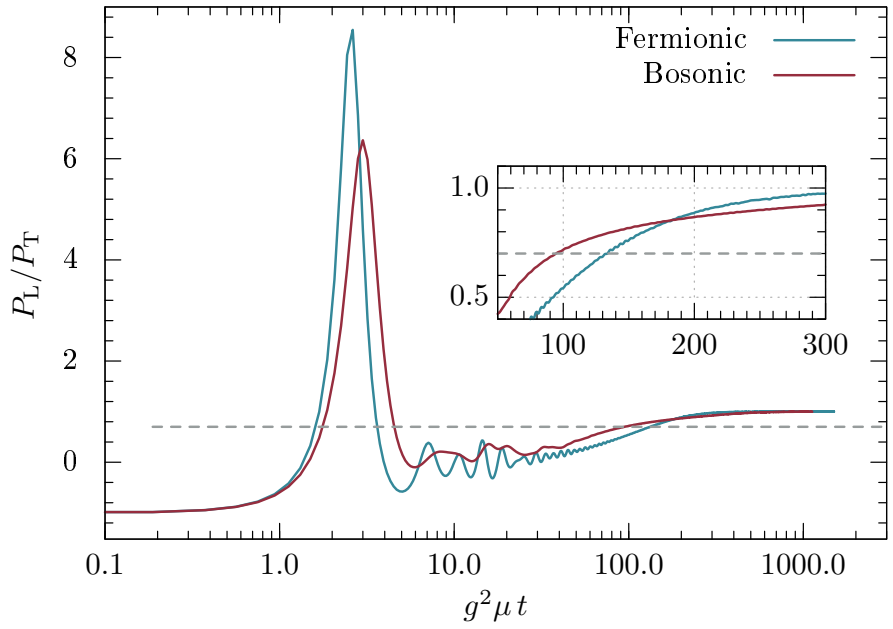

Figure 6.15: Evolution of the ratio of longitudinal over transverse pressure indicating isotropisation of the systems. The inlet enlarges the region, where isotropisation is reached. Simulation parameters according to table 6.5.

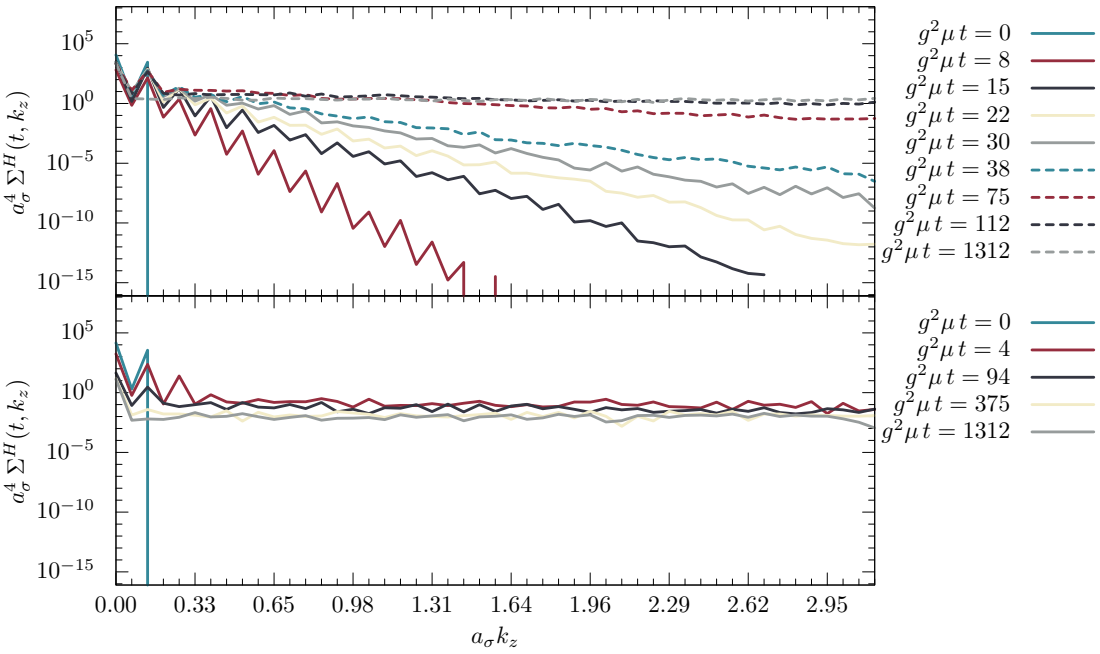

Figure 6.16: Evolution of the spectral decomposition of the chromo-electric energy density with fermions (lower plot) and without fermions (upper plot). Simulation parameters according to table 6.5.

medium produced in a heavy ion collision. Furthermore, including additional observables like a pseudo occupation number for fermions [233] will give an improved understanding of the ongoing physics. During our work, new colour glass condensate inspired initial conditions were been developed by Gelis and Epelbaum [234], which when implemented in pure SU(2) simulations gave an isotropisation time comparable to hydrodynamic results [58]. The question arises, if the isotropisation time remains competitive with hydrodynamics, when the correct gauge group of QCD is used.

A more theoretical consideration is the study of Gribov copies. Although a gauge fixed spectral decomposition of fields is frequently used in the study of thermalisation processes, so far the effect of Gribov copies has never been studied. Having implemented a gauge fixing routine on the lattice Gribov copies can easily be produced by the mother and daughter method [181].

Besides isotropisation of the quark-gluon plasma, one could study the effect of fermions on other processes regarding thermalisation such as turbulences and cascades [207, 235–237], emergence of an attractor [57, 238] or Bose-Einstein condensation [239, 240]. The influence of magnetic and electric fields on the fermions or the inclusion of a finite chemical potential are further studies within the semi-classical model of QCD with respect to the quark-gluon plasma.

6.6 Conclusions

In this chapter we investigated the isotropisation of the quark-gluon plasma produced in a heavy ion collision via a chromo-Weibel instability. We treated the emerging far from

equilibrium dynamics in a semi-classical approach to QCD on the lattice. The required initial conditions were borrowed from colour glass condensate effective theory.

Based on these initial conditions we have performed the first bosonic SU(3) simulations. In agreement with other studies of classical dynamics [53, 159], we have found that choosing a different gauge group does not change the overall dynamics, but it has an effect on precise numbers. In order to achieve an isotropisation time comparable with results from equivalent SU(2) simulations we had to increase the fluctuation seed from $\Delta = 0.2$ to $\Delta = 0.7$.

We also found evidence for the emergence of a chromo-Weibel instability using the colour group SU(3). For that we employed a new observable, the energy density mapped to two-dimensional position space, which displayed the filaments created by the instability. Furthermore we developed a new approach to the spectral decomposition of the chromo-electric field, which in contrast to older observables constitutes a gauge invariant quantity. It excludes ambiguities concerning the gauge freedom and is free of Gribov copies. Additionally, it reduces the numeric effort drastically, since no numerically expensive gauge fixing routine is required.

For the very first time we investigated the effect of fermions on the isotropisation process by employing the semi-classical approach to QCD established in chapter 5. We observed a transfer of energy from the bosons to the fermions, which can be interpreted as fermion production from highly populated bosonic fields as found in a 2PI (two particle irreducible) approach [241]. Furthermore the interaction of the bosonic fields with the fermions influences the isotropisation time. Compared to a pure bosonic run we have found an increase of the isotropisation time from $t_{\mathrm{iso}} \approx 9.3\,\mathrm{fm}$ to $t_{\mathrm{iso}} \approx 13.2\,\mathrm{fm}$.

7 Summarising conclusions

In this thesis we studied real time quantities and processes of the quark-gluon plasma. We employed the fundamental theory of QCD allowing for predictions from first principles. Treating QCD on the lattice enabled us to access non-perturbative regimes and for the very first time we computed a hydrodynamic transport coefficient without having to resort to maximum entropy methods or functional input. Furthermore we established a semi-classical formulation of QCD that we applied to investigate the effects of dynamic fermions as well as of using the correct colour group of QCD, SU(3), on the isotropisation process of the quark-gluon plasma.

In this work we have calculated the second order hydrodynamic transport coefficient κ for the Yang-Mills plasma using lattice perturbation theory and Monte Carlo simulations. From calculations both in strong and weak coupling limits, we expect a temperature dependence of $\kappa \sim T^2$. In the investigated temperature range $2T_\mathrm{c} < T < 10T_\mathrm{c}$ our data is consistent with this expectation. Our quantitative result for the transport coefficient is $\kappa = 0.36(15)T^2$. Within the error bars, it agrees with predictions from AdS/CFT correspondence rescaled to the field content of Yang-Mills theory as well as leading order perturbation theory.

An investigation of the isotropisation process via a chromo-Weibel instability is impeded by the fact that the pre-equilibrium phase in a heavy ion collision constitutes a system far from equilibrium. Furthermore isotropisation is a dynamic process and its investigation requires a treatment in real time. For this reason we established a semi-classical lattice approach to QCD facilitating a first principle description of real time processes far from equilibrium.

In the investigation of the isotropisation process in heavy ion collisions, we borrowed initial conditions from the colour glass condensate effective theory. Studying the pure bosonic dynamics with colour group SU(3) in a static box, we found evidence for the emergence of a chromo-Weibel instability. We used a new gauge invariant approach to the spectral decomposition of the chromo-electric field, avoiding numerically costly gauge fixing routines. As for isotropisation, we observed similar overall dynamics, when compared to equivalent SU(2) studies. However, computing the isotropisation time we have found a significant difference. This suggests that the difference between different colour groups is not negligible when it comes to precise numbers.

For the very first time we investigated quantitatively the effect of fermions on the isotropisation process using a semi-classical approach to QCD. The observed energy transfer from bosons to fermions can be interpreted as fermion production from highly populated bosonic fields. In comparison to the pure bosonic study, the inclusion of fermions increased the isotropisation from 9.3 fm to 13.2 fm using a fluctuation seed of $\Delta = 0.7$. This first study suggests that the inclusion of fermions has a non-negligible effect on the isotropisation process.

Overall, in this thesis we provide extensive studies on real time observables of the quark-gluon plasma. Based on a computation of the transport coefficient κ as well as

an investigation of isotropisation processes, we demonstrated that selected real time observables relevant in heavy ion collisions are accessible by lattice QCD and thus from first principles. This is particular important to give reliable predictions regarding the study of heavy ion collisions at RHIC, LHC and FAIR.

A Conventions

A.1 System of units

Throughout the whole thesis we work in natural units with $\hbar = c = k_\mathrm{B} = 1$. Thus all units are given by some power of energy. The conversion to the International System of Units is performed by the constants from [2]

$$\hbar = 1.054571726(47) \cdot 10^{-34}\,\mathrm{J\,s}\ , \tag{A.1}$$

$$c = 299792458\,\mathrm{m\,s^{-1}}\ , \tag{A.2}$$

$$k_\mathrm{B} = 8.6173324(78) \cdot 10^{-5}\,\mathrm{eV\,K^{-1}}\ . \tag{A.3}$$

Lattice spacings differ from this rule and are given in units of length, 'fm'. The conversion from energy to length and vice versa can be performed with

$$\hbar c = 1 = 197.3269718(44)\,\mathrm{MeV\ fm}\ . \tag{A.4}$$

A.2 Notation for relativity

A.2.1 Minkowski space time

In Minkowski space time we use the metric tensor

$$g_{\mu\nu} = g^{\mu\nu} = \begin{pmatrix} 1 & 0 & 0 & 0 \\ 0 & -1 & 0 & 0 \\ 0 & 0 & -1 & 0 \\ 0 & 0 & 0 & -1 \end{pmatrix} \tag{A.5}$$

with Greek indices running over $\mu = 0, 1, 2, 3$ and Roman indices denoting only spatial components $i = 1, 2, 3$. Three-vectors are denoted by boldface type. The contravariant and covariant displacement vectors read $x^\mu = \left(x^0, \mathbf{x}\right)$ and $x_\mu = \left(x^0, -\mathbf{x}\right)$, respectively. Note that the derivative operator is 'naturally lowered' $\partial_\mu = \frac{\partial}{\partial x^\mu} = \left(\frac{\partial}{\partial x^0}, \nabla\right)$.

A.2.2 Light-cone coordinates

Describing an ultra-relativistic heavy ion collision using light-cone coordinates is highly favourable. In light-cone coordinates the two coordinates

$$x^\pm \equiv \frac{t \pm z}{\sqrt{2}} \tag{A.6}$$

are null coordinates and all other coordinates $x_\perp$ are spatial. The light-cone is defined by $x^\pm = 0$. In ultra-relativistic heavy ion collisions the nuclei travel close to the light-cone and collide at $x^+ = x^- = 0$.

A.2.3 Euclidean space time

By a Wick rotation from real to imaginary time $t \to \mathrm{i}\tau$ we change from Minkowski space time to Euclidean space time, where the metric tensor reads

$$\delta_{\mu\nu} = \begin{pmatrix} 1 & 0 & 0 & 0 \\ 0 & 1 & 0 & 0 \\ 0 & 0 & 1 & 0 \\ 0 & 0 & 0 & 1 \end{pmatrix}. \tag{A.7}$$

To distinguish between both notations the Euclidean time component is labelled τ or x_4. Contravariant and covariant vectors are treated equally and the displacement vector reads $x^\mu = x_\mu = (\mathbf{x}, x_4)$.

A.3 Representations of SU(2) and SU(3) generators

As a representation for the generators of the group SU(2) we choose the Pauli matrices

$$\sigma_1 = \begin{pmatrix} 0 & 1 \\ 1 & 0 \end{pmatrix}, \qquad \sigma_2 = \begin{pmatrix} 0 & -\mathrm{i} \\ \mathrm{i} & 0 \end{pmatrix}, \qquad \sigma_3 = \begin{pmatrix} 1 & 0 \\ 0 & -1 \end{pmatrix}. \tag{A.8}$$

One representation for the generators of the group SU(3) are the Gell-Mann matrices

$$\begin{aligned}
\lambda^1 &= \begin{pmatrix} 0 & 1 & 0 \\ 1 & 0 & 0 \\ 0 & 0 & 0 \end{pmatrix}, \qquad \lambda^2 = \begin{pmatrix} 0 & -\mathrm{i} & 0 \\ \mathrm{i} & 0 & 0 \\ 0 & 0 & 0 \end{pmatrix}, \qquad \lambda^3 = \begin{pmatrix} 1 & 0 & 0 \\ 1 & -1 & 0 \\ 0 & 0 & 0 \end{pmatrix}, \\
\lambda^4 &= \begin{pmatrix} 0 & 0 & 1 \\ 0 & 0 & 0 \\ 1 & 0 & 0 \end{pmatrix}, \qquad \lambda^5 = \begin{pmatrix} 0 & 0 & -\mathrm{i} \\ 0 & 0 & 0 \\ \mathrm{i} & 0 & 0 \end{pmatrix}, \qquad \lambda^6 = \begin{pmatrix} 0 & 0 & 0 \\ 0 & 0 & 1 \\ 0 & 1 & 0 \end{pmatrix}, \\
\lambda^7 &= \begin{pmatrix} 0 & 0 & 0 \\ 0 & 0 & -\mathrm{i} \\ 0 & \mathrm{i} & 0 \end{pmatrix}, \qquad \lambda^7 = \frac{1}{\sqrt{3}} \begin{pmatrix} 1 & 0 & 0 \\ 0 & 1 & 0 \\ 0 & 0 & -2 \end{pmatrix}
\end{aligned} \tag{A.9}$$

with the generators given by

$$T^a = \frac{1}{2}\lambda^a. \tag{A.10}$$

A.4 Dirac matrices

Imposing the anticommutation relation in Minkowski space time

$$\{\gamma^\mu, \gamma^\nu\} = 2g^{\mu\nu} \times \mathbb{1}_{4\times 4}\ , \tag{A.11}$$

the four Dirac matrices or γ-matrices generate a matrix representation of the Clifford Algebra. The Minkowski metric $g^{\mu\nu}$ is given by (A.5) and $\mathbb{1}_{n\times n}$ denotes the $n \times n$ identity matrix. Throughout this thesis we work with the Dirac representation for the Dirac matrices, i.e.

$$\gamma_0 = \begin{pmatrix} \mathbb{1}_{2\times 2} & 0 \\ 0 & -\mathbb{1}_{2\times 2} \end{pmatrix}, \qquad \gamma_i = \begin{pmatrix} 0 & \sigma_i \\ -\sigma_i & 0 \end{pmatrix}, \tag{A.12}$$

where the σ_i are the Pauli matrices (A.8).

A.5 Fourier transforms and distributions

A.5.1 Heavyside step function and Kronecker delta

The Heavyside step function is given by

$$\theta(x) = \begin{cases} 0 & \text{for } x < 0 \\ 1 & \text{for } x \geq 0 \end{cases} . \tag{A.13}$$

The Kronecker delta is defined as

$$\delta_{ij} = \begin{cases} 0 & \text{for } i \neq j \\ 1 & \text{for } i = j \end{cases} . \tag{A.14}$$

A.5.2 Fourier transforms in Minkowski space time

The Fourier transforms in Minkowski space time read

$$f(q) = \int \mathrm{d}^4x \; \mathrm{e}^{-\mathrm{i}qx} f(x) \; , \tag{A.15a}$$

$$f(x) = \int \frac{\mathrm{d}^4q}{(2\pi)^4} \; \mathrm{e}^{\mathrm{i}qx} f(q) \; . \tag{A.15b}$$

The δ-distribution is defined by

$$\delta(x-y) = \int \frac{\mathrm{d}^4q}{(2\pi)^4} \; \mathrm{e}^{\mathrm{i}q(x-y)} \; . \tag{A.16}$$

A.5.3 Fourier transforms in Euclidean space time

The Fourier transforms in continuous Euclidean space time at finite temperature read

$$f(q) = \int_0^{1/T} \mathrm{d}\tau \int \mathrm{d}^3x \; \mathrm{e}^{-\mathrm{i}qx} f(x) \; , \tag{A.17a}$$

$$f(x) = T \sum_{\omega_n=-\infty}^{\infty} \int \frac{\mathrm{d}^3q}{(2\pi)^3} \; \mathrm{e}^{\mathrm{i}qx} f(q) \; , \tag{A.17b}$$

whereas on the lattice they are

$$f(q) = \sum_x \mathrm{e}^{-\mathrm{i}qx} f(x) \; , \tag{A.18a}$$

$$f(x) = \frac{1}{V} \sum_q \mathrm{e}^{\mathrm{i}qx} f(q) \; , \tag{A.18b}$$

with the lattice volume $V = \prod_\mu a_\mu N_\mu = T^{-1} \prod_i a_i N_i$.

B Calculations regarding the transport coefficient κ

B.1 Hypercubic symmetry of the energy-momentum tensor

The correlator $\langle T_{xy}(x)T_{xy}(y)\rangle \equiv \langle T_{12}(x)T_{12}(y)\rangle$ can be expressed in terms of diagonal energy-momentum tensor elements by exploiting rotation invariance

$$\langle T'_{12}(x)T'_{12}(y)\rangle = \langle T_{12}(x)T_{12}(y)\rangle \,, \tag{B.1}$$

on a spatially isotropic lattice (and medium) under rotations by $\alpha = \frac{\pi}{4}$ about the z-direction. The transformation of a second rank tensor reads

$$T'_{\mu\nu}(x) = \left(M_z^{-1}\right)_{\mu\alpha}\left(M_z^{-1}\right)_{\nu\beta} T_{\alpha\beta}(x), \tag{B.2}$$

and the corresponding transformation matrix is given by

$$M_z^{-1} = \begin{pmatrix} 1 & 0 & 0 & 0 \\ 0 & \cos\alpha & \sin\alpha & 0 \\ 0 & -\sin\alpha & \cos\alpha & 0 \\ 0 & 0 & 0 & 1 \end{pmatrix} = \frac{1}{\sqrt{2}} \begin{pmatrix} \sqrt{2} & 0 & 0 & 0 \\ 0 & 1 & 1 & 0 \\ 0 & -1 & 1 & 0 \\ 0 & 0 & 0 & \sqrt{2} \end{pmatrix}. \tag{B.3}$$

For the energy-momentum tensor components of interest, this means

$$T'_{12}(x) = \frac{1}{2}\left(T_{22} - T_{11}\right), \tag{B.4}$$

where we use $T_{12} = T_{21}$. With the definition of the energy-momentum tensor (4.23) we find for the correlator

$$\begin{aligned} T'_{12}(x)T'_{12}(y) &= \frac{1}{4}\left(T_{22}(x)T_{22}(y) - T_{22}(x)T_{11}(y) - T_{11}(x)T_{22}(y) + T_{11}(x)T_{11}(y)\right) \\ &= \frac{1}{4}\left(\theta_{22}(x)\theta_{22}(y) + \theta_{11}(x)\theta_{11}(y) - \theta_{22}(x)\theta_{11}(y) - \theta_{11}(x)\theta_{22}(y)\right). \end{aligned} \tag{B.5}$$

Note that the trace anomaly θ cancels completely. From rotation invariance follows

$$\langle\theta_{22}(x)\theta_{11}(y)\rangle = \langle\theta_{11}(x)\theta_{22}(y)\rangle\,, \qquad \langle\theta_{11}(x)\theta_{11}(y)\rangle = \langle\theta_{22}(x)\theta_{22}(y)\rangle\,, \tag{B.6}$$

and the correlator expressed in diagonal elements reads

$$\langle T_{12}(x)T_{12}(y)\rangle = \frac{1}{2}\left(\langle\theta_{11}(x)\theta_{11}(y)\rangle - \langle\theta_{11}(x)\theta_{22}(y)\rangle\right). \tag{B.7}$$

B.2 Results for finite Matsubara sums

Exemplary, we present the computation of the finite Matsubara sum

$$\frac{1}{N_\tau}\sum_{n=1}^{N_\tau}\frac{1}{\widetilde{k}^2} \tag{B.8}$$

in more detail. Introducing the following definition for spatial momenta

$$\frac{4}{a_\tau^2}\omega^2 \equiv \widetilde{k}_i^2, \tag{B.9}$$

and inserting the definition of lattice momenta (3.20) for k_0 results in

$$\frac{1}{N_\tau}\sum_{n=1}^{N_\tau}\frac{1}{\widetilde{k}^2} = \frac{1}{N_\tau}\sum_{n=1}^{N_\tau}\frac{-a_\sigma^2}{\mathrm{e}^{\mathrm{i}k_0 a_\tau} - 2 + \mathrm{e}^{-\mathrm{i}k_0 a_\tau} - 4\omega^2}\ . \tag{B.10}$$

By introducing the function $g(z)$

$$\frac{1}{z}g(z) \equiv \frac{1}{z^2 - 2z - 4\omega^2 z + 1}, \qquad z \equiv \mathrm{e}^{\mathrm{i}k_0 a_\tau}, \tag{B.11}$$

we can solve the finite Matsubara sum by applying the formula [140]

$$\frac{1}{N_\tau}\sum_{n=1}^{N_\tau} g(z) = -\sum_i \frac{\mathrm{Res}_{\bar{z}_i}\left(\frac{1}{z}g(z)\right)}{\bar{z}_i^{N_\tau} - 1}. \tag{B.12}$$

We compute the residua by identifying the poles of $\frac{g(z)}{z}$ as

$$z_1 = 1 + 2\omega^2 + 2\omega\sqrt{\omega^2 + 1}, \tag{B.13a}$$

$$z_2 = 1 + 2\omega^2 - 2\omega\sqrt{\omega^2 + 1}, \tag{B.13b}$$

which can be simplified to

$$z_1 = \mathrm{e}^{a_\sigma E_1}, \qquad z_2 = \mathrm{e}^{-a_\sigma E_1}, \tag{B.14}$$

by using

$$\omega^2 = \frac{a_\tau^2}{4}\widetilde{k}_i^2 = \sinh^2\left(\frac{a_\sigma E_1}{2}\right) \tag{B.15}$$

with E_1 to be determined later. Then the finite Matsubara sum reads

$$\frac{1}{N_\tau}\sum_{n=1}^{N_\tau}\frac{1}{\widetilde{k}^2} = \frac{a_\tau^2}{2\sinh(a_\sigma E_1)}\left(1 + \frac{2}{\mathrm{e}^{a_\sigma N_\tau E_1} - 1}\right). \tag{B.16}$$

Using the definition of lattice momenta (3.20) we determine E_1 from the equation

$$\omega^2 = \xi^{-2}\sum_i \sin^2\left(\frac{a_\sigma k_i}{2}\right) = \sinh^2\left(\frac{a_\sigma E_1}{2}\right). \tag{B.17}$$

Lattice perturbation theory operates at small lattice spacings. A Taylor expansion of (B.17) in lattice spacings gives

$$\xi^{-2}\sum_i k_i^2 - \xi^{-2}\frac{a_\sigma^2}{12}\sum_i k_i^4 + \mathcal{O}(a_\sigma^4) = E_1^2 + \frac{a_\sigma^2}{12}E_1^4 + \mathcal{O}(a_\sigma^4). \tag{B.18}$$

Making an ansatz

$$E_1 = E^{(0)} - a_\sigma^2 E^{(2)} + \mathcal{O}(a_\sigma^4), \tag{B.19}$$

we can solve the defining equation (B.18) and find

$$E_1(k_i) \equiv \xi^{-1}|k_i\,| - \frac{a_\sigma^2}{24|k_i\,|}\left(\xi^{-1}\sum_i k_i^4 + \xi^{-3}|k_i\,|^4\right) + \mathcal{O}(a_\sigma^4). \tag{B.20}$$

In the following we define

$$E_1 \equiv E(k_i), \tag{B.21a}$$
$$E_2 \equiv E(k_i + q_i). \tag{B.21b}$$

Plugging (B.20) into (B.16) gives the final result for the Matsubara sum. The additive renormalisation in terms of subtracting the vacuum contribution discussed in section 4.3.3 can easily be performed by discarding the temperature independent term in (B.16). Note that on the lattice the temperature is given by (3.18).

With the definitions

$$A \equiv \frac{1}{\cosh(a_\sigma E_1) - \cosh(a_\sigma E_2)}, \tag{B.22a}$$
$$B \equiv \frac{1}{\tanh(a_\sigma E_2)}\,\frac{1}{\mathrm{e}^{a_\sigma N_\tau E_2} - 1} - \frac{1}{\tanh(a_\sigma E_1)}\,\frac{1}{\mathrm{e}^{a_\sigma N_\tau E_1} - 1}, \tag{B.22b}$$
$$C_1 \equiv \frac{1}{\sinh(a_\sigma E_1)}, \tag{B.22c}$$
$$C_2 \equiv \frac{1}{\sinh(a_\sigma E_2)}, \tag{B.22d}$$

the evaluation of the other finite Matsubara sums (4.50) gives the following results

$$\frac{1}{N_\tau}\sum_{n=1}^{N_\tau}\frac{1}{\widetilde{(k+q)^2}} = \frac{a_\tau^2}{2}\left(1 + \frac{2}{\mathrm{e}^{a_\sigma N_\tau E_2} - 1}\right)C_2, \tag{B.23a}$$
$$\frac{1}{N_\tau}\sum_{n=1}^{N_\tau}\frac{1}{\widetilde{k}^2\widetilde{(k+q)^2}} = \frac{a_\tau^4}{4}\Big(C_2\mathrm{e}^{a_\sigma E_2} - C_1\mathrm{e}^{a_\sigma E_1}\Big)A + \frac{a_\tau^4}{2}AB, \tag{B.23b}$$
$$\frac{1}{N_\tau}\sum_{n=1}^{N_\tau}\frac{\widetilde{k}\widetilde{(k+q)}}{\widetilde{k}^2\widetilde{(k+q)^2}} = \frac{a_\tau^2}{\mathrm{e}^{a_\sigma N_\tau E_2} - 1}C_2 + \frac{a_\tau^4}{2}\left(\widetilde{k}_i\widetilde{(k_i+q_i)} - \widetilde{k}_i^2\right)AB, \tag{B.23c}$$
$$\frac{1}{N_\tau}\sum_{n=1}^{N_\tau}\frac{\left(\widetilde{k}\widetilde{(k+q)}\right)^2}{\widetilde{k}^2\widetilde{(k+q)^2}} = -\frac{a_\tau^2}{\mathrm{e}^{a_\sigma N_\tau E_2} - 1}\left(\widetilde{(k_i+q_i)} - \widetilde{k}_i\right)^2 C_2$$

$$+\frac{a_\tau^4}{2}\left(\widetilde{k}_i(\widetilde{k_i+q_i})-\widetilde{k}_i^2\right)^2 AB, \tag{B.23d}$$

$$\frac{1}{N_\tau}\sum_{n=1}^{N_\tau}\frac{1}{\widetilde{k}^2}=\frac{a_\tau^2}{2}\left(1+\frac{2}{\mathrm{e}^{a_\sigma N_\tau E_1}-1}\right)C_1. \tag{B.23e}$$

B.3 Remaining three-momentum integration

As an example we compute the contribution

$$I_1\equiv(N_c^2-1)\int_{-\frac{\pi}{a_\sigma}}^{\frac{\pi}{a_\sigma}}\frac{\mathrm{d}^3k}{(2\pi)^3}\,\frac{1}{a_\tau N_\tau}\sum_{n=1}^{N_\tau}\frac{\widetilde{k}_y^2}{\widetilde{k}^2} \tag{B.24}$$

to the transport coefficient κ. Evaluating the finite Matsubara sum by (B.16) gives

$$I_1=(N_c^2-1)a_\tau\int_{-\frac{\pi}{a_\sigma}}^{\frac{\pi}{a_\sigma}}\frac{\mathrm{d}^3k}{(2\pi)^3}\,\frac{\widetilde{k}_y^2}{2\sinh(a_\sigma E_1)}\left(1+\frac{2}{\mathrm{e}^{a_\sigma N_\tau E_1}-1}\right). \tag{B.25}$$

Expanding the integral around the continuum limit extends the integration limits to infinity. The corresponding Taylor expansion in small lattice spacings results in

$$\begin{aligned}I_1=(N_c^2-1)\frac{a_\tau}{a_\sigma^3}\int_{-\infty}^{\infty}\frac{\mathrm{d}^3\hat{k}}{(2\pi)^3}&\left(\frac{\hat{k}_y^2}{a_\sigma^2}-\frac{\hat{k}_y^4}{12a_\sigma}\right)\\
&\times\left(\frac{1}{\xi^{-1}\hat{k}}-\frac{\xi^{-1}\hat{k}}{6}+\frac{1}{24\hat{k}^3\xi^{-2}}\left(\xi^{-1}\hat{k}_i^4+\xi^{-3}|\hat{k}_i\,|^4\right)\right)\\
&\times\left(\frac{1}{\mathrm{e}^{N_\tau\hat{k}\xi^{-1}}-1}+\frac{N_\tau\mathrm{e}^{N_\tau\hat{k}\xi^{-1}}}{\left(\mathrm{e}^{N_\tau\hat{k}\xi^{-1}}-1\right)^2}\frac{1}{24\hat{k}}\left(\xi^{-1}\hat{k}_i^4+\xi^{-3}|\hat{k}_i\,|^4\right)\right),\end{aligned} \tag{B.26}$$

where we make the substitution $\hat{k}=a_\sigma k$ and omit terms of order $\mathcal{O}(a_\sigma^4)$. Performing the angular integration gives

$$\begin{aligned}I_1=\frac{a_\tau}{a_\sigma^5}\int_0^\infty\frac{\mathrm{d}\hat{k}}{(2\pi)^3}\Bigg(&\frac{\pi\hat{k}^3\left(20240-756\hat{k}^2(1+5\xi^{-2})+\hat{k}^4\left(-41+189\xi^{-2}\right)\right)}{22680\xi^{-1}}\\
&\times\frac{1}{\mathrm{e}^{N_\tau\hat{k}\xi^{-1}}-1}\\
&+\frac{\pi\hat{k}^6\left(864864\left(3+5\xi^{-2}\right)\right)}{77837760}\,\frac{N_\tau\mathrm{e}^{N_\tau\hat{k}\xi^{-1}}}{\left(\mathrm{e}^{N_\tau\hat{k}\xi^{-1}}-1\right)^2}\Bigg).\end{aligned} \tag{B.27}$$

If the integration includes an outer momentum q, we would expand in this as well to reproduce the low momentum expansion (4.20). Performing the remaining integrals

$$\int_0^\infty\mathrm{d}k\,\frac{k^{2n+1}}{\mathrm{e}^{N_\tau k}-1},\qquad\int_0^\infty\mathrm{d}k\,\frac{N_\tau\mathrm{e}^{N_\tau k}}{\left(\mathrm{e}^{N_\tau k}-1\right)^2}\,k^{2n} \tag{B.28}$$

with $n \in \mathbb{N}$ gives the result (4.52c):

$$I_1 = (N_c^2 - 1)\frac{\pi^2}{90}\frac{1}{(a_\tau N_\tau)^4} + (N_c^2 - 1)\frac{1}{(a_\tau N_\tau)^6}\left(\frac{\pi^4}{378}a_\sigma^2 + \frac{\pi^4}{378}a_\tau^2\right). \tag{B.29}$$

In general the calculation of the other integrals of (4.52) parallels the presented steps, but is more involved due to the more complicated form and extra momentum q.

C Numeric data regarding the transport coefficient κ

C.1 Transport coefficient κ from AdS/CFT correspondence

$\frac{T}{T_c}$	$\frac{\kappa}{T^2}$	$\frac{T}{T_c}$	$\frac{\kappa}{T^2}$	$\frac{T}{T_c}$	$\frac{\kappa}{T^2}$
0.7	0.00042(6)	1.3	0.11324(7)	9	0.1641(1)
0.74	0.00064(7)	1.34	0.11639(7)	10	0.1647(1)
0.78	0.00092(8)	1.38	0.11917(6)	20	0.1676(2)
0.82	0.00127(6)	1.42	0.12165(6)	30	0.1686(2)
0.86	0.00175(5)	1.46	0.12388(6)	40	0.1692(2)
0.9	0.00239(6)	1.5	0.12588(7)	50	0.1695(2)
0.94	0.00337(9)	2	0.14083(7)	60	0.1698(2)
0.98	0.0053(1)	2.5	0.14776(8)	80	0.1703(2)
1	0.0276(2)	3	0.15193(9)	100	0.1706(3)
1.02	0.05842(6)	3.5	0.15468(9)	200	0.1714(3)
1.06	0.07632(9)	4	0.15666(8)	300	0.1718(3)
1.1	0.0869(1)	4.5	0.15819(8)	400	0.1721(3)
1.14	0.09450(8)	5	0.15939(9)	500	0.1722(3)
1.18	0.10062(7)	6	0.16118(9)	600	0.1724(3)
1.22	0.10560(9)	7	0.16242(9)	800	0.1726(3)
1.26	0.10968(7)	8	0.16337(9)	1000	0.1727(3)

Table C.1: AdS/CFT correspondence result for the second order transport coefficient κ/T^2 matched to number of degrees in Yang-Mills theory according to the instructions in section 4.2.2.

C.2 Intermediate results regarding a computation of the transport coefficient κ in lattice Yang-Mills theory

In this section we present numeric intermediate results for run (i) of table 4.1.

n	$G^{\tau}_{0,T}(q)$	$G^{\tau}_{0,T_{\mathrm{vac}}}(q)$	$G^{\sigma}_{0,T}(q)$	$G^{\sigma}_{0,T_{\mathrm{vac}}}(q)$	$G^{\tau\sigma}_{0,T}(q)$	$G^{\tau\sigma}_{0,T_{\mathrm{vac}}}(q)$
0	−0.3(6)	2.(2)	0.1(1)	−0.5(4)	0.03(39)	0.4(1.3)
1	0.1982(2)	0.2009(2)	0.04092(4)	0.03768(4)	0.0283(1)	0.0320(1)
2	0.1985(2)	0.2005(2)	0.04092(4)	0.03766(4)	0.0280(1)	0.0319(1)
3	0.1984(2)	0.2003(2)	0.04076(4)	0.03759(4)	0.0278(1)	0.0314(1)
4	0.1983(2)	0.2002(2)	0.04071(4)	0.03743(4)	0.0273(1)	0.0312(1)
5	0.1981(2)	0.2000(2)	0.04059(4)	0.03730(4)	0.0271(1)	0.0308(1)

Table C.2: Simulation results for the bare correlators $G^{\tau}_{0,T}$, $G^{\sigma}_{0,T}$ and $G^{\tau\sigma}_{0,T}$ and their vacuum parts $G^{\tau}_{0,T_{\mathrm{vac}}}$, $G^{\sigma}_{0,T_{\mathrm{vac}}}$, $G^{\tau\sigma}_{0,T_{\mathrm{vac}}}$ in momentum space for six momentum modes n fulfilling the constraint (4.34).

n	$G^{\tau}_{0}(q)$	$G^{\sigma}_{0}(q)$	$G^{\tau\sigma}_{0}(q)$
0	−3.(3)	0.7(5)	−0.4(1.4)
1	−0.0027(3)	0.00324(5)	−0.0037(2)
2	−0.0019(3)	0.00327(5)	−0.0040(2)
3	−0.0020(3)	0.00317(5)	−0.0035(2)
4	−0.0019(3)	0.00329(5)	−0.0039(2)
5	−0.0019(3)	0.00329(5)	−0.0036(2)

Table C.3: According to (4.39) vacuum subtracted correlators of table C.2.

i	$\langle\theta^{i}_{00}\rangle_1$	$\langle\theta^{i}_{11}\rangle_2$	$\langle\theta^{i}_{22}\rangle_3$	$\langle\theta^{i}_{33}\rangle_4$
τ	−1.447172(1)	0.4823904(9)	0.4823868(9)	0.4823887(8)
σ	0.6218880(7)	−0.2072959(4)	−0.2072969(5)	−0.2072961(1)

Table C.4: Diagonal energy-momentum tensor elements evaluated on lattices (4.41) in order to compute the renormalisation ratio $Z_{\sigma}(\beta,\xi)/Z_{\tau}(\beta,\xi)$.

	T	T_{vac}
$\langle\theta^{\tau}_{11}\rangle$	−0.4768093(3)	−0.48239182(8)
$\langle\theta^{\tau}_{22}\rangle$	−0.4768096(3)	−0.48239191(8)
$\langle\theta^{\tau}_{33}\rangle$	−0.4768099(3)	−0.48239181(8)

	T	T_{vac}
$\langle\theta^{\sigma}_{11}\rangle$	0.2100439(1)	0.20729721(4)
$\langle\theta^{\sigma}_{22}\rangle$	0.2100440(1)	0.20729719(4)
$\langle\theta^{\sigma}_{33}\rangle$	0.2100438(1)	0.20729725(4)

Table C.5: Energy-momentum tensor elements required to compute the absolute renormalisation factor $Z_{\tau}(\beta,\xi)$ from equivalence to the pressure.

D Lattice formulation of semi-classical quantum chromodynamics

D.1 Lagrangian and Hamiltonian mechanics

The law governing the Lagrangian and Hamiltonian mechanics [242,243] is the principle of stationary action or Hamilton's principle

$$\delta S = 0. \tag{D.1}$$

The system is described by an action $S = \int_{t_0}^{t_1} \mathrm{d}t\, L$, where $L(q, \dot{q}, t)$ denotes the system's Lagrangian function and q_i and $\dot{q}_i$ are the generalised coordinates and velocities, where $i = 1, \ldots, s$ counts the number of degrees of freedom. Hamilton's principle can be applied to derive the Euler-Lagrange equations

$$\frac{\mathrm{d}}{\mathrm{d}t}\frac{\partial L}{\partial \dot{q}_i} - \frac{\partial L}{\partial q_i} = 0, \tag{D.2}$$

which correspond to the s equations of motion describing the system's time evolution. A complete equivalent to the Lagrangian formalism is the Hamiltonian one based on conjugated momenta

$$p_i = \frac{\partial L}{\partial \dot{q}_i}, \tag{D.3}$$

instead of generalised velocities. The relevant Hamiltonian function is connected to the Lagrangian function by a Legendre transformation

$$H(p, q, t) = \sum_i p_i \dot{q}_i - L(p, q, t). \tag{D.4}$$

The equations of motion can be derived from Hamilton's equations

$$\dot{q}_i = \frac{\partial H}{\partial p_i}, \qquad \dot{p}_i = -\frac{\partial H}{\partial q_i}. \tag{D.5}$$

The time evolution of some function $f(q, p, t)$ is given by

$$\frac{\mathrm{d}f}{\mathrm{d}t} = \frac{\partial f}{\partial t} + \{H, f\}, \qquad \{H, f\} \equiv \sum_i \left(\frac{\partial H}{\partial p_i}\frac{\partial f}{\partial q_i} - \frac{\partial H}{\partial q_i}\frac{\partial f}{\partial p_i} \right), \tag{D.6}$$

where $\{H, f\}$ denotes the Poisson bracket.

Both formalisms can be extended to classical field theories by the following replacements in the variables

$$q_i \to \phi(t, \mathbf{x}), \qquad \dot{q}_i \to \partial_0 \phi(t, \mathbf{x}), \qquad p_i \to \pi(t, \mathbf{x}) = \delta \mathcal{L} / \delta(\partial_0 \phi), \tag{D.7}$$

the introduction of Lagrangian and Hamiltonian densities

$$L = \int \mathrm{d}^3x \; \mathcal{L}[\phi, \partial_\mu \phi], \qquad H = \int \mathrm{d}^3x \; \mathcal{H}[\phi, \partial_\mu \phi] \tag{D.8}$$

and use of the functional calculus.

D.2 Derivation of the lattice QCD Hamiltonian

Starting from the system's Lagrangian $\mathcal{L}^{\mathrm{M}}_{\mathrm{tot}} = \mathcal{L}^{\mathrm{M}}_{\mathrm{G}} + \mathcal{L}^{\mathrm{M}}_{\mathrm{F}}$ with the bosonic part defined in (5.1) and the fermionic one in (5.5), we rewrite the gluonic part $\mathcal{L}^{\mathrm{M}}_{\mathrm{G}}$ by using the temporal gauge (5.7)

$$\begin{aligned}
\mathrm{Tr}\left(\dot{U_i}^{\dagger}(x)\dot{U_i}(x)\right) &= \mathrm{Tr}\left(\frac{U_i^\dagger(x) - U_i^\dagger(x+\hat{0})}{a_\tau}\,\frac{U_i(x) - U_i(x+\hat{0})}{a_\tau}\right) \\
&= \frac{1}{a_\tau^2}\left(2N_c - 2\,\mathrm{Re}\,\mathrm{Tr}\left(U_i^\dagger(x)U_i(x+\hat{0})\right)\right) \\
&= \frac{2N_c}{a_\tau^2}\left(1 - \frac{1}{N_c}\,\mathrm{Re}\,\mathrm{Tr}\left(U_i^\dagger(x)U_0(x)U_i(x+\hat{0})U_0^\dagger(x+\hat{i})\right)\right) \\
&= \frac{2N_c}{a_\tau^2}\left(1 - \frac{1}{N_c}\,\mathrm{Re}\,\mathrm{Tr}\,U_{0i}(x)\right).
\end{aligned} \tag{D.9}$$

We can express the left hand side of the upper equation in terms of the chromo-electric gauge field (5.8b)

$$\begin{aligned}
\mathrm{Tr}\left(\dot{U_i}^{\dagger}(x)\dot{U_i}(x)\right) &= \mathrm{Tr}\left\{\left(-\mathrm{i}ga_\sigma U_i^\dagger(x)E_i(x)\right)\left(\mathrm{i}ga_\sigma E_i(x)U_i(x)\right)\right\} \\
&= \frac{g^2a_\sigma^2}{2}E_i^a(x)E_i^a(x)
\end{aligned} \tag{D.10}$$

and obtain for the gluonic Lagrangian

$$\mathcal{L}^{\mathrm{M}}_{\mathrm{G}}[U_i, E_i] = -\frac{\beta}{\xi a_\sigma^3 a_\tau}\sum_{i<j}\left(1 - \frac{1}{N_c}\,\mathrm{Re}\,\mathrm{Tr}\,U_{ij}(x)\right) + \frac{1}{2}E_i^a(x)E_i^a(x). \tag{D.11}$$

Choosing the bosonic and fermionic generalised coordinates to be

$$\phi^a_{\mathrm{G},i}(x) = A_i^a(x), \qquad \partial_0\phi^a_{\mathrm{G},i}(x) = E_i^a(x), \tag{D.12}$$

$$\phi_{\mathrm{F}}(x) = \psi(x), \qquad \partial_0\phi_{\mathrm{F}}(x) = \widetilde{\mathcal{D}}_0\psi(x), \tag{D.13}$$

where the temporal covariant derivative (5.4c) becomes trivial in temporal gauge, yields for the conjugated momenta

$$\pi^a_{\mathrm{G},i}(x) = E_i^a(x), \qquad \pi_{\mathrm{F}}(x) = \mathrm{i}\overline{\psi}(x)\gamma_0. \tag{D.14}$$

Rescaling the fields and the mass term

$$\psi'(x) = a_\sigma^{3/2}\psi(x), \qquad E_i'(x) = a_\sigma^2 g E_i(x), \qquad m' = a_\sigma m, \tag{D.15}$$

we find for the Hamiltonian function in Minkowski space time with the discrete covariant derivatives defined in (5.4) the following expression:

$$\begin{aligned} H[U_i, E_i, \psi, \overline{\psi}] &= a_\sigma^3 \sum_{\mathbf{x}} \mathcal{H}[U_i, E_i, \psi, \overline{\psi}] \\ &= \sum_{\mathbf{x}} \Bigg\{ \frac{\beta}{a_\sigma} \sum_{i<j} \left(1 - \frac{1}{N_c} \operatorname{Re} \operatorname{Tr} U_{ij}(x) \right) + \frac{1}{2 a_\sigma g^2} E_i^{a\prime}(x) E_i^{a\prime}(x) \\ &\quad - \mathrm{i} \overline{\psi}'(x) \gamma_i \widetilde{\mathcal{D}}^i \psi'(x) + \frac{m'}{a_\sigma} \overline{\psi}'(x) \psi'(x) \\ &\quad - \frac{a_\sigma r}{2} \overline{\psi}'(x) \mathcal{D}_i^{\mathrm{b}} \mathcal{D}_i^{\mathrm{f}} \psi(x) \Bigg\}. \end{aligned} \tag{D.16}$$

D.3 Derivation of the lattice QCD equations of motion

Formally the equations of motion for the links are derived from the Poisson brackets. A more elegant way is to directly apply the time derivative to the definition of the links (5.8a) and plug in the chromo-electric fields (5.8b). In terms of the rescaled fields (D.15) one finds

$$\dot{U}_i(x) = \frac{\mathrm{i}}{a_\sigma} E_i(x) U_i(x). \tag{D.17}$$

We derive the equations of motion for the fermions from Hamilton's equations

$$\begin{aligned} \dot{\psi}(x) = -\mathrm{i} \frac{\delta H}{\delta \psi^\dagger(x)} &= -\mathrm{i} \frac{m}{a_\sigma} \gamma_0 \psi(x) - \frac{1}{2 a_\sigma} \gamma_0 \gamma_i \left(U_i(x) \psi(x + \hat{\imath}) - U_i^\dagger(x - \hat{\imath}) \psi(x - \hat{\imath}) \right) \\ &\quad + \mathrm{i} \frac{r}{2 a_\sigma} \gamma_0 \sum_i \left(U_i(x) \psi(x + \hat{\imath}) - 2\psi(x) + U_i^\dagger(x - \hat{\imath}) \psi(x - \hat{\imath}) \right), \end{aligned} \tag{D.18}$$

as well as for the chromo-electric fields[1]

$$\dot{E}_i^a(x) = -\frac{\delta H}{\delta A_i^a(x)} \equiv \dot{F}_i^a(x) + \dot{G}_i^a(x), \tag{D.19}$$

where we compute the fermionic and bosonic contributions, $\dot{F}_i^a$ and $\dot{G}_i^a$, separately. The fermionic contribution reads

$$\begin{aligned} \dot{F}_i^a(x) &= \mathrm{i} \frac{g^2}{a_\sigma} \sum_{\mathbf{y}} \delta^{ab} \Bigg\{ \frac{\mathrm{i}}{2} \overline{\psi}(y) \gamma_i \Big(T^b U_i(y) \psi(y + \hat{\imath}) \delta_{y,x} + U_i^\dagger(y - \hat{\imath}) T^b \psi(y - \hat{\imath}) \delta_{y - \hat{\imath}, x} \Big) \\ &\qquad + \frac{r}{2} \overline{\psi}(y) \Big(T^b U_i(y) \psi(y + \hat{\imath}) \delta_{x,y} - U_i^\dagger(y - \hat{\imath}) T^b \psi(y - \hat{\imath}) \delta_{y - \hat{\imath}, x} \Big) \Bigg\} \\ &= -\frac{N_c}{\beta a_\sigma} \Big(\overline{\psi}(x) \gamma_i T^a U_i(x) \psi(x + \hat{\imath}) + \overline{\psi}(x + \hat{\imath}) \gamma_i U_i^\dagger(x) T^a \psi(x) \Big) \\ &\quad + \mathrm{i} \frac{r N_c}{\beta a_\sigma} \Big(\overline{\psi}(x) T^a U_i(x) \psi(x + \hat{\imath}) - \overline{\psi}(x + \hat{\imath}) U_i^\dagger(x) T^a \psi(x) \Big), \end{aligned} \tag{D.20}$$

[1] Note that all equations of motion are derived for the rescaled fields and we use the Hamiltonian function instead of the density introducing further powers of a_σ.

while the bosonic one is given by

$$\begin{aligned}
\dot{G}_k^a(x) = \frac{2}{a_\sigma}\sum_{\mathbf{y}}\sum_{i<j}\operatorname{Re}\operatorname{Tr}\Big\{ \mathrm{i}\Big(& T^b U_{ij}(y)\delta_{x,y}\delta_{ik}\delta^{ab} \\
& + U_i(y)T^bU_j(y+\hat{i})U_i^\dagger(y+\hat{j})U_j^\dagger(y)\delta_{x,y+\hat{i}}\delta_{jk}\delta^{ab} \\
& - U_i(y)U_j(y+\hat{i})U_i^\dagger(y+\hat{j})T^bU_j^\dagger(y)\delta_{y+\hat{j},x}\delta_{ik}\delta^{ab} \\
& - U_i(y)U_j(y+\hat{i})U_i^\dagger(y+\hat{j})U_j^\dagger(y)T^b\delta_{xy}\delta_{jk}\delta^{ab}\Big)\Big\} \\
= \frac{1}{a_\sigma}\sum_j \operatorname{Re}\operatorname{Tr}\Big\{ & \mathrm{i}T^a\Big(U_{kj}(x) - U_{kj}(x-\hat{j}) + U_{kj}^\dagger(x-\hat{j}) - U_{kj}^\dagger(x)\Big)\Big\} \\
= -\frac{1}{a_\sigma}\sum_j \operatorname{Im}\operatorname{Tr}\Big\{ & T^a\Big(U_{kj}(x) - U_{kj}^\dagger(x) + U_{kj}^\dagger(x-\hat{j}) - U_{kj}(x-\hat{j})\Big)\Big\} \\
= -\frac{2}{a_\sigma}\sum_{j\neq k}\operatorname{Im}\operatorname{Tr}\Big\{ & T^a\Big(U_{kj}(x) - U_{kj}(x-\hat{j})\Big)\Big\}. \qquad \text{(D.21)}
\end{aligned}$$

Thus the chromo-electric fields evolve according to

$$\begin{aligned}
\dot{E}_i^a(x) = & -\frac{2}{a_\sigma}\sum_{j\neq i}\operatorname{Im}\operatorname{Tr}\Big\{T^a\Big(U_{ij}(x) - U_{ij}(x-\hat{j})\Big)\Big\} \\
& - \frac{N_c}{\beta a_\sigma}\Big(\overline{\psi}(x)\gamma_i T^a U_i(x)\psi(x+\hat{i}) + \overline{\psi}(x+\hat{i})\gamma_i U_i^\dagger(x)T^a\psi(x)\Big) \\
& + \mathrm{i}\frac{rN_c}{\beta a_\sigma}\Big(\overline{\psi}(x)T^aU_i(x)\psi(x+\hat{i}) - \overline{\psi}(x+\hat{i})U_i^\dagger(x)T^a\psi(x)\Big). \qquad \text{(D.22)}
\end{aligned}$$

We derive Gauss law by applying the Euler-Lagrange equations (D.2) with respect to A_0 before fixing the gauge. Separating the contributions, we find for the bosonic part

$$\begin{aligned}
\left(\partial_0\frac{\delta L_{\mathrm{G}}^{\mathrm{M}}}{\delta\dot{A}_0^a(x)} - \frac{\delta L_{\mathrm{G}}^{\mathrm{M}}}{\delta A_0^a(x)}\right)_{A_0^a=0} = & \frac{2a_\sigma}{ga_\tau}\sum_{i,\mathbf{y}}\operatorname{Re}\operatorname{Tr}\Big\{\mathrm{i}\Big(T^bU_{0i}(y)\delta_{x,y}\delta^{ab} - U_0(y)U_i(y+\hat{0}) \\
& \times U_0^\dagger(y+\hat{i})T^bU_i^\dagger(y)\delta_{x,y+\hat{i}}\delta^{ab}\Big)\Big\}_{U_0=\mathbb{1}} \\
= & \frac{2a_\sigma}{ga_\tau}\sum_i\operatorname{Re}\operatorname{Tr}\Big\{\mathrm{i}T^a\Big(U_i(x+\hat{0})U_i^\dagger(x) - U_i(x)U_i^\dagger(x) \\
& - U_i^\dagger(x-\hat{i})U_i(x+\hat{0}-\hat{i}) \\
& + U_i^\dagger(x-\hat{i})U_i(x-\hat{i})\Big)\Big\} \\
= & \frac{2a_\sigma}{g}\sum_i\operatorname{Re}\operatorname{Tr}\Big\{\mathrm{i}T^a\Big(\dot{U}_i(x)U_i^\dagger(x) - U_i^\dagger(x-\hat{i})\dot{U}_i(x-\hat{i})
\end{aligned}$$

$$\times U_i^\dagger(x-\hat{i})U_i(x-\hat{i})\Big)\Big\}$$
$$= -\frac{2}{g}\sum_i \mathrm{Re}\,\mathrm{Tr}\Big\{T^a\Big(E_i(x) - U_i^\dagger(x-\hat{i})E_i(x-\hat{i})$$
$$\times U_i(x-\hat{i})\Big)\Big\}, \tag{D.23}$$

where we used the unitarity of the links $U_i U_i^\dagger = \mathbb{1}$ and applied their equation of motion (D.17). The fermionic contribution reads

$$\left(\partial_0 \frac{\delta L_\mathrm{F}^\mathrm{M}}{\delta \dot{A}_0^a(x)} - \frac{\delta L_\mathrm{F}^\mathrm{M}}{\delta A_0^a(x)}\right)_{A_0^a=0} = \frac{g}{2}\sum_{\mathbf{y}} \overline{\psi}(y)\gamma_0\Big(T^b U_0(y)\psi(y+\hat{0})\delta_{x,y}\delta^{ab}$$
$$+ U_0^\dagger(y-\hat{0})T^b\psi(y-\hat{0})\delta_{x,y-\hat{0}}\delta^{ab}\Big)_{U_0=\mathbb{1}}$$
$$= \frac{g}{2}\Big(\overline{\psi}(x)\gamma_0 T^a\psi(x+\hat{0}) + \overline{\psi}(x+\hat{0})\gamma_0 T^a\psi(x)\Big). \tag{D.24}$$

Finally, Gauss law takes the form

$$0 = \sum_i \mathrm{Re}\,\mathrm{Tr}\Big\{T^a\Big(E_i(x) - U_i^\dagger(x-\hat{i})E_i(x-\hat{i})U_i(x-\hat{i})\Big)\Big\}$$
$$- \frac{N_c}{2\beta}\Big(\overline{\psi}(x)\gamma_0 T^a\psi(x+\hat{0}) + \overline{\psi}(x+\hat{0})\gamma_0 T^a\psi(x)\Big). \tag{D.25}$$

D.4 Stochastic fermions

Our semi-classical formulation of QCD is based on the introduction of stochastic fermions. In the following we derive the substitution rule $\psi \leftrightarrow \psi_\mathrm{G}$ for the correlator $\langle\overline{\psi}(x)\psi(y)\rangle$.

We insert the mode function expansion of the fermionic field (5.23) into the correlator and use that only $\langle b_s b_r^\dagger\rangle$ gives a non-vanishing contribution, which we evaluate by the anticommutator rules (5.22). Performing one momentum integral as well as one spin sum gives

$$\langle\overline{\psi}(x)\psi(y)\rangle\big|_{x_0=y_0} = \int \frac{\mathrm{d}^3p}{(2\pi)^3}\,\frac{1}{2p_0}\sum_s \bar{v}_s(\mathbf{p})v_s(\mathbf{p})\mathrm{e}^{-\mathrm{i}\mathbf{p}(\mathbf{x}-\mathbf{y})}. \tag{D.26}$$

With the normalisation of the spinors (5.32) follows

$$\langle\overline{\psi}(x)\psi(y)\rangle\big|_{x_0=y_0} = -\int \frac{\mathrm{d}^3p}{(2\pi)^3}\,\frac{2m}{p_0}\mathrm{e}^{-i\mathbf{p}(\mathbf{x}-\mathbf{y})}. \tag{D.27}$$

Next we evaluate the gendered correlator $\langle\overline{\psi}_\mathrm{M}(x)\psi_\mathrm{F}(y)\rangle$ in the same way. Using the mode function expansion of the gendered fermions (5.24) and the correlators of complex

random numbers (5.25) we find

$$\left\langle \overline{\psi}_{\mathrm{M}}(x)\psi_{\mathrm{F}}(y)\right\rangle\big|_{x_0=y_0} = \frac{1}{2}\int \frac{\mathrm{d}^3p}{(2\pi)^3}\,\frac{1}{2p_0}\sum_s \Big(\bar{u}_s(\mathbf{p})u_s(\mathbf{p})\mathrm{e}^{\mathrm{i}\mathbf{p}(\mathbf{x}-\mathbf{y})} - \bar{v}_s(\mathbf{p})v_s(\mathbf{p})\mathrm{e}^{-\mathrm{i}\mathbf{p}(\mathbf{x}-\mathbf{y})}\Big), \tag{D.28}$$

where we have performed one momentum integral as well as one spin sum. Inserting the normalisation of the spinors and substituting $\mathbf{p} \to -\mathbf{p}$ gives

$$\left\langle \overline{\psi}(x)\psi(y)\right\rangle\big|_{x_0=y_0} = \int \frac{\mathrm{d}^3p}{(2\pi)^3}\,\frac{2m}{p_0}\mathrm{e}^{-i\mathbf{p}(\mathbf{x}-\mathbf{y})}. \tag{D.29}$$

Thus we find the substitution rule (5.27a). The rule regarding the other correlator $\frac{1}{2}\left\langle\left[\psi_\alpha(x),\overline{\psi}_\beta(y)\right]\right\rangle$ can be found analogously.

D.5 Lattice Dirac equation

In order to solve the classical equations of motion numerically, we have to discretise the time direction as we discuss in section 5.3. Applying the central difference (3.4c) to equation (5.14) the completely discretised free ($U_i = \mathbb{1}$) Dirac equation reads

$$\begin{aligned} 0 = {} & \psi(x-\hat{0}) - \psi(x+\hat{0}) - 2\mathrm{i}\xi^{-1}m\gamma_0\psi(x) - \xi^{-1}\gamma_0\gamma_i\left(\psi(x+\hat{i}) - \psi(x-\hat{i})\right) \\ & + \mathrm{i}r\gamma_0\xi^{-1}\sum_i\left(\psi(x+\hat{i}) - 2\psi(x) + \psi(x-\hat{i})\right). \end{aligned} \tag{D.30}$$

Being interested in initial conditions allows us to evaluate the Dirac equation at $t = 0$. By inserting the ansatz $\psi(t=0,\mathbf{x}) = u(\mathbf{p})\exp(\mathrm{i}\mathbf{p}\mathbf{x})$ we find

$$\begin{aligned} 0 = {} & u(\mathbf{p})\mathrm{e}^{\mathrm{i}\mathbf{p}\mathbf{x}}\Big\{\left(\mathrm{e}^{\mathrm{i}p_0a_\tau} - \mathrm{e}^{-\mathrm{i}p_0a_\tau}\right) - 2\mathrm{i}\xi^{-1}m\gamma_0 - \xi^{-1}\gamma_0\sum_i\gamma_i\left(\mathrm{e}^{\mathrm{i}p_ia_\sigma} - \mathrm{e}^{-\mathrm{i}p_ia_\sigma}\right) \\ & + \mathrm{i}r\gamma_0\xi^{-1}\sum_i\left(\mathrm{e}^{\mathrm{i}p_ia_\sigma} - 2 + \mathrm{e}^{-\mathrm{i}p_ia_\sigma}\right)\Big\} \end{aligned} \tag{D.31}$$

$$\begin{aligned} = {} & 2\mathrm{i}\xi^{-1}\Big\{\xi^{-1}\sin(a_\tau p_0) - m\gamma_0 - \gamma_0\sum_i\gamma_i\sin(a_\sigma p_i) \\ & - r\gamma_0\sum_i\left(1-\cos(a_\sigma p_i)\right)\Big\}u(\mathbf{p})\mathrm{e}^{\mathrm{i}\mathbf{p}\mathbf{x}}. \end{aligned} \tag{D.32}$$

Introducing the notation

$$s_0 \equiv \xi\sin(a_\tau p_0), \qquad s_i \equiv \sin(a_\sigma p_i), \qquad \mu \equiv m + r\sum_i\left(1-\cos(a_\sigma p_i)\right), \tag{D.33}$$

for lattice momenta and the mass including the Wilson term, we recover the usual continuum Dirac equation in momentum space

$$(\gamma_\mu s^\mu - \mu)u(\mathbf{p}) = 0. \tag{D.34}$$

Making an ansatz

$$u(\mathbf{p}) = \begin{pmatrix} \varphi \\ \xi \end{pmatrix} \tag{D.35}$$

for the spinor field $u(\mathbf{p})$ we find the following solutions of the Dirac equation

$$u^s(\mathbf{p}) = \begin{pmatrix} s_0(\mathbf{p}) + \mu(\mathbf{p}) \\ \sigma_i s_i(\mathbf{p}) \end{pmatrix} \xi^s, \qquad \text{with} \quad \xi^0 = \begin{pmatrix} 1 \\ 0 \end{pmatrix}, \quad \xi^1 = \begin{pmatrix} 0 \\ 1 \end{pmatrix} \tag{D.36}$$

with the Pauli matrices (A.8). We obtain the solutions for antiparticles from the Dirac equation with $\mu \to -\mu$. They read

$$v^s(\mathbf{p}) = \begin{pmatrix} \sigma_i s_i(\mathbf{p}) \\ s_0(\mathbf{p}) + \mu(\mathbf{p}) \end{pmatrix} \xi^s. \tag{D.37}$$

Their explicit form is given in equation (5.30) with a normalisation according to (5.32) by the normalisation factor (5.31).

E Isotropisation of the quark-gluon plasma: Numeric details

E.1 Poisson equation

Setting up the colour glass condensate inspired initial conditions, see section 6.2.1, requires solving the Poisson equation

$$\frac{\mathrm{d}^2\phi(x)}{\mathrm{d}x^2} = \rho(x). \tag{E.1}$$

Firstly, we illustrate the idea in the continuous one dimensional case. Performing the Fourier transform (A.15) on both $\phi(x)$ and $\rho(x)$ one finds

$$\phi(k) = -\frac{\rho(k)}{k^2}. \tag{E.2}$$

Going back to position space by another Fourier transform, the solution to the Poisson equation reads

$$\phi(x) = -\frac{1}{2\pi}\int \mathrm{d}k\ \frac{\sigma(k)}{k^2}\mathrm{e}^{\mathrm{i}kx}. \tag{E.3}$$

The two-dimensional Poisson equation on the lattice (6.6a), which we are interested in, reads

$$\begin{aligned}\frac{1}{a_\sigma^2}\big(&\phi(x+1,y)+\phi(x-1,y)-2\phi(x,y)\\ &+\phi(x,y+1)+\phi(x,y-1)-2\phi(x,y)\big) = -\rho(x,y).\end{aligned} \tag{E.4}$$

As in the continuous case we obtain the solution by going to momentum space using the discrete Fourier transform (A.18). Employing periodic boundary conditions a separation of variables gives the solution in momentum space

$$\phi(k_x,k_y) = \frac{a_\sigma^2\rho(k_x,ky)}{4-\mathrm{e}^{-\mathrm{i}k_x}-\mathrm{e}^{\mathrm{i}k_x}-\mathrm{e}^{-\mathrm{i}k_y}-\mathrm{e}^{\mathrm{i}k_x}}, \tag{E.5}$$

with the Fourier transformed source $\rho(k_x,k_y)$. The solution in position space is obtained by another Fourier transform $\phi(k_x,k_y)\to\phi(x,y)$.

E.2 Investigation of discretisation artefacts

Starting from the initial conditions discussed in section 6.2.1 we investigate the effect of discretisation errors. To this end we compute the total energy density (6.21c) and

the ratio of pressures (6.23) for different anisotropies ξ and transversal volumes $N_\perp^2$. The simulation parameters are listed table in E.1. As shown in figure E.1 and E.2 discretisation errors for the energy density are negligible compared to the statistical errors. Regarding the pressure ratio we are not able to resolve any discretisation errors.

Run	$g^2\mu^{\mathrm{L}}$	$N_\perp$	N_z	ξ	Δ	N_{ens}	$\mathrm{N}_{\mathrm{time}}$
Anisotropy	5	24	48	16, 20, 25	0.6	5	1600, 2000, 2500
Volume	3.75	24, 32, 40	96	20	0.6	5	4000

Table E.1: Parameters for runs checking discretisation effects. In order to check for volume effects we run three simulation on different transverse lattice sizes $N_\perp$. To check effects of the temporal discretisation we vary the anisotropy ξ and concomitant the number of time steps N_{time}.

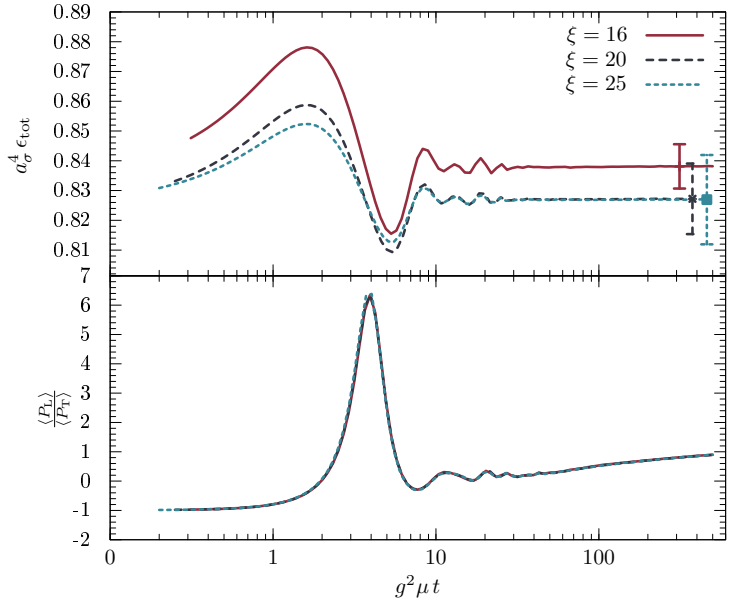

Figure E.1: Total energy density ϵ_{tot} and pressure ratio $\frac{P_{\mathrm{L}}}{P_{\mathrm{T}}}$ versus time for different anisotropies ξ. Since the statistical errors do not change significantly over time, we only show error bars at one time step in the upper plot. In the lower plot the error bars are below 1 %.

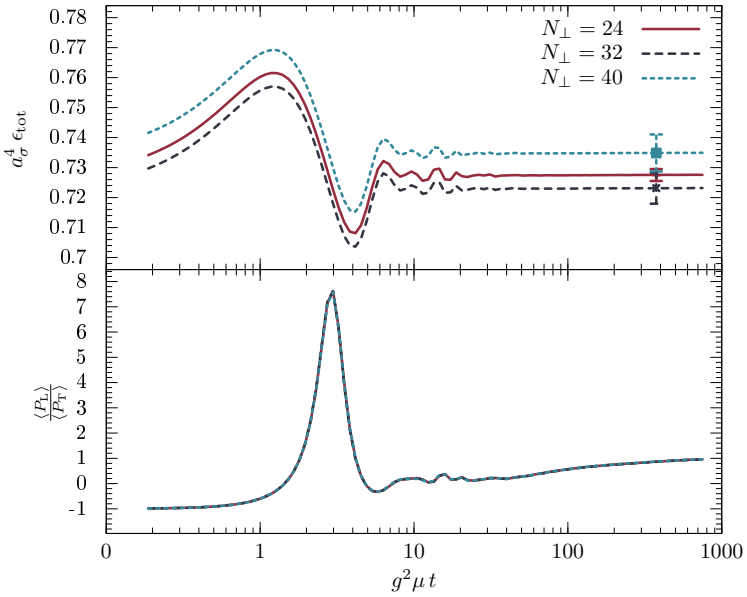

Figure E.2: Total energy density ϵ_{tot} and pressure ratio $\frac{P_\mathrm{L}}{P_\mathrm{T}}$ versus time for different transverse lattice extents N_σ. Since the statistical errors do not change significantly, we only show error bars at one time step in the upper plot. In the lower plot the error bars are below 1 %.

Bibliography

[1] D. Perkins, *Introduction to High Energy Physics*. Cambridge University Press, 2000.

[2] **Particle Data Group** Collaboration, J. Beringer et al., *Review of Particle Physics (RPP)*, *Phys.Rev.* **D86** (2012) 010001.

[3] **ATLAS Collaboration** Collaboration, G. Aad et al., *Observation of a new particle in the search for the Standard Model Higgs boson with the ATLAS detector at the LHC*, *Phys.Lett.* **B716** (2012) 1–29, [arXiv:1207.7214].

[4] **CMS Collaboration** Collaboration, S. Chatrchyan et al., *Observation of a new boson at a mass of 125 GeV with the CMS experiment at the LHC*, *Phys.Lett.* **B716** (2012) 30–61, [arXiv:1207.7235].

[5] F. Englert and R. Brout, *Broken symmetry and the mass of gauge vector mesons*, *Phys. Rev. Lett.* **13** (Aug, 1964) 321–323.

[6] P. W. Higgs, *Broken symmetries and the masses of gauge bosons*, *Phys. Rev. Lett.* **13** (Oct, 1964) 508–509.

[7] J. C. Collins and M. J. Perry, *Superdense matter: Neutrons or asymptotically free quarks?*, *Phys. Rev. Lett.* **34** (May, 1975) 1353–1356.

[8] G. Chapline and M. Nauenberg, *Asymptotic freedom and the baryon-quark phase transition*, *Phys. Rev. D* **16** (Jul, 1977) 450–456.

[9] B. A. Freedman and L. D. McLerran, *Fermions and gauge vector mesons at finite temperature and density. iii. the ground-state energy of a relativistic quark gas*, *Phys. Rev. D* **16** (Aug, 1977) 1169–1185.

[10] **PHENIX Collaboration** Collaboration, K. Adcox et al., *Formation of dense partonic matter in relativistic nucleus-nucleus collisions at RHIC: Experimental evaluation by the PHENIX collaboration*, *Nucl.Phys.* **A757** (2005) 184–283, [nucl-ex/0410003].

[11] B. Back, M. Baker, M. Ballintijn, D. Barton, B. Becker, et al., *The PHOBOS perspective on discoveries at RHIC*, *Nucl.Phys.* **A757** (2005) 28–101, [nucl-ex/0410022].

[12] **BRAHMS Collaboration** Collaboration, I. Arsene et al., *Quark gluon plasma and color glass condensate at RHIC? The Perspective from the BRAHMS experiment*, *Nucl.Phys.* **A757** (2005) 1–27, [nucl-ex/0410020].

[13] **STAR Collaboration** Collaboration, J. Adams et al., *Experimental and theoretical challenges in the search for the quark gluon plasma: The STAR Collaboration's critical assessment of the evidence from RHIC collisions*, *Nucl.Phys.* **A757** (2005) 102–183, [nucl-ex/0501009].

[14] J. Rafelski and B. Müller, *Strangeness production in the quark-gluon plasma*, *Phys. Rev. Lett.* **48** (Apr, 1982) 1066–1069.

[15] M. Gyulassy and M. Plumer, *Jet Quenching in Dense Matter*, *Phys.Lett.* **B243** (1990) 432–438.

[16] T. Matsui and H. Satz, *J/ψ Suppression by Quark-Gluon Plasma Formation*, *Phys.Lett.* **B178** (1986) 416.

[17] K. Fukushima and T. Hatsuda, *The phase diagram of dense QCD*, *Rept.Prog.Phys.* **74** (2011) 014001, [arXiv:1005.4814].

[18] M. Stephanov, *QCD phase diagram: An Overview*, *PoS* **LAT2006** (2006) 024, [hep-lat/0701002].

[19] C. Gattringer and C. Lang, *Quantum Chromodynamics on the Lattice: An Introductory Presentation*. Lecture notes in physics. Springer Berlin Heidelberg, 2010.

[20] Y. Aoki, G. Endrodi, Z. Fodor, S. Katz, and K. Szabo, *The Order of the quantum chromodynamics transition predicted by the standard model of particle physics*, *Nature* **443** (2006) 675–678, [hep-lat/0611014].

[21] P. de Forcrand, *Simulating QCD at finite density*, *PoS* **LAT2009** (2009) 010, [arXiv:1005.0539].

[22] S. P. Klevansky, *The nambu—jona-lasinio model of quantum chromodynamics*, *Rev. Mod. Phys.* **64** (Jul, 1992) 649–708.

[23] G. Aarts, *Developments in lattice QCD for matter at high temperature and density*, arXiv:1312.0968.

[24] D. Sexty, *Simulating full QCD at nonzero density using the complex Langevin equation*, arXiv:1307.7748.

[25] M. Fromm, J. Langelage, S. Lottini, M. Neuman, and O. Philipsen, *Onset Transition to Cold Nuclear Matter from Lattice QCD with Heavy Quarks*, *Phys.Rev.Lett.* **110** (2013), no. 12 122001, [arXiv:1207.3005].

[26] T. Kloiber and C. Gattringer, *Dual Methods for Lattice Field Theories at Finite Density*, arXiv:1310.8535.

[27] A. Kurkela, P. Romatschke, and A. Vuorinen, *Cold Quark Matter*, *Phys.Rev.* **D81** (2010) 105021, [arXiv:0912.1856].

[28] N. Haque, M. G. Mustafa, and M. Strickland, *Two-loop HTL pressure at finite temperature and chemical potential*, *Phys.Rev.* **D87** (2013) 105007, [arXiv:1212.1797].

[29] N. Haque, J. O. Andersen, M. G. Mustafa, M. Strickland, and N. Su, *Three-loop HTLpt Pressure and Susceptibilities at Finite Temperature and Density*, arXiv:1309.3968.

[30] P. Romatschke and U. Romatschke, *Viscosity Information from Relativistic Nuclear Collisions: How Perfect is the Fluid Observed at RHIC?*, *Phys.Rev.Lett.* **99** (2007) 172301, [arXiv:0706.1522].

[31] D. Teaney, J. Lauret, and E. V. Shuryak, *Flow at the SPS and RHIC as a quark gluon plasma signature*, *Phys.Rev.Lett.* **86** (2001) 4783–4786, [nucl-th/0011058].

[32] P. Huovinen, P. Kolb, U. W. Heinz, P. Ruuskanen, and S. Voloshin, *Radial and elliptic flow at RHIC: Further predictions*, *Phys.Lett.* **B503** (2001) 58–64, [hep-ph/0101136].

[33] P. Kolb, U. W. Heinz, P. Huovinen, K. Eskola, and K. Tuominen, *Centrality dependence of multiplicity, transverse energy, and elliptic flow from hydrodynamics*, *Nucl.Phys.* **A696** (2001) 197–215, [hep-ph/0103234].

[34] T. Hirano and K. Tsuda, *Collective flow and two pion correlations from a relativistic hydrodynamic model with early chemical freezeout*, *Phys.Rev.* **C66** (2002) 054905, [nucl-th/0205043].

[35] P. F. Kolb and R. Rapp, *Transverse flow and hadrochemistry in Au+Au collisions at (S(NN))**(1/2) = 200-GeV*, *Phys.Rev.* **C67** (2003) 044903, [hep-ph/0210222].

[36] U. W. Heinz and R. Snellings, *Collective flow and viscosity in relativistic heavy-ion collisions*, *Annu. Rev. Nucl. Part. Sci.* **63** (2013) 123–151, [arXiv:1301.2826].

[37] Y. Aoki, Z. Fodor, S. Katz, and K. Szabo, *The Equation of state in lattice QCD: With physical quark masses towards the continuum limit*, *JHEP* **0601** (2006) 089, [hep-lat/0510084].

[38] S. Durr, Z. Fodor, J. Frison, C. Hoelbling, R. Hoffmann, et al., *Ab-Initio Determination of Light Hadron Masses*, *Science* **322** (2008) 1224–1227, [arXiv:0906.3599].

[39] H. B. Meyer, *A Calculation of the shear viscosity in SU(3) gluodynamics*, *Phys.Rev.* **D76** (2007) 101701, [arXiv:0704.1801].

[40] A. Amato, G. Aarts, C. Allton, P. Giudice, S. Hands, et al., *Electrical conductivity of the quark-gluon plasma across the deconfinement transition*, arXiv:1307.6763.

[41] A. Francis and O. Kaczmarek, *On the temperature dependence of the electrical conductivity in hot quenched lattice QCD*, *Prog.Part.Nucl.Phys.* **67** (2012) 212–217, [arXiv:1112.4802].

[42] O. Philipsen and C. Schäfer, *The second order hydrodynamic transport coefficient κ for the gluon plasma from the lattice*, *JHEP* **1402** (2014) 003, [arXiv:1311.6618].

[43] E. Shuryak, *Physics of Strongly coupled Quark-Gluon Plasma*, *Prog.Part.Nucl.Phys.* **62** (2009) 48–101, [arXiv:0807.3033].

[44] P. B. Arnold, J. Lenaghan, G. D. Moore, and L. G. Yaffe, *Apparent thermalization due to plasma instabilities in quark-gluon plasma*, *Phys.Rev.Lett.* **94** (2005) 072302, [nucl-th/0409068].

[45] A. Mueller, A. Shoshi, and S. Wong, *A Possible modified 'bottom-up' thermalization in heavy ion collisions*, *Phys.Lett.* **B632** (2006) 257–260, [hep-ph/0505164].

[46] D. Bodeker, *The Impact of QCD plasma instabilities on bottom-up thermalization*, *JHEP* **0510** (2005) 092, [hep-ph/0508223].

[47] A. Rebhan, P. Romatschke, and M. Strickland, *Dynamics of quark-gluon-plasma instabilities in discretized hard-loop approximation*, *JHEP* **0509** (2005) 041, [hep-ph/0505261].

[48] P. B. Arnold, G. D. Moore, and L. G. Yaffe, *The Fate of non-Abelian plasma instabilities in 3+1 dimensions*, *Phys.Rev.* **D72** (2005) 054003, [hep-ph/0505212].

[49] M. Attems, A. Rebhan, and M. Strickland, *Instabilities of an anisotropically expanding non-Abelian plasma: 3D+3V discretized hard-loop simulations*, *Phys.Rev.* **D87** (2013) 025010, [arXiv:1207.5795].

[50] A. Rebhan, M. Strickland, and M. Attems, *Instabilities of an anisotropically expanding non-Abelian plasma: 1D+3V discretized hard-loop simulations*, *Phys.Rev.* **D78** (2008) 045023, [arXiv:0802.1714].

[51] P. Romatschke and A. Rebhan, *Plasma Instabilities in an Anisotropically Expanding Geometry*, *Phys.Rev.Lett.* **97** (2006) 252301, [hep-ph/0605064].

[52] J. Berges, S. Scheffler, and D. Sexty, *Bottom-up isotropization in classical-statistical lattice gauge theory*, *Phys.Rev.* **D77** (2008) 034504, [arXiv:0712.3514].

[53] J. Berges, D. Gelfand, S. Scheffler, and D. Sexty, *Simulating plasma instabilities in SU(3) gauge theory*, *Phys.Lett.* **B677** (2009) 210–213, [arXiv:0812.3859].

[54] P. Romatschke and R. Venugopalan, *Collective non-Abelian instabilities in a melting color glass condensate*, *Phys.Rev.Lett.* **96** (2006) 062302, [hep-ph/0510121].

[55] P. Romatschke and R. Venugopalan, *The Unstable Glasma*, *Phys.Rev.* **D74** (2006) 045011, [hep-ph/0605045].

[56] K. Fukushima and F. Gelis, *The evolving Glasma*, *Nucl.Phys.* **A874** (2012) 108–129, [arXiv:1106.1396].

[57] J. Berges, K. Boguslavski, S. Schlichting, and R. Venugopalan, *Universal attractor in a highly occupied non-Abelian plasma*, arXiv:1311.3005.

[58] T. Epelbaum and F. Gelis, *Pressure isotropization in high energy heavy ion collisions*, *Phys.Rev.Lett.* **111** (2013) 232301, [arXiv:1307.2214].

[59] K. Fukushima, *Evolving Glasma and Kolmogorov Spectrum*, *Acta Phys.Polon.* **B42** (2011) 2697–2715, [arXiv:1111.1025].

[60] K. Fukushima, *Turbulent pattern formation and diffusion in the early-time dynamics in the relativistic heavy-ion collision*, *Phys.Rev.* **C89** (2014) 024907, [arXiv:1307.1046].

[61] E. Iancu and R. Venugopalan, *The Color glass condensate and high-energy scattering in QCD*, hep-ph/0303204.

[62] F. Gelis, E. Iancu, J. Jalilian-Marian, and R. Venugopalan, *The Color Glass Condensate*, *Ann.Rev.Nucl.Part.Sci.* **60** (2010) 463–489, [arXiv:1002.0333].

[63] F. Gelis, *Color Glass Condensate and Glasma*, *Int.J.Mod.Phys.* **A28** (2013) 1330001, [arXiv:1211.3327].

[64] S. Borsanyi and M. Hindmarsh, *Low-cost fermions in classical field simulations*, *Phys.Rev.* **D79** (2009) 065010, [arXiv:0809.4711].

[65] M. Gell-Mann, *Symmetries of baryons and mesons*, *Phys. Rev.* **125** (1962), no. 3 1067–1084.

[66] Y. Ne'eman, *Deviations of strong interactions from a gauge invariance*, *Nucl. Phys.* **26** (1961), no. 222-229.

[67] M. Gell-Mann, *A schematic model of baryons and mesons*, *Phys. Lett.* **8** (1964), no. 214-215.

[68] G. Zweig, *An su(3) model for strong interaction symmetry and its breaking*, .

[69] N. Yang, C. and Mills, R. L., *Conservation of isotopic spin and isotopic gauge invariance*, *Phys. Rev.* **96** (1954), no. 1 191–195.

[70] D. J. Gross and F. Wilczek, *Ultraviolet behavior of non-abelian gauge theories*, *Phys. Rev. Lett.* **30** (1973) 1343–1346.

[71] H. D. Politzer, *Reliable perturbative results for strong interactions?*, *Phys. Rev. Lett.* **30** (1973) 1346–1349.

[72] G. 'tHooft, *Renormalization of massless yang-mills fields*, *Nuclear Physics B* **33** (1971), no. 1 173 – 199.

[73] G. 'tHooft, *Renormalizable lagrangians for massive yang-mills fields*, *Nuclear Physics B* **35** (1971), no. 1 167 – 188.

[74] M. Peskin and D. Schroeder, *An Introduction to Quantum Field Theory*. Advanced book classics. Addison-Wesley Publishing Company, 1995.

[75] T. Cheng and L. Li, *Gauge Theory of Elementary Particle Physics*. Oxford Science Publications. Clarendon Press, 1984.

[76] L. Ryder, *Quantum Field Theory*. Cambridge University Press, 1996.

[77] I. Kapusta, J. and Gale, C, *Finite-Temperature Field Theory. Principles and Applications*. Cambridge University Press, New York, 2. ed., 2006.

[78] M. Laine, "Basics of thermal field theory, a tutorial on perturbative computations." `http://www.laine.itp.unibe.ch/basics.pdf`, 2013. (Accessed: 8.01.2014).

[79] M. Le Bellac, *Thermal Field Theory*. Cambridge University Press, Cambridge, 1996.

[80] P. B. Arnold, G. D. Moore, and L. G. Yaffe, *Transport coefficients in high temperature gauge theories. 1. Leading log results*, *JHEP* **0011** (2000) 001, [hep-ph/0010177].

[81] P. B. Arnold, G. D. Moore, and L. G. Yaffe, *Transport coefficients in high temperature gauge theories. 2. Beyond leading log*, *JHEP* **0305** (2003) 051, [hep-ph/0302165].

[82] H. B. Meyer, *Transport Properties of the Quark-Gluon Plasma: A Lattice QCD Perspective*, *Eur.Phys.J.* **A47** (2011) 86, [arXiv:1104.3708].

[83] J. Berges, *Introduction to nonequilibrium quantum field theory*, *AIP Conf.Proc.* **739** (2005) 3–62, [hep-ph/0409233].

[84] N. Landsman and C. van Weert, *Real- and imaginary-time field theory at finite temperature and density*, *Physics Reports* **145** (1987), no. 3–4 141 – 249.

[85] G. Aarts and J. Smit, *Classical approximation for time dependent quantum field theory: Diagrammatic analysis for hot scalar fields*, *Nucl.Phys.* **B511** (1998) 451–478, [hep-ph/9707342].

[86] M. Laine, G. D. Moore, O. Philipsen, and M. Tassler, *Heavy Quark Thermalization in Classical Lattice Gauge Theory: Lessons for Strongly-Coupled QCD*, *JHEP* **0905** (2009) 014, [arXiv:0902.2856].

[87] E. Braaten and R. D. Pisarski, *Deducing Hard Thermal Loops From Ward Identities*, *Nucl.Phys.* **B339** (1990) 310–324.

[88] E. Braaten and R. D. Pisarski, *Simple effective Lagrangian for hard thermal loops*, *Phys.Rev.* **D45** (1992) 1827–1830.

[89] J.-P. Blaizot and E. Iancu, *The Quark gluon plasma: Collective dynamics and hard thermal loops*, *Phys.Rept.* **359** (2002) 355–528, [hep-ph/0101103].

[90] T. Appelquist and R. D. Pisarski, *Hot yang-mills theories and three-dimensional qcd*, *Phys. Rev.* **D23** (1981).

[91] P. H. Ginsparg, *First Order and Second Order Phase Transitions in Gauge Theories at Finite Temperature*, *Nucl.Phys.* **B170** (1980) 388.

[92] A. D. Linde, *Infrared Problem in Thermodynamics of the Yang-Mills Gas*, *Phys.Lett.* **B96** (1980) 289.

[93] D. Bieletzki, K. Lessmeier, O. Philipsen, and Y. Schroder, *Resummation scheme for 3d Yang-Mills and the two-loop magnetic mass for hot gauge theories*, *JHEP* **1205** (2012) 058, [arXiv:1203.6538].

[94] D. Y. Grigoriev and V. Rubakov, *Soliton Pair Creation at Finite Temperatures. Numerical Study in (1+1)-dimensions*, *Nucl.Phys.* **B299** (1988) 67–78.

[95] D. Bodeker, *Classical real time correlation functions and quantum corrections at finite temperature*, *Nucl.Phys.* **B486** (1997) 500–514, [hep-th/9609170].

[96] I. Montvay and G. Münster, *Quantum Fields on a Lattice*. Cambridge Monographs on Mathematical Physics. Cambridge University Press, 1994.

[97] T. DeGrand and DeTar, C., *Lattice Methods for Quantum Chromodynamics*. World Scientific Publishing, Singapur, 2006.

[98] H. Rothe, *Lattice Gauge Theories: An Introduction*. Lattice Gauge Theories: An Introduction. World Scientific, 2005.

[99] G. Wilson, K. *Confinement of quarks*, *Phys. Rev. D* **10** (1974), no. 8 2445–2459.

[100] **CP-PACS Collaboration** Collaboration, Y. Namekawa et al., *Thermodynamics of SU(3) gauge theory on anisotropic lattices*, *Phys.Rev.* **D64** (2001) 074507, [hep-lat/0105012].

[101] R. Sommer, *A New way to set the energy scale in lattice gauge theories and its applications to the static force and alpha-s in SU(2) Yang-Mills theory*, *Nucl.Phys.* **B411** (1994) 839–854, [hep-lat/9310022].

[102] **APE Collaboration** Collaboration, M. Albanese et al., *Glueball Masses and String Tension in Lattice QCD*, *Phys.Lett.* **B192** (1987) 163–169.

[103] T. R. Klassen, *The Anisotropic Wilson gauge action*, *Nucl.Phys.* **B533** (1998) 557–575, [hep-lat/9803010].

[104] S. Capitani, *Lattice perturbation theory*, *Phys. Rept.* **382** (2003) 113–302, [hep-lat/0211036].

[105] G. C. Wick, *The evaluation of the collision matrix*, *Phys. Rev.* **80** (1950) 268.

[106] D. Faddeev, L. and Popov, V. N., *Feynman diagrams for the yang-mills field*, *Physics Letters B* **25** (1967), no. 1 29 – 30.

[107] K. Rummukainen, "Monte carlo simulations in physics." http://cc.oulu.fi/~tf/tiedostot/pub/montecarlo/. (Accessed 14.3.2014).

[108] M. Creutz, *Monte carlo study of quantized su(2) gauge theory*, *Phys. Rev. D* **21** (1980), no. 8 2308–2315.

[109] D. Kennedy, A. and Pendleton, B. J., *Improved heatbath method for monte carlo calculations in lattice gauge theories*, *Phys. Lett.* **156B** (1985), no. 5,6 393–399.

[110] N. Cabibbo and E. Marinari, *A new method for updating su(n) matrices in computer simulations of gauge theories*, *Phys. Lett.* **119B** (1982), no. 4,5,6 387–390.

[111] G. Edwards, R. and Joo, B., *The chroma software system for lattice qcd*, *Nuclear Physics B - Proceedings Supplements* **140** (2005) 832.

[112] "Juropa." http://www.fz-juelich.de/ias/jsc/EN/Expertise/Supercomputers/JUROPA/JUROPA_node.html. Accessed: 2014-03-07.

[113] "Juqueen." http://www.fz-juelich.de/ias/jsc/EN/Expertise/Supercomputers/JUQUEEN/JUQUEEN_node.html. Accessed: 2014-03-07.

[114] "Loewe-csc." http://csc.uni-frankfurt.de/?id=51. Accessed: 2014-03-07.

[115] P. Romatschke, *New Developments in Relativistic Viscous Hydrodynamics*, *Int. J. Mod. Phys.* **E19** (2010) 1–53, [arXiv:0902.3663].

[116] L. D. Landau and E. M. Lifshitz, *Fluid Mechanics, Second Edition: Volume 6 (Course of Theoretical Physics)*. Course of theoretical physics / by L. D. Landau and E. M. Lifshitz, Vol. 6. Butterworth-Heinemann, 2 ed., Jan., 1987.

[117] M. Kranyš, *Relativistic hydrodynamics with irreversible thermodynamics without the paradox of infinite velocity of heat conduction*, *Il Nuovo Cimento B Series 10* **42** (1966), no. 1 51–70.

[118] B. Betz, D. Henkel, and D. Rischke, *From kinetic theory to dissipative fluid dynamics*, *Prog.Part.Nucl.Phys.* **62** (2009) 556–561, [arXiv:0812.1440].

[119] I. Muller, *Zum Paradoxon der Warmeleitungstheorie*, *Z.Phys.* **198** (1967) 329–344.

[120] W. Israel and J. Stewart, *Transient relativistic thermodynamics and kinetic theory*, *Annals Phys.* **118** (1979) 341–372.

[121] R. Baier, Romatschke, P., Son, D. T., Starinets, A. O., and Stephanov, M. A., *Relativistic viscous hydrodynamics, conformal invariance, and holography*, *JHEP* **04** (2008) 100, [arXiv:0712.2451].

[122] G. D. Moore and K. A. Sohrabi, *Thermodynamical second-order hydrodynamic coefficients*, *JHEP* **1211** (2012) 148, [arXiv:1210.3340].

[123] R. Kubo, *Statistical-mechanical theory of irreversible processes. i. general theory and simple applications to magnetic and conduction problems*, *Journal of the Physical Society of Japan* **12** (1957), no. 6 570–586, [http://journals.jps.jp/doi/pdf/10.1143/JPSJ.12.570].

[124] G. D. Moore and K. A. Sohrabi, *Kubo Formulae for Second-Order Hydrodynamic Coefficients*, *Phys.Rev.Lett.* **106** (2011) 122302, [arXiv:1007.5333].

[125] Y. Kohno, M. Asakawa, and M. Kitazawa, *Shear viscosity to relaxation time ratio in SU(3) lattice gauge theory*, arXiv:1112.1508.

[126] S. Caron-Huot, *Asymptotics of thermal spectral functions*, *Phys.Rev.* **D79** (2009) 125009, [arXiv:0903.3958].

[127] S. Bhattacharyya, *Constraints on the second order transport coefficients of an uncharged fluid*, *JHEP* **1207** (2012) 104, [arXiv:1201.4654].

[128] K. Jensen, M. Kaminski, P. Kovtun, R. Meyer, A. Ritz, et al., *Towards hydrodynamics without an entropy current*, *Phys.Rev.Lett.* **109** (2012) 101601, [arXiv:1203.3556].

[129] G. Munoz, *Lagrangian field theories and energy-momentum tensors*, *American Journal of Physics* **64** (1996), no. 9 1153–1157.

[130] P. Romatschke and Son, D. T., *Spectral sum rules for the quark-gluon plasma*, *Phys.Rev.* **D80** (2009) 065021, [arXiv:0903.3946].

[131] J. M. Maldacena, *The Large N limit of superconformal field theories and supergravity*, *Adv.Theor.Math.Phys.* **2** (1998) 231–252, [hep-th/9711200].

[132] O. Aharony, S. S. Gubser, J. M. Maldacena, H. Ooguri, and Y. Oz, *Large N field theories, string theory and gravity*, *Phys.Rept.* **323** (2000) 183–386, [hep-th/9905111].

[133] E. D'Hoker and D. Z. Freedman, *Supersymmetric gauge theories and the AdS / CFT correspondence*, hep-th/0201253.

[134] S. Borsanyi, G. Endrodi, Z. Fodor, S. Katz, and K. Szabo, *Precision SU(3) lattice thermodynamics for a large temperature range*, *JHEP* **1207** (2012) 056, [arXiv:1204.6184].

[135] S. Caracciolo, G. Curci, P. Menotti, and A. Pelissetto, *The restoration of poincare invariance and the energy momentum tensor in lattice gauge theories*, *Nucl.Phys.Proc.Suppl.* **17** (1990) 611–614.

[136] F. Karsch and H. Wyld, *Thermal Green's Functions and Transport Coefficients on the Lattice*, *Phys.Rev.* **D35** (1987) 2518.

[137] H. B. Meyer, *Cutoff Effects on Energy-Momentum Tensor Correlators in Lattice Gauge Theory*, *JHEP* **0906** (2009) 077, [arXiv:0904.1806].

[138] M. Luscher, S. Sint, R. Sommer, and P. Weisz, *Chiral symmetry and O(a) improvement in lattice QCD*, *Nucl.Phys.* **B478** (1996) 365–400, [hep-lat/9605038].

[139] H. B. Meyer, *Energy-momentum tensor correlators and viscosity*, *PoS* **LATTICE2008** (2008) 017, [arXiv:0809.5202].

[140] P. Kaste and Rothe, H. J., *Lattice artefacts in the non-Abelian Debye screening mass in one loop order*, *Phys. Rev.* **D56** (1997) 6804–6815, [hep-lat/9704014].

[141] H. Elze, K. Kajantie, and J. I. Kapusta, *Screening and Plasmon in QCD on a Finite Lattice*, *Nucl.Phys.* **B304** (1988) 832.

[142] J. Engels, F. Karsch, and H. Satz, *Finite Size Effects in Euclidean Lattice Thermodynamics for Noninteracting Bose and Fermi Systems*, *Nucl.Phys.* **B205** (1982) 239.

[143] C. Allton, *Lattice Monte Carlo data versus perturbation theory*, hep-lat/9610016.

[144] B. Lucini, M. Teper, and U. Wenger, *Topology of SU(N) gauge theories at T = 0 and T = T(c)*, *Nucl.Phys.* **B715** (2005) 461–482, [hep-lat/0401028].

[145] G. Boyd et al., *Thermodynamics of SU(3) Lattice Gauge Theory*, *Nucl. Phys.* **B469** (1996) 419–444, [hep-lat/9602007].

[146] S. Datta and S. Gupta, *Does the QCD plasma contain gluons?*, *Phys.Rev.* **D67** (2003) 054503, [hep-lat/0208001].

[147] **WHOT-QCD Collaboration** Collaboration, Y. Maezawa et al., *Electric and Magnetic Screening Masses at Finite Temperature from Generalized Polyakov-Line Correlations in Two-flavor Lattice QCD*, *Phys.Rev.* **D81** (2010) 091501, [arXiv:1003.1361].

[148] J. Langelage, G. Munster, and O. Philipsen, *Strong coupling expansion for finite temperature Yang-Mills theory in the confined phase*, *JHEP* **0807** (2008) 036, [arXiv:0805.1163].

[149] W. H. Press, S. A. Teukolsky, W. T. Vetterling, and B. P. Flannery, *Numerical Recipes 3rd Edition: The Art of Scientific Computing*. Cambridge University Press, New York, NY, USA, 3 ed., 2007.

[150] **APE Collaboration** Collaboration, M. Albanese et al., *Glueball Masses and String Tension in Lattice QCD*, *Phys.Lett.* **B192** (1987) 163–169.

[151] A. Hasenfratz and F. Knechtli, *Flavor symmetry and the static potential with hypercubic blocking*, *Phys.Rev.* **D64** (2001) 034504, [hep-lat/0103029].

[152] C. Morningstar and M. J. Peardon, *Analytic smearing of SU(3) link variables in lattice QCD*, *Phys.Rev.* **D69** (2004) 054501, [hep-lat/0311018].

[153] L. Giusti and H. B. Meyer, *Implications of Poincare symmetry for thermal field theories in finite-volume*, *JHEP* **1301** (2013) 140, [arXiv:1211.6669].

[154] K. Symanzik, *Continuum Limit and Improved Action in Lattice Theories. 1. Principles and phi**4 Theory*, *Nucl.Phys.* **B226** (1983) 187.

[155] K. Symanzik, *Continuum Limit and Improved Action in Lattice Theories. 2. O(N) Nonlinear Sigma Model in Perturbation Theory*, *Nucl.Phys.* **B226** (1983) 205.

[156] J. Ambjorn, T. Askgaard, H. Porter, and M. Shaposhnikov, *Sphaleron transitions and baryon asymmetry: A Numerical real time analysis*, *Nucl.Phys.* **B353** (1991) 346–378.

[157] G. D. Moore, *Measuring the broken phase sphaleron rate nonperturbatively*, *Phys.Rev.* **D59** (1999) 014503, [hep-ph/9805264].

[158] J. Ambjorn, T. Askgaard, H. Porter, and M. Shaposhnikov, *Lattice Simulations of Electroweak Sphaleron Transitions in Real Time*, *Phys.Lett.* **B244** (1990) 479–487.

[159] G. D. Moore and M. Tassler, *The Sphaleron Rate in SU(N) Gauge Theory*, *JHEP* **1102** (2011) 105, [arXiv:1011.1167].

[160] M. Laine, O. Philipsen, and M. Tassler, *Thermal imaginary part of a real-time static potential from classical lattice gauge theory simulations*, *JHEP* **0709** (2007) 066, [arXiv:0707.2458].

[161] F. Hebenstreit, J. Berges, and D. Gelfand, *Real-time dynamics of string breaking*, *Phys.Rev.Lett.* **111** (2013) 201601, [arXiv:1307.4619].

[162] G. Aarts and J. Smit, *Real time dynamics with fermions on a lattice*, *Nucl.Phys.* **B555** (1999) 355–394, [hep-ph/9812413].

[163] G. D. Moore, *Motion of Chern-Simons number at high temperatures under a chemical potential*, *Nucl.Phys.* **B480** (1996) 657–688, [hep-ph/9603384].

[164] G. D. Moore, *Real time simulations in lattice gauge theory*, *Nucl.Phys.Proc.Suppl.* **83** (2000) 131–135, [hep-lat/9907009].

[165] J.-P. Blaizot and E. Iancu, *The Quark gluon plasma: Collective dynamics and hard thermal loops*, *Phys.Rept.* **359** (2002) 355–528, [hep-ph/0101103].

[166] U. Kraemmer and A. Rebhan, *Advances in perturbative thermal field theory*, *Rept.Prog.Phys.* **67** (2004) 351, [hep-ph/0310337].

[167] J. O. Andersen and M. Strickland, *Resummation in hot field theories*, *Annals Phys.* **317** (2005) 281–353, [hep-ph/0404164].

[168] G. D. Moore and N. Turok, *Classical field dynamics of the electroweak phase transition*, *Phys.Rev.* **D55** (1997) 6538–6560, [hep-ph/9608350].

[169] G. Aarts and J. Berges, *Classical aspects of quantum fields far from equilibrium*, *Phys.Rev.Lett.* **88** (2002) 041603, [hep-ph/0107129].

[170] H. B. Nielsen and M. Ninomiya, *Absence of Neutrinos on a Lattice. 2. Intuitive Topological Proof*, *Nucl.Phys.* **B193** (1981) 173.

[171] H. B. Nielsen and M. Ninomiya, *Absence of Neutrinos on a Lattice. 1. Proof by Homotopy Theory*, *Nucl.Phys.* **B185** (1981) 20.

[172] H. B. Nielsen and M. Ninomiya, *No Go Theorem for Regularizing Chiral Fermions*, *Phys.Lett.* **B105** (1981) 219.

[173] J. B. Kogut and L. Susskind, *Hamiltonian Formulation of Wilson's Lattice Gauge Theories*, *Phys.Rev.* **D11** (1975) 395.

[174] G. Giudice, M. Peloso, A. Riotto, and I. Tkachev, *Production of massive fermions at preheating and leptogenesis*, *JHEP* **9908** (1999) 014, [hep-ph/9905242].

[175] D. Boyanovsky, H. de Vega, R. Holman, and J. Salgado, *Nonequilibrium Bose-Einstein condensates, dynamical scaling and symmetric evolution in the large N Phi**4 theory*, *Phys.Rev.* **D59** (1999) 125009, [hep-ph/9811273].

[176] J. Baacke, K. Heitmann, and C. Patzold, *Nonequilibrium dynamics of fermions in a spatially homogeneous scalar background field*, *Phys.Rev.* **D58** (1998) 125013, [hep-ph/9806205].

[177] W. Nolting, *Grundkurs Theoretische Physik 6: Statistische Physik*. Grundkurs Theoretische Physik / Wolfgang Nolting. Springer, 2005.

[178] S. Schlichting, *Non-Equilibrium Dynamics and Thermalization of Weakly Coupled Non-Abelian Plasma*. PhD thesis, 2013.

[179] J. Berges and T. Gasenzer, *Quantum versus classical statistical dynamics of an ultracold bose gas*, *Phys. Rev. A* **76** (Sep, 2007) 033604.

[180] V. Gribov, *Quantization of Nonabelian Gauge Theories*, *Nucl.Phys.* **B139** (1978) 1.

[181] L. Giusti, M. Paciello, C. Parrinello, S. Petrarca, and B. Taglienti, *Problems on lattice gauge fixing*, *Int.J.Mod.Phys.* **A16** (2001) 3487–3534, [hep-lat/0104012].

[182] J. Mandula and M. Ogilvie, *The Gluon Is Massive: A Lattice Calculation of the Gluon Propagator in the Landau Gauge*, *Phys.Lett.* **B185** (1987) 127–132.

[183] U. Wolff, *CRITICAL SLOWING DOWN*, *Nucl.Phys.Proc.Suppl.* **17** (1990) 93–102.

[184] A. D. Sokal, *How to beat critical slowing down: 1990 update*, *Nucl.Phys.Proc.Suppl.* **20** (1991) 55–67.

[185] A. Kurkela and G. D. Moore, *UV Cascade in Classical Yang-Mills Theory*, *Phys.Rev.* **D86** (2012) 056008, [arXiv:1207.1663].

[186] F. Hebenstreit, J. Berges, and D. Gelfand, *Simulating fermion production in 1+1 dimensional QED*, *Phys.Rev.* **D87** (2013) 105006, [arXiv:1302.5537].

[187] V. Kasper, F. Hebenstreit, and J. Berges, *Fermion production from real-time lattice gauge theory in the classical-statistical regime*, arXiv:1403.4849.

[188] P. M. Saffin and A. Tranberg, *Real-time Fermions for Baryogenesis Simulations*, *JHEP* **1107** (2011) 066, [arXiv:1105.5546].

[189] P. M. Saffin and A. Tranberg, *Dynamical simulations of electroweak baryogenesis with fermions*, *JHEP* **1202** (2012) 102, [arXiv:1111.7136].

[190] Z.-G. Mou, P. M. Saffin, and A. Tranberg, *Ensemble fermions for electroweak dynamics and the fermion preheating temperature*, *JHEP* **1311** (2013) 097, [arXiv:1307.7924].

[191] P. Arnold, *Hot b violation, the lattice, and hard thermal loops*, hep-ph/9701393.

[192] P. A. Dirac, *Quantized Singularities in the Electromagnetic Field*, *Proc.Roy.Soc.Lond.* **A133** (1931) 60–72.

[193] K. Huang, *Statistical Mechanics*. John Wiley & Sons, 2 ed., 1987.

[194] K. Fukushima, D. E. Kharzeev, and H. J. Warringa, *The Chiral Magnetic Effect*, *Phys.Rev.* **D78** (2008) 074033, [arXiv:0808.3382].

[195] G. Bali, F. Bruckmann, G. Endrodi, Z. Fodor, S. Katz, et al., *The QCD phase diagram for external magnetic fields*, *JHEP* **1202** (2012) 044, [arXiv:1111.4956].

[196] P. Buividovich, M. Chernodub, E. Luschevskaya, and M. Polikarpov, *Numerical evidence of chiral magnetic effect in lattice gauge theory*, *Phys.Rev.* **D80** (2009) 054503, [arXiv:0907.0494].

[197] M. Laine, G. D. Moore, O. Philipsen, and M. Tassler, *Heavy Quark Thermalization in Classical Lattice Gauge Theory: Lessons for Strongly-Coupled QCD*, *JHEP* **0905** (2009) 014, [arXiv:0902.2856].

[198] M. Tannenbaum, *Recent results in relativistic heavy ion collisions: From 'a new state of matter' to 'the perfect fluid'*, *Rept.Prog.Phys.* **69** (2006) 2005–2060, [nucl-ex/0603003].

[199] D. Teaney, J. Lauret, and E. Shuryak, *A Hydrodynamic description of heavy ion collisions at the SPS and RHIC*, nucl-th/0110037.

[200] P. M. Chesler and L. G. Yaffe, *Horizon formation and far-from-equilibrium isotropization in supersymmetric Yang-Mills plasma*, *Phys.Rev.Lett.* **102** (2009) 211601, [arXiv:0812.2053].

[201] Y. V. Kovchegov and A. Taliotis, *Early Time Dynamics in Heavy Ion Collisions from AdS/CFT Correspondence*, *Phys.Rev.* **C76** (2007) 014905, [arXiv:0705.1234].

[202] D. Grumiller and P. Romatschke, *On the collision of two shock waves in AdS(5)*, *JHEP* **0808** (2008) 027, [arXiv:0803.3226].

[203] V. Balasubramanian, A. Bernamonti, J. de Boer, N. Copland, B. Craps, et al., *Thermalization of Strongly Coupled Field Theories*, *Phys.Rev.Lett.* **106** (2011) 191601, [arXiv:1012.4753].

[204] M. P. Heller, R. A. Janik, and P. Witaszczyk, *The characteristics of thermalization of boost-invariant plasma from holography*, *Phys.Rev.Lett.* **108** (2012) 201602, [arXiv:1103.3452].

[205] R. Baier, A. H. Mueller, D. Schiff, and D. Son, *'Bottom up' thermalization in heavy ion collisions*, *Phys.Lett.* **B502** (2001) 51–58, [hep-ph/0009237].

[206] D. Molnar and M. Gyulassy, *Saturation of elliptic flow and the transport opacity of the gluon plasma at RHIC*, *Nucl.Phys.* **A697** (2002) 495–520, [nucl-th/0104073].

[207] J. Berges, K. Boguslavski, S. Schlichting, and R. Venugopalan, *Turbulent thermalization process in heavy-ion collisions at ultrarelativistic energies*, arXiv:1303.5650.

[208] T. Lappi and L. McLerran, *Some features of the glasma*, *Nucl.Phys.* **A772** (2006) 200–212, [hep-ph/0602189].

[209] **H1 and ZEUS Collaboration** Collaboration, F. Aaron et al., *Combined Measurement and QCD Analysis of the Inclusive e+- p Scattering Cross Sections at HERA*, *JHEP* **1001** (2010) 109, [arXiv:0911.0884].

[210] A. Krasnitz and R. Venugopalan, *The Initial gluon multiplicity in heavy ion collisions*, *Phys.Rev.Lett.* **86** (2001) 1717–1720, [hep-ph/0007108].

[211] U. W. Heinz, *QUARK - GLUON TRANSPORT THEORY*, *Nucl.Phys.* **A418** (1984) 603C–612C.

[212] S. Mrowczynski, *Plasma instability at the initial stage of ultrarelativistic heavy ion collisions*, *Phys.Lett.* **B314** (1993) 118–121.

[213] Y. Pokrovsky and A. Selikhov, *Filamentation in a Quark - Gluon Plasma*, *JETP Lett.* **47** (1988) 12–14.

[214] A. Kurkela and G. D. Moore, *Bjorken Flow, Plasma Instabilities, and Thermalization*, *JHEP* **1111** (2011) 120, [arXiv:1108.4684].

[215] A. Kurkela and G. D. Moore, *Thermalization in Weakly Coupled Nonabelian Plasmas*, *JHEP* **1112** (2011) 044, [arXiv:1107.5050].

[216] E. S. Weibel, *Spontaneously Growing Transverse Waves in a Plasma Due to an Anisotropic Veloc ity Distribution*, *Phys.Rev.Lett.* **2** (1959) 83–84.

[217] S. Mrowczynski, *Instabilities driven equilibration of the quark-gluon plasma*, *Acta Phys.Polon.* **B37** (2006) 427–454, [hep-ph/0511052].

[218] S. Mrowczynski, *Color filamentation in ultrarelativistic heavy ion collisions*, *Phys.Lett.* **B393** (1997) 26–30, [hep-ph/9606442].

[219] M. Strickland, *Thermalization and isotropization in heavy-ion collisions*, arXiv:1312.2285.

[220] L. D. McLerran and R. Venugopalan, *Gluon distribution functions for very large nuclei at small transverse momentum*, *Phys.Rev.* **D49** (1994) 3352–3355, [hep-ph/9311205].

[221] L. D. McLerran and R. Venugopalan, *Computing quark and gluon distribution functions for very large nuclei*, *Phys.Rev.* **D49** (1994) 2233–2241, [hep-ph/9309289].

[222] L. D. McLerran and R. Venugopalan, *Green's functions in the color field of a large nucleus*, *Phys.Rev.* **D50** (1994) 2225–2233, [hep-ph/9402335].

[223] A. Krasnitz and R. Venugopalan, *Nonperturbative computation of gluon minijet production in nuclear collisions at very high-energies*, *Nucl.Phys.* **B557** (1999) 237, [hep-ph/9809433].

[224] A. Krasnitz and R. Venugopalan, *The Initial energy density of gluons produced in very high-energy nuclear collisions*, *Phys.Rev.Lett.* **84** (2000) 4309–4312, [hep-ph/9909203].

[225] A. Muronga, *Causal theories of dissipative relativistic fluid dynamics for nuclear collisions*, *Phys.Rev.* **C69** (2004) 034903, [nucl-th/0309055].

[226] G. Denicol, T. Kodama, and T. Koide, *The effect of shear and bulk viscosities on elliptic flow*, *J.Phys.* **G37** (2010) 094040, [arXiv:1002.2394].

[227] G. Denicol, T. Koide, and D. Rischke, *Dissipative relativistic fluid dynamics: a new way to derive the equations of motion from kinetic theory*, *Phys.Rev.Lett.* **105** (2010) 162501, [arXiv:1004.5013].

[228] R. Baier, P. Romatschke, and U. A. Wiedemann, *Dissipative hydrodynamics and heavy ion collisions*, *Phys.Rev.* **C73** (2006) 064903, [hep-ph/0602249].

[229] U. W. Heinz, *Early collective expansion: Relativistic hydrodynamics and the transport properties of QCD matter*, arXiv:0901.4355.

[230] B. Schenke, S. Jeon, and C. Gale, *Elliptic and triangular flow in event-by-event (3+1)D viscous hydrodynamics*, *Phys.Rev.Lett.* **106** (2011) 042301, [arXiv:1009.3244].

[231] J. Casalderrey-Solana, M. P. Heller, D. Mateos, and W. van der Schee, *From full stopping to transparency in a holographic model of heavy ion collisions*, *Phys. Rev. Lett. 111,* **181601** (2013) 181601, [arXiv:1305.4919].

[232] W. van der Schee, P. Romatschke, and S. Pratt, *A fully dynamical simulation of central nuclear collisions*, *Phys.Rev.Lett.* **111** (2013) 222302, [arXiv:1307.2539].

[233] J. Berges, D. Gelfand, and D. Sexty, *Amplified Fermion Production from Overpopulated Bose Fields*, *Phys.Rev.* **D89** (2014) 025001, [arXiv:1308.2180].

[234] T. Epelbaum and F. Gelis, *Fluctuations of the initial color fields in high energy heavy ion collisions*, *Phys.Rev.* **D88** (2013) 085015, [arXiv:1307.1765].

[235] P. B. Arnold and G. D. Moore, *QCD plasma instabilities: The NonAbelian cascade*, *Phys.Rev.* **D73** (2006) 025006, [hep-ph/0509206].

[236] S. Schlichting, *Turbulent thermalization of weakly coupled non-abelian plasmas*, *Phys.Rev.* **D86** (2012) 065008, [arXiv:1207.1450].

[237] P. B. Arnold and G. D. Moore, *The Turbulent spectrum created by non-Abelian plasma instabilities*, *Phys.Rev.* **D73** (2006) 025013, [hep-ph/0509226].

[238] J. Berges, K. Boguslavski, S. Schlichting, and R. Venugopalan, *Basin of attraction for turbulent thermalization and the range of validity of classical-statistical simulations*, arXiv:1312.5216.

[239] J. Berges and D. Sexty, *Bose condensation far from equilibrium*, *Phys.Rev.Lett.* **108** (2012) 161601, [arXiv:1201.0687].

[240] T. Epelbaum and F. Gelis, *Role of quantum fluctuations in a system with strong fields: Spectral properties and Thermalization*, *Nucl.Phys.* **A872** (2011) 210–244, [arXiv:1107.0668].

[241] J. Berges, J. Pruschke, and A. Rothkopf, *Instability-induced fermion production in quantum field theory*, *Phys.Rev.* **D80** (2009) 023522, [arXiv:0904.3073].

[242] L. Landau and E. Lifshitz, *Mechanics*. Butterworth Heinemann. Butterworth-Heinemann, 1976.

[243] W. Nolting, *Analytische Mechanik*. Grundkurs: Theoretische Physik / Wolfgang Nolting. Springer, 2011.